



12th International Conference on Magnetic Resonance Microscopy

“The Heidelberg Conference”

&

The Colloquium on Mobile NMR

Book of Abstracts



August 25th – 29th 2013 Cambridge, England, UK

www.ceb.cam.ac.uk/ICMRM12



Conference Schedule

Time	Sunday 25th August	Monday 26th August	Tuesday 27th August	Wednesday 28th August	Thursday 29th August
09:00		Plenary 2: Klaas Prüssmann	Biomedical 1 09:00 - 10:40	Plenary 3: Warren S. Warren	
10:00	Arrival and Registration: 10:00 - 17:00	MR Hardware 09:50 - 11:00		Exotic and Emerging NMR 09:50 - 10:50	Flow and Diffusion 1 09:30 - 10:50
11:00	Educational 1 11:20 - 13:00	Coffee 11:00 - 11:30	Coffee 10:40 - 11:20	Coffee 10:50 - 11:20	Coffee 11:00 - 11:30
12:00		Hyperpolarisation 11:30 - 13:00	Biomedical 2 11:20 - 13:00	MR Microscopy 11:20 - 13:00	Engineering and Materials 11:20 - 13:00
13:00	Lunch in Poster and Exhibition Halls 13:00 - 14:30	Lunch in Poster and Exhibition Halls 13:00 - 14:30	Lunch in Poster and Exhibition Halls 13:00 - 14:30		Lunch in Poster and Exhibition Halls 13:00 - 14:15
14:00					Flow and Diffusion 2 14:15 - 15:35
15:00	Educational 2 14:30 - 16:10	Low field - Colloquium on Mobile NMR 14:30 - 16:30	Young Investigators 14:30 - 16:30		Coffee 15:35 - 16:00
16:00	Coffee 16:10 - 16:50	Coffee and Poster Session A (Odd Numbers) 16:30 - 18:30	Coffee and Poster Session B (Even Numbers) 16:30 - 18:30	Excursions to Duxford and the Cambridge Colleges 13:00 - 17:30	General Meeting 16:00 - 16:50
17:00	Conference Opening and Plenary 1: Lucio Frydman				Close
18:00	Opening Drinks and Buffet in the Poster and Exhibition Halls 18:00 - 21:00	Dinner in Dining Hall 18:30 - 20:00	Dinner in Dining Hall 18:30 - 20:00		
19:00				Pre-Dinner Reception 18:45 - 19:30	
20:00				Conference Dinner Trinity Great Hall 19:30 - 22:00	

Programme

Sunday 25th August

Educational session 1

Chair: Eiichi Fukushima

ID	Time	Speaker	Title
Edu1	11:20	James Keeler	Introduction to NMR relaxation
Edu2	12:10	Sarah Codd	Flow and diffusion

13:00 - 14:30 Lunch

Educational session 2

Chair: Siegfried Stapf

ID	Time	Speaker	Title
Edu3	14:30	Craig Meyer	Non-cartesian sampling and sparse image reconstruction
Edu4	15:20	Malcolm Levitt	Long-lived spin states

16:10 - 16:50 Coffee

Conference Opening and Plenary Session 1

ID	Time	Speaker	Title
	16:50	Lynn Gladden	Introductory remarks
Plen1	17:00	Lucio Frydman	Ultrafast multidimensional magnetic resonance: Principles and applications

18:00 - 21:00
Buffet Dinner in the Poster and
Exhibition Halls
Sponsored by Bruker



Monday 26th August

Plenary Session 2

Chair: Bernhard Blümich

ID	Time	Speaker	Title
Plen2	09:00	Klaas Prüssmann	Mind the field - dynamic magnetometry in MR systems

Session: MR Hardware

Chair: Bernhard Blümich

ID	Time	Speaker	Title and authors
O1	09:50	Patrick Vogel	A first bimodal MPI/MRI tomograph <i>P. Vogel, S. Lothar, M.A. Rückert, W.H. Kullmann, P.M. Jakob, F. Fidler, V.C. Behr</i>
O2	10:10	Dimitrios Sakellariou	A portable permanent-magnet analyzer for High-Resolution ¹ H Magic Angle Spinning NMR spectroscopy <i>A. Soleilhavoup, C. Hugon, J. Alonso, A. Guiga and D. Sakellariou</i>
O3	10:30	Bruce Balcom	Magnetic resonance imaging of fluids in porous media with metallic core holders <i>B. Balcom</i>
	10:50	Andrew Coy	Vendor Presentation: Magritek

11:00 - 11:30 Coffee

Session: Hyperpolarisation

Chair: Malcolm Levitt

ID	Time	Speaker	Title and authors
O4	11:30	Simon Duckett	Utilizing parahydrogen derived hyperpolarization to improve MRI <i>S. B. Duckett, R. E. Mewis, K. D. Atkinson, G. G. R. Green, R. A. Green, L. A. R. Highton and L. S. Lloyd</i>
O5	12:00	Igor Koptug	Parahydrogen-induced hyperpolarization for MR imaging and spectroscopic applications <i>K.V. Kovtunov, V.V. Zhivonitko, I.V. Skovpin, D.A. Barskiy, O.G. Salnikov, I.V. Koptug</i>
O6	12:20	Thomas Prisner	Dynamic nuclear polarization at 9.2 T <i>V. Denysenkov, P. Neugebauer, J. Krummenacker, T. Prisner</i>
O7	12:40	Joseph Six	Hyperpolarized ¹²⁹ Xe as MRI contrast agent in combustion processes <i>J. S. Six, K.F. Stupic, G.E. Pavlovskaya, and T. Meersmann</i>

13:00 - 14:30 Lunch

Session: Colloquium on Mobile NMR

Chair: Peter Blümler

ID	Time	Speaker	Title and authors
O8	14:30	Katsumi Kose	Outdoor plant measurements using compact/mobile MRI systems <i>K. Kose, Y. Terada and T. Haishi</i>
O9	15:00	Stephen Altobelli	Earth's field NMR for detection of thin layer of liquids <i>S. A. Altobelli, E. Fukushima, A. F. McDowell, T. Z. Zhang</i>
O10	15:20	Martin Hürlimann	Broadband CPMG sequence with composite excitation and short composite refocusing pulses <i>V. D.M. Koroleva, S. Mandal, Y.-Q. Song, M. D. Hürlimann</i>
O11	15:40	Petrik Galvosas	Determining pore length scales and connectivity of rock cores using low-field NMR <i>H. Liu, M. N. d' Eurydice, P. Galvosas</i>
O12	16:00	Ernesto Danieli	Compact and homogeneous Halbach arrays for applications to NMR spectroscopy and MRI <i>E. Danieli, J. Perlo, J. Perlo, B. Blümich and F. Casanova</i>

16:30 - 18:30
Poster Session A (Odd Numbers)
Sponsored by MR Solutions



18:30 - 20:00
Dinner in the Dining Hall
Sponsored by Shell



Tuesday 27th August

Session: Biomedical 1

Chair: Klaas Prüssmann

ID	Time	Speaker	Title and authors
O13	09:00	Axel Haase	Observation of in vivo metabolism using hyperpolarized ¹³ C MR <i>A. Haase</i>
O14	09:30	Alessandro Proverbio	Multimodality characterization of microstructure by the combination of diffusion NMR and time domain diffuse scattering spectroscopy <i>A. Proverbio, B. Siow, A. Gibson, D. Alexander</i>
O15	09:50	Yang Xia	Critical points in articular cartilage where T ₁ change is balanced under different gadolinium concentrations and mechanical strains <i>Y. Xia, N. Wang</i>
O16	10:10	Jim Pope	NMR Micro-imaging of the human eye <i>J.M. Pope, P.K. Verkicharla, F. Sepehrband, S. Kasthurirangan and D.A. Atchison</i>
	10:30	Bruker	Vendor Presentation: Bruker

10:40 - 11:20 Coffee

Session: Biomedical 2

Chair: Yang Xia

ID	Time	Speaker	Title and authors
O17	11:20	John Pauly	Unconventional slice-selective RF pulses and pulse pairs <i>J. M. Pauly</i>
O18	11:50	Thomas Meersmann	Lung surface sensitive MRI contrast using hyperpolarized ⁸³ Kr <i>J.S. Six, T. Hughes – Riley, D.M.L. Lilburn, A.C. Dorkes, K.F. Stupic, D.E. Shaw, P.G. Morris, I.P. Hall, G.E. Pavlovskaya, and T. Meersmann</i>
O19	12:10	Gary Hui Zhang	Detailed laminar characteristics of the neocortex revealed by NODDI <i>M. Kleinnijenhuis, H. Zhang, D. Wiedermann, D. Norris, A-M. van Cappellen van Walsum</i>
O20	12:30	Siegfried Stapf	Low-field investigations of enzymatically degraded articular cartilage and its constituents <i>E.Rössler, C. Mattea, S. Stapf</i>
	12:50	Oxford Instruments	Vendor Presentation: Oxford Instruments

13:00 - 14:30 Lunch

Session: Young Investigators
Sponsored by Schlumberger

Chair: Bruce Balcom



ID	Time	Speaker	Title and authors
YI1	14:30	Einar Fridjonsson	MR measurements of colloid suspension dynamics in micro-capillary and porous media <i>E. O. Fridjonsson, M. L. Johns, S. L. Codd, and J. D. Seymour</i>
YI2	14:50	Stefan Hertel	Magnetic resonance Pore Imaging as a novel tool for porous media characterization <i>S. A. Hertel, M. Hunter and P. Galvosas</i>
YI3	15:10	Nicolas Joudiou	First HR-MAS NMR Slice-Localized Spectroscopy (S.L.S.) and C.S.I. of living drosophila <i>N. Joudiou, F. Louat, M. Decoville, S. Mème, J-C. Beloeil, V. Sarou Kanian</i>
YI4	15:30	Alexander Tayler	Exploring the fundamental hydrodynamics of turbulent single and multiphase flows using Compressed Sensing Spiral MRI <i>A. B. Tayler, M. Benning, A. J. Sederman, D. J. Holland and L. F. Gladden</i>
YI5	15:50	Joshua Bray	Turbulent Rayleigh-Bénard convection in a supercritical fluid <i>Joshua M. Bray, Sarah L. Codd, Joseph D. Seymour</i>
YI6	16:10	Eva Paciok	The Grotthuß-Mechanism in nanoporous silicates and its implications to diffusion studies in natural porous media <i>E. Paciok, A. Haber, M. Van Landeghem, and B. Blümich</i>

16:30 - 18:30	Poster Session B (Even Numbers) Sponsored by Oxford Instruments	 <i>The Business of Science®</i>
---------------	--	--

18:30 - 20:00	Dinner in the Dining Hall
---------------	----------------------------------

Wednesday 28th August

Plenary Session 3

Chair: Joe Seymour

ID	Time	Speaker	Title
Plen3	09:00	Warren S. Warren	New approaches to enhance signal and contrast in MR microscopy

Session: Exotic and Emerging NMR**Chair: Joe Seymour**

ID	Time	Speaker	Title and authors
O21	09:50	Peter Blümler	T2* of minutes to 100 hours! HP-gases for spin clocks and magnetometers <i>P. Blümler, A. Nikiel, M. Repetto, K. Tullney, S. Karpuk, W. Heil</i>
O22	10:10	Clare Grey	Following function in real time: New NMR and MRI methods for studying structure and dynamics in fuel cells and supercapacitors <i>C. Grey</i>
O23	10:30	Yi-Qiao Song	Two-dimensional NQR using ultra-broadband electronics <i>S. Mandal, Y.-Q. Song</i>

10:50 - 11:20 Coffee**Session: MR Microscopy****Chair: Henk Van As**

ID	Time	Speaker	Title and authors
O24	11:20	Jürgen Hennig	MicroMR with Multiarray-Coils <i>J. Hennig, J.G. Korvink</i>
O25	11:50	Tim Brox	Stress coupled NMR velocimetry <i>T.I. Brox, R. Fischer, S. Kuczera, W. Kittler, B.S. Douglass, and P. Galvosas</i>
O26	12:10	Melanie Britton	Magnetic Resonance Imaging of electrochemical systems <i>M. M. Britton</i>
O27	12:30	Luisa Ciobanu	3D Diffusion prepared FISP for single cell MR microscopy <i>I.O. Jelescu, F. Geffroy, D. Le Bihan, L. Ciobanu</i>

13:00 - 17:30 Conference Excursion**18:45 - 22:00 Dinner in Trinity Great Hall
Sponsored by Magritek**

Thursday 29th August

Session: Flow and Diffusion 1

Chair: Yi-Qiao Song

ID	Time	Speaker	Title and authors
O28	09:30	Peter Jakob	Molecular and cellular MRI: Challenges and potential solutions <i>P. Jakob</i>
O29	10:00	Martin Benning	Reducing acquisition times of dynamic MRI measurements via contrast-enhanced compressed sensing <i>M. Benning, D. Allen, J. Beech, L. Gladden, D. Holland, V. Kersemans, M. Mantle, S. Smart, C. Schönlieb, T. Valkonen</i>
O30	10:15	Christoph Arns	A pore-scale analysis of common capillary pressure measurements using 1D NMR and tomographic images <i>C.H. Arns, I. Shikhov</i>
O31	10:35	Yaniv Katz	Optimization of dPDFG for the quantification of pore size distribution <i>Y. Katz and U. Nevo</i>

10:50 - 11:20 Coffee

Session: Engineering and Materials

Chair: Melanie Britton

ID	Time	Speaker	Title and authors
O32	11:20	Ben Newling	Eddy currents & turbulent eddies <i>B. Newling, A. Adair, O. Adegbite, F. Goora, B. J. Balcom</i>
O33	11:50	Michael Johns	Structural information from MRI signal moment analysis: Application to ROM biofouling <i>M.L. Johns, E.O. Fridjonsson, S.J. Vogt and S.A. Creber</i>
O34	12:10	Feng Deng	A new sequence for measuring NMR relaxation in flowing fluid <i>F. Deng, L. Xiao, G. Liao, Y. Wu, W. Xu, C. He</i>
O35	12:25	Sarah Vogt	Displacement-relaxation correlations of biofilm growth in porous media <i>S. J. Vogt, A. B. Sanderlin, J. D. Seymour, and S. L. Codd</i>
O36	12:40	Urša Mikac	The influence of media pH and ionic strength on hydrogel formation and drug release from xanthan tablets <i>U. Mikac, A. Sepe, J. Kristl, and S. Baumgartner</i>

13:00 - 14:15 Lunch

Session: Flow and Diffusion 2**Chair: Petrik Galvosas**

ID	Time	Speaker	Title and authors
O37	14:15	Daniel Topgaard	Magic-angle spinning of the q-vector in diffusion MRI <i>D. Topgaard</i>
O38	14:45	Susan Law	Sizing of reverse micelles in microemulsions using NMR measurements of diffusion <i>S.J. Law, M.M. Britton</i>
O39	15:00	Guangzhi Liao	NMR responses in porous media with digital rock technique <i>T. An, L. Xiao, G. Liao, X. Li, H. Liu, Z. Zhang</i>
O40	15:15	Henk Van As	TD-NMR, DOSY and MRI of chloroplasts? <i>H. Van As, E. Nonhebel, S. Pagadala</i>

15:35 - 16:00 **Coffee****16:00 - 16:50** **General Meeting****16:50** **Close**

Welcome to ICMRM12

Dear Colleagues,

It is a pleasure to welcome you to the 12th International Conference on Magnetic Resonance Microscopy (ICMRM12) in Cambridge, UK held under the auspices of the Spatially Resolved Magnetic Resonance (SRMR) Division of the AMPERE (*Atomes et Molécules Par Études Radio-Électriques*) Society. The ICMRM is a biennial meeting and this year's conference marks 22 years of enhancing scientific knowledge, understanding and cooperation in this research area.

The conference series began with the "Heidelberg Conference" in 1991 and 1993, and moved to Würzburg in 1995. Because of the diverse international character of the conference attendees the original Executive Committee of the SRMR Division planned that the conference should ultimately rotate between Europe, North America and Asia in order to further the aim of international understanding and cooperation. Since ICMRM4 in Albuquerque (New Mexico) the conference has been held in Heidelberg, Nottingham, Snowbird (Utah), Utsunomiya (Japan), Aachen, Montana, Beijing and returns to the UK this year.

The meetings have regularly attracted 160-190 delegates from all over the world: this year the conference welcomes 178 attendees from 15 countries, delivering 4 educational tutorials, 3 plenaries, 40 oral research presentations and 99 poster research presentations, details of which are found within these pages.

As well as a poster competition for graduate students and the image beauty competition, the Young Investigators session will take place on Tuesday afternoon. The six finalists have been chosen by a set of international reviewers based on the quality of their submitted extended abstracts; and the winner of this prestigious award will be announced at the Conference Dinner on Wednesday night. This year the award is being renamed the Sir Paul Callaghan Young Investigators Award, in memory of the contribution of one of the leading scientists in our field. Paul will be forever remembered within this community for his own scientific advances along with his infectious enthusiasm, and his development and interest in the research of young scholars, many of whom now play integral and leading roles in the research presented at this conference.

The local organizers welcome you to Fitzwilliam College and the University of Cambridge. The University of Cambridge has recently celebrated its 800th anniversary and is a great historic seat of learning, providing a stimulating, world class location for academic cooperation, discussion and scientific development. The two colleges which will be accommodating the conference represent contrasting elements of the University of Cambridge: Trinity College was founded by King Henry VIII in 1546, and is the *alma mater* of many illustrious scientists (Charles Babbage, Sir Isaac Newton, J. J. Thompson, Lord Rayleigh, Ernest Rutherford, among many others) and famous figures (Charles, Prince of Wales, Lord Byron, A. A. Milne, once more to name but a few). Fitzwilliam College began in 1869 as a non-collegiate institution, providing Cambridge education to undergraduates who were unable to afford membership of a college. The college as it stands today was built in 1966. We hope that you will find intellectual stimulation with many other participants throughout the conference. It is also an opportunity to renew old friendships and develop new ones.

We would like to acknowledge the very generous support of ICMRM12 by all of our sponsors. I hope you will think of them when tucking into your cheese and port in the Great Hall at Trinity College, or sheltering under your umbrella! Many are exhibiting here and I encourage you to visit their stands to see what new initiatives are being developed in commercial magnetic resonance.

"To explain all nature is too difficult a task for any one man or even for any one age. 'Tis much better to do a little with certainty, & leave the rest for others that come after you, than to explain all things by conjecture without making sure of any thing." (Isaac Newton, Trinity College)

Andy Sederman and Lynn Gladden
Conference Chairs

Division of Spatially Resolved Magnetic Resonance of AMPERE Society

The Division was founded in 1995 during the 3rd meeting on Magnetic Resonance Microscopy. The purpose of the division is to advance the subject of Spatially Resolved Magnetic Resonance by means of the International Conference organized biennially across the world along with symposia, summer schools and workshops. The governing organization of the Division consists of the Executive Committee, the Division Committee and the General Membership composed of conference attendees who are automatically members of the AMPERE Society.

Executive Committee Meeting:

The Executive Committee is responsible for the management, administration and finances of the SRMR Division. The following members of the Executive Committee are asked to attend the Executive Committee Meeting

Chair:	B. Balcom (CAN)
Vice Chair:	M. Johns (AUS)
Treasurer:	H. Van As (N)
Secretary General:	S. Codd (US)
Vice Secretary General:	I. Koptug (R)
Past-Conference Chair:	L. Xiao (C)
Conference Chair:	A. Sederman/L. Gladden (UK)
Past Chair:	B. Blümich (D)
Advisors:	E. Fukushima (US) A. Haase (D)

The meeting will take place in the Music room during the Monday lunch break. Lunch will be provided.

Division Committee Meeting:

The Division Committee is responsible for carrying out the business of the Division, including the scientific organization of the conference. The following members of the Division Committee are asked to attend the Division Committee Meeting.

All above members of the Executive Committee

(2007-2013) A. Coy, K. Kose, Y. Seo

(2009-2015) S. Appelt, P. Basser, L. Bouchard, M. Britton, F. Casanova, S. Handa, L. Ciobanu, M. Hurlimann, B. Manz, M. McCarthy, B. Newling, D. Sakellariou, A. Sederman, I. Sersa

(2011-2017) J. Brown, P. Glover, J. Hennig, D. Holland, M. Hunter, S. Stapf, Y.-Q. Song, R. Xie, P. Yang

The meeting will take place in the Wilson Court common room during the Tuesday lunch break. Lunch will be provided.

General Meeting:

The General Meeting has the final authority of the Division. All conference attendees are automatically members of the General Meeting and are encouraged to attend. The General Meeting will take place in the Auditorium on Thursday afternoon.

Conference General Information

Organising committee:

Andy Sederman (Co-Chair)	University of Cambridge
Lynn Gladden (Co-Chair)	University of Cambridge
Daniel Holland	University of Cambridge
Melanie Britton	University of Birmingham
Mick Mantle	University of Cambridge
Mike Johns	University of Western Australia

MRRC, University of Cambridge student helpers

Mohamed Ainte	Luke Baker	Oliver Bartlett	Thomas Blythe
Pierre Bräuer	Jules Camp	Chen (Charlie) Chen	Hilary Fabich
Yunan Peng	Zhi (George) Qiao	Nicholas Ramskill	Matthew Renshaw
Christine Schmaus	Yuting (Bella) Wu	Qingyuan Zheng	Kostas Ziovas

Staff

Tricia Ellis-Evans	Pace Projects
--------------------	---------------

Venues:

The conference is being held on site at Fitzwilliam College (see maps) and all talks will be held in the Auditorium. Exhibitors and posters (which can be left up all week) will be located on the 1st floor of the Hall building in rooms 13 and 17 on the map of Fitzwilliam.

Coffee and tea breaks as well as lunches and the opening drinks/buffet will also be held in rooms 13 and 17 (some seating is available in room 16).

Dinner on Monday and Tuesday will be in the Dining Hall.

The conference dinner is being held at Trinity College – see below for details.

Registration and help desk

The registration and help desk will be situated outside the Auditorium on Sunday and will then move to the 1st floor of the Hall building. The desk will remain open during the conference hours for the duration of the conference.

Excursions

Two parallel excursions will take place on Wednesday afternoon. No lunch will be provided in college.

Tour of Cambridge Colleges – This is a tour around some of Cambridge's most historic Colleges including King's College and its chapel. The tour will start from the Market Square in the centre of Cambridge at 14:30 and last approximately 2 hours. Cost £20.

Imperial War Museum Duxford – This museum is home to an impressive collection of over two hundred aircraft as well as tanks, military vehicles and boats. Transport (leaving immediately after the second morning session) and a packed lunch will be provided. The return bus will leave Duxford at 16:45. Cost £30.

There are still a limited number of tickets available for both of these tours which can be booked at the help desk.

Further details can be found on the conference website or at the help desk.

Conference Dinner

The conference dinner will be held in Trinity College on Wednesday evening. Trinity College is 15-20 mins walk (just under a mile) from Fitzwilliam College and can be accessed either from Bridge Street or from Queen's Road. Feel free to make your own way there but student helpers will act as guides leaving Fitzwilliam College Porters' Lodge at 18:30 and 18:45.

There is a drinks reception from 18:45-19:30 under the Wren Library in Neville's Court followed by the Conference Dinner in the Great Hall. A College plan can be found at www.trin.cam.ac.uk/?pageid=289

Dress code: Jacket and tie preferred (Gowns need not be worn!)

Local transport information

Taxis – There are a number of local taxi firms. Panther (01223 715715) and A1 Cabco (01223 525555) have large fleets. A taxi between the railway station and Fitzwilliam College is likely to cost around £10.

Buses – Citi5 and Citi6 depart from just outside Fitzwilliam College on Huntingdon Road and go to the centre of Cambridge (Bridge Street stop is close to the entrance to Trinity College). To get to the station, a change of bus is required at Emmanuel Street (Citi1, Citi3, Citi7 and Citi8 all go to the station).

Bikes – Bikes are available to hire from a number of places in Cambridge. www.stationcycles.co.uk/ at the railway station is one of the most convenient and can also be found under the Grand Arcade shopping centre near the Market Square..

Foot – Cambridge is a small city and most of it can be easily accessed on foot. Even the station, the far side of the city, is only 2.3 miles (~45 mins) from Fitzwilliam College.

Internet access at Fitzwilliam College

WiFi is available in all meeting rooms and communal areas in college and is available in most of the college accommodation. The password is available from the help desk.

If you cannot get WiFi access in your room, wired access is available – we will have a limited number of cables which can be borrowed.

College bar and drinks tickets

Additional drinks can be bought at the bar with cash only (credit/debit cards are not accepted). The bar will be open until 23:30 on Sunday, Monday and Tuesday.

Cash

The nearest ATM to Fitzwilliam College is at the Esso garage marked on the Map of Cambridge. A small charge is made for withdrawals at this ATM. Most ATMs situated in banks will not charge for cash withdrawals.

Public holiday

Please be aware that Monday 26th August is a national holiday in England. Shops and public transport are likely to operate reduced hours/services similar to Sundays.

Presentation and Competition Instructions

Oral presentations

The duration of individual talks is given in the program. Please time your talk so that you allow approximately 5 minutes for questions and discussion. A technical assistant will be available 45 minutes before the 1st session of the day if you wish to load your presentation to the laptop or test your own laptop for compatibility. Please try and test your presentation the day before your session.

Poster presentations

Posters may stay up during the entire conference, from Sunday morning until the close of the conference on Thursday afternoon. Poster boards are 2m × 1m in a portrait orientation. Tape will be provided to attach your posters to the boards.

Poster Session A: 16:30-18:30 on Monday – Odd numbered posters

Poster Session B: 16:30-18:30 on Tuesday – Even numbered posters

Student poster competition

Please attach a green label identifying your poster as eligible for this competition. Labels can be obtained from the help desk. You must be a student presenting your own work to be eligible.

Image beauty competition

As in previous years, we will be having an Image Beauty Competition. Please bring along your entries, which can be submitted either at the conference help desk or by putting them up on the image beauty poster board. Remember – anything goes: artistic or beautiful, artefact or perfect - even ugly, all will be judged! Feel free to submit multiple entries. The winners will be announced after the Conference Dinner.

More details and a list of previous winners can be found at:

https://files.oakland.edu/users/xia/web/ICMRM_BeautyContest/ICMRM_BeautyContest.html

Instructions for Exhibitors

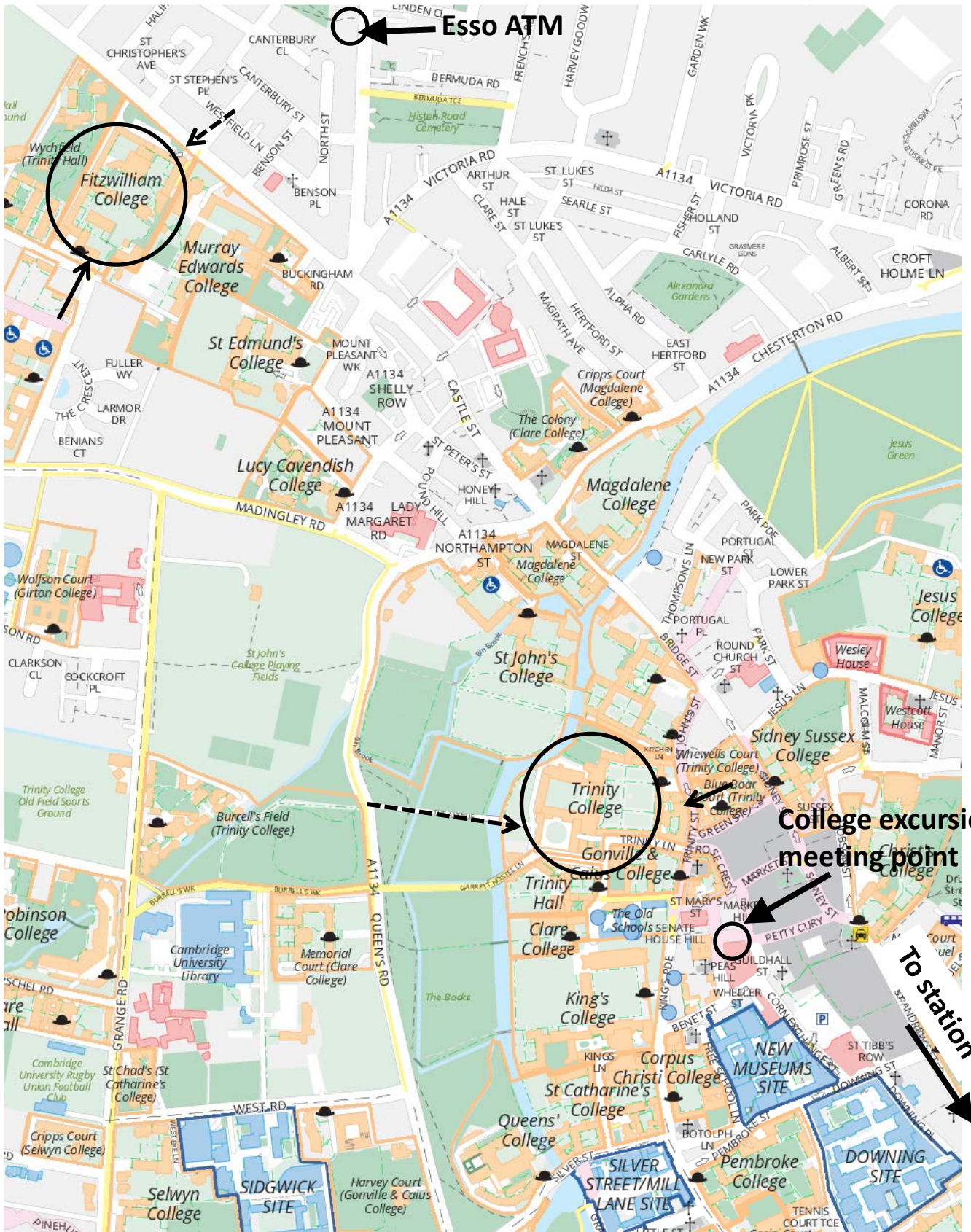
Exhibition space is in the same rooms as the poster sessions. Setup can begin at 10:00 on Sunday 25th August and the space must be cleared by 17:00 on Thursday 29th August.

Map of Fitzwilliam College



Map of Cambridge

Also at <http://map.cam.ac.uk/>



- College front entrance
- College rear entrance

Plenary Lectures

Plen 1

Ultrafast multidimensional magnetic resonance: principles and applications

Lucio Frydman

Department of Chemical Physics, Weizmann Institute of Science, Rehovot, 76100, Israel

Over a decade ago we proposed and demonstrated a scheme enabling the acquisition of arbitrary multidimensional NMR spectra and/or images (MRI), within a single scan. This is by contrast to the hundreds or thousands of scans that are usually needed to collect this kind of data. Provided that the target molecule's signal is sufficiently strong, the acquisition time of nD MR scans can thus be shortened by several orders of magnitude. This new “ultrafast” methodology is compatible with existing multidimensional pulse sequences and can be implemented using conventional hardware. The manner by which the spatiotemporal encoding of the MR interactions proceeds will be summarized. The new horizons that are opened by these protocols will also be exemplified, particularly in connection with a variety of MRI and MRS projects we are currently involved with in preclinical and clinical fields. The incorporation into these experiments of nuclear hyperpolarization procedures capable of increasing the sensitivity of these single-scan nD MR acquisitions by factors ranging from 10^3 - 10^6 , will also be assessed.

Plen 2

Mind the field – dynamic magnetometry in MR systems

K.P. Pruessmann^a

^aInstitute for Biomedical Engineering, University and ETH Zurich, Zurich, Switzerland

This contribution will be dedicated to the exploration of NMR as a mechanism of performing highly sensitive measurements of magnetic fields and field dynamics in MR systems. Exploiting the strength and uniformity of the background field in MR magnet bores, field information of remarkable precision can be obtained straightforwardly by recording and analyzing NMR signals from small droplets of sample liquid contained in miniature probeheads. Using this mechanism, field resolutions down to several tens of picotesla are currently accomplished at a sampling rate of 1 kHz. Higher sampling rates up to the order of MHz are readily achieved at field resolutions in the nano- to microtesla range. The current design and modes of operation of such probes will be discussed in the first part of the presentation¹.

One major objective of magnetometry in MR systems is to enhance MRI results by recording the spatiotemporal field evolution during the imaging process and accounting for any imperfections at the image reconstruction stage². Field perturbations from 0th spatial order (uniform) to very high spatial orders frequently occur in MRI scans due to hardware imperfections, physiological susceptibility effects, and external sources. Spatiotemporal measurement of such fields is accomplished with an array of NMR probes surrounding the volume of interest³. The resulting knowledge of field evolution can then be incorporated in extended signal models that enable enhanced reconstruction by treatment as general inverse problems. In this context, special attention will be given to the important distinction between measuring the magnetic field per se and measuring its integral over time, which is required for image reconstruction purposes. The inverse problem and the current algorithms for solving it will also be briefly surveyed^{4,5}.

In recent advanced implementations, knowledge of spatiotemporal field evolution is used not only retrospectively at the reconstruction stage but also immediately for real-time field adjustments, which prove particularly useful for handling thermal hardware drifts and physiological field perturbations in in-vivo studies. Besides the immediate imaging application, measurements of spatiotemporal field evolution also serve for the characterization and calibration of MR hardware. In particular, they prove highly useful for establishing transfer properties of gradient and shim chains and for calculating compensatory pre-distortion of driving waveforms.

The final part of the presentation will be dedicated to magnetometry tasks that exploit and challenge the sensitivity limits of the NMR probing mechanism. The first of these is recording subtle fields that arise from physiological motion, particularly from cardiac motion. The second, even more challenging task is measuring the longitudinal component of nuclear magnetization in a sample by sensing its far-range magnetic field. This capability is demonstrated by direct observation of longitudinal relaxation in sample liquids, enabling highly sensitive relaxometry requiring only a single inversion preparation.

References:

1. De Zanche N et al. NMR Probes for Measuring Magnetic Fields and Field Dynamics in MR Systems. *Magnetic Resonance in Medicine* 2008;60(1):176-186.
2. Barmet C et al. Spatiotemporal Field Monitoring for MR. *Magnetic Resonance in Medicine* 2008;60(1):187-197.
3. Barmet C et al. A transmit/receive system for magnetic field monitoring of in-vivo MRI. *Magnetic Resonance in Medicine* 2009;62:269-276.
4. Wilm BJ et al. Higher-order reconstruction for MRI in the presence of spatiotemporal field perturbations. *Magnetic Resonance in Medicine* 2011;65(6):1690-1701.
5. Wilm BJ et al. Fast higher-order MR image reconstruction using singular-vector separation. *IEEE Transactions on Medical Imaging* 2012;31(7):1396-403.

Plen 3

New Approaches to Enhance Signal and Contrast in MR Microscopy

W. S. Warren

Departments of Chemistry, Radiology, Biomedical Engineering and Physics, Duke University

I will discuss two recent research directions in my lab, which are intended to address some of the fundamental limitations of conventional approaches to magnetic resonance microscopy:

1. Hyperpolarization methods may drastically increase the range of species which can be explored in magnetic resonance microscopy, but the most important issue is short T_1 relaxation times. A recent insight has been that it is possible to make extremely long-lived hyperpolarization, stored in a state which is protected by symmetry from interacting with the outside environment (such as the singlet state, $(\alpha\beta-\beta\alpha)/2^{1/2}$). The basic challenge is that the same symmetry property that reduces relaxation in such disconnected states also makes it difficult to load population into them, or later convert this population to observable magnetization for detection. The initial solution was to create singlets between chemically inequivalent spins¹, preserved using spin locking sequences or by rapid translation to very low magnetic field. However, this creates serious challenges for many imaging applications, and more recent work has focused on slightly inequivalent spins². Alternatively, ref [3] used chemical transformation to pump singlets between chemically equivalent spins. Ref. [4] drastically generalized this approach, showing that if the molecule has the right combination of couplings, it is possible to transfer population in and out of chemically equivalent singlet states at high field, using only rf pulses to make the transfer.

Here we present a variety of molecules with biologically relevant structures and long-lived states (for example using diphenylacetylene (DPA) as a building block), using combinations of ^{15}N , ^{13}C , ^{19}F and ^1H . We also present two new results which significantly extend the generality of the approach in reference 4. First we demonstrate a unique and highly counterintuitive advantage of the equivalent spin approach: the long-lived state has substantial carbon character, but can be accessed from thermal equilibrium or bulk magnetization using **only proton pulses and proton detection**. For example, DPA (with carbon-13 on the acetylene) has a proton T_1 less than 4s, but the singlet state pumped and detected only through the hydrogen channel lasts five minutes. Second, we show that a fundamental challenge to screening for useful compounds (synthesizing molecules with carbon-13 in the right positions) can be overcome by high field NMR at natural abundance, where carefully targeted sequences can select only the signal from the correct doubly labeled species. The idea of looking for doubly labeled carbon at natural abundance is not new (the INADEQUATE sequence has been used for years) but existing approaches do not work on equivalent carbons, so this required some novel pulse sequence development as well. Taken as a whole, these results significantly brighten the prospects for hyperpolarized imaging.

2. Dipolar field effects provide a unique window into subvoxel image structure⁵, on a distance scale intermediate between typical image resolution and diffusion-limited distances (tens to hundreds of microns). Recent experimental advances have enhanced sensitivity and improved our ability to look for “dipolar surprisal images”—that is to say, structural features that arise not just because the magnetization is structured, but reflect the local anisotropy. Examples primarily in tissue imaging will be presented, including temperature imaging, alternatives to diffusion tensor imaging, and distinguishing between different types of adipose tissue.

References

1. Carravetta, M., O.G. Johannessen, and M.H. Levitt, Phys. Rev. Lett 92, 153003 (2004)
2. M. Tayler and M. H. Levitt, Phys Chem Chem Phys 13, 5556–60 (2011).
3. W. S. Warren, E. R. Jenista, R. T. Branca and X. Chen, Science 323, 1711–4 (2009).
4. Y. Feng, R. M. Davis and W. S. Warren, Nature Physics 8, 831–837 (2012)
5. W. S. Warren, “Concentrated Solution Effects”, Encyclopedia of Magnetic Resonance (2011), DOI: 10.1002/9780470034590.emrstm0088.pub2

Educational

Edu 1

Introduction to NMR relaxation

James Keeler

Department of Chemistry, University of Cambridge, Lensfield Rd, Cambridge, CB2 1EW

In this tutorial session I will aim to introduce some of the key ideas needed to understand relaxation processes in NMR. Particular emphasis will be placed on understanding what a correlation function is, how this is characterized by a correlation time, and how the correlation function is related to the spectral density. For longitudinal relaxation it is also helpful to consider the dynamics of the populations of energy levels and how these are related to the z -magnetization.

A model will be presented for describing transverse relaxation based on an analogy with chemical exchange. The similarities and differences between longitudinal and transverse relaxation will be emphasized.

There will be no discussion of the details of different relaxation mechanisms or motional models, nor will experimental methods be considered.

The discussion will follow closely the approach taken in Chapter 9 of *Understanding NMR Spectroscopy*, second edition, Wiley, 2010.

Edu 2

Flow and Diffusion

Sarah L. Codd^a

Department of Mechanical Engineering, Montana State University, Bozeman, USA

The use of spin echoes to determine diffusive molecular motion was first demonstrated in 1950. In 1965 pulsed gradients (PGSE) were added and highlighted a direct relationship between the echo amplitude and the self-diffusion coefficient of the spins. This was the start of an exciting exploration into what information could be accessed by non-invasively measuring and comparing the average motion of fluids over various time windows. PGSE sequences have been developed to explore progressively shorter times and smaller distances, and to separate coherent and stochastic motion over a spectrum of times. In particular, unique information has been yielded in turbulent flows, rheology of complex fluids such as polymers, emulsions and colloids, liquid flow in porous materials, and gas transport in porous media. In this educational presentation, the range of techniques for encoding for the flow and diffusion of fluids using PGSE magnetic resonance will be covered.

Edu 3

Non-Cartesian Sampling and Sparse Image Reconstruction

Craig H. Meyer

Departments of Biomedical Engineering and Radiology, University of Virginia, USA

MRI data is acquired as samples of the spatial Fourier transform of the object. The spatial Fourier transform domain is also known as k-space, so we refer to MRI data collection as k-space sampling. The most common k-space sampling pattern is to sample on a regular Cartesian grid. Cartesian sampling has many advantages, including simple FFT image reconstruction, robustness to B₀ field inhomogeneity, and the ability to restrict the field of view (FOV) along one dimension using a receiver filter. However, non-Cartesian methods of data sampling also have advantages for certain applications. In this educational lecture, we will discuss various aspects of non-Cartesian sampling. Another alternative to fully sampling Cartesian k-space is to undersample k-space and then use prior information to effectively fill in the missing data. We will give a brief introduction to the idea of sparse data sampling and to the corresponding image reconstruction methods.

The most common non-Cartesian trajectories are radial (or projection reconstruction) and spiral trajectories. Radial trajectories collect data along a series of rotated lines in k-space. The initial MRI experiments by Paul Lauterbur used radial trajectories, and the corresponding image reconstruction problem is similar to that for computed tomography (CT). One method for radial scanning is to scan from one edge of k-space to the other, rotating the readout gradients on subsequent excitations to fill in k-space. Another method is to scan from the center of k-space out, which requires twice as many readouts for equivalent sampling. Center-out sampling enables imaging with an ultrashort echo time (UTE), which enables the imaging of very-short T₂ species. It also minimizes diffusion weighting, which makes it an excellent method for diffusion-limited MR microscopy. Spiral k-space scanning has some of the same properties as radial scanning, and can be used to collect more k-space data after an excitation than either Cartesian or radial sampling. It is thus an efficient method for rapid MRI. Both radial and spiral scanning are robust to object motion, because of the repetitive sampling of the center of k-space and the option of collecting this center at the start of the readout. We will discuss various aspects of trajectory design, including optimizing gradient waveforms under gradient constraints, variable-density scans, and 3D scans.

A number of technical issues must be addressed for a robust non-Cartesian scan. First of all, it is necessary to know the k-space location of each sample, so we will discuss k-space trajectory measurement and modeling techniques. Image reconstruction is more involved than for Cartesian scan. Gridding image reconstruction is a well-established and rapid method that involves convolving the data onto a Cartesian grid and performing an FFT. Especially for spiral scan, off-resonance effects such as B₀ field inhomogeneity and concomitant gradients can lead to image blur. We will discuss methods for correcting for off-resonance effects in image reconstruction. Finally, parallel imaging methods must be adapted for non-Cartesian scans, and we will discuss non-iterative and iterative methods of non-Cartesian parallel image reconstruction.

One method for rapid MR data collection is k-space undersampling, which means collecting data with a k-space density below the Nyquist rate. This can be used for both Cartesian and non-Cartesian scanning. Parallel imaging is one method for filling in the missing data, using the data from multiple receiver coils. It is also possible to use information about the sparsity of the data to fill in the data. One example of this is temporal sparsity in dynamic MRI, where successive images in a dynamic data set are very similar. Undersampled dynamic MR data sets can be reconstructed using a variety of methods, including kt-BLAST and Kalman filtering methods. More generally, undersampled data sets that are compressible in any domain can be reconstructed using non-linear iterative image reconstruction techniques. We will give a brief overview of these methods for sparse MR image reconstruction, which are based on the techniques of compressed sensing.

Edu 4

Long-lived spin states

Malcolm H. Levitt^a,

^aSchool of Chemistry, University of Southampton, SO17 1BJ, UK

Long-lived spin states are states of coupled magnetic nuclei that are, to some degree, isolated from the other states, under common relaxation processes. The use of long-lived states allows the experimentalist to transcend the usual "T₁ limit" on the usable lifetime of information, or polarization, that can be stored in the nuclear spin system. The topic of long-lived states is closely related to the phenomenon of spin isomers, such as that exhibited by the parahydrogen and orthohydrogen spin isomers of H₂.

One example of a long-lived state is the singlet state of a coupled pair of spins-1/2. Singlet relaxation times have been shown to exceed T₁ by more than an order of magnitude in favourable circumstances. Careful molecular design has led to singlet lifetimes exceeding 30 minutes in room-temperature solutions.

I will discuss the phenomenon of singlet nuclear spin order in a variety of contexts - including gas-phase parahydrogen, small molecules in solution, and some examples in solids. I will discuss how nuclear singlet spin order may be generated from magnetization, how it is maintained, and how it is converted back into observable magnetization.

Some recent developments in our group will be discussed, including some of the following:

- direct generation of hyperpolarized nuclear singlet order using dynamic nuclear polarization
- storage and repeated detection of hyperpolarized ¹³C nuclear singlet order in solution, over a total time of 30 minutes
- the use of ¹⁸O substitution to access long-lived nuclear singlet states
- demonstration MRI experiments involving hyperpolarized nuclear singlet order
- detection of hyperpolarized ¹³C singlet order in vivo
- modelling of nuclear singlet relaxation in solution using molecular dynamics and quantum chemistry
- NMR detection of singlet-triplet conversion between ortho-water and para-water in the solid state.
- Long-lived states in systems of 3 and 4 spins.

References:

1. M. Carravetta, O. G. Johannessen and M. H. Levitt, *Phys. Rev. Letters* **92**, 153003 (2004).
2. M. Carravetta and M. H. Levitt, *J. Am. Chem. Soc.* **126**, 6228-6229 (2004).
3. G. Pileio, M. Carravetta and M. H. Levitt, *Phys. Rev. Lett.* **103**, 083002 (2009).
4. W. S. Warren, E. Jenista, R. T. Branca and X. Chen, *Science* **323**, 1711-1714 (2009).
5. G. Pileio, M. Carravetta and M. H. Levitt, *Proc. Nat. Acad. Sci. USA* **107**, 17135-17139 (2010).
6. M. C. D. Tayler and M. H. Levitt, *Phys. Chem. Chem. Phys.* **13**, 5556-5560 (2011).
7. M. C. D. Tayler and M. H. Levitt, *Phys. Chem. Chem. Phys.* **13**, 9128-9130 (2011).
8. Y. Feng, R. M. Davis and W. S. Warren, *Nat Phys* **8**, 831-837 (2012).
9. M. H. Levitt, *Ann. Rev. Phys. Chem.* **63**, 89-105 (2012).
10. G. Pileio, J. T. Hill-Cousins, S. Mitchell, I. Kuprov, L. J. Brown, R. C. D. Brown and M. H. Levitt, *J. Am. Chem. Soc.* **134**, 17494-17497 (2012).
11. N. Salvi, R. Buratto, A. Bornet, S. Ulzega, I. Rentero Rebollo, A. Angelini, C. Heinis and G. Bodenhausen, *J. Am. Chem. Soc.* **134**, 11076-11079 (2012).
12. M. C. D. Tayler, I. Marco-Rius, M. I. Kettunen, K. M. Brindle, M. H. Levitt and G. Pileio, *J. Am. Chem. Soc.* **134**, 7668-7671 (2012).
13. A. Trabesinger, *Nat Phys* **8**, 781-782 (2012).
14. G. Pileio, S. Bowen, C. Laustsen, M. C. D. Tayler, J. T. Hill-Cousins, L. J. Brown, R. C. D. Brown, J. H. Ardenkjaer-Larsen and M. H. Levitt, *J. Am. Chem. Soc.* **135**, 5084-5088 (2013).

Young Investigators

MR measurements of colloid suspension dynamics in micro-capillary and porous media

Einar O. Fridjonsson^{a,c}, Michael L. Johns^a, Sarah L. Codd^b, Joseph D. Seymour^c*

*Current address.

^aSchool of Mechanical and Chemical Engineering, University of Western Australia, Australia

^bDepartment of Mechanical and Industrial Engineering, Montana State University, MT, USA

^cDepartment of Chemical and Biological Engineering, Montana State University, MT, USA

Colloidal suspensions are ubiquitous, occurring in many applications of soft matter¹, drug delivery², filtration technology³ and physiology (*e.g.* blood flow). The study of colloidal suspension dynamics is receiving renewed attention due to the flow control offered by microfluidic devices to manipulate complex fluid flows⁴. In this work we present the results of dynamic NMR experiments on colloidal suspensions flowing inside both a micro-capillary and porous media. This work presents the first empirical data confirming that the mean square displacement (MSD) is proportional to time to a power (α) greater than 2 (*i.e.* greater than ballistic diffusion) for concentrated colloidal suspensions ($\phi = 0.22$). The colloidal suspensions used in this work are mono-modal NMR active $1.25 \pm 0.46 \mu\text{m}$ radius colloidal particles (see Figure 1) prepared through an evaporative emulsion process⁵. The spherical particles have an oil-core, which allows for the spectral differentiation of the particles and the suspending fluid. The micro-capillary has a $125\mu\text{m}$ radius, while the porous medium is a 10mm diameter by 50mm long column, filled with $125\mu\text{m}$ radius polystyrene spheres resulting in pore throats of the order of $100\mu\text{m}$.

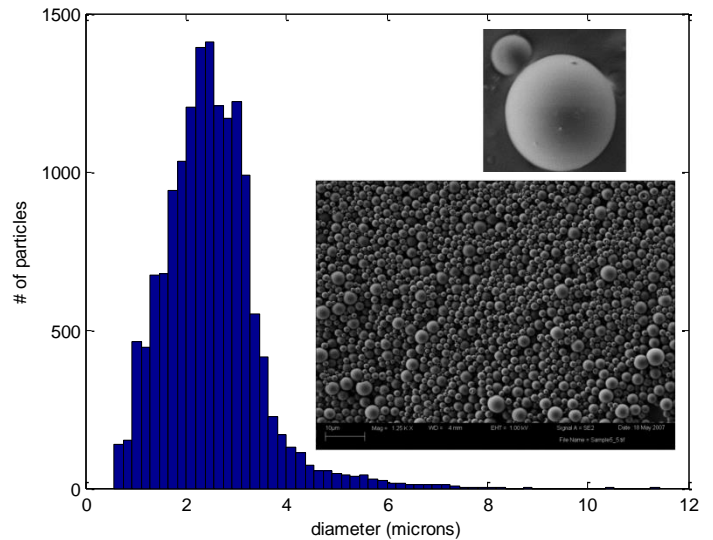


Fig. 1. Shows the particle size distribution of colloidal suspension obtained using light microscopy. A field emission microscopy (FEM) image of two neighboring particles. FEM image of a collection of particles.

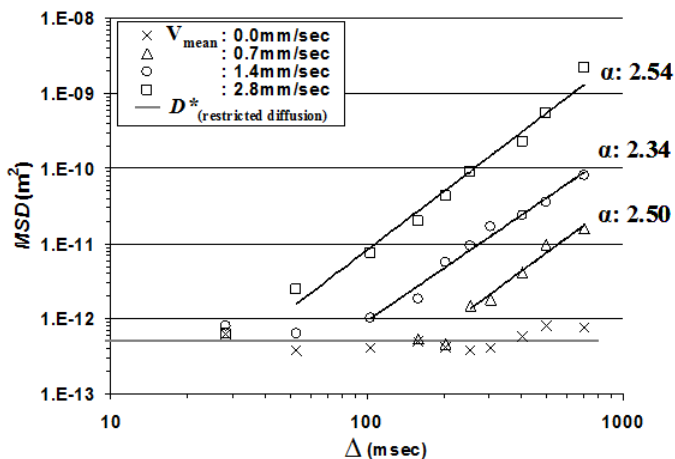


Fig. 2. Effective diffusion coefficient of colloid particles (D^*) measured at flow rates from 0.0 to 0.5mL/hr using velocity compensated PFG-SE experiments. After onset of irreversibility data is fit with $\text{MSD}(\Delta) = 2D^*\Delta^\alpha$ to obtain the anomalous time dependent collective dynamics scaling.

It is well known that for colloidal suspensions in the absence of shear the mean square displacement (MSD) is proportional to t , while in simple shear flow the MSD is proportional to t^2 . One might therefore assume that when Brownian motion and shear combine, that the MSD should be proportional to t^α with $1 < \alpha < 2$ a “fractal Brownian motion” process. It has however theoretically been shown⁶ that for isolated Brownian particles $\alpha = 3$. Figure 2 shows the colloidal MSD as a function of observation time (Δ) for a velocity compensated PFG-SE experiment, demonstrating $2.34 \leq \alpha \leq 2.54$ for a concentrated colloidal suspension ($\phi = 0.22$). Recently Griffiths and Stone⁷ have studied the non-linear hydrodynamic interactions which drive concentration fluctuations in colloidal suspensions, producing a useful theoretical framework for the

current NMR experiments; demonstrating that shear-enhanced diffusion (axial dispersion) due to cross-stream migration is significantly reduced compared with Taylor dispersion. The non-dimensional equation numerically solved for the colloidal concentration spreading in the axial direction and fit to the NMR results is⁷

$$\frac{\partial C}{\partial \tau} = \frac{\partial}{\partial s} \left(\left(\frac{1}{Pe^2} (1 + Pe \cdot f(C) + D(C)) \right) \frac{\partial C}{\partial s} \right) \quad (1)$$

where $Pe = \bar{u}R / D_m$, $\tau = \frac{\bar{u}^2 R^2 t}{L^2 D_m}$, $s = \frac{z - \bar{u}t}{L}$ and $f(C) = \frac{AC}{1 + \beta C}$, where A and β are constants.

Using this theoretical framework we analyze the results of velocity compensated PFG-SE experiments on colloidal suspensions, demonstrating μ -Rheo-NMR as a powerful tool to study microrheology⁸. This microrheological information is in-turn used to clarify and model results obtained from extensive work on colloidal transport and deposition in a model porous medium (see Figure 3) where the change in flow field due to particle deposition is investigated using MRI (Fig.3a), velocity maps (Fig.3b), NMR spectroscopy (Fig.3c), diffraction peaks (Fig.3d) and propagators (Fig.3e). Furthermore we present future experimental extensions of current high-magnetic field NMR results to low-magnetic field NMR using the same colloidal particle suspensions to investigate dynamics in consolidated (sand) material and rock matrices. These research avenues will be discussed in the context of results obtained to date and the value of the comparative high-field vs. low-field, micro- vs. macro-rheological experimental approach adopted to study colloidal suspension dynamics using NMR.

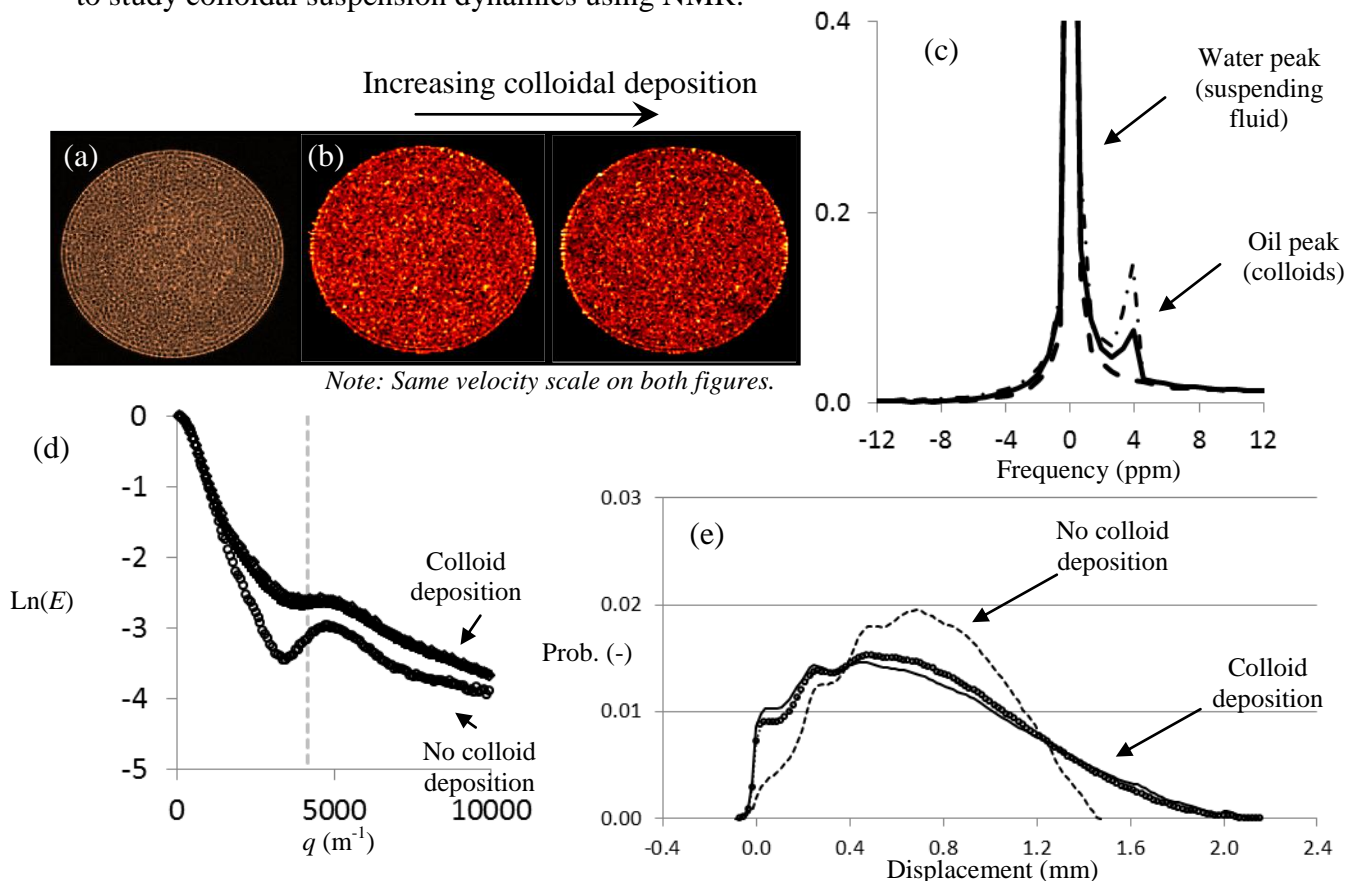


Fig. 3. Shows (a) MRI, (b) velocity maps, (c) frequency spectrum, (d) diffraction experiments, (e) propagators of water flow through model bead pack before and after colloidal particle deposition.

References:

1. W.B. Russel, D.A. Saville, W.R. Schowalter, Colloidal Dispersions, Cambridge University Press, 1992.
2. R.J. Shipley, S.L. Waters, M.J. Ellis, J. Biotech. Bioeng. 102 (2011) 382.
3. R.J. Wakeman, S.T. Thuraisingham, Filt. Sep. 26 (1989) 277.
4. T.M. Squires, S.R. Quake, Rev. Mod. Phys. 77 (2005) 977.
5. A. Loxley, B. Vincent, J. Colloid Interface Sci. 208 (1998) 49.
6. T.G.M. Van den Ven, J. Colloid Interface Sci. 62 (1977) 352.
7. M. Griffiths, H.A. Stone, EPL 97 (2012) 58005.
8. T.G. Mason and D.A. Weitz, Phys. Rev. Lett. 74 (1995) 1250.

Magnetic Resonance Pore Imaging as a novel tool for porous media characterization

S. A. Hertel^a, M. Hunter^{a,b} and P. Galvosas^a

^aMacDiarmid Institute, School of Chemical and Physical Sciences, University of Wellington, Wellington 6021, New Zealand; ^bMagritek Ltd., 6021 Wellington, New Zealand

The structure of porous materials is important in many areas of basic and applied science. Various Nuclear Magnetic Resonance (NMR) techniques are applied to study porous media on different length scales. Among them diffusive-diffraction Pulsed Gradient Spin Echo (PGSE) NMR is able to resolve features of the pore space on the micrometer scale. However, this technique only measures the modulus square of the structure factor, which yields the pore density correlation function upon Fourier transformation.

Here, we present experimental evidence that it is possible to obtain the full structure factor with a recently suggested modification² of the PGSE NMR experiment. By replacing the first narrow gradient by a long weak gradient (Fig. 1 a), the diffusing nuclei attain an average phase that corresponds to the center of mass of the pore. The second narrow gradient then imposes a local phase which is proportional to the position of the spins relative to the center of mass of their respective pores. This way the spin echo attenuation is proportional to the structure factor (not just its squared modulus), which allows one to obtain the pore density function by a simple Fourier transformation of the spin echo attenuation².

While this method promises a wealth of information that was previously inaccessible, it poses several challenges to the experimentalist. First, two very differently shaped pulses have to be incremented simultaneously, while maintaining equal areas under the gradient functions to guarantee matched gradients. Second, data acquired by MRPI converges slower to the desired structure factor with increasing observation time as compared to the standard diffusive-diffraction PGSE method, thus reaching limits imposed by NMR relaxation quickly. We solved these problems mainly by replacing the long gradient by many alternating gradient pulses interspersed by 180° RF-pulses, see Fig. 1 (c).

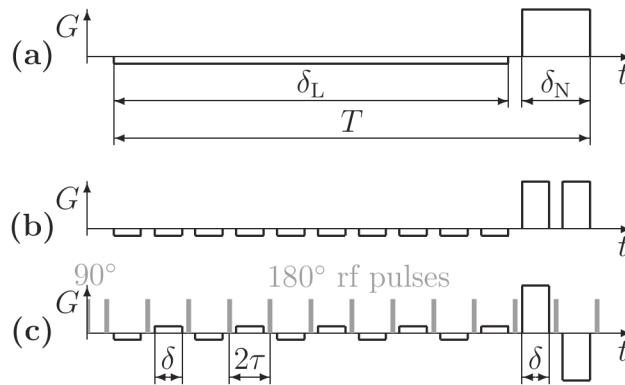


Fig. 1: Effective gradient scheme of the experiment as suggested by Laun et al. [4] (a) and its replacement used for this work (b). The actual applied gradients were alternating, interspersed with RF-pulses (c). This results in a CPMG-like pulse sequence with a leading 90° excitation pulse followed by a train of 180° pulses. Note: gradients are incremented stepwise, although this is not shown in the figure.

Our adaptation which we call Magnetic Resonance Pore Imaging (MRPI)³ creates a hybrid between Magnetic Resonance Imaging (MRI) and PGSE NMR. In particular its two-dimensional version allowed us to obtain average pore images with an unprecedented resolution as compared to conventional MRI, see Fig. 2.

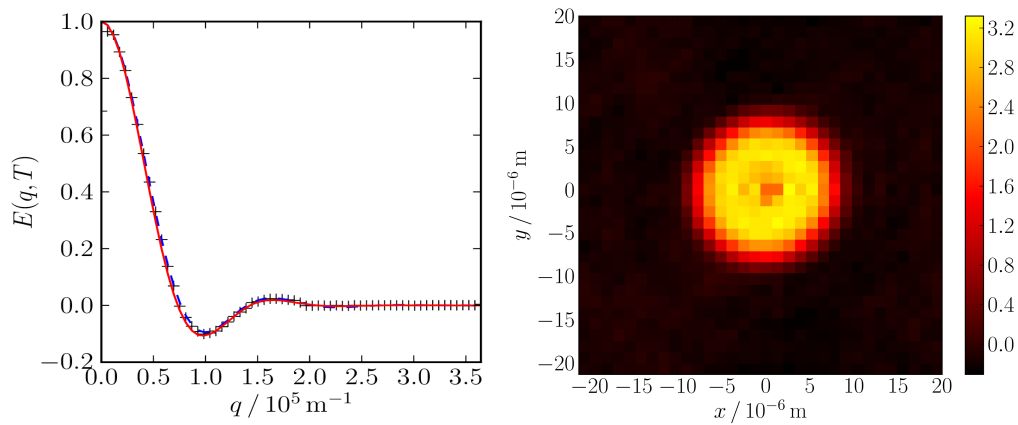


Fig.2: Real part (+) of the NMR signal delivering the average structure factor of cylindrical capillaries with a diameter of 19 μm . Solid line: Monte Carlo simulation. Dotted line: Fit of the experimental data (left). Average pore image as obtained by applying a two-dimensional MRPI pulse scheme followed by 2D Fourier transformation (right).

We demonstrate that MRPI integrates well with proven concepts of MRI and offers great potential to characterize even heterogeneous porous structures by mapping the MRPI signal on MRI images, see Fig. 3. Furthermore, we discuss the experimental implementation of MRPI and the use of Phase Incremented Echo Train Acquisition (PIETA)⁴ to study the various contributing coherence pathways to the MRPI signal.

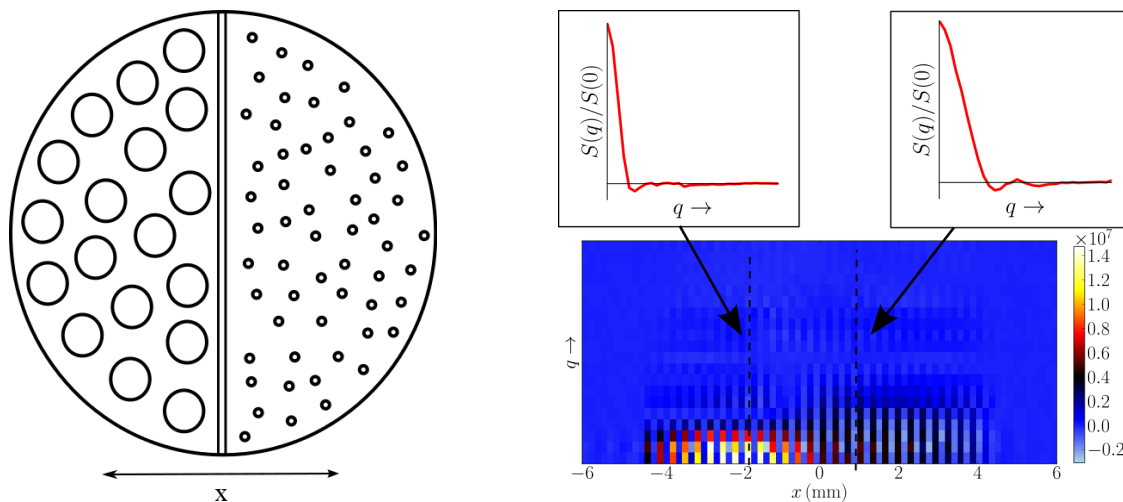


Fig.3: Sketch of the sample with two separated domains of capillaries (20 μm and 10 μm in diameter). Sketch not to scale (left). Mapping of the structure factor of the two pore sizes onto a 1D cross section in x-direction through the sample (right). In the surface plot at the bottom the two domains can clearly be distinguished. Corresponding structure factors can be extracted and analyzed separately as demonstrated in the upper two figures.

References:

1. P. T. Callaghan, A. Coy, D. Macgowan, K. J. Packer and F. O. Zelaya, Diffraction-like effects in NMR diffusion studies of fluids in porous solids, *Nature* 351 (6326), 467, (1991)
2. F. B. Laun, T. A. Kuder, W. Semmler and B. Stieltjes, Determination of the defining boundary in nuclear magnetic resonance diffusion experiments, *Phys. Rev. Lett.* 107, 048102, (2011)
3. S. Hertel, M. Hunter and P. Galvosas, Magnetic Resonance Pore Imaging, a tool for porous media research, *Phys. Rev. E* 87 (2013) 030802(R)
4. J. H. Baltisberger *et al.*, Phase incremented echo train acquisition in NMR spectroscopy, *J. Chem. Phys.* 136 (2012) 211104

YI 3

First HR-MAS NMR Slice-Localized Spectroscopy (S.L.S.) and C.S.I. of living drosophila

N. Joudiou^a, F. Louat^a, M. Decoville^a, S. Mème^a, J-C. Beloeil^a, V. Sarou Kanian^b

^aCentre de Biophysique Moléculaire, CNRS, Orléans, France; ^bConditions Extrêmes et Matériaux : Haute température et Irradiation, CNRS, Orléans, France

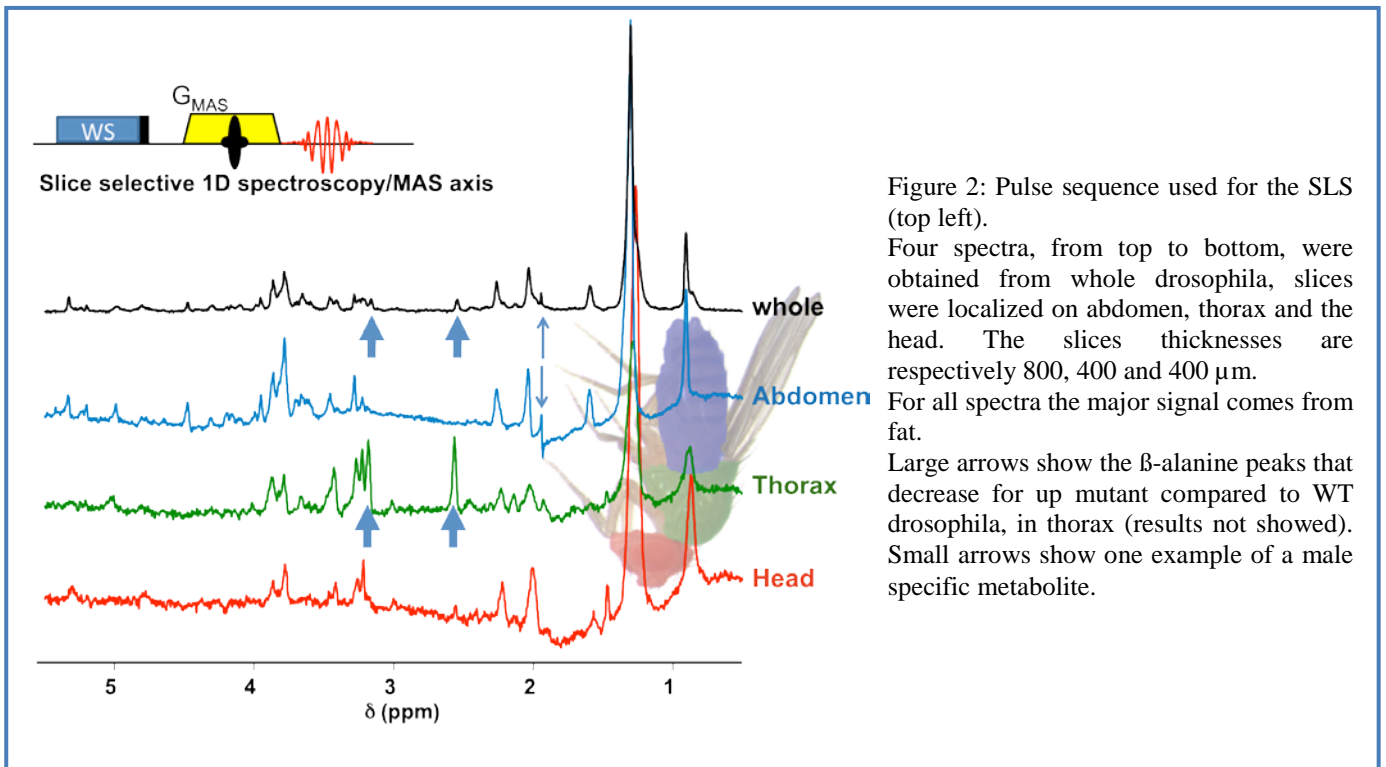
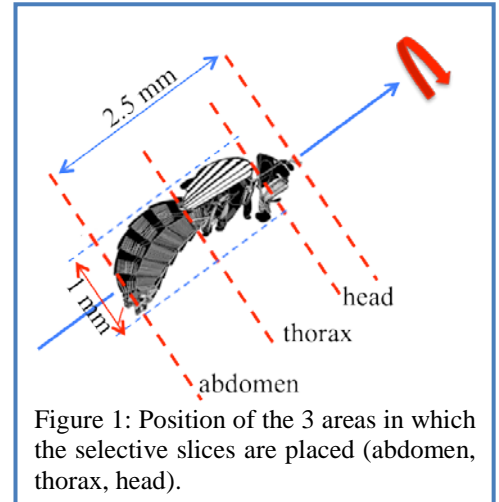
Results:

In drosophila, it is not very useful to select a true localized voxel for two main reasons: by reducing the volume we drastically reduce the sensitivity of the experiment (as x^3) and we do not really need to localize a smaller volume than "the abdomen" for example (Fig. 1). Semi-localization was limited to the acquisition of a spectrum with a frequency selective pulse (corresponding to the thickness of the slice, in presence of a magnetic field gradient parallel to the rotation axis by use of 3 gradients (x, y, z; z being the vertical axis of the magnet)).

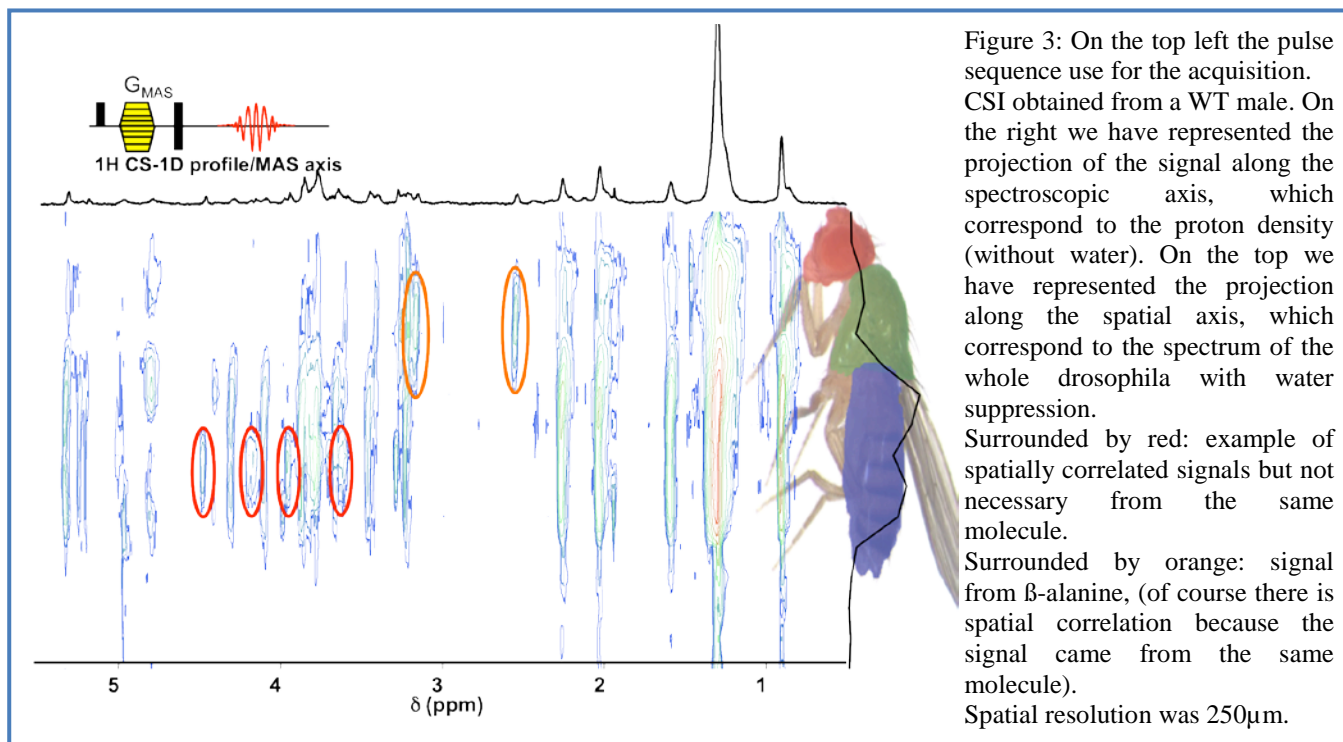
We identified numerous metabolites (with 1D and 2D global spectroscopy) and their localization with the SLS.

Those experiments permit to obtain our first biological results.

For example, we showed that β -alanine (which is present in muscle at high concentration) was decreased in the *up¹⁰¹* mutant compared to WT (wild type) and that several metabolites were different in male and female abdomen (for example male specific galactoside³).



Another way to obtain localization of metabolites is to use a 2D CSI experiment. Generally, C.S.I. (Chemical Shift Imaging) corresponds to a 2D mapping of spectra (corresponding to 3D, 2 spatial and 1 spectroscopic dimension) from a slice. In our case, for sensitivity reasons, we used a C.S.I. experiment with obtaining a 2D acquisition with the horizontal dimension being the chemical shift and the vertical dimension being the spatial position on the rotation axis (Fig. 3).



Discussion:

We verified that spectra from the head, thorax and abdomen were well localized by using examples documented in the literature (for instance the decrease of β -alanine in thorax muscle, or the presence of the male specific metabolite in abdomen). The efficiency of the semi-localized acquisition of ^1H HRMAS spectra has been proved on two examples that open numerous possibilities of study of metabolism in genetically modified drosophila. The semi-localization (head/thorax/abdomen) gives a much more precise information than global spectroscopy on the observed metabolism. CSI brings up information on the spatial relations of metabolites; this experiment gives the information: if 2 signals are on the same ordinate (Fig. 3), they correspond to ^1H on the same molecule or (more interestingly) to ^1H in the same localization versus the global axis of the fly.

References:

1. Meme S. et al, 2013), Magn. Reson. Imaging, 31(1); 109-19
2. Righi V. et al, 2010, Int. J. Mol. Med., 26(2):175-84
3. Chen P.S. et al, Biochemistry, 1977, 16(18):4080-5.

Exploring the fundamental hydrodynamics of turbulent single and multiphase flows using Compressed Sensing Spiral MRI

A. B. Tayler, M. Benning, A. J. Sederman and L. F. Gladden

Magnetic Resonance Research Centre, Department of Chemical Engineering and Biotechnology, University of Cambridge, Cambridge CB3 0HE, UK

Recent advances in fast magnetic resonance imaging (MRI) have enabled the measurement of quantitative, temporally resolved flow fields for turbulent single and multiphase flows. In particular, the combination of compressed sensing with under-sampled spiral imaging has allowed the measurement of velocity maps at up to 188 images per second while maintaining high robustness to fluid flow and shear¹. In this talk, applications of this technique towards the characterisation of fundamental hydrodynamic phenomena are explored for a range of systems.

To successfully image highly transient flows all data must be acquired with approximately 2.5 ms if spatial blurring is to be constrained within a single pixel of dimension 500 μm . This is approximately an order of magnitude faster than can be acquired with conventional echo-planar imaging. To overcome this problem, low tip-angle spiral imaging was used to sample substantially below the Nyquist rate. Images were reconstructed by solving a Tikhonov regularisation problem that promotes a sparse representation of the image:

$$\mathbf{M} \in \arg \min_{\mathbf{M}} \left\{ \|\mathbf{F}\mathbf{M} - \mathbf{y}\|_2^2 + \alpha \|\nabla\mathbf{M}\|_1 \right\}$$

where \mathbf{M} is the image being reconstructed, F is the Fourier transform operator, \mathbf{y} is the measured \mathbf{k} -space data, α is a heuristic regularisation parameter and ∇ is the gradient operator, which is used for sparsification. As long as the undersampling artefacts are incoherent in the sparse domain, the image may be separated from the artefacts without compromising image resolution.

These measurements have been used to characterise turbulent single phase and multiphase flows. An example of the former is given in Figure 1, which shows a 3D velocity map of single phase pipe flow at a Reynolds number of 4,500. These data were sampled at approximately 1.5% of the Nyquist rate, with images recovered by regularisation in four dimensions (three spatial dimensions and time). The structure of turbulent wall instabilities, highlighted by the green box, is revealed as the instabilities form and are translated along the pipe. The ability to produce temporally resolved 3D velocity measurements also enables the calculation of spatial velocity gradients, which are necessary for the quantitation of pressure and stress.

The present technique is also applicable to optically opaque systems, such as dense multiphase flows. In investigating these systems, the wake behaviour of single rising bubbles was firstly characterised, as shown in Figure 2, before examining the interaction of multiple bubbles. These measurements reveal that in addition to the well known counter-rotating vortices existent in the longitudinal plane, there exists a secondary mode of vorticity in the horizontal plane. The direction of core wake flow for a single bubble is seen to be antiphase with the direction of bubble secondary motion, as the secondary vorticities reverse direction following every wake shedding event. When multiple bubbles are present, this secondary wake vorticity gives rise to turbulent

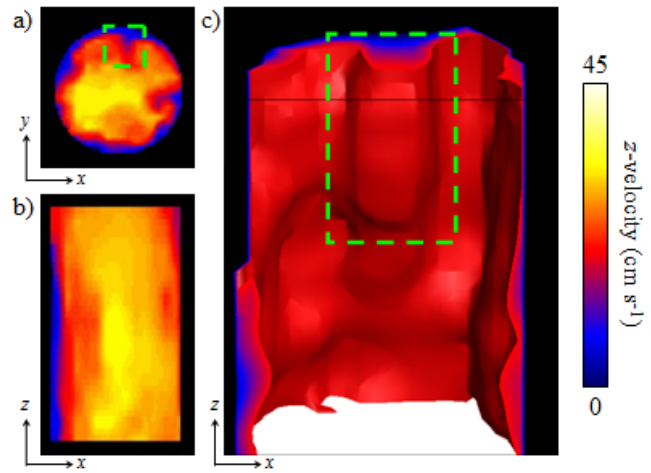


Fig. 1: Three dimensional velocity maps acquired of single phase pipe flow at $Re = 4,500$. a) Vertical and b) horizontal slices of the system extracted from the data, and c) a 3D render demonstrating a 20 cm s^{-1} isosurface. Note that all velocities above 20 cm s^{-1} have been rendered transparent in this image. The spatial and temporal resolution of these images were $390 \mu\text{m} \times 390 \mu\text{m}$ and 10.1 ms.

structures which extend over multiple bubble length scales¹. The influence of secondary wake vorticity on bubble path deviations and turbulence in multiphase flow has not been quantified before, and offers new insight into the hydrodynamics that govern the behaviour of these systems.

Chemical shift artefacts, which occur when an off-resonant signal component is on the same order of magnitude as the image bandwidth, are a commonly encountered problem when applying ultra-fast imaging to multiphase systems. This problem has been overcome by allowing for off-resonant signal in the compressed sensing regularisation model:

$$\mathbf{M} \in \arg \min_{\mathbf{M}} \left\{ \left\| \sum_{k=0}^n F \mathbf{M}_k e^{i2\pi\Omega_k t} - \mathbf{y} \right\|_2^2 + \sum_{k=0}^n \alpha_k \|\nabla \mathbf{M}_k\|_1 \right\}$$

where n is the number of components present in the signal, Ω is the chemical shift frequency and $\mathbf{M} = (\mathbf{M}_0, \dots, \mathbf{M}_n)$. By reconstructing images in this way, it is possible to simultaneously measure both the internal and external flow fields for oil droplets rising through water. Droplets of polydimethylsiloxane (PDMS) rising through water was selected as a model system as it contains only two resonant frequencies, however the model may be extended to several signal components for the examination of more complex systems, or for the *in-situ* quantitation of mass transfer and chemical reaction. Some example images of this type are shown in Figure 3. It is clear from these data that while some element of the expected counter-rotating vortices² are present in the internal flow field, a greater influence is had by the changing droplet shape. These shape oscillations, which generate large scale translational shifts within the drop, become more pronounced for lower viscosity droplets, and appear to be the dominant factor influencing droplet-side hydrodynamics. These measurements, and along with those described above, demonstrate the great potential held by new imaging techniques in the phenomenological characterisation of fluid flow.

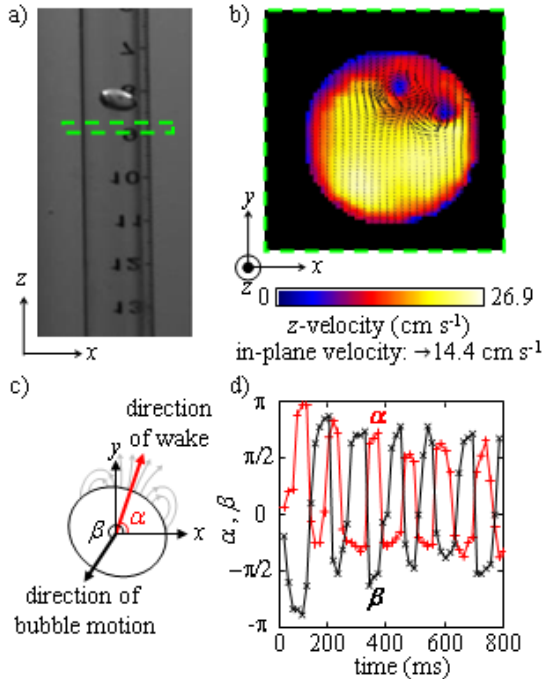


Fig. 2: a) A photograph of an air bubble held static in a contraction against a downward flow. b) An example horizontal plane velocity map acquired at the location indicated by the dotted box in a). The spatial resolution of this image was $390 \mu\text{m} \times 390 \mu\text{m}$ and the temporal resolution 15.8 ms. c) Schematic showing the co-ordinates system used within the bubble reference frame. d) Comparison of direction of bubble wake and bubble motion over several wake shedding events. The antiphase nature of these data reflects the coupling between bubble secondary motion and secondary wake vorticity.

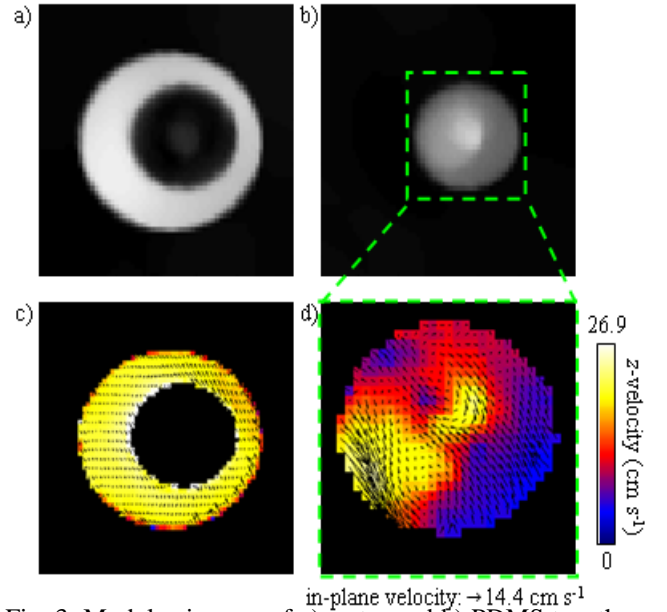


Fig. 3: Modulus images of a) water and b) PDMS together with velocity images of each phase (c and d). Note that image c) represents the velocity in the laboratory frame, while the mean velocity of each velocity component has been subtracted from image d), such that the velocity field shown reflects the droplet frame of reference. All four of these images were extracted from a single dataset.

References:

1. A.B. Tayler *et al.*, Phys. Rev. Lett. 108, 264505, 2012.
2. R. Clift *et al.*, Bubbles, Drops, and Particles, Dover, 1978.

YI 5

Turbulent Rayleigh-Bénard Convection in a Supercritical Fluid

Joshua M. Bray^a, Sarah L. Codd^a, Joseph D. Seymour^b,

Departments of ^aMechanical and Industrial Engineering, ^bChemical and Biological Engineering
Montana State University, USA

Convection of a fluid near its critical point is marked by the divergence of several transport parameters, which results in high sensitivity to variations in temperature and pressure^{1,2} and access to large Rayleigh numbers ($Ra \approx 10^{14}$). Invasive measurement techniques such as hot wire anemometry will alter the thermodynamic phase of the fluid causing undesirable perturbations and measurement error while critical opalescence may confound optical methods. Advancement of our understanding of convective dynamics in the supercritical regime is essential for diverse modern applications such as chromatography, "green" solvents, and carbon sequestration, and to this end, NMR provides non-invasive characterization for diverse aspects of the flows². Specifically, PGSE methods yield both spatially-resolved maps of velocities in the convection pattern^{3,4} and ensemble-averaged statistics of the impact of turbulence on molecular motion^{5,6}. The latter is of particular interest due to the "filtering" of velocities with correlation times longer than the inter-pulse delay (Δ) in the double-PGSE sequence⁷. This permits isolation of the smallest scales of turbulence and may shed experimental light on current controversies surrounding superstatistical descriptions of turbulence⁸.

The archetypal convection problem is the Rayleigh-Bénard cell, in which a temperature gradient elicits convection via density instability⁹. A high-pressure, low-aspect ratio ($\Gamma = 1/35$) PEEK convection cell was fabricated for use in the magnet. Pressure was regulated via an ISCO 500D syringe pump, while temperature gradients were imposed via an in-probe forced hot air system. Supercritical hexafluoroethane (C_2F_6) was chosen because of the strong ^{19}F NMR signal and for its relatively accessible critical point ($P_c = 30.8$ bar, $T_c = 19.9^\circ C$), and convection was studied at pressures near- and far-above the critical point ($P = 32$ and 70 bar), with and without an applied temperature gradient ($\Delta T = 2.5^\circ C$). A Bruker 300 MHz Super Wide Bore magnet with 1.5 T/m xyz gradients was used to acquire maps of convection velocity and double-PGSE propagators over a range of displacement observation times, $\Delta = 5$ –800 ms.

The velocity maps show Rayleigh-Bénard patterns of convection and demonstrate the effects of the near-critical density divergence (Fig. 1). Supercritical C_2F_6 showed a "bulls-eye" pattern, in contrast with liquid water (far below its critical point), which exhibited a two-lobe "convection roll" pattern. The bulls-eye originates from the large isothermal compressibility of the fluid and heat transfer at the wall boundaries, and it was possible to reverse the flow by isolating heat input to just the bottom of the vessel (and not the walls). The enhanced isothermal compressibility near the critical point resulted in more rapid convection at 32 bar than at 70 bar (not shown), and even with no applied heating, rapid, stable convection was observed at 32 bar due to a thermal gradient within the temperature resolution of the experiment. With an applied $2.5^\circ C$ temperature gradient, the convection velocities at both pressures were characteristically turbulent.

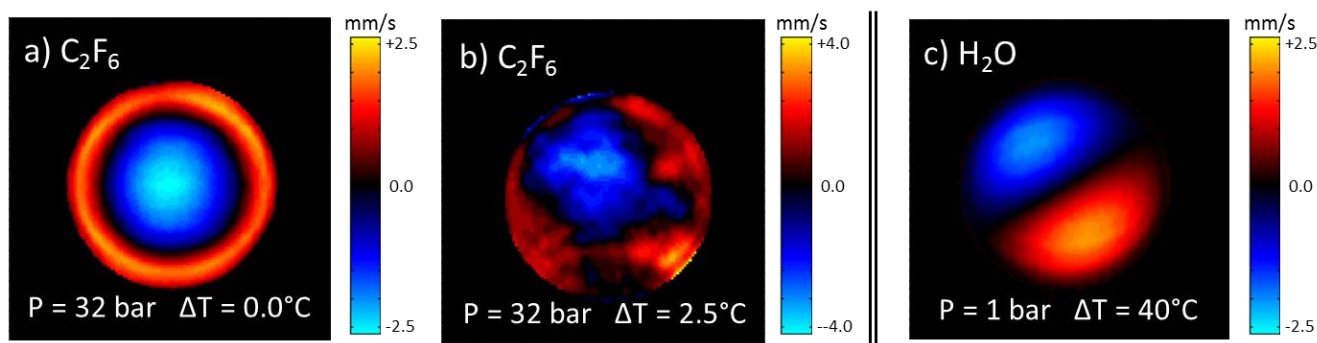


Figure 1: Axial velocity maps of supercritical hexafluoroethane (a,b) and liquid water (c) undergoing convection. (To be submitted.)

The double-PGSE propagators (Fig. 2) provide an advection-insensitive measure of velocity changes⁷. In turbulent flows, the spectrum of velocity fluctuations occurs over a continuum of scales that range from the integral scale of the mean flow to the Kolmogorov microscale length, η , at which viscous dissipation occurs¹⁰. Accurate determination of motion statistics is essential for validation of turbulence models^{11,12}, and NMR directly measures the detailed Lagrangian displacement statistics without reliance on invasive probes or on tracer-particles as a proxy for the motion. The displacement time (Δ) dependence of the propagators reveals a progression from Gaussian statistics (characteristic of pure diffusion) toward non-Gaussian distributions with high-velocity "wings" (characteristic of turbulence). This progression is due to double-PGSE refocusing advective motion over the measurement time scale, which effectively "filters" out the spectrum of fluctuations that have velocity correlation times longer than Δ .

Superstatistics¹¹ has emerged in recent literature as an argument for system heterogeneity as a dynamical basis for non-Boltzmann statistical thermodynamics. It has proven an exceptionally successful theory for modeling turbulent dynamics. Stochastic dynamics are described by a Langevin equation in which friction (γ) and/or force (σ) parameters vary, together describing the local Boltzmann statistics of particle motions via the (so-called) inverse temperature, β . System heterogeneity, introduced by turbulent puffs, produces spatial correlation over a hierarchy of scales and generates a distribution, $f(\beta)$ from which the probability of states $P(x)$ is determined—"a statistics of a statistics". Different microscale statistics $f(\beta)$ produce distributions such as stretched exponentials and power laws¹², having the respective functional forms:

$$(1) P(x) = Ae^{-(x/k)^\alpha} \quad (2) P(x) = A \frac{1}{\left(1 - \frac{x^2}{k^2}\right)^{1-\alpha}}.$$

Here, A and k are constants, and α is the exponent of the distribution. Both forms were found to describe propagator data such as those in Fig. 2, although the power law (Eqn. 2) gave better agreement in the wings (after accounting for diffusive broadening). The power α reveals a marked transition to non-Gaussian statistics, which proved sensitive to the small-scale threshold of turbulence, η . Relatively small variation of the power law exponent at larger Δ suggests similarity in the structure of turbulence over those scales; however, the small-scale structure of turbulence has traditionally been elusive to measurement¹³, and what variation is observed might inform the appropriateness of the superstatistics $f(\beta)$ chosen to describe dynamics in those ranges.

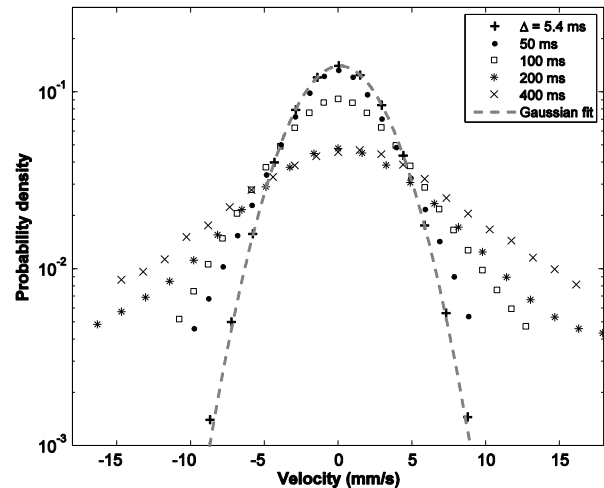


Fig. 2: Double-PGSE propagators for convecting C_2F_6 at $P=32$ bar and $\Delta T=2.5^\circ C$. Increasing the Δ delay time introduces sensitivity to turbulent fluctuations with longer correlation times. (To be submitted.)

1. P. Carles, J. Supercrit. Fluid. 53 (2010) 2-11.
2. E.M. Rassi, S.L. Codd, and J.D. Seymour, J. Magn. Reson. 214 (2012) 309-314.
3. P.T. Callaghan, Oxford University Press (1991).
4. A.J. Sederman, M.D. Mantle, C. Buckley, and L.F. Gladden, J. Magn. Reson. 166-2 (2004) 182-189.
5. P.G. De Gennes, Phy. Lett. A 29-1 (1969) 20-21.
6. D.O. Kuethe and J.-H. Gao, Phys. Rev. E 51-4 (1995) 3252-3262.
7. A. Caprihan and J.D. Seymour, J. Magn. Reson. 144-1 (2000) 96-107.
8. A. Cho, Science 297-5585 (2002) 1268-1269.
9. L.P. Kadanoff, Phys. Today 54-8 (2001) 34-39.
10. H. Tennekes and J.L. Lumley, The MIT Press (1972).
11. E.G.D. Cohen, Physica D 193-1 (2004) 35-52.
12. C. Beck, Physica A 365-1 (2006) 96-101.
13. U. Frisch and S.A. Orszag, Phys. Today 43-1 (1990) 24-32.

**The Grotthuß-Mechanism in Nanoporous Silicates
and its Implications to Diffusion Studies in Natural Porous Media**

E. Paciok^a, A. Haber^b, M. Van Landeghem^c, and B. Blümich^a

^aInstitut für Technische und Makromolekulare Chemie, RWTH Aachen University, Germany

^bE.ON Energy Research Centre, RWTH Aachen University, Germany

^cSaint-Gobain Recherche, Aubervillier, France

The measurement of T_2 - T_2 relaxation exchange on a low-field NMR platform is a most suitable, cheap and straightforward tool to reveal the mechanism of diffusive mass transfer in porous systems^{1,2}. Applied to water in a model porous system, the so-called Stöber-silicates, two relaxation sites were identified: the silicate surface, which holds 25% of water, and the pore water holding 75%. Employing our recently developed model to simulate diffusive relaxation exchange³, we were able to derive the precise kinetic exchange rate for protons migrating between those two sites. Measuring this exchange rate in dependence on temperature and exchange time, Arrhenius-behaviour was observed. The according activation energy was found to be 7 kJ/mol, which is strong evidence that the ultrafast Grotthuß mechanism of chemical proton exchange is *the only* mechanism of proton migration in nanoporous silicates, and that translational diffusion of water molecules is largely inhibited⁴. Considering the fact that most natural porous media contain large silicate surfaces, our results imply that any method that uses proton diffusion as the sole measure for the general mass transfer properties of natural soil or rock, may produce erroneous results and may lead to wrong modeling and conclusions.

In highly non-uniform multi-phase systems, such as liquids in porous media, using resonance and frequency as a means to track mass transfer is tricky if not impossible, since the effects of susceptibility-induced magnetic field inhomogeneities on resonance and frequency override those from changes in chemical environment. Alternatively, 2D-exchange NMR can employ diffusion or relaxation instead of resonance as labels to track site populations and exchange processes. Here, two-dimensional, doubly modulated multi-exponentials are recorded, which are inverted into exchange maps using a numerical approximation of the Inverse Laplace Transform⁵. T_2 - T_2 relaxation exchange maps are interpreted qualitatively in terms of surface-proximity or pore size distributions, and mass transfer can be studied on different timescales and related to intra- or inter-pore diffusion and pore connectivity^{2,6}. In order to derive quantitative information, commonly some pre-knowledge of the pore space is required and exchange needs to be modeled, in order to disentangle the effects of simultaneous diffusion and relaxation. Recently, a kinetic multi-site relaxation exchange model was introduced independently by two groups^{3,7}. Irrespective of pore structure and connectivity, it allows a) simulating exchange to model experimental data from systems with few discrete relaxation sites and delivers precise kinetic exchange rates.

In this work, we employed the combination of T_2 - T_2 exchange measurements and kinetic modeling to investigate diffusion of water confined in dense packings of spherical silica nanoparticles in dependence on temperature and exchange time. Figure 1 shows an example of measured and simulated 2D exchange data. The two distinct relaxation sites were attributed to bulk

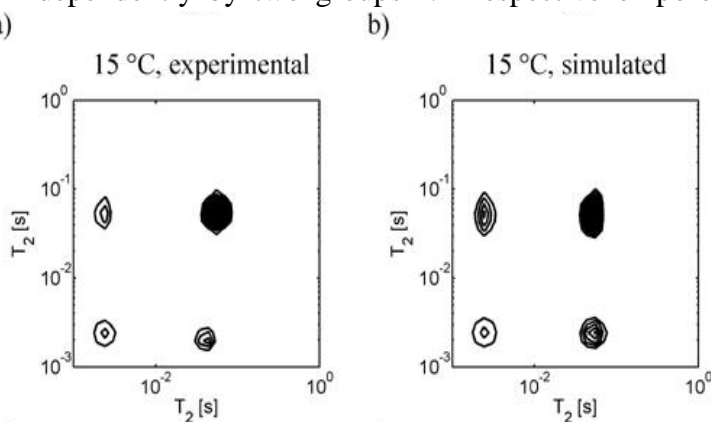


Fig. 1 Comparison of measured (a) and simulated (b) T_2 - T_2 exchange maps. The data was acquired at 15 °C and an exchange time of 70 ms.

pore-water and water bound to the silicate surface, respectively. The exchange was modeled according to first-order exchange kinetics and the results complied fully with the experimental data. In the range of 5°C to 25°C the kinetic exchange rate constant k was found to be surprisingly low with 7 s^{-1} to 9 s^{-1} . Moreover, fitting its temperature-dependence with the Arrhenius law produced a scaling factor A of 157 s^{-1} and an activation energy E_A of merely 7 kJ/mol , which is well below the activation energy for self-diffusion in water with 19 kJ/mol (cf. Fig. 2).

Since the exchange is facilitated by diffusion, the activation energy of the exchange process directly reflects on the activation energy of diffusion between the silicate surface and the bulk pore-water. The low value indicates a pure Grotthuß mechanism of proton transfer via chemical chain-reactions, where the 7 kJ/mol corresponds to the rotational energy that is needed for a water molecule to rotate in such a way that it can pass on a recently accepted proton to the next molecule in line. With our results we argue that there is no physical exchange of molecular water between these two sites. Also, the layer of water rigidly bound to the silicate surface must extend over tens of nanometers, since the protons that exhibit fast relaxation make up 25% of the entire proton ensemble. The Grotthuß mechanism is usually only found in systems with a large proton excess. However, Kornyshev *et al.* predicted that any system containing a high amount of silicate may behave like a proton-excess system, with protons being able to move very fast along rigid structures of water molecules⁸. In addition, our findings are in good agreement with NMR measurements in quartz nano-channels by Tsukahara *et al.*⁹ and recent results measured in zeolites by Filippov *et al.*¹⁰. The implications of these findings are manifold, the most important being that, given a certain temperature, pH and chemical composition of a porous medium, there must exist a critical surface-to-volume ratio beyond which ultrafast proton transfer via the Grotthuß mechanism macroscopically dominates over the comparatively slow proton transfer via the translational motion of water molecules. Any method that uses proton transfer to quantify mass transfer in a porous medium will lead to wrong conclusions, when this critical point is exceeded and the Grotthuß mechanism is not discerned. That is why our current research is aimed at better defining the limits of NMR and conductometry in porous media, and at better understanding the underlying molecular processes.

References:

1. B. Blümich, F. Casanova, M. Dabrowski, E. Danieli, L. Evertz, A. Haber, M. Van Landeghem, S. Haber-Pohlmeier, A. Olaru, J. Perlo, O. Sucre, *New J. Phys.* 13 (2011) 015003.
2. A. Haber, F. Casanova, S. Haber-Pohlmeier, B. Blümich, *Vadose Zone J.* 9 (2010) 893.
3. M. Van Landeghem, A. Haber, J.-B. D’Espinose De Lacaillerie, B. Blümich, *Concepts Magn. Reson. Part A* 36 (2010) 153.
4. E. Paciok, A. Haber, M. Van Landeghem, B. Blümich, *Z. Phys. Chem.* 226 (2012) 1243.
5. L. Venkataramanan, Y.-Q. Song, and M. D. Hürlimann, *IEEE Trans. Signal Process.* 50 (2002) 1017.
6. K. E. Washburn and P. T. Callaghan, *Phys. Rev. Lett.* 97 (2006) 175502.
7. M. Fleury and J. Soualem, *J. Colloid Interface Sci.* 336 (2009) 250.
8. A. A. Kornyshev, A. M. Kuznetsov, E. Spohr, and J. Ulstrup, *J. Phys. Chem. B* 107 (2003) 3351.
9. T. Tsukahara, W. Mizutani, K. Mawatari, and T. Kitamori, *J. Phys. Chem. B* 113 (2009) 10808.
10. A. Filippov, S. V. Dvinskikh, A. Khakimov, M. Grahn, H. Zhou, I. Furo, O. N. Antzutkin, and J. Hedlund, *Magn. Reson. Imag.* 30 (2012) 1022.

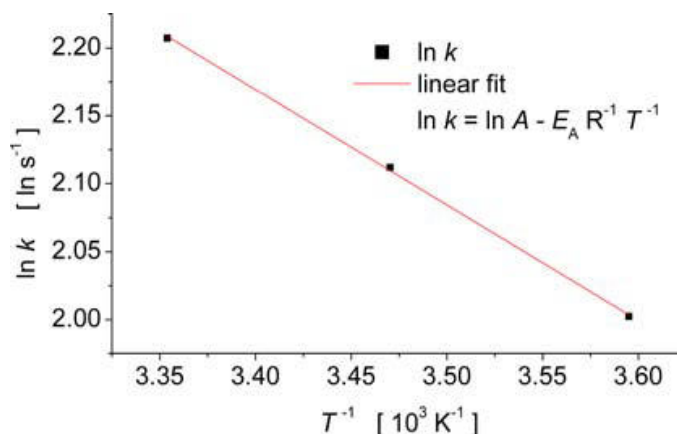


Fig. 2 Arrhenius plot for the temperature-dependent proton exchange rate constant k . The Arrhenius factor A and the activation energy E_A can be extracted from the linear fit, since both are expected to be fairly constant throughout the investigated temperature interval.

Oral Presentations

A first bimodal MPI/MRI tomograph

P. Vogel^{a,b,c,*}, *S. Lothar*^{a,b,*}, *M.A. Rückert*^{a,c}, *W.H. Kullmann*^c, *P.M. Jakob*^{a,b}, *F. Fidler*^b, *V.C. Behr*^a

*equal contribution

^aDepartment of Experimental Physics 5 (Biophysics), University of Würzburg, Germany

^bResearch Center for Magnetic Resonance Bavaria e.V. (MRB), Germany

^cInstitute of Medical Engineering, University of Applied Sciences Würzburg-Schweinfurt, Germany

Magnetic Particle Imaging (MPI) was firstly presented in 2005¹. It is based on the nonlinear response of ferromagnetic material and the fact that the magnetization saturates at sufficiently high magnetic fields. For imaging a field free point (FFP) of a strong gradient on the order of 1-7 T/m is moved through the sample. Commonly, this gradient is generated by permanent magnets. Only from inside the FFP a MPI signal can be detected, otherwise the SPIOs saturates and the signal generation is suppressed¹. In contrast to MRI, MPI directly detects the concentration and distribution of superparamagnetic iron-oxide nanoparticles (SPIOs) without any background of tissue. The first overlaid image, showing both imaging modalities, was published in 2009, but the datasets were acquired in separate scanners and a co-registration was required².

At first glance both modalities do not seem to match, because on the one hand the B_0 field of the MR system saturates the SPIOs and on the other hand the strong gradient of the MPI system disturbs the MRI. In this abstract a bimodal MPI/MRI tomograph is presented, which use electrically switchable magnetic fields. For MRI a low-field-MRI (LFMRI) device was chosen^{3,4} and for MPI the Traveling-Wave-MPI approach was used⁵. The advantage of combining both modalities in one device with the same receiver coil is that neither the sample has to be re-positioned nor any co-registration algorithm is required for overlaying the images.

The TWMPI device operates at an excitation frequency of about 16 kHz and generates MPI signal in the range up to 400 kHz. This frequency range matches perfectly with the resonance frequency of the LFMRI system for a B_0 field of about 1.1 mT (47.1 kHz for ^1H). A switchable prepolarizing coil (30 mT) is used to improve the LFMRI signal⁶. The TWMPI device works with an array of 20 individual coil elements (dLGA), where each coil is driven with a sinusoidal current and a phase shift between adjacent elements to yield one period over the scanner size (traveling-wave concept). This results in two FFPs traveling linearly along the symmetry axis, which can be arbitrarily moved with two perpendicular saddle coil systems through the volume (FoV).

Fig. 1 A shows a sketch of the MPI/MRI system: (1)-(3) are the B_0 field generator, the 3D gradient system and the prepolarizing unit of the LFMRI system. (4) and (5) are the dLGA and the two saddle coil systems. (6/7) represents the switchable receiver coil. Both experiments were performed successively without moving the sample. The second grape of the sample was prepared with undiluted Resovist® (Bayer Schering) (see fig. 1 B). The LFMRI image shows a signal extinction inside the second grape, where the overlaid TWMPI image shows exactly the position of the SPIOs. The acquisition time for the LFMRI projection was 11 min (8 averages) and 4.35 s for one TWMPI slice (4000 averages).

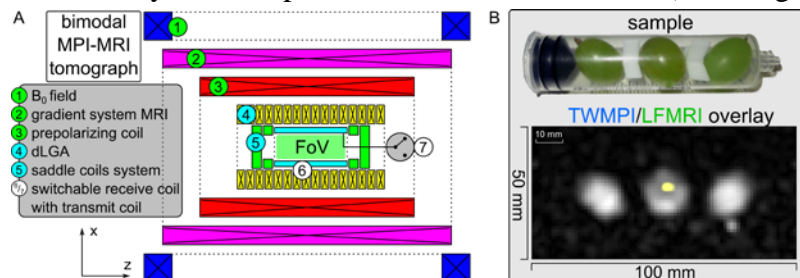


Fig. 1: A: sketch of the bimodal MPI/MRI scanner with switchable receiver coil (6/7). B: Three Bavarian grapes, where the second is prepared with undiluted Resovist®. The overlaid image shows exactly the position of the SPIOs.

1. Gleich B., Weizenecker J.: Tomographic imaging using the nonlinear response of magnetic particles, *Nature* 2005.
2. Weizenecker J. et al.: Three-dimensional real-time in vivo magnetic particle imaging, *Phys. Med. Biol.* 54, 2009.
3. Trahms, L. and Burghoff, M.: NMR at very low fields, *Magn Reson Imaging*, 28, 1244-125, 2010.
4. Pruessmann, K. P.: Less is more, *Nature*, 455, 43, 2008.
5. Vogel P. et al.: Slicing Frequency Mixed Traveling Wave for 3D MPI, *Proc. IWMPPI*, 231f., 2012.
6. Packard M. and Varian R. *Phys. Rev.*, 93, 941, 1954.

A portable permanent-magnet analyzer for High-Resolution ^1H Magic Angle Spinning NMR spectroscopy

A. Soleilhavoup^a, C. Hugon^{b,1}, J. Alonso^a, A. Guiga^a and D. Sakellariou^{a,b}

^aCEA, DSM, IRAMIS, SIS2M, LSDRM CEA Saclay F-91191 Gif-sur-Yvette, France

^bDépartement de Chimie, Ecole Normale Supérieure, Paris, France

Nuclear Magnetic Resonance (NMR) spectroscopy is one of the best non-destructive non-invasive methods for chemical analysis. However, and even more than for liquid-state studies, the development of solid-state NMR to an industrial scale has been limited by the cost and the complexity of the required equipment. The recent development of NMR using low-cost permanent magnets has so far been limited to low resolution relaxation studies or high resolution on liquid samples. Some years ago we proposed a general methodology to design, build and correct permanent magnets for NMR and MRI based on Spherical Harmonics Expansion and used it to make a longitudinal field 0.1T low-cost prototype [1,2]. We introduce here a novel high-resolution, low-field Magic Angle Spinning (MAS) NMR instrumentation based on low-cost a 0.8T longitudinal field portable permanent magnet and a 7mm MAS probe for liquids and solids. Its homogeneity performance is equivalent to high-field superconducting magnets over standard sample volumes. We also show dramatic enhancement from susceptibility and field inhomogeneity averaging and how this can be used for studying complex chemical structures such as the lipidic composition of seeds and other heterogeneous materials without any sample preparation.

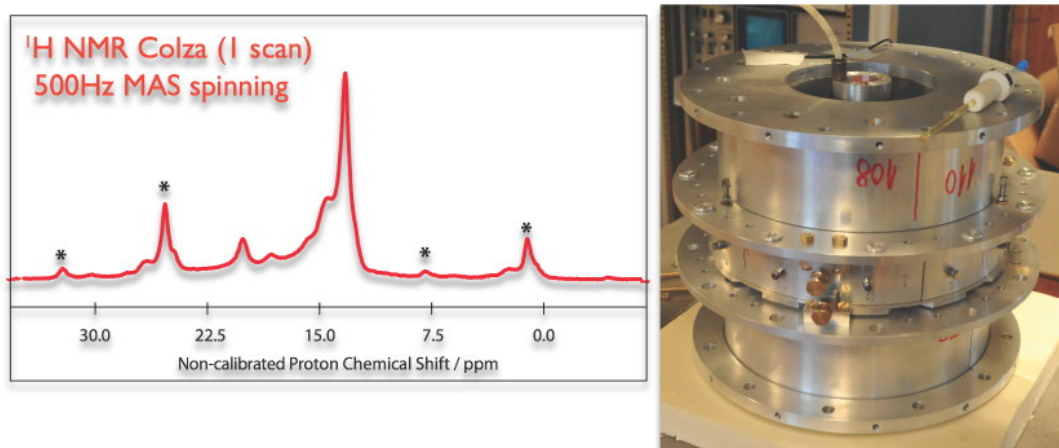


Fig. 1: Left: Single scan HR-MAS ^1H spectrum from colza seeds spinning at ~ 600 Hz. Right: Photo of the portable 0.8T MR analyzer, with a standard 5mm liquid-state NMR sample.

References:

1. C. Hugon, P. M. Aguiar, G. Aubert and D. Sakellariou, C. R. Chimie 13, (2010) 388-393.
2. C. Hugon, F. D'Amico, G. Aubert and D. Sakellariou, J. Magn. Reson. 205, (2010) 75-85.

¹ Current address: Oxford Instrument, Industrial Analysis, OX13 5QX Abingdon, United Kingdom.

O3

Magnetic Resonance Imaging of fluids in porous media with metallic core holders

B. Balcom

Department of Physics, University of New Brunswick, Fredericton,
New Brunswick, Canada E3B 5A3

Magnetic resonance is well known in the petroleum research and development world through down-hole logging and companion laboratory MR measurements of bulk fluid properties. Magnetic Resonance Imaging is less well known, but there is growing recognition that laboratory imaging studies, with core plug samples, will provide valuable new information on fluid properties and fluid behavior in the reservoir. Potential measurements of interest include both core analysis measurements and studies of model flooding procedures, including studies of enhanced oil recovery mechanisms.

This presentation will concentrate on the translation of quantitative MR/MRI methods for core analysis studies to metallic core holders fabricated from high strength non-magnetic metal alloys. An important consideration are eddy currents introduced in the metal vessel as a result of the switched magnetic field gradients inherent to spatial encoding and motion sensitization. The electrical conductivity of the nitronic 60 alloys we favor is dramatically lower than for copper or aluminum and thus eddy currents decay quite rapidly. Gradient waveform measurement and pre-equalization adjustment techniques permit magnetic field gradient pulses, with metallic core holders, to switch almost as fast as those undertaken without a metal core holder. The RF probe, inside the metal case of the core holder, is dramatically more sensitive than RF probes located outside of traditional MR compatible core holders due to the principle of reciprocity.

Rapid magnetic field gradient switching is required for observation of short T_2 species that are common in non-ideal rock core samples. SPRITE and SE-SPI MRI measurements of core plug flooding measurements in metallic core holders, with pre-equalized gradient waveforms, will be presented.

O4

Utilizing parahydrogen derived hyperpolarization to improve MRI

Simon B. Duckett, Ryan E. Mewis, Kevin D. Atkinson, Gary G. R. Green, Richard A. Green, Louise A. R. Highton and Lyrelle S. Lloyd

Centre for Hyperpolarisation in Magnetic Resonance, University of York, Heslington, York, YO10 5DD, UK

MRI plays a role in non-invasive diagnosis and clinical research. However, as with NMR spectroscopy, MRI suffers from low sensitivity. At 1.5 T, only 1 in every 200,000 hydrogen atoms present in a sample contribute positively to an image when working at physiological temperatures. Hyperpolarization deals with the generation of non-equilibrium populations of nuclear spins to provide enhanced sensitivity to both NMR and MRI experiments. This talk focuses on demonstrating how *parahydrogen* can be used to rapidly hyperpolarize substrates and thereby facilitate their imaging.¹ As parahydrogen, exists in a pure magnetic state the potential to produce images where the inherent proton sensitivity is improved by 200,000 fold at 1.5 T is possible. Indeed 100% polarization has been generated for a pair of metal hydride protons using this method. A new route to substrate hyperpolarization with parahydrogen has been termed signal amplification by reversible exchange (SABRE) has been developed in our research group.² Results are presented for the hyperpolarization targets nicotinamide and pyrazine. Figure 1 illustrates how both ¹H and ¹³C measurements can be facilitated.

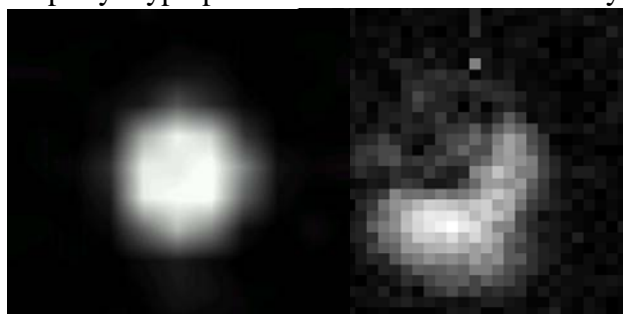


Fig. 1: Hyperpolarization of nicotinamide and pyrazine using SABRE allow both ¹³C and ¹H MRI images to be recorded.

References:

1. C. R. Bowers and D. P. Weitekamp, *Physical Review Letters*, 1986, 57, 2645-2648.
2. R. W. Adams, J. A. Aguilar, K. D. Atkinson, M. J. Cowley, P. I. P. Elliott, S. B. Duckett, G. G. R. Green, I. G. Khazal, J. Lopez-Serrano and D. C. Williamson, *Science*, 2009, 323, 1708-1711.

Parahydrogen-induced hyperpolarization for MR imaging and spectroscopic applications

K.V. Kovtunov, V.V. Zhivonitko, I.V. Skovpin, D.A. Barskiy, O.G. Salnikov, I.V. Koptuyug

^a International Tomography Center, SB RAS, 3A Institutskaya St., Novosibirsk 630090, Russia, and Novosibirsk State University, 2 Pirogova St., Novosibirsk 630090, Russia

Many spectroscopic and imaging studies are hampered by the limited sensitivity of NMR, thus significant efforts are being invested in the development of efficient hyperpolarization techniques. One promising approach is parahydrogen-induced polarization (PHIP). Conventionally, it is based on the homogeneous hydrogenation of a substrate with parahydrogen ($p\text{H}_2$). However, the presence of the dissolved transition metal complex catalyst significantly complicates the production of pure (e.g., biocompatible) hyperpolarized solutions and does not allow one to produce hyperpolarized fluids in a continuous mode. Two approaches that can overcome these limitations will be discussed. The first one is based on the biphasic gas-liquid hydrogenation whereby a mixture of gaseous substrate and $p\text{H}_2$ is bubbled through the solution of a homogeneous catalyst, and the hyperpolarized product is observed in the gas phase. In addition, subsequent dissolution of the hyperpolarized gas in a pure solvent can be used to produce solutions of hyperpolarized molecules. The extension to the hyperpolarization of vapors would significantly broaden the range of molecules that can be hyperpolarized using this method. Another approach relies on the heterogeneous gas-solid or liquid-solid hydrogenations over a broad range of different catalyst types. Apart from the immobilized transition metal complexes and supported metal nanoparticles, other types of heterogeneous catalysts are demonstrated to produce significant PHIP effects. Both approaches mentioned above allow one to cleanly separate the hyperpolarized products from the catalysts, and to run the process in a continuous mode. Several applications of hyperpolarized substances in the MRI experiments will be presented, including spatially resolved visualization of catalytic conversion in microreactors and microfluidic chips.

Further significant expansion of hyperpolarization technology is potentially possible through the use of nuclear spin isomers of molecules other than H_2 . The extremely long-lived nature of the spin states of nuclear spin isomers is one of the highly attractive features for their use in NMR/MRI. However, while the separation or enrichment of nuclear spin isomers by several experimental techniques has been demonstrated, the quantities produced to date were far from being sufficient for an NMR experiment. Here, we demonstrate experimentally the production of nuclear spin isomers of molecules other than H_2 , estimate their lifetime under ambient conditions, and use them to produce hyperpolarization in a chemical reaction. Further developments of this subfield of magnetic resonance should allow one to overcome certain limitations associated with the use of $p\text{H}_2$, e.g., in the PHIP-based studies of heterogeneous catalytic processes where dissociative chemisorption of $p\text{H}_2$ on metal surfaces significantly diminishes the observed signal enhancements. In addition, it is demonstrated that in some cases one does not need a chemical reaction to break the intrinsic symmetry of nuclear spin isomers of molecules and to produce hyperpolarization.

This work was partially supported by the grants from RFBR (##11-03-00248, 12-03-00403, 12-03-31386-mol), RAS (#5.1.1), SB RAS (##60, 61, 57, 122), the support of leading scientific schools (#NSH-2429.2012.3), the Council on Grants of the Russian President (MK-4391.2013.3) and the program of the Russian Government to support leading scientists (# 11.G34.31.0045).

References:

1. K.V. Kovtunov, V.V. Zhivonitko, I.V. Skovpin, D.A. Barskiy, I.V. Koptuyug, *Top. Curr. Chem.*, **2012**, DOI: 10.1007/128_2012_371.
2. V.V. Zhivonitko, V.-V. Telkki, J. Leppaniemi, G. Scotti, S. Fransilla, I.V. Koptuyug, *Lab Chip* 13 (2013) 1554.
3. V.V. Zhivonitko, V.-V. Telkki, I.V. Koptuyug, *Angew. Chem. Int. Ed.* 51 (2012) 8054.
4. I.V. Skovpin, V.V. Zhivonitko, R. Kaptein, I.V. Koptuyug, *Appl. Magn. Reson.* 44 (2012) 289.
5. D.A. Barskiy, K.V. Kovtunov, A. Primo, A. Corma, R. Kaptein, I.V. Koptuyug, *ChemCatChem* 4 (2012) 2031.

Dynamic nuclear polarization at 9.2 T

V. Denysenkov, P. Neugebauer, J. Krummenacker, T. Prisner

Institute of Physical and Theoretical Chemistry and Center of Biomolecular Magnetic Resonance,
Goethe University Frankfurt, Germany

We could show for the first time that dynamic nuclear polarization in liquid solutions allows enhancing proton NMR signals by up to a factor of $\sim 93^{1,2}$. To achieve an effective MW excitation of the liquid sample without excessive heating of the liquid a double resonance structure for the electron and nuclear spin (260 GHz/ 400 MHz) has been developed, that allows for up to 200 nl of liquid sample places on the flat mirror of a Fabry-Perot resonator³. Potential applications of this method to magnetic resonance microscopy and magnetic resonance imaging will be discussed⁴.

References:

1. M.J. Prandolini, V.P. Denysenkov, M. Gafurov, B. Endeward & T. Prisner; High-Field Dynamic Nuclear Polarization in Aqueous Solutions, *J.Am.Chem.Soc.*, 131 (2009), 6090
2. P. Neugebauer, J. Krummenacker, V. Denysenkov, G. Parigi, C. Luchinat & T. Prisner Liquid state DNP of water at 9.2 T: an experimental access to saturation *Phys. Chem. Chem. Phys.*, 15 (2013), 6049
3. V. Denysenkov, & T. Prisner; Liquid State Dynamic Nuclear Polarization Probe with Fabry-Perot Resonator at 9.2 Tesla *J.Magn.Reson.*, 217 (2012), 1
4. J. Krummenacker, V. Denysenkov, M. Terekhov, L. Schreiber & T. Prisner; DNP in MRI: An in-bore approach at 1,5 T, *J.Magn.Reson.*, 215 (2012), 94-99

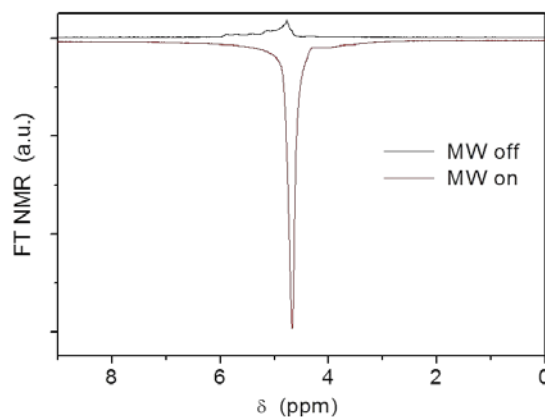


Fig. 1: Dynamic nuclear polarization of a liquid solution of TEMPOL (40 mM) in water at room temperature. The positive signal corresponds to the proton NMR signal without application of MW irradiation; the negative enhanced signal corresponds to the Overhauser DNP enhanced signal under irradiation with 2 W of MW at 260 GHz frequency.

Hyperpolarized ^{129}Xe as MRI contrast agent in combustion processes

J. S. Six, K.F. Stupic, G.E. Pavlovskaya, and T. Meersmann

University of Nottingham, Sir Peter Mansfield Magnetic Resonance Centre, Nottingham, NG7 2RD, UK

Very short relaxation times associated with radical reaction mechanisms in combustion processes impose a significant obstacle for *in situ* MRI of combustion. Additional limitations are associated with the low spin density in the combustion zone and the unfavorable Boltzman equilibrium spin population at the high temperatures in the flame region. These problems were demonstrated by Glover et al.¹ whose pioneering ^1H SPRITE MR images show the methane entering the combustion zone but not in the combustion region.

The adverse effect of an unfavorable Boltzman distribution and low spin density may be overcome using hyperpolarized molecules, however the fast relaxation requires a hyperpolarized probe that does not radicalize in the combustion process. Anala et al. demonstrated that hyperpolarized (hp) ^{129}Xe mixed to methane may serve as a ‘spy’ in 2D EXCSY NMR spectroscopy of methane combustion. However, it remained unexplored whether the hyperpolarized state is sustainable throughout the entire combustion process. Furthermore, the mixing process proved to be cumbersome and a high inert gas concentration in the fuel was required to provide sufficient signal intensity.

The technical challenge has now been overcome through direct spin exchange optical pumping (SEOP) of ^{129}Xe -fuel mixtures³. Continuous flow SEOP of the gas mixture, containing 85% CH_4 , 5% Xe , and 10% N_2 allows for a fairly straightforward experimental setting of the MRI experiment. The resulting stream of combustible fuel and hp ^{129}Xe as an MRI contrast agent is fed continuously from the SEOP cell into a combustor located within the superconducting magnet. MRI scans of the pre-combustion region, the actual flame, and the exhaust area are obtained and compared to the same setting without ignition. The MR images demonstrate that ^{129}Xe sustains much of its hyperpolarized nuclear spin state throughout the flame and exhaust regions.

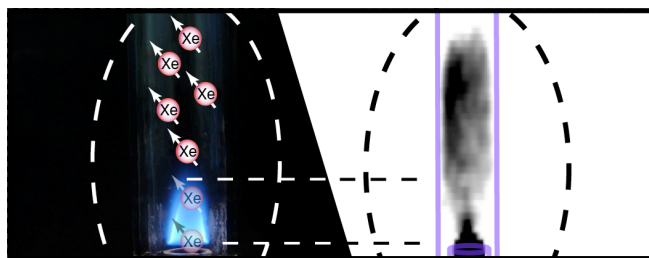


Fig. 1: A photograph of the actual combustion zone (left), overlaid with a sketch symbolizing hp ^{129}Xe , and hp ^{129}Xe MRI (right) of the same region. Dark regions in the MRI indicate high ^{129}Xe signal intensity.

The combustion resistance of the ^{129}Xe hyperpolarized nuclear spin state opens up fluid dynamics studies with MR velocimetry of combustion processes as demonstrated by velocity profiles of gas flow within the combustor. In addition, SEOP of hydrogen – xenon mixtures is explored. Practical aspects of MRI of combustion with hyperpolarized (hp) ^{129}Xe are presented.

References:

1. P. M. Glover, B. Newling, C. Poirier and B. J. Balcom, *J. Magn. Res.*, **176** (2005) 79.
2. S. Anala, G. E. Pavlovskaya, P. Pichumani, T. J. Dieken, M. D. Olsen and T. Meersmann, *J. Am. Chem. Soc.*, **125** (2003) 13298.
3. K.F. Stupic, J. S. Six, M.D. Olsen, G.E. Pavlovskaya, and T. Meersmann, *Phys. Chem. Chem. Phys.*, **15**, (2013), 94.

Outdoor plant measurements using compact/mobile MRI systems

K. Kose^a, Y. Terada^a, T. Haishi^b

^aInstitute of Applied Physics, University of Tsukuba, ^bMRTechnology Inc.

Openness and portability of compact permanent magnets with high homogeneity and high field-strength have opened new MRI applications [1]. In these years, we have developed several compact and/or mobile MRI systems for outdoor plant measurements, which we will review in this lecture.

In 2006, we first tried to measure MR images of a living maple tree in outdoor environments using a 0.3 T and 80 mm gap permanent magnet (weight = 56 kg) [2]. We successfully measured several cross-sections of the tree. However, we found many problems for outdoor tree measurements. The first is that it is difficult to place the “sweet spot” of the magnet in the trunk or branch of a tree, because their positions and directions are arbitrary. The second is that it is usually difficult and/or time-consuming to set-up MRI systems in outdoor environments. The third is that external noise is usually much more intense compared with laboratory environments.

In 2011, we solved these problems by constructing an electrically mobile MRI system with a flexible magnet positioning system and electromagnetic shielding both for the RF probe and the tree as shown in Fig.1 [3]. By using this system, we measured ADC maps for healthy and diseased branches of a pear tree and demonstrated the difference between them as shown in Fig.2. In 2012, we developed a mobile MRI using a 0.12 T and 17 cm gap permanent magnet for a larger tree (diameter = 6~8 cm) as shown Figs.3 and 4. This project is now in progress using a 0.2 T and 16 cm gap permanent magnet (weight = 500 kg) as shown in Fig.5 and will be reported in this conference.

In 2010, we measured relaxation times of pear fruit *in situ* using a 0.2 T and 16 cm gap (200 kg) permanent magnet mobile MRI as shown in Figs.6 and 7 [4]. Good linear relationship between $1/T_2$ and $(\text{cell size})^{-1}$ for two water components measured for harvested fruits validated and refined the *in situ* measurements, which demonstrated the usefulness of the mobile MRI system.

(*) All the permanent magnets in this study were developed by NEOMAX Engineering, Takasaki, Japan.

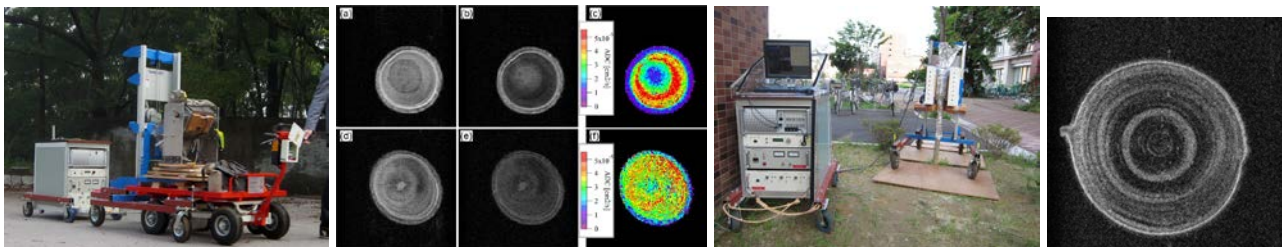


Fig.1 Electrically Mobile MRI Fig.2 Healthy/diseased branches Fig.3 MRI for Japanese zelkova Fig.4 Cross-section



Fig.5 0.2T, 16 cm magnet Fig.6 Mobile MRI (200kg) Fig.7 In-situ measurements

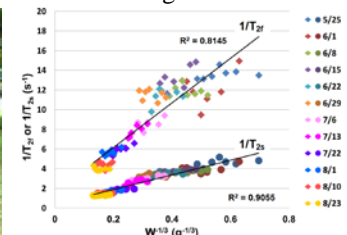


Fig.8 $1/T_2$ vs $(\text{cell size})^{-1}$

References

1. K. Kose, T. Haishi, S. Handa, Applications of permanent magnet compact MRI systems, in “Magnetic Resonance Microscopy”, ed. S. L. Codd and J. D. Seymour, WILEY-VCH, 2009, Weinheim.
2. F. Okada, S. Handa, S. Tomiha, K. Ohya, K. Kose, T. Haishi, S. Utsuzawa, K. Togashi, Development of a portable MRI for outdoor measurements of plants, the 6th CMMR, Aachen, Germany, 6–8 September (2006).
3. T. Kimura, Y. Geya, Y. Terada, K. Kose, T. Haishi, H. Gemma, Y. Sekozawa, Development of a mobile magnetic resonance imaging system for outdoor tree measurements. Rev. Sci. Instrum. **82**, 053704 (2011).
4. Y. Geya, T. Kimura, H. Fujisaki, Y. Terada, K. Kose, T. Haishi, H. Gemma, Y. Sekozawa, Longitudinal NMR parameter measurements of Japanese pear fruit during the growing process using a mobile magnetic resonance imaging system. J Magn Reson **226**, 45-51 (2013).

Earth's field NMR for detection of thin layer of liquids

S. A. Altobelli, E. Fukushima, A. F. McDowell, T. Z. Zhang

ABQMR, Albuquerque, New Mexico, USA

A non-invasive measurement of moisture content near the vadose zone surface would be useful for water balance calculations involving evaporation. Near surface moisture measurement could also be used to evaluate earthen dams' integrity. Remote detection techniques of accidental oil spills under ice will be needed for oil spill response in the Arctic. The various techniques tried so far have not been fully satisfactory and we present Earth's field NMR (EFNMR) as a possible solution to the problem.

At present, EFNMR is used with very large circular and figure-eight antennae to detect water or organic pollutants at depths roughly comparable to the coil's horizontal extent. In contrast, this work performs EFNMR on thin samples located at depths shallow compared to their horizontal extents. We built a flat coil that has a uniformly sensitive region that corresponds to this geometry. The flat coil winding approximates a rectangular current sheet with uniform current density. The return currents are routed to the outer edges of the rectangular coil mount.

The main magnetic field component generated by the current sheet is parallel to the sheet and orthogonal to the current flow direction. The wire density can be quite high at the ~ 2 kHz proton Larmor frequency in Earth's field, limited only by the ~ 150 km wavelength of the current. We have made test coils whose current sheet area is ~ 61 cm square with wire density of up to 16/cm. An important feature of the coil is the overall topology that is equivalent to a multiple turn figure-eight coil that is quite insensitive to long-range power line or other interference. Using the flat coils with both commercial and homemade consoles (without pre-polarization), we obtained $S/N > 25$ in ten accumulations from shallow pans of water containing ~ 26 liters of water.

There are many technical challenges peculiar to the problem of detecting relatively thin layers of oil beneath ice. We report our progress in dealing with two: the need for shorter recovery time and the need to suppress the ever-present and dominant signal from seawater.

We have reduced the "dead time" required after a pulse to 8ms by using relays to switch critical damping resistors into the circuitry as part of our transmit/receive switch. In laboratory experiments we perform similar machinations to quiet the system after shutting off the pre-polarization current.

We will suppress the water signal with an adiabatic inversion of oil and water magnetization that experiences a wide range of B_1 , and then to exploit the difference in T_1 between oil and water. At earth's field, the adiabatic sweep is required to go much farther than the Larmor frequency, presenting us with the problem of sweeping through zero. We address this by sweeping to resonance from above, for example, with a tangent sweep, performing a quick 180° phase shift, followed by an upward return sweep. An implication of this type of sweep in this little visited corner of parameter space is that the coil cannot be tuned while one sweeps many times the Larmor frequency.

This project is funded by Exxon Mobil Upstream Research Company in order to develop technology to detect spilled/leaked oil under Arctic sea ice. We acknowledge assistance by J. Bench, D. Kuethe, J. Boros, L. Chavez, and N. Sowko. Andrew McDowell now works for One Resonance Sensors, San Diego, CA, USA.

Broadband CPMG sequence with composite excitation and short composite refocusing pulses

Van D.M. Koroleva^a, Soumyajit Mandal^b, Yi-Qiao Song^b, Martin D. Hürlimann^b

^a School of Engineering and Applied Sciences, Harvard University, Cambridge MA 02138, USA

^b Schlumberger-Doll Research, Cambridge, MA 02139, USA

We demonstrate that CPMG sequences with phase-modulated refocusing pulses of the same duration as the standard 180° pulses can generate echo trains with significantly increased amplitudes compared to the standard CPMG sequence in the case when there is a large range of Larmor frequencies across the sample. The best performance is achieved with symmetric phase-alternating (SPA) composite refocusing pulses of the form $\alpha_{-y} \beta_{+y} \alpha_{-y}$. In comparison to standard 180° pulses, we show that with SPA refocusing pulses with $\alpha \cong 27^\circ$ and $\beta \cong 126^\circ$, it is possible to double the signal-to-noise ratio without increasing the total pulse duration or power consumption of the refocusing pulses. The increased bandwidth of these pulses more than compensates for the decrease in performance in the vicinity of resonance. To achieve the full benefit of the broadband nature of the SPA pulses in a CPMG sequence, it is necessary to combine these refocusing pulses with a broadband excitation pulse. When it is not possible to use a short, high amplitude excitation pulse, we show that phase-alternating (PA) excitation pulses are suitable for this purpose. We present a detailed analysis of the underlying spin dynamics of these new pulse sequences and confirm the simulations with experiments. We show that for samples with $T_1/T_2 > 1$, the new sequences in grossly inhomogeneous fields do not only generate echoes with an increased amplitude, but also with an increased decay time. We analyze the diffusion properties and show quantitatively that the broadband sequences have a substantially higher diffusion sensitivity compared with the standard CPMG sequence. Finally, we show that when SPA refocusing pulses are combined with so-called ‘axis-matching excitation pulses’, even higher gains in performance can be achieved.

References:

1. V. D. M. Koroleva, S. Mandal, Y. Q. Song, and M. D. Hürlimann, *J. Magn. Reson.* **230**, 64 (2013).

Determining pore length scales and connectivity of rock cores using low-field NMR

H. Liu, M. N. d' Eurydice, P. Galvosas

MacDiarmid Institute for Advanced Materials and Nanotechnology

School of Chemical and Physical Sciences, Victoria University of Wellington, New Zealand

Low-field NMR is well suited to determine permeability, wettability, connectivity and pore size distributions in porous materials¹, becoming increasingly significant for oil, geothermal and hydrological industries. In this context NMR methods were developed to provide the pore length of rock cores, either utilizing the induced internal gradient fields², or scaling the relaxation distribution to the pore size distribution with an estimated surface relaxivity¹. However, these techniques can only be applied if internal magnetic gradient fields are sufficiently high² or if prior knowledge on the sample exists¹. Regarding these constraints, we propose a more general approach which allows one to directly determine the pore length scales of rocks using Pulsed Field Gradient (PFG)-NMR at 2 MHz ¹H resonance frequency, which has the potential to improve the applicability and reliability of these NMR methods for industrial environments.

PFG techniques record the averaged net displacement of mobile spins during the observation time Δ . In the long time limit, displacements will be determined by the geometry of the porous system^{3, 4}. Thus, information of the internal pore space becomes available via a set of experiments with varying observation times. This delivers an estimate of the pore length scales of rock samples, where the kernel of the numerical inversion during data processing is modified in order to take into account the contributions of the restricted diffusion.

Correlations between the transverse relaxation time T_2 and droplet sizes were acquired for water-in-oil emulsions⁵. In a similar approach, we correlate T_2 with the pore length scale in a two-dimensional experiment. The surface relaxivity ρ_2 of rock cores can then be determined from this 2D correlation map, which in turn allows calibrating *in situ* data from NMR well-logging. Furthermore, the pore connectivity of rock samples is studied using spatially-resolved T_1 profiles. Regarding that higher connectivity can be expected for similar adjacent T_1 profiles, a corresponding correlation function may be obtained during data processing.

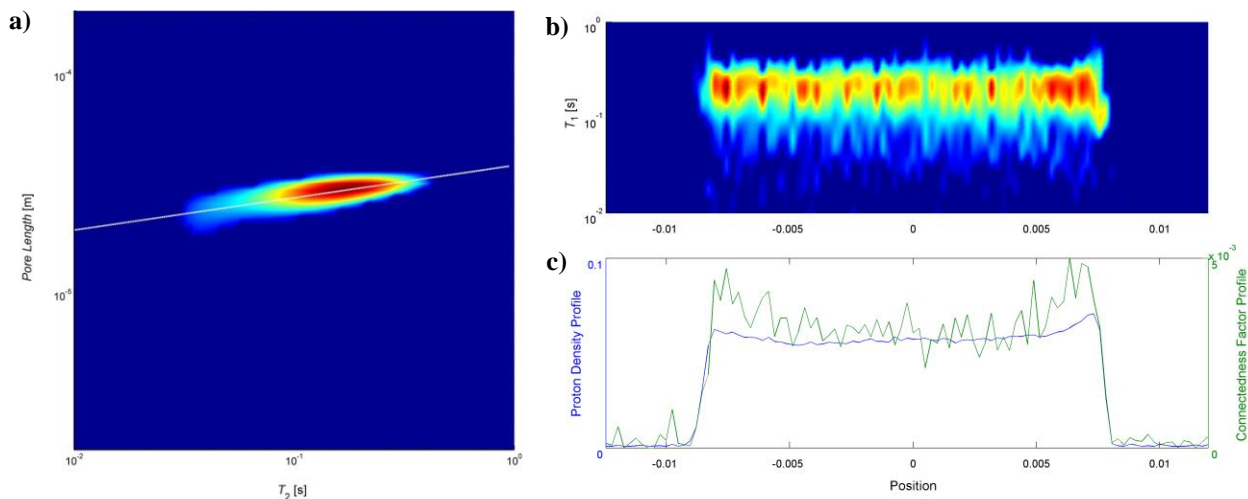


Fig.1 a) 2D T_2 - R correlation map of sandstone sample. The slope of distribution reflects the intensity of surface relaxivity ρ_2 in this core sample; b) spatially-resolved T_1 profiles of sandstone along imaging axis; c) connectivity factor profile (green) of sandstone core compared to the proton density profile (blue).

References:

- [1] A.T. Watson, C.P. Chang, Prog. Nucl. Magn. Reson. Spectrosc. 31 (1997) 343.
- [2] Y.Q. Song, S. Ryu, P. N. Sen, Nature, 406 (2000) 178.
- [3] C.H. Neuman, J. Chem. Phys. 60 (1974) 4508.
- [4] P.T. Callaghan, Oxford University Press, New York, 1991.
- [5] C.P. Aichele, M. Flaum, T. Jiang, G.J. Hirasaki, W.G. Chapman, J. Colloid Interface Sci. 315(2007) 607.

Compact and homogeneous Halbach arrays for applications to NMR spectroscopy and MRI

Ernesto Danieli^a, Josefina Perlo^a, Juan Perlo^b, Bernhard Blümich^a, and Federico Casanova^b

^aITMC, RWTH Aachen University, Worringerweg 1, D-52074, Aachen, Germany, ^bMagritek GmbH, Pauwelsstr. 19 - D-52074, Aachen, Germany

Conventional NMR spectrometers use large and expensive superconducting magnets to generate the strong and highly homogeneous magnetic fields required by this technique to work. Such magnets need regular refilling with cryogenic liquids and must be installed in specially adapted rooms to fulfill the needed working conditions. These issues preclude their installation in chemistry laboratories, where chemical reactions are safely run, or in industrial environments for quality control applications. However, during the last years important progress has been reported in the development of compact NMR magnets built from permanent magnets, which can achieve different degrees of versatility at reasonable magnetic field strength and homogeneity. Among the different geometries available, Halbach arrays present a high ratio of sample volume over magnet volume, which makes them convenient for in-situ measurements.

In this presentation, we will report different magnets based on the mentioned geometry optimized for MR imaging and high-resolution NMR spectroscopy. In particular we will show examples of applications where a low-field MR tomograph was used to obtain spatial information of extruded samples passing through the magnet. By acquiring real time MR images of rubber profiles we could determine the inner geometry in a non-destructive way, which is important for process control during production. The same system was used to acquire MR velocity maps of flowing systems. In particular we applied this methodology to characterize the influence on the flow pattern in arteries when stents are implanted to close aneurisms. Chemical analysis is another area that benefits from the use of mobile NMR spectrometers. The constant improvement of permanent magnet technology has made it possible today to resolve the signals of reactants dissolved at concentrations of the order of 1 mmol/L in the crowded spectra of a reaction medium. We will present the results obtained for a few chemical reactions within or at the output of the reactor, and we will discuss the particular issues encountered in each case.

Observation of in vivo metabolism using hyperpolarized ^{13}C MR

A. Haase

Institute for Medical Engineering (IMETUM), Technische Universität München, Germany

Metabolic imaging using hyperpolarized ^{13}C -labelled substances allows the detection and quantification of cellular metabolism in-vivo. Compared to gold-standard metabolic imaging modalities like PET, ^{13}C metabolic MR imaging (13CMMR) enables a differentiation between metabolic pathways and molecules. This constitutes a major advantage, as downstream metabolites such as lactate, which is formed by LDH from pyruvate, can be identified by their unique chemical shift properties. Such 13CMMR is a novel imaging modality with increased biochemical specificity as compared to conventional MRI. At the same time, the relatively short-lived hyperpolarized state constitutes the major disadvantage of the method, as the magnetization irreversibly decays within tens of seconds. As a result, preferably metabolic processes happening at very short timescales may be assessed by the method, which implies that instead of probing steady-state kinetic processes as in PET, a short ^{13}C -substance bolus is employed to study the metabolic conversion on a very short timescale.

Part of our work is a comparison to PET and development of fast MR imaging methods for ^{13}C . Although the ^{13}C substances are hyperpolarized, a major result from first experiments is the insight that despite the hyperpolarization, the technique is still at the edge of signal-to-noise (SNR), although physiological or even supra-physiological concentrations of the ^{13}C -labelled substances are usually injected. We revealed that PET and ^{13}C assess complimentary information, i.e. on different timescales and different metabolic pathways. As a consequence we now focus on the technological development of more advanced MR imaging methods, quantification of metabolic conversion by kinetic modeling, and at the same time to diversify the range of substances employed.

Multimodality characterization of microstructure by the combination of diffusion NMR and time domain diffuse scattering spectroscopy

Alessandro Proverbio^a, Bernard Siow^{b,c}, Adam Gibson^a, Daniel Alexander^c

^a Department of Medical Physics and Bioengineering, UCL, WC1E 6BT London, UK; ^b Centre for Advanced Biological Imaging, UCL, WC1E 6DD, London, UK; ^c Centre for Medical Image Computing, UCL, WC1E 6BT London, UK

Investigation of tissue microstructure with non-invasive histology is a key challenge for medical imaging. Diffusion NMR (dNMR) can investigate the dimension of compartments (such as cells or axons) restricting the diffusion of water molecules. Time Domain Diffuse Scattering Spectroscopy (DSS) is sensitive to size and density of scatterers in the tissue (e.g. nuclei and organelles). Here, we provide a proof of concept that combining information from dNMR and DSS, via a joint signal model, improves estimation of microstructural features compared to biophysical model of tissue microstructure informed by either modality alone.

To demonstrate the idea, we used an oil-in-water emulsion sample (Sainsbury's commercial light mayonnaise) containing spherical oil droplets, and we investigated the average radius r , log-normally distributed with spread parameter σ , and volume fraction ψ .

dNMR measurements were performed with a Stimulated Echo (G up to 1T/m, and Δ up to 700ms) sequence applied with a 9.4T Varian experimental system. The signal model assumes restricted diffusion in spherical compartments, and it estimates: diffusivity coefficient D , r and σ [1].

DSS measurements were performed with a time-domain system transilluminating a sample with a 780nm wavelength pulse laser, and a detector measures the Temporal Point Spread Function (TPSF) of the photons emerging from a sample [2]. The model assumes a Diffusion Approximation [3], and uses Mie theory [4] to relate a single scatterer size parameter, r , and volume fraction, ψ , to the TPSF.

The combined model fitting minimizes a weighted sum of the fitting errors from the two signals to obtain, r , σ , and ψ , at the same time. Confocal Laser Scanning Microscopy (CLSM) provides ground truth r , σ , and ψ for the sample.

Figure 1 shows the estimates of r and ψ obtained from experimental signals. The combined model shows more accurate and precise estimates of r compared to DSS and dNMR alone. The error bars represent the standard deviation of the chain of estimates obtained with a MCMC algorithm, proving an improvement of selectivity in combined model of about 75% versus dNMR ones. Finally, combining dNMR with DSS improves the estimation of ψ reducing the error to less than 2% even though dNMR is not directly sensitive to ψ ; the improvement comes about by improving the estimate of r , which is linked to ψ via DSS model.

In conclusion, a common model informed by both DSS and dNMR signals refines the estimation of parameters detectable with both of them since it fuses complementary information. Moreover, the fitting of the non-common parameters is facilitated, leading to a better performance. A natural application of this modality is the study of cellular structure in cancer, where DSS and diffusion MRI can be combined.

References [1] G. Zaccanti *et al.*, Appl. Opt., 36(19):4587–4599, 1997. [2] F. Schmidt *et al.*, Rev. Sci. Instrum., 71(1):256-265, 2000. [3] W. J. Wiscombe, Appl. Opt., 19(9):1505–1509, 1980. [4] R.M. Cotts *et al.*, J. Chem. Phys., 48(11):4938–4945, 1968

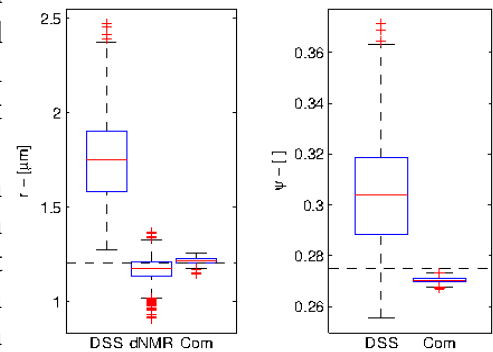


Figure 1: Estimation of r and ψ from the experimental signals. The boxplots are obtained from a Monte Carlo Markov Chain (MCMC). In the plots, the bars represent the standard deviation, the whiskers mark the last non-outlier data, and the pluses are the outliers. CLSM estimates are also shown in dashed line.

Critical points in articular cartilage where T_1 change is balanced under different gadolinium concentrations and mechanical strains

Y. Xia, N. Wang,

Departments of Physics, Oakland University, Rochester, MI 48309, USA

The concentration of glycosaminoglycans (GAG) in articular cartilage determines the depth-dependent load-bearing properties of the tissue. To investigate the T_1 changes due to the mechanical strain in the presence of gadolinium (Gd) contrast agent, μ MRI T_1 experiments were carried out on compressed cartilage when the tissue was immersed in various concentrations of Gd ions.

Methods: Fresh canine cartilage-bone blocks were soaked in the Gd solution with different $\text{Gd}(\text{DTPA})^{2-}$ concentrations (Magnevist), ranging from 0 to 1 mM. T_1 experiments were carried out at the magic angle under different static compressions (0-40%), on a Bruker AVANCE II 300 micro-imager. The echo time was 7.2 ms; and the repetition time decreased steadily from 1.5 s without Gd to 0.5 s with 1 mM Gd immersion respectively. The thickness was 1 mm and the 2D in-plane pixel size was 17.6 μm .

Results: Fig 1 summarizes the T_1 results, with the 2D T_1 images in (1a) and the 1D T_1 depth profiles in (1b). A number of features were clearly visible. (1) T_1 decreased when the Gd concentration in the solution increased, no matter whether the tissue was loaded or not. (2) Without compression, T_1 in the surface tissue reduced more rapidly than that in the deep tissue. The surface T_1 values were higher than T_1 in the deep tissue without Gd, but became lower when the Gd concentration increased to 0.4 mM or higher. (3) T_1 profiles showed less clear depth-dependency when the tissue was compressed, even at a modest 20 % overall strain. Fig 1c showed the mean T_1 values for the native tissue at different Gd concentrations. There were two critical equilibrium points in the strain-dependent T_1 plots of native tissue: (0.30 mM, 0.82 s) between 0% strain and 20% strain, and (0.52 mM, 0.62 s) between 0% strain and 40% strain. No critical point was found from the same experiments of the trypsin-degraded tissue.

Discussion: Articular cartilage is known to have a depth-dependent GAG concentration, which governs its depth-dependent mechanical properties. The strain-dependent T_1 profiles in cartilage are due precisely to this depth-dependent mechanical property of the tissue. Compression can cause a significant reduction of T_1 values when the Gd concentration was low (less than 0.4 mM), or an increase of T_1 values when the Gd concentration was high. A novel observation is the critical equilibrium point in the native tissue, which marks the particular Gd concentrations where the T_1 in a GAG-poor location (where T_1 drops faster at a higher Gd concentration) meets the T_1 in a GAG-rich location (where T_1 drops slower at the same Gd concentration). The critical point of T_1 suggests the quantification of GAG in articular cartilage by clinical MRI should, in principle, consider the load or loading history of the patients, as well as the concentration of gadolinium contrast agent in the tissue.

Acknowledgements: This project was funded by an R01 grant from NIH (AR 52353).

References:

(1) Y. Xia, et al., Magn. Reson. Med. 65 (2011) 1733. (2) S. Zheng and Y. Xia, Magn. Reson. Med. 63 (2010) 25.

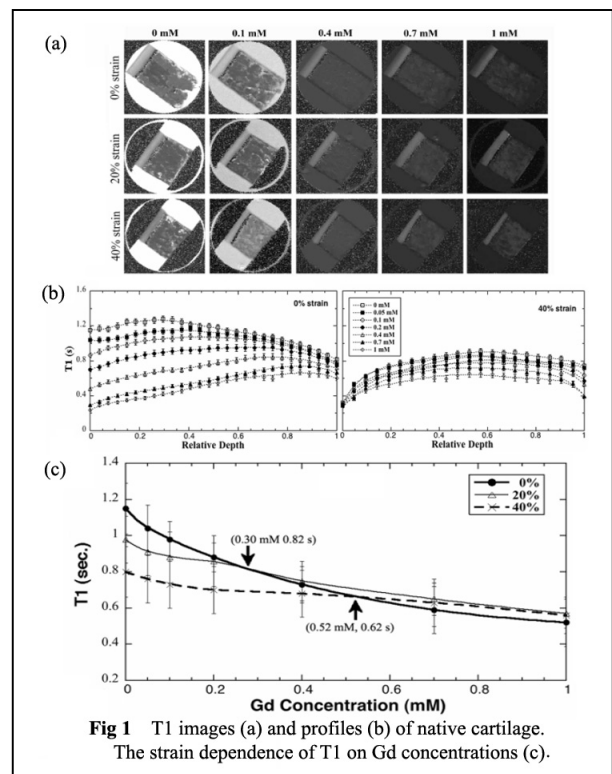


Fig 1 T_1 images (a) and profiles (b) of native cartilage. The strain dependence of T_1 on Gd concentrations (c).

NMR Micro-imaging of the human eye

J.M. Pope^{1,3}, P.K. Verkicharla^{2,3}, F. Sepehrband³, S. Kasthurirangan^{2,3} and D.A. Atchison^{2,3}

School of Chemistry, Physics & Mechanical Engineering¹, School of Optometry² and Institute of Health and Biomedical Innovation³, Queensland University of Technology, GPO Box 2434 Brisbane, Australia 4001

We have employed NMR micro-imaging to study properties of the human eye that are not readily measurable by standard techniques of optometry. We have developed a novel MRI method for measuring the refractive index distribution through the eye lens non-invasively¹ and for observing changes in gradient index (GRIN) that occur with age and degree of accommodation². Recently we have used high resolution MRI to measure the dimensions and shape of the retina (important in understanding the development of myopia). We have also employed diffusion tensor imaging to study transport properties of the lens³ (changes in which contribute to the development of senile cataract).

Unlike a conventional glass or plastic lens, where refraction of light takes place only at the surfaces, the eye lens exhibits a refractive index distribution, so that refraction occurs continuously through the lens. Using optical methods, to date it has not been possible to measure the refractive index distribution non-invasively without making assumptions about the form of the distribution. We have developed an MRI technique that for the first time allows us to map the refractive index distribution of human eye lenses both in vitro and in vivo and to investigate changes with age and state of accommodation. The results have provided new insights into the aging of the lens and the origins of presbyopia - the loss of the ability to focus on near objects (i.e. to 'accommodate') with age.

We have also shown that NMR micro-imaging of the human eye can provide useful biometric data of value in developing new methods for restoring accommodation and the treatment of refractive errors such as myopia (short sightedness)⁴. Conventional optical methods such as slit lamp photography and phakometry are unable to fully characterise changes in lens shape and equatorial radius with age and state of accommodation due to their inability to image behind the iris. Accurate measurements of lens thickness and the axial length of the eye (important in myopia) are also subject to uncertainties arising from incomplete knowledge of the refractive index distribution.

The eye lens has no vasculature, so transport of nutrients and waste products into and out of the lens, which is important for maintaining lens health and preventing development of cataract, relies primarily on passive diffusion. We measured water transport in the human eye lens in vitro using both isotope (D₂O) substitution and diffusion tensor imaging (DTI). The results showed that a barrier to diffusion develops around the lens nucleus with age, which may inhibit transport of antioxidants (glutathione) into the nucleus and contribute to the onset of senile cataract.

References:

1. C. E. Jones, D.A. Atchison, R. Meder, J.M. Pope, *Vision Res.* 45, (2005), 2352.
2. S. Kasthurirangan, E.L. Markwell, D. A. Atchison and J. M. Pope *Investigative Ophthalmology and Visual Science* 49, (2008), 2531.
3. B. A. Moffat, J. M. Pope, *Exp. Eye Res.* 74, (2002), 677.
4. S. Kasthurirangan, E. L. Markwell, D. A. Atchison and J. M. Pope, *J. Vision* 11(3), (2011), 1.

Unconventional slice-selective RF pulses and pulse pairs

John M. Pauly

Dept. of Electrical Engineering, Stanford, CA, USA

RF pulses play an important role in MRI, exciting, refocusing, and preparing the magnetization for imaging. Most RF pulses are windowed sincs, linear phase SLR pulses¹, or adiabatic pulses. This presentation will describe other types of pulses that can be designed based on the SLR approach. These design the magnetization at a time in the pulse sequence, and then solve for one or more pulses that achieve this. By exploiting non-linear phase, the results can be lower peak power, increased selectivity, and short echo times.

The SLR approach represents the rotation produced by an RF pulse by two spinor-domain polynomials $A(z)$ and $B(z)$, where $z = \exp(i2\pi\gamma Gx\Delta t)$. These are essentially z -transforms, as used in digital signal processing. Typically $B(z)$ is chosen to be a linear phase FIR filter with a frequency response $DFT(B(z))$ that matches the desired slice profile, scaled to $\sin(\theta/2)$, where θ is the flip angle. $A(z)$ is chosen to be consistent with $B(z)$. A back recursion on $A(z)$ and $B(z)$ produces the RF pulse (Fig. 1). This gives excellent excitation, inversion, and spin echo pulses, which are widely used.

Usually $A(z)$ is chosen so as to minimize RF power. This corresponds to the minimum phase $A(z)$. However, there are significant benefits from adding additional phase to $A(z)$, or $B(z)$, or both. Adding phase to $A(z)$ can be used to generate a self-refocusing excitation pulse (Fig 2). Adding quadratic phase to $B(z)$ reduces peak power, allowing very selective saturation pulses², as well as insensitivity to B1 variations³. Non-linear phase excitation and refocusing pulses can be matched to produce linear phase spin-echoes⁴, where the excitation and spin echo pulse can partially or completely overlap⁵. This allows very short echo times, which is useful for ³¹P spectroscopic imaging⁶. An example pulse pair is shown in Fig 3. The delay between the 90 and 180 can be anything, including completely overlapping to produce a self-refocused pulse. In addition, the slice profile is more selective than either to 90 or 180 individually.

References:

1. J Pauly, P Le Roux, D Nishimura, A Macovski, *IEEE TMI* 10 (1), 53-65
2. Schulte RF, Tsao J, Boesiger P, Pruessmann KP. *JMR*. 2004 Jan;166(1):111-22.
3. Balchandani P, Pauly J, Spielman D. *MRM*. 2010 Sep;64(3):843-51
4. Zun Z, Hargreaves BA, Pauly J, Zaharchuk G. *MRM*. 2013 Jul 15.
5. Lim KO, Pauly J, Webb P, Hurd R, Macovski A. *MRM*. 1994 Jul;32(1):98-103.
6. Balchandani P, Yamada M, Pauly J, Yang P, Spielman D. *MRM* 2009 Jul;62(1):183-92.

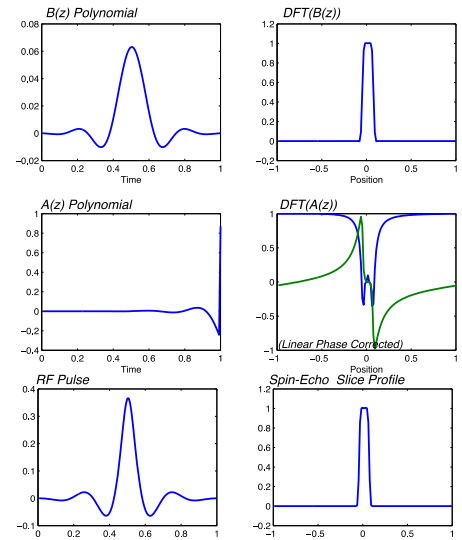


Fig 1. Spin-echo pulse design. $B(z)$ determines the flip angle profile, $A(z)$ minimize power, and a back recursion produces the RF pulse.

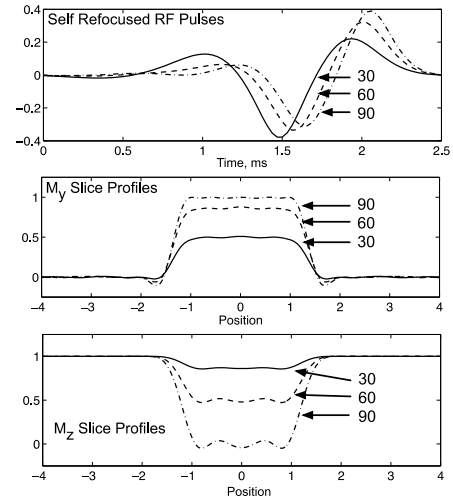


Fig 2. Self-refocused RF pulses for flip angles of 30, 60, and 90. The RF power is that of an excitation and a spin echo pulse.

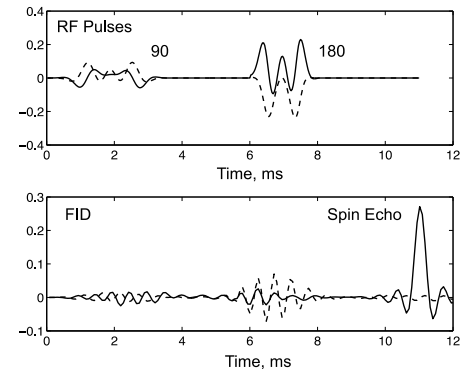


Fig 3. Non-linear phase pulse pair (top) produces a linear phase spin echo (bottom).

Lung surface sensitive MRI contrast using hyperpolarized ^{83}Kr

J.S. Six^{a,b}, T. Hughes – Riley^{a,b}, D.M.L. Lilburn^{a,b}, A.C. Dorkes^{a,c}, K.F. Stupic^{a,b}, D.E. Shaw^d, P.G. Morris^{a,c}, I.P. Hall^b, G.E. Pavlovskaya^{a,b}, and T. Meersmann^{a,b}

University of Nottingham, Sir Peter Mansfield Magnetic Resonance Centre^a, School of Clinical Sciences^b, School of Physics and Astronomy^c, Nottingham, NG7 2RD, UK

^dCity Hospital Nottingham, Nottingham Respiratory Research Unit, Nottingham NG5 1PB, UK

The ^{83}Kr longitudinal (T_1) relaxation weighted MRI contrast was previously shown to be indicative of the specific surface treatment in a porous model system¹. Unlike ^3He and ^{129}Xe , the ^{83}Kr nucleus possesses a nuclear spin $I = 9/2$ and thus a non-vanishing electric quadrupole moment that serves as a probe for electric field gradients (EFGs). The EFGs are predominantly generated during brief collision and adsorption events of the noble gas atoms with the surrounding surfaces, resulting in rapid T_1 relaxation that is detected in the gas phase. This surface sensitive ^{83}Kr contrast is affected by the surface to volume ratio (S/V), surface composition, surface temperature, and surface adsorption of molecules². On the down side, quadrupolar relaxation also restricts the hp ^{83}Kr signal intensity and applications of hp ^{83}Kr MRI were limited thus far to conceptual studies showing low resolution images and NMR relaxation measurement in excised lungs with little chance to provide data about internal structure or function of the organ³.

Methodological advances⁴ presented in this work lead to a substantial increase in the ^{83}Kr hyperpolarization and the resulting signal intensity. Using the improved methodology for spin exchange optical pumping of isotopically enriched ^{83}Kr , internal anatomical details of *ex vivo* rodent lung can be resolved with hyperpolarized ^{83}Kr MRI after krypton inhalation. The different ^{83}Kr relaxation times found between airways and alveolar regions are used to corroborate surface sensitive MRI contrast in lungs. As a novel contrast agent, hyperpolarized ^{83}Kr has promising applications for diagnostic pulmonary imaging.

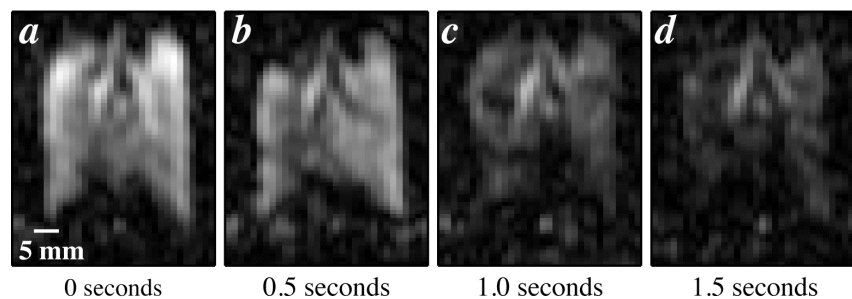


Fig. 1.: Series of hp ^{83}Kr MR images demonstrating surface sensitive T_1 weighted contrast. (a) Hp ^{83}Kr VFA FLASH MRI of excised rat lung using 3 mm slice selection. (b – d) MR images as in (a) with a relaxation delay t_d between hp ^{83}Kr inhalation and acquisition as indicated in the figure. The major airways are visibly less affected than the alveolar space by increasing t_d values.

References:

1. G.E. Pavlovskaya, Z.I. Cleveland, K.F. Stupic, R.J. Basaraba, and T. Meersmann*, Proc. Nat. Acad. Sci., **102**, (2005) 18275.
2. Z.I. Cleveland, K.F. Stupic, G.E. Pavlovskaya, J.E. Repine, J.B. Wooten, and T. Meersmann*, "J. Am. Chem. Soc. **129**, (2007), 1784.
3. K.F. Stupic, N.D. Elkins, G.E. Pavlovskaya, J.E. Repine and T. Meersmann, "Physics in Medicine and Biology, **56** (2011) 3731-3748
4. J.S. Six, T. Hughes – Riley, K.F. Stupic, G.E. Pavlovskaya, and T. Meersmann, PLOS-ONE, **7**, (2012), e49927

Detailed laminar characteristics of the neocortex revealed by NODDI

M. Kleinnijenhuis^{a,b}, H. Zhang^c, D. Wiedermann^d, D. Norris^b, A-M. van Cappellen van Walsum^{a,b}

^aDepartment of Anatomy, Radboud University Nijmegen Medical Centre, ^bDonders Institute for Brain, Cognition and Behaviour, Radboud University Nijmegen, ^cDepartment of Computer Science, University College London, ^dMax Planck Institute for Neurological Research, Cologne

Diffusion weighted imaging (DWI) can provide a rich description of cortical architecture, *in vivo*¹ as well as *ex vivo*². Diffusion properties of the primary visual cortex (V1) have been shown to be layer-specific³. Here, we extend these findings by fitting the NODDI tissue model⁴ to multi-shell DWI data to support an improved division of cortical layers.

Samples of human V1 were fixed in formalin (>2 months), soaked in phosphate buffered saline (>72h) and scanned in a proton-free fluid. Diffusion data were acquired for eight shells ($b=0-20000 \text{ smm}^{-2}$) sampled in 384 directions with 200 μm isotropic spatial resolution on a 9.4T preclinical MR system equipped with a cryogenic probe. Four tissue compartments (1. neurite volume fraction (axons+dendrites/cylindrical structures); 2. space around the cylinders; 3. a CSF compartment; 4. an isotropic restricted compartment⁵) and the fibre orientation dispersion (kappa, concentration around the dominant direction) were fitted using the NODDI toolbox.

On the basis of the neurite volume fraction (ficvf) the cortex could be divided in three layers: the superficial layers, the stria of Gennari and the deep layers. Neurite density was higher in deep vs. superficial layers, but highest for the stria of Gennari. The contrast between the layers was larger for neurite density (ficvf) as compared to the mean kurtosis (left graph). The orientation dispersion resolves additional layers. From pial to the WM surface, the superficial layers show a gradient of increasing dispersion (decreasing kappa) towards the stria of Gennari. In the cortex below the stria of Gennari can be subdivided in three layers showing with high-low-high coherence. Putatively, the low coherence layer represent the inner band of Baillarger. These patterns were reproduced in a sample of a second specimen.

The layer-specificity of diffusion in the cortex can be resolved better in NODDI parameter maps as compared to standard alternatives.

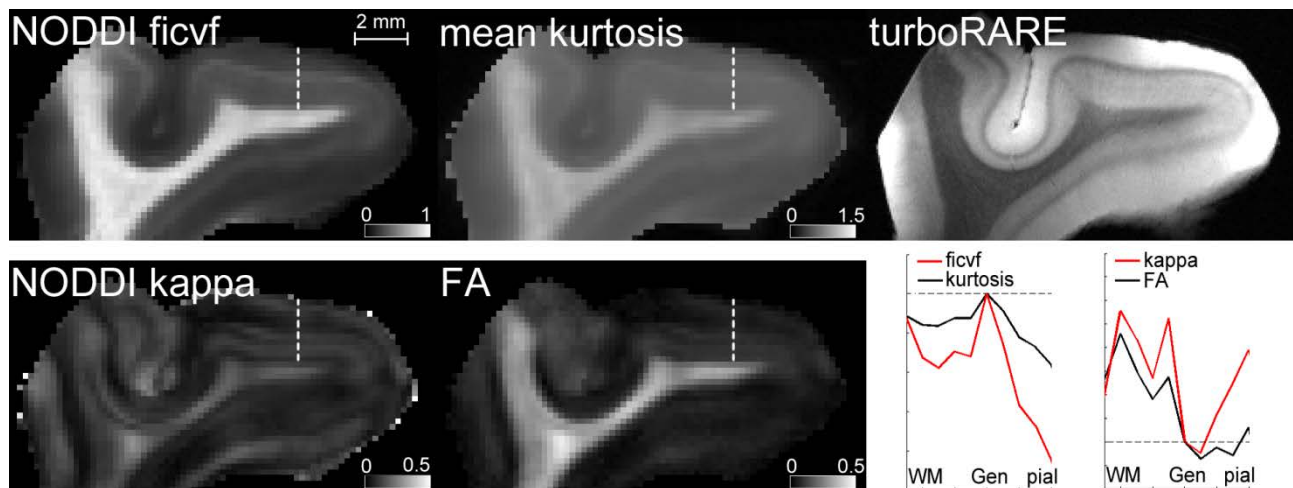


Figure 1. NODDI parameter maps (ficvf=neurite volume fraction; kappa=Watson concentration) and reference images (fa=fractional anisotropy). Graphs show cortical profiles along the dashed lines on the left, normalized to the value in the stria of Gennari (WM=gray-white matter boundary; Gen=stria of Gennari).

References:

1. Heidemann et al, NeuroImage 60 (2012), 967-978
2. Miller et al., NeuroImage 59 (2012), 2284-2297
3. Kleinnijenhuis et al., Cortex (2012), doi: 10.1016/j.cortex.2012.11.015
4. Zhang et al., NeuroImage 60 (2012), 1000-1016
5. Alexander et al., NeuroImage 52 (2010), 1374-1389

Low-field investigations of enzymatically degraded articular cartilage and its constituents

E. Rössler, C. Mattea, S. Stapf

Dept. of Technical Physics II, TU Ilmenau, 98584 Ilmenau, Germany

The layered structure of mammalian articular cartilage is reflected by a pronounced depth dependence of T_2 , which is a consequence of different degrees of order of the collagen fibers but also of a gradient of water and glycosaminoglycan (GAG) concentration, respectively. The orientational order results in an angular dependence of T_2 that becomes less pronounced at greater distance from the joint surface [1]. T_1 , however, at conventional laboratory field strengths shows little variation in comparison.

In this study, the dependence of magnetic resonance relaxation times in bovine articular cartilage is investigated at low magnetic field strength of 0.27 T and 0.44 T using portable scanners. One-dimensional, depth-dependent scans were carried out with spatial resolutions between 20 and 50 μm . While a systematic variation of T_2 is found that is in agreement to similar mammalian cartilage observed at high fields, T_1 also shows a strong depth dependence that correlates with the separation of the tissue into three distinct zones. This pronounced effect is explained by the increased T_1 contrast commonly found towards smaller magnetic field strengths, a consequence of slow and anisotropic molecular reorientations that dominate the relaxation dispersion at low magnetic resonance frequencies [2].

Superposed onto the power-law dependence of T_1 are the so-called quadrupolar dips, significantly reduced relaxation times in the region between about 10 and 70 mT which indicate cross-relaxation of protons with the partially immobilized nitrogen nuclei in amino acids in collagen and glycosaminoglycans (GAGs). Varying the composition, water content or structural integrity of cartilage affects both the general frequency dependence of T_1 and the shape of the quadrupolar dips, providing a possible diagnostic access to arthropathies such as osteoarthritis (OA). A statistical correlation between the degree of OA and the magnitude of the quadrupolar dips has been identified [3], but it remains unclear whether this dependence must be assigned to changes in the GAGs, collagen or both.

In the second part of this work, the effect of enzymes onto cartilage and its constituents is investigated as a model for osteoarthritis, and results are compared to measurements carried out at human healthy and OA cartilage tissue. While trypsin is known to separate GAGs from the proteoglycan backbone – the distribution of residual GAG having been investigated at low field by the use of the ionic contrast agent Gd-DTPA –, collagenase attacks the collagen structure exclusively. Nitrogen nuclei in both substances are shown to contribute to the quadrupolar dips in a similar way. Experiments for both constituents as well as fresh and enzyme-treated bovine articular cartilage were carried out and the relaxivity in the region of the quadrupolar dips were quantified. The observed strong dependence on water concentration is interpreted by a fast-exchange model and is discussed in conjunction with the low-field imaging results.

References:

1. Y. Xia, *Magic-angle effect in magnetic resonance imaging of articular cartilage: a review*, Invest. Radiol. 35 (2000) 602.
2. E. Rössler, C. Mattea, A. Mollova, S. Stapf, *Low-field one-dimensional and direction-dependent relaxation imaging of bovine articular cartilage*, J. Magn. Reson. 213 (2011) 112.
3. L.M. Broche, G.P. Ashcroft, D.J. Lurie, *Detection of osteoarthritis in knee and hip joints by fast field-cycling NMR*, Magn. Reson. Med. 68 (2012) 358.

T_2^* of minutes to 100 hours!
HP- gases for spin clocks and magnetometers

P. Blümler, A. Nikiel, M. Repetto, K. Tullney, S. Karpuk, W. Heil,

Institute of Physics, University of Mainz, Germany

Hyperpolarization of noble gases (e.g. ^3He , ^{129}Xe) by optical pumping is well known in NMR. The wide interest and high price of these isotopes made it necessary to find ways of polarizing large quantities with high polarization degrees, store them for transport, administer, collect and recycle them. The instrumentation developed for this closed loop will be presented.

While NMR studies of lungs and materials with such hyperpolarized gases are well known in the community¹, we would like to give an overview of some recent developments and research in more fundamental physics.

The nuclear spins of gases can have very long relaxation times. Especially the long coherence time of the NMR-signal, T_2^* , allows for extremely precise measurements of magnetic fields and related physical properties. However, to obtain such extremely long lasting signals the sample has to be kept in suitable containers, low pressure and very homogeneous fields. Another prerequisite is that it can be hyperpolarized to overcome the low spin density under such conditions. We have developed such magnetometers for fields ranging from micro- to several Tesla.

Earlier work at very low fields showed that T_1 and T_2^* times in the order of hundred hours can be obtained and used in $^3\text{He}/^{129}\text{Xe}$ co-located spin clocks². Here, both isotopes are located in the same vessel and hence experience the same environmental influences. Then the phase relation between the two precession frequencies can be used as an extremely sensitive “spin-clock” to probe for non-magnetic spin interactions such as the sidereal variation of the $^3\text{He}/^{129}\text{Xe}$ frequency induced by Lorentz-violating couplings.

While low magnetic fields ($< 10^{-2}$ T) can also be measured extremely precisely (10^{-17}) by SQUID or SERF³, NMR offers the highest precision at high fields for which we developed a dedicated ^3He magnetometer. In difference to the previous work at low field a special variant of metastability optical pumping had to be developed to hyperpolarize ^3He in such high fields and special care had to be taken for the choice of materials in its direct vicinity due to magnetic susceptibility effects. At the moment we observed T_2^* times of 100 s in standard NMR magnets, which already allows for ultra-precise (10^{-12}) field measurements. We developed this instrument especially for field monitoring during high precision mass-spectroscopy using Penning traps to test for the standard model.

While most of the motivation of our research is driven by testing fundamental physical models, the developed instrumentation and solved technical problems may find the interest of a broader NMR audience.

References:

1. see for instance: D. M. L. Lilburn et al., J. Magn. Reson. **229** (2013) 173-186 and references therein.
2. C. Gemmel et al., Eur. Phys. J. D **57** (2010) 303-320.
3. J. C. Allred et al., Physical Review Letters **89** (13) (2002), 130801

Following function in real time: New NMR and MRI methods for studying structure and dynamics in fuel cells and supercapacitors

Clare P. Grey^{1,2}

¹Department of Chemistry, University of Cambridge, Cambridge, UK

²Department of Chemistry, Stony Brook University, Stony Brook, USA

A full understanding of the operation of a battery, battery and fuel cell requires that we utilize methods that allow devices or materials to be probed while they are operating (i.e., *in-situ*). This allows, for example, the transformations of the various cell components to be followed under realistic conditions without having to disassemble and take apart the cell. To this end, the application of new *in* and *ex-situ* Nuclear Magnetic Resonance (NMR), pulse field gradient (PFG) and magnetic resonance imaging (MRI) approaches to correlate structure and dynamics with function in lithium-ion and lithium air batteries, fuel cells membranes and supercapacitors will be described. The *in-situ* approach allows processes to be captured, which are very difficult to detect directly by *ex-situ* methods. For example, we can detect side reactions involving the electrolyte and the electrode materials, sorption processes at the electrolyte-electrode interface, and processes that occur during extremely fast charging and discharging. *Ex-situ* NMR investigations allow more detailed structural studies to be performed to correlate local and long-range structure with performance in both batteries and fuel cell materials.

In this talk, I will describe the use of NMR spectroscopy to probe local structure changes in lithium ion batteries focusing on our work with the anode material Si, on lithium air cathodes, and to investigate Li dendrite formation in lithium metal batteries. Finally, the application of NMR to examine double layer formation in electrolytic double layer capacitors (supercapacitors) will be described.

Two-dimensional NQR using ultra-broadband electronics

Soumyajit Mandal, *Yi-Qiao Song*

Schlumberger-Doll Research, Cambridge, MA, USA

We have previously described a broadband instrument (called a non-resonant magnetic resonance system) that can effectively excite and detect NMR and NQR signals over a wide frequency range [1, 2]. Our current system operates between 100 kHz and 3.2 MHz using an un-tuned sample coil and ultra-broadband electronics. The major benefits of this instrument compared to conventional NQR/NMR systems include increased robustness and elimination of the need for tuning adjustments in the hardware. Here we describe its use for performing two-dimensional (2D) scans, which allow better interpretation of complex NQR spectra by detecting the connected resonances.

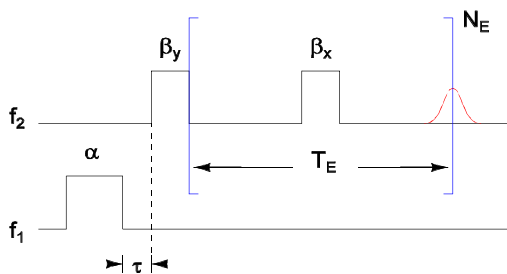


Figure 1: A perturb-detect pulse sequence that detects coupling between two NQR lines.

when f_1 and f_2 match two of the three possible NQR lines for one site with spin $I = 1$, hence changing the amplitude of the SLSE signal detected at f_2 . Such changes thus determine whether two lines in an NQR spectrum are coupled, i.e., arise from the same site within a molecule. The coupling can be conveniently detected by measuring the *difference spectrum*, i.e., by subtracting two sets of scans, one with the perturbation pulse turned on and the other with it turned off.

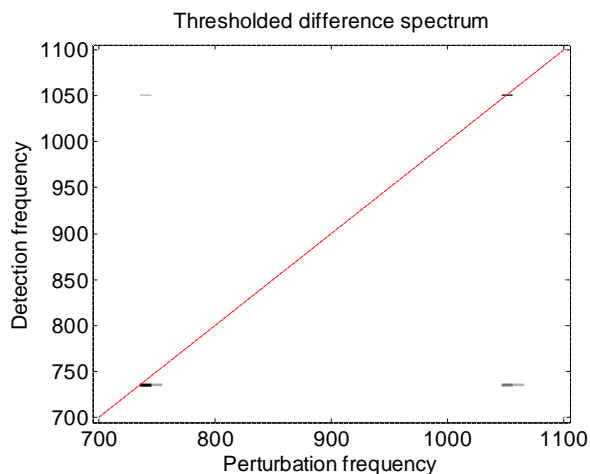


Figure 2: Measured 2D difference spectrum of a glycine sample between 700 kHz and 1.1 MHz. The output was thresholded to highlight significant amplitude changes (larger than $\pm 25\%$ of the maximum signal amplitude). The dashed line represents the diagonal ($f_1 = f_2$).

Figure 1 shows an NQR pulse sequence that takes advantage of the ability of our broadband electronics to rapidly change the operating frequency. It is a modification of the basic spin-locked spin-echo (SLSE) sequence, and consists of a single perturbation pulse of flip angle α and RF frequency f_1 , followed by detection with an SLSE sequence at RF frequency f_2 . The delay τ is kept short enough to avoid relaxation. The perturbation pulse causes population transfers between nuclear energy levels

We have applied this technique to ^{14}N NQR measurements. Figure 2 shows the measured 2D difference spectrum of a powder sample containing glycine. It clearly shows four negative peaks. These peaks are broader along the perturbation axis, where their width is set by the bandwidth of the perturbation pulse, than along the detection axis, where it is set by the length of the echo acquisition windows. The diagonal peaks at 737 kHz and 1.052 MHz match lines in a normal 1D spectrum. The cross-peaks show that these lines have coupled populations and originate from a single site. Moreover, both cross-peaks are negative, implying that the lines correspond to the $-$ and $+$ transitions, respectively. This result matches what we expect from our glycine sample. We have also performed similar experiments on mixtures of compounds, with good results.

[1] S. Mandal, S. Utsuzawa, Y.-Q. Song, *Microporous and Mesoporous Materials*, *in press* (2013).

[2] S. Mandal, Y.-Q. Song, *Experimental NMR Conference (ENC) proceedings*, poster 187 (2012).

MicroMR with Multiarray-Coils

J. Hennig^a, J.G. Korvink^b

^aDepartment of Radiology, Medical Physics, University Medical Center, Freiburg, Germany

^bFRIAS and Department of Microsystems Engineering (IMTEK), University Freiburg, Germany

MicroMR is typically performed on samples contained in an appropriate device, which can be anything ranging between a simple NMR testtube and a sophisticated microfluidic device. The container can be equipped with a small RF-coil to maximize the SNR of the sample, and to ensure that the investigated object is properly contained within the sensitive volume of the coil. This configuration has found widespread use in biomedical research.

Multiarray-coils promise to further broaden the scope of applications of microMR. An array of $N \times M$ small coils maintains the high sensitivity afforded by the individual small coil element, but allows increasing the volume of investigation to a larger scale, as defined by the size of the total coil array. This allows to perform imaging with microscopic resolution on more extended samples such as cell ensembles, or tissues, and tissue specimen like skin biopsies or anatomical slices.

Conventional flat microcoils are based on a flat spiral design, which allows for easy fabrication by planar processes. A key challenge in the design of our coil arrays was to achieve a flexible 3D-process, which allows to realize small solenoid coils to improve the homogeneity and thus the SNR of each coil element. Fabrication was performed with an automatic wirebonding machine, which rapidly winds multiple small coils of diameter 0.2-5 mm around SU8-posts (Figure 1).

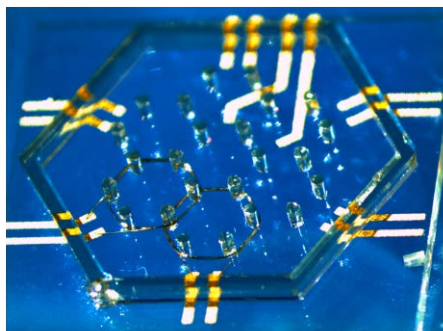


Figure 1: Two of seven solenoid coils (each 2 mm diameter) wound around SU8 posts using a wirebonding machine [1].

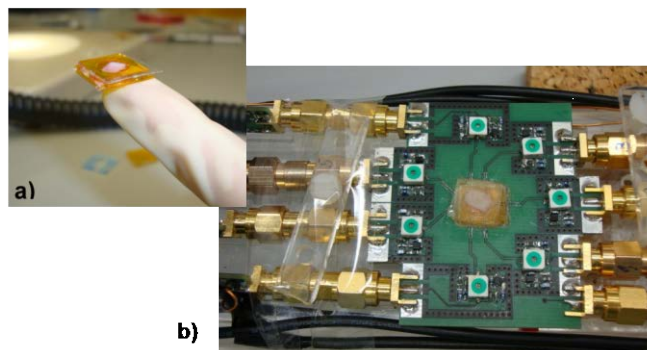


Figure 2: Current microcoil assembly including electronics (b) and sample holder (a) containing a skin biopsy [2].

The current setup consists of an array of 7 overlapping solenoid coils (Figure 1), which is used in a 9.4 T horizontal bore magnet (Bruker Biospin, Karlsruhe). Figure 3 shows a recent example of imaging a fixed hippocampal culture in comparison to optical microscopy.

Further developments towards larger coil arrays require the realization of 3D approaches with respect to the coil electronics, as well as new concepts for handling of simultaneously acquired multichannel data, which is currently under way in J.G. Korvink's lab. To improve SNR we are currently exploring the use of parahydrogen induced hyperpolarization (PHIP) as well as the SABRE-technique to boost sensitivity for metabolic microimaging with our setup.

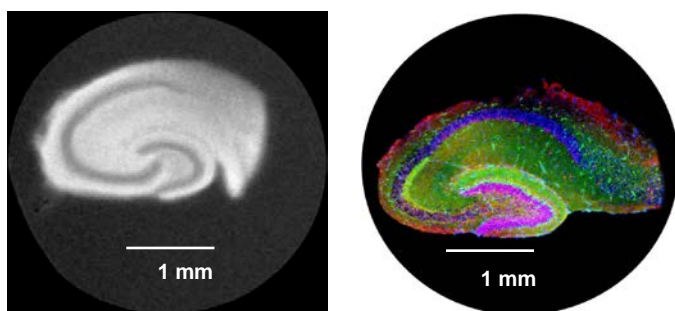


Figure 3: Visualization of neuronal structures in a fixed Organotypic hippocampal slice culture (OHSC) using MR microscopy, compared to optical microscopy of histologically stained cryosections.

References:

1. Gruschke OG et al. Lab on a chip phased-array MR multi-platform analysis system. *Lab Chip* 2012;12(3):495-502.2012
2. Goebel K et al. MR Microscopy of Diseased Human Skin Using Phased-Array of Microcoils at 9.4 T: First Results. Proc. 21st Annual Meeting ISMRM, Salt Lake City, p.2908 (2013)

Stress coupled NMR velocimetry

T.I. Brox^a, R. Fischer^b, S. Kuczera^a, W. Kittler^a, B.S. Douglass^a, P. Galvosas^a

^aMacDiarmid Institute for Advance Materials and Nanotechnology, School of Chemical and Physical Sciences, Victoria University of Wellington, Wellington, New Zealand, ^bInstitute of Physics, Ilmenau University of Technology, Ilmenau, Germany

Nuclear magnetic resonance (NMR) spectroscopy and velocimetry have become unique tools for the investigation of complex fluids under shear¹. Past improvements have enriched the information learned about soft matter systems through combined rheological and NMR (rheo-NMR) experiments. In this research we have rethought the traditional rheo-NMR experimental set-up and built an NMR compatible rheometer (Fig. 1). In our design, the shearing cell is mounted directly to the drive shaft prior to loading into the NMR system. Assembling this stand-alone rheometer outside of the magnet allows for precision alignment of components and eliminates mechanical backlash.

To measure the stress response of materials under shear during NMR experiments, an inline torque sensor has been added to our drive shaft. The torque sensor has a measurement range of $(70.6 \pm 0.4) \times 10^{-3}$ Nm, appropriate for current studies of complex fluids in cylindrical Couette geometries. Previous work has realised simultaneous measurements of global rheological parameters during NMR experiments. However, to date this approach has only been used for a cone-and-plate geometry coupled to ²H NMR spectroscopy². Independent of the NMR system our instrument functions as a stand-alone rheometer and torque measurements have been benchmarked to a commercially available instrument (AR2000, TA Instruments) with a custom geometry that matches the rheo-NMR shear cell.

Eliminating backlash from the newly designed NMR compatible rheometer allows for large amplitude oscillatory shear (LAOS) experiments³. To accomplish oscillatory and other advanced motion (e.g. start-up) profiles, rotation is driven from a stepper motor operating with feedback from a high resolution optical encoder placed directly between the drive shaft and the shearing cell.

Additionally we have built a three-axis gradient set for a 2 MHz NMR system (Rock Core Analyzer, Magritek) allowing for magnetic resonance imaging experiments to be performed at low fields. Combining this benchtop imaging system with the set-up described above may form

the foundation of a low-cost and compact NMR coupled rheometer.

References:

1. P. T. Callaghan, Rep. Prog. Phys. 62 (1999) 599.
2. D. A. Grabowski and C. Schmidt, Macromolecules 27 (1994) 2632.
3. K. Hyun et al., Prog. Polym Sci. 36 (2011) 1697.

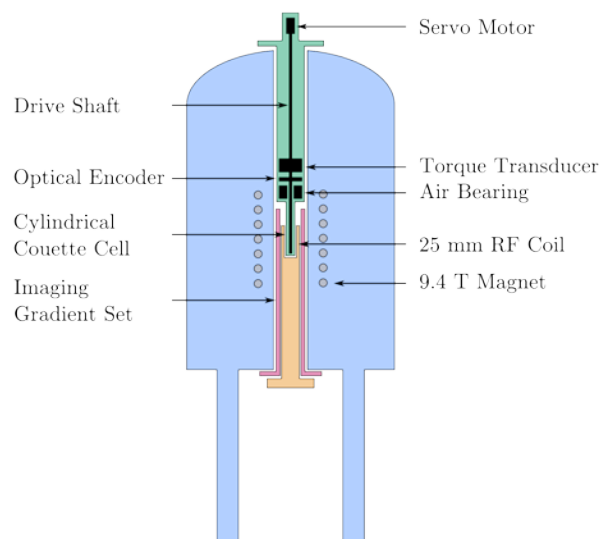


Fig. 1: Cross section schematic of NMR rheometer instrument installed in a superconducting magnet.

Magnetic Resonance Imaging of electrochemical systems

Melanie M. Britton

Department of Chemistry, University of Birmingham, Birmingham, UK

MRI has long been recognised as one of the leading techniques used in medical diagnosis and research. However, what makes this technique an excellent tool for imaging the brain also makes it highly effective for studying complex, heterogeneous chemical systems. Our research involves the application and development of magnetic resonance imaging (MRI) techniques to measure and visualise chemistry in a diverse range of applications¹. Recently, there has been increasing interest in the application of MRI for visualising electrochemical processes²⁻⁴. In our

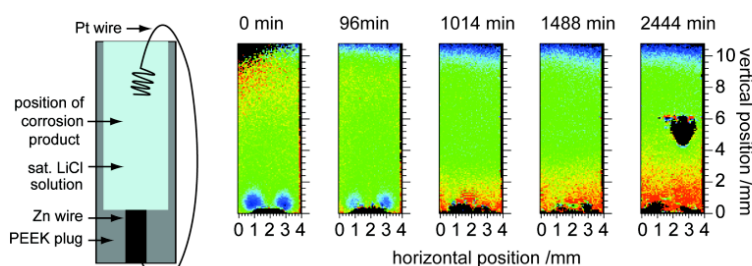


Fig. 1 Electrochemical cell and MR images mapping distribution of Zn ions in electrolyte during corrosion through changes in the relaxation time of the electrolyte². Lower T_1 values indicate Zn^{2+} species and higher T_1 values indicate $ZnCl_x^y$

original paper², we demonstrated the ability of MRI to visualise compositional changes within an electrolyte above an electrochemically active (corroding) metal surface. Image contrast was produced using the relaxation time of water molecules in the electrolyte, which were sensitive to increases in the concentration of Zn^{2+} ions, as well as changes

in the speciation of the Zn ions (Fig. 1).

One issue that has limited the more widespread application of MRI to electrochemical systems, has been the presence of metals in most electrochemical cells, which give rise to imaging artifacts^{5,6}. We have, however, found that through careful selection of the geometry and orientation of the metal in the cell with respect to both B_0 and B_1 , imaging artifacts can be eliminated sufficiently to enable viable measurements to be made close to the active metal surface⁷. Using this method, a number of electrochemical systems have been investigated and will be presented. These include visualization of the distribution of chemical species associated with the zinc and oxygen electrochemistry in an alkaline electrolyte in a zinc-air battery⁷ (Fig. 2) and the corrosion of copper. A variety of methods for achieving image contrast have been employed and will be discussed.

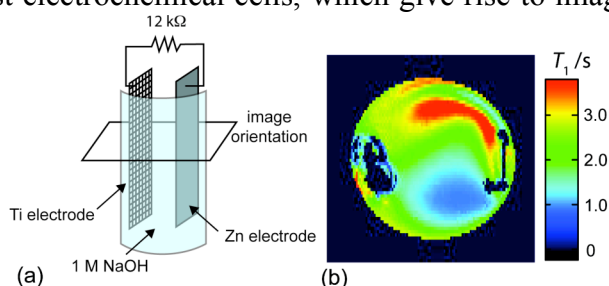


Fig. 2 (a) Schematic diagram of a model Zn-air cell and (b) MRI of chemical gradients during Zn dissolution in Zn-air cell⁷.

References:

1. M. M. Britton, *Chem. Soc. Rev.* 39 (2010) 4036.
2. A. J. Davenport, M. Forsyth, M. M. Britton, *Electrochem. Comm.* 12 (2010) 44.
3. M. Klett, *et al.* *J. Am. Chem. Soc.* 134 (2012) 14654.
4. S. Chandrashekar *et al.* *Nature Mat.* 11 (2012) 311.
5. C. R. Camacho, D. B. Plewes, R. M. Henkelman, *J. Magn. Reson. Imag.* 5 (1995) 75.
6. H. Graf, *et al.* *Med. Phys.* 33 (2006) 124.
7. P. M. Bayley, *et al.* (2013) submitted.

3D Diffusion prepared FISP for single cell MR microscopy

I.O. Jelescu^a, F. Geffroy^a, D. Le Bihan^a, L. Ciobanu^a

^aNeuroSpin, CEA Saclay, Gif-sur-Yvette, France

MR microscopy is in need of a sequence that allows rapid diffusion measurements with high spatial resolution. The use of EPI for MR microscopy at ultra-high magnetic fields leads to severe artifacts related to susceptibility differences, eddy currents and mechanical vibration. A diffusion-prepared fast imaging with steady-state free precession (DP-FISP) sequence has been recently proposed for *in vivo* preclinical imaging¹. In this work, a 3D DP-FISP sequence for MR microscopy was implemented and tested on phantoms. Measurements of apparent diffusion coefficients (ADCs) in isolated *Aplysia* neurons are presented.

Methods: A 3D DP-FISP with centric encoding was implemented on a 17.2 T imaging system (Bruker BioSpin). Acquisitions were performed at 19°C using a 700 μm diameter, homebuilt, microcoil as RF transceiver. Diffusion preparation and FISP read-out timings were minimized to limit T₁ relaxation. Phantom validation: The sequence was tested against a standard diffusion-weighted spin-echo (DW-SE) sequence on three phantoms. The phantoms were glass capillaries filled with solutions of various T₁s and diffusion coefficients, similar to values measured in biological samples^{2,3}. Sequence parameters were as follows: 7 b-values spanning 10 – 600 s/mm²; $\tau/\tau' = 10/2.5$ ms; TE/TR = 2.6/5.2 ms; matrix 190x32x24; (25 μm)³ resolution; NA = 4; TA = 1h7m. 3D DW-SE parameters were the same as for DP-FISP, except the following: 128x32x24 matrix; TE = 18.45 ms; TR = 3 s; NA = 1; TA = 4h29m. ADCs were estimated from each data set and compared between the two sequences. Signal-to-noise ratio (SNR) was evaluated on b=10 and 600 s/mm² images for both DP-FISP and DW-SE.

Single cell imaging: Single neurons were mechanically isolated from the abdominal ganglion of *Aplysia californica* and inserted into a glass capillary filled with artificial sea water (ASW). ADCs were measured with the 3D DP-FISP sequence.

Results and discussion: Table 1 collects T₁ and ADC measurements in phantoms. The DP-FISP sequence produces ADC estimates in excellent agreement with DW-SE. However, going to higher b-values with DP-FISP will introduce non-negligible T₁ relaxation effects. The use of the sequence in an extended b range is being explored, in order to render it adequate for biexponential fitting in biological samples. The 3D DP-FISP displays very good SNR per unit time performance, similar to DW-SE. Figure 1 shows representative DP-FISP diffusion measurements in an *Aplysia* neuron. The technique brings considerable improvement compared to previous methods, which only allowed single slice acquisitions within the time imparted by cell viability³.

References :

1. Lu L, Erokwu B, Lee G, Gulani V, Griswold MA, Dell KM, Flask CA. Magn Reson Med. 2012;68(3):868-73.
2. Jelescu IO, Nargeot R, Le Bihan D, Ciobanu L. NeuroImage 2013;76(0):264-271.
3. Hsu EW, Aiken NR and Blackband SJ. Am J Physiol. 1996;271(6 Pt 1): C1895-900.

Phantom	T ₁ (ms)	DW-SE ADC (10 ⁻³ mm ² /s)	DP-FISP ADC (10 ⁻³ mm ² /s)	Error (%)
ASW	2960 ± 21	1.92 ± 0.01	1.91 ± 0.01	- 0.5
NaCl, CuSO ₄	1315 ± 10	2.01 ± 0.01	1.99 ± 0.03	- 1.0
Dodecane	1455 ± 15	0.76 ± 0.01	0.76 ± 0.01	< 0.1

Table 1. T₁ at 17.2 T and ADC estimates in each phantom, measured with DW-SE and DP-FISP. The uncertainties represent the standard deviations of the fits.

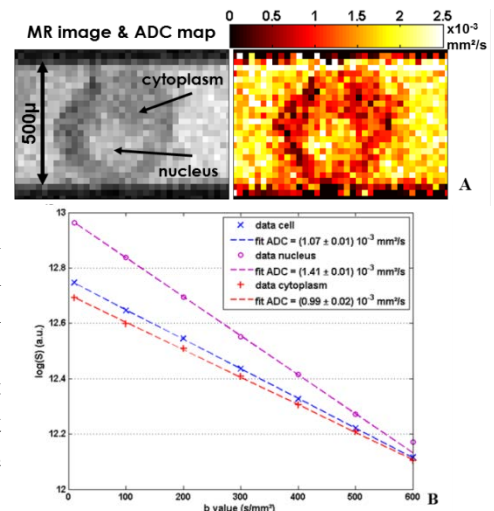


Figure 1. A: MR image (b=10 s/mm²) and ADC parametric map of *Aplysia* neuron. B: Fits from DP-FISP data in the entire cell and cellular compartments.

Molecular and cellular MRI: Challenges and potential solutions

Peter Jakob

Department of Experimental Physics 5 & MRB e.V., University of Würzburg, Germany

Molecular & Cellular Imaging (MCI) is “the in-vivo characterization and measurement of biological processes at the cellular and molecular level” and aims to image molecular abnormalities associated with diseases and to monitor cell assemblies such as macrophages or stem cells. However, so far, since MRI compared to other imaging techniques is traditionally a low sensitivity modality (orders of magnitude less sensitive than other techniques, such as PET, SPECT or optical fluorescence microscopy), MCI via MRI faces major technical/methodological challenges:

- (1) How to address the chief limiting factor “sensitivity”
- (2) How to unambiguously detect target structures & facilitate their robust quantification
- (3) How to make pre and post contrast images obsolete

In this context, it is important to remember, that MRI contrast agents (such as e.g. coated superparamagnetic iron oxide nanoparticles or paramagnetic agents) are not detected directly, but indirectly, since they only influence the MR signal. This makes a one-to-one identification of labeled structures in many cases difficult, if not impossible. Therefore, new approaches, which allow for a “background-free” identification, imaging and quantification of the labeled structures, are required.

In this presentation methodological innovations in combination with their contrast agents/tracer counterparts are introduced. These approaches (¹⁹F-MRI, Delta Relaxation Enhanced MRI, Magnetic Particle Imaging) enhance the ability to distinguish the molecular/cellular target signal from any background magnetic resonance signal, which greatly facilitates a “Hot-Spot” interpretation of the images in a way similar to PET or SPECT.

Reducing acquisition times of dynamic MRI measurements via contrast-enhanced compressed sensing

M. Benning^a, D. Allen^b, J. Beech^b, L. Gladden^a, D. Holland^a, V. Kersemans^b, M. Mantle^a, S. Smart^b, C. Schönlieb^c, T. Valkonen^c

^aDepartment of Chemical Engineering & Biotechnology, University of Cambridge, ^bDepartment of Oncology, University of Oxford, ^cDepartment of Applied Mathematics & Theoretical Physics, University of Cambridge

In both industrial and medical imaging many important applications require a fast acquisition of MRI measurements in order to study dynamic phenomena. Two prominent examples are phase-encoded velocity imaging [1], to image the velocity distribution in single- and multi-phase flows, and dynamic contrast-enhanced MRI (DCE-MRI), to examine the uptake kinetics of Gd-chelate contrast agents.

In [2], a significant speedup is achieved by applying compressed sensing (CS) techniques to acquire sub-sampled k -space data. However, the model considered in [3] reduces the contrast of the signal, involves

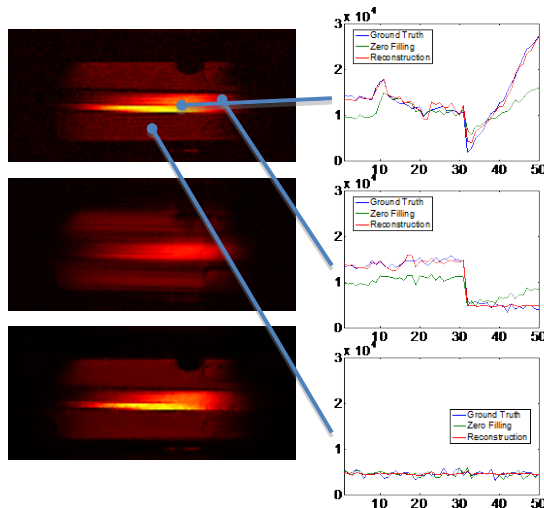


Fig. 4: DCE-MRI dataset of steady and flowing water in a pipe. The images on the left represent a coronal slice of the fully sampled data, the zero-filling reconstruction and a Bregman-iterated total variation reconstruction. The plots on the right correspond to temporal courses of the data for the points located in the left-hand-side of the figure.

proposed strategy are reasonably close or do even coincide. For the DCE data we perform a full 4D total variation-based reconstruction of 20% line-sub-sampled k -space data. The results in Figure 4 show that the proposed strategy is a powerful tool to recover noise-free DCE-MRI reconstructions with significant improvement in contrast while speeding up the acquisition time.

References:

1. M. Johns, A. Sederman, A. Bramley, and L. Gladden, Local transitions in flow phenomena through packed beds identified by MRI, *AIChE journal* 46.11 (2000) 2151-2161.
2. M. Lustig, D. Donoho and J. Pauly, Sparse MRI: The application of compressed sensing for rapid MR imaging, *Magn. Reson. Med.* 58 (2007) 1182-1195.
3. S. Osher, M. Burger, D. Goldfarb, J. Xu and W. Yin, An iterative regularization method for total variation- based image restoration, *SIAM Multiscale Model. Simul.* 4 (2005) 460-489.

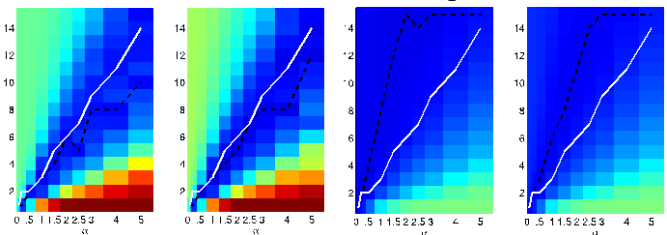


Fig. 1: PSNR values between the ground truth and Bregman iterations (y-axis) for different initial choices of the regularisation parameter (x-axis). The white line corresponds to choice of the method, while the black dashed line corresponds to the optimal PSNR value. The two plots on the left show the PSNR values between the magnitude images, for 33% and 15% sub-sampling, respectively. The two on the right show the PSNR values for the same sub-sampling, but of the phase images.

the a-priori selection of a regularisation parameter and produces stair-casing artefacts.

We present a strategy that is based on the so-called Bregman iteration [3], which overcomes these limitations.

We apply this strategy to a synthetic phase-encoded velocity dataset as well as real DCE-MRI data. In Figure 1 the PSNR values between the ground truth synthetic data and 15 Bregman iterates (each for different initial choices of the regularisation parameter) are visualised. The iterate that yields the best PSNR value and the one selected by the

A pore-scale analysis of common capillary pressure measurements using 1D NMR and tomographic images

C.H. Arns^a, I. Shikhov^a,

^aSchool of Petroleum Engineering, The University of New South Wales, Sydney, Australia

The measurement of capillary pressure curves is an essential tool to characterize unsaturated flows in porous media. Three commonly used laboratory techniques, namely, the porous plate (PP), centrifuge (CM), and mercury intrusion drainage methods, usually provide non-identical results which are difficult to reconcile. The two methods allowing further core analysis, PP and CM, lead to very different equilibrium fluid saturation profiles (Figure 1) and there has been much discussion about the interpretation of CM data in the literature [1,2]. Recent advances in the interpretation of centrifuge capillary drainage measurements include the measurement of saturation profiles using MRI [3]. This allows more confident interpretation since the definition of an average saturation for this method is problematic.

In this paper we compare measured NMR 1D saturation and T_2 profiles with numerically simulated ones for two different samples. Depicted in Figure 2 below are the saturation profiles for a reconstructed Fontainebleau sandstone [4], which is a very homogeneous and clean sandstone of 13% porosity. We further consider a heterogeneous reservoir rock as well as a heterogeneous model structure generated in a dual-scale modeling process. The selection of samples allows us to access the impact of structural heterogeneity on the interpretation of NMR relaxation responses as function of position in the core. In particular, we compare the NMR 1D resolved T_2 spectra measured at 2MHz with responses simulated on the basis of the 3D tomographic images and comment on the derivation of relative permeability curves using relaxometry.

References:

1. G.L. Hassler and E. Brunner, Trans. AIME, (1945) 160, 114-123.
2. P. Forbes, Society of Core Analysts (SCA), SCA Survey, SCA-9714 (1997).
3. D.P. Green, J.R. Dick, M. McAloon, P.F. de J. Cano-Barrita, J. Burger, B. Balcom, Int. Symp. SCA, [SCA2008-01], 2008.
4. F. Latief, B. Biswal, U. Fauzi and R. Hilfer, Phys. A, (2010) 389, 1607-1618.

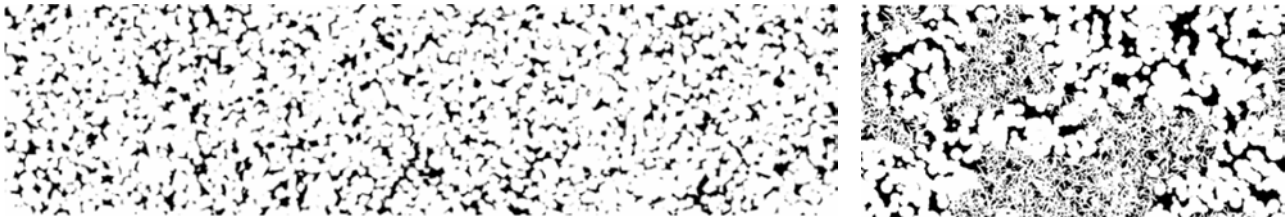


Fig. 1: *Left*: Reconstructed Fontainebleau sandstone. *Right*: Heterogeneous dual-scale structure generated by a combination of Gaussian Random Fields and Poisson processes. Both samples are 15mm long.

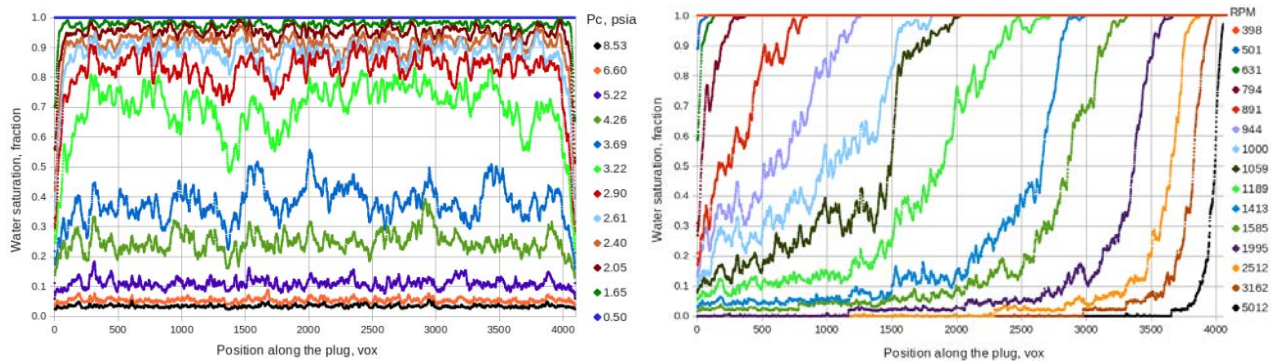


Fig. 1: Air-brine saturation profiles for Fontainebleau sandstone. *Left*: Porous plate method. *Right*: Centrifuge method. The z-position is given in voxel units (4096 voxels at a resolution of 3.66 μ m for a sample length of 15mm).

Optimization of dPFG for the quantification of pore size distribution

Y. Katz and U. Nevo

Department of Biomedical Engineering, the Iby and Aladar Fleischman Faculty of Engineering,
Tel-Aviv University, Tel-Aviv, Israel

Introduction Non-invasive characterization of porous media using NMR measurements has been the subject of extensive research in recent years. The double pulse field gradient (dPFG) NMR pulse sequence and multiple correlation function (MCF) method¹ were shown both experimentally² and theoretically to allow the estimation of polydisperse pore-size distributions (PSDs). The acquired signal is a superposition of NMR signals from different pores, weighted by their PSD. The estimation of the PSD is done by transforming the integral equation into a set of linear equations and solving the ill-posed problem². The selection of the experimental parameters in such ill-posed problem is a crucial step for an accurate estimation, and this is the goal of this work.

The Optimization Framework we optimize the experimental protocol and the choice of discrete PSD sampling points with no prior knowledge of the PSD. In the first step, proper dPFG experimental set is chosen for fixed sampling points. To this end, we formulated an optimality criterion based on maximizing the design matrix rank and minimizing the condition number while taking into account the signal strength (to maintain an adequate SNR). This set was found using a random-restart hill-climbing algorithm which improves the objective function. The second step involves picking the adequate discrete PSD sampling points for a fixed set of experiments. To do so, we use the k-means algorithm to cluster the NMR signals from many pores into K groups that define the new sampling points. This framework can be repeated several times until convergence.

The Estimation Process The parameters from the optimization were used to estimate a two-dimensional PSD of cylindrical layer. To the best of our knowledge, this is the first time an NMR experiment has been used to estimate such complex shapes. A number of PSDs were estimated from NMR data simulated numerically with the addition of noise.

Implementation Theoretical NMR signals from cylindrical shells signals were calculated using the MCF method. The inner radius was chosen to be between 23 – 38 [μm] in step of .5 [μm] and the pore width between 11 – 18 [μm] in step of 1 [μm], resulting in 248 uniformly distributed sampling points. The angular-q-space dPFG parameters were: $G_d = 40:460[\text{mT}/\text{m}]$, $\Delta = 5:350[\text{msec}]$, $\Delta\varphi = 0^\circ:180^\circ$, $\delta = 3[\text{msec}]$, $\tau_m = 0$ and $N = 300$ experiments.

Results The optimization framework produced insights regarding the optimal experimental set and sampling points: **(a)** Experimental set with multiple experimental parameters changed (G_d , Δ , $\Delta\varphi$) is profoundly superior (Table 1). **(b)** The optimal set tends to contain experiments with higher gradient strength. **(c)** Non-uniformly spaced sampling points minimize the sum of squared error. **(d)** The optimization shows a clear trend of improving the average correlation of the design matrix². The simulated PSDs were reliably estimated by using the above framework.

Summary and Conclusions The above optimization framework has many advantages, such as: mathematical simplicity; easy implementation; compliance to other experiments and adaptiveness to improvements. The estimation process showed that the condition number and the NMR signal intensity play a crucial role in the quality of the estimation. The above estimation and optimization framework is applicable for polydisperse pores of any geometry that fits the MCF approach.

References

1. D. S. Grebenkov, J. Chem. Phys. 128 (2008) 134702.
2. D. Benjamini and U. Nevo, Journal of Magnetic Resonance 230 (2013) 198.

Experiment type	Matrix rank	Condition #
300 gradients	31	Infinity
300 angles	45	infinity
Asymptotic signal – 100 gradients and 100 angles	128	infinity
80 big deltas and 80 angles	172	Infinity
80 big deltas and 80 gradients – single PFG	162	Infinity
80 big deltas and 80 gradients – dPFG	199	Infinity
80 gradients and 80 angles	217	Infinity
70 big deltas, 60 gradients and 13 angles	248 (full rank)	3.1e12
20 Big deltas1, 20 big deltas2, 60 gradient and 13 angles	248 (full rank)	1.2e12

Table 1: Performance of the optimization framework for different experimental sets - condition number and rank

Eddy currents and turbulent eddies

B. Newling^a, A. Adair^a, O. Adegbite^c

F. Goora^b, B. J. Balcom^a

Departments of ^aPhysics, ^bElectrical Engineering and ^cInterdisciplinary Studies, UNB MRI Centre, University of New Brunswick, Fredericton, NB E3B 5A, Canada

In materials MRI the use of purely phase encoded techniques (SPI [1], SPRITE [2] and the like [3]) has certain advantages: the constant encoding time (t_p) between excitation and detection of every k-space point eliminates chemical shift and magnetic susceptibility artefacts and the encoding time can be kept relatively short, on the order of hundreds of microseconds. The short t_p is vital when the substance under study has very short T_2 , but can also be advantageous in the study of processes with short timescales, such as fast, turbulent flow [4].

We typically sensitise a SPRITE sequence to motion using bipolar gradients applied during t_p , an approach which places considerable demands on the gradient switching. Eddy currents prevent ideal switching, which we can correct by acquiring a template scan with the flow stopped, but this is not always practical, not least because of the doubling of experimental time. We can empirically *trim* the bipolar gradient by inspection, in a motion-encoding version of pre-emphasis, but this is a rather subjective and time-consuming. In this paper we will present a philosophically different approach to optimising the gradient switch, which has grown out of work on the development of a metal vessel for pressurised MRI [5]. In *pre-equalisation*, we use a magnetic resonance method [6] to measure the impulse response of the entire excitation/detection system and use that impulse response to design *a priori* the appropriate waveform to be sent to the gradient amplifiers.

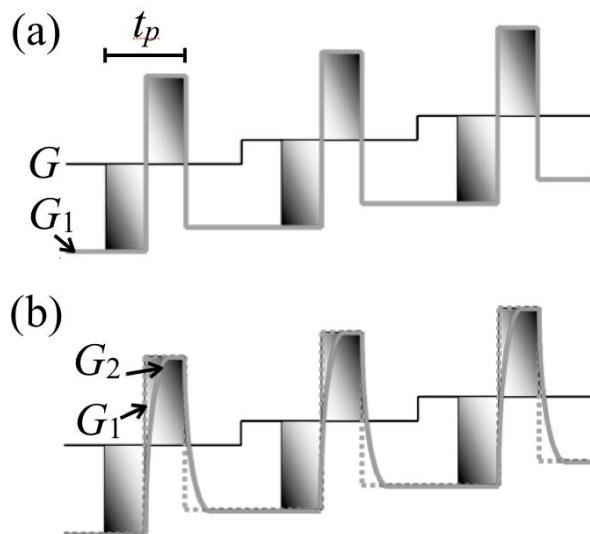


Fig. 1 (and only). (a) G shows a part of the conceptual gradient waveform required for motion sensitised SPRITE: a bipolar gradient is superimposed upon a SPRITE ramp. G_1 is the actual desired gradient waveform, with reduced switching but the same effect in the encoding interval t_p . (b) G_2 is a schematic of the actual magnetic field gradient experienced by the sample, which must be matched to G_1 (dotted), by one of the methods discussed, for accurate quantification of turbulent flow. Adapted from [7].

The motion-sensitized SPRITE sequence is shown to inform the CFD modeling of turbulence and to shed light on the anisotropy of the eddies in turbulent flow.

References:

1. S. Emid, J. Creighton, *Physica* 128B (1985) 81.
2. B. Balcom, R. MacGregor, S. Beyea, D. Green, R. Armstrong, T. Bremner, *J. Magn. Res. A* 123 (1996) 131.
3. S. Gravina, D. Cory, *J. Magn. Reson. B* 104 (1994) 53; A. Webb, *Concepts in Magn. Reson.* 22A (2004) 25.
4. B. Newling, C. Poirier, Yang Zhi, J. Rioux, A. Coristine, D. Roach, B. Balcom, *Phys. Rev. Lett.* 93 (2004) 154503.
5. F. Goora, Hui Han, M. Ouellette, B. Colpitts, B. Balcom, *IEEE Trans. Magnetics* 49 (2013) 2920.
6. Han Hui, A. Ouriadov, E. Fordham, B. Balcom, *Concepts in Magnetic Resonance* 36A (2010) 349.
7. A. Adair, MSc. thesis, University of New Brunswick (2008).

Structural information from MRI signal moment analysis: Application to ROM biofouling

M.L. Johns^a, E.O. Fridjonsson^a, S.J. Vogt^a and S.A. Creber^b

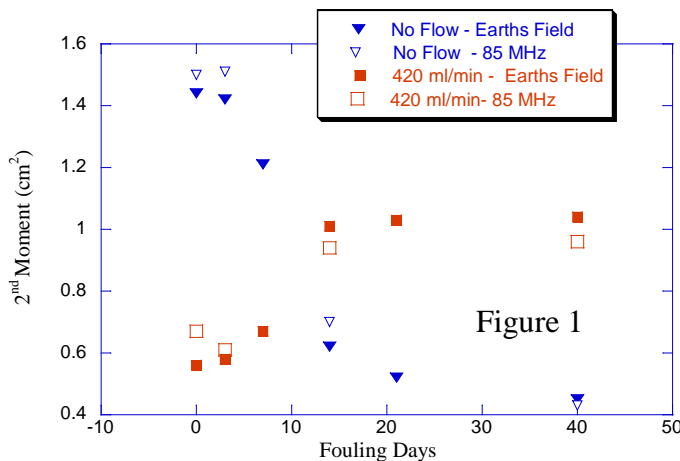
^a School of Mechanical and Chemical Engineering, The University of Western Australia, 35 Stirling Highway, Crawley WA 6009, Australia

^b Dept of Chemistry and Chemical Engineering, RMCC, PO Box 17000, Station Forces Kingston, Ontario, K7K 7B4, Canada

Previously (at the MRRC, University of Cambridge) we have demonstrated that high resolution, high field MRI is able to provide exquisite insight into the development of bio-fouling in reverse osmosis membrane modules (ROMs), as used for desalination¹. Here we will demonstrate that using an earth's magnetic field NMR device (Magritek Terranova), we are able to engineer the acquisition such that it is sensitive to the onset of bio-fouling in these ROM devices. Specifically we judiciously acquire signal around the centre of k -space such that the first three moments of the NMR signal distribution (in the specified direction: k) are extracted from the measured signal intensity ($S(k)$) and phase ($\phi(k)$) using Equation 1:

$$\phi(k) \approx \langle x \rangle k - \frac{1}{6} \gamma^3 k^3, \quad \ln \left| \frac{S(k)}{S_{\max}} \right| \approx -\frac{1}{2} \sigma^2 k^2 \quad (1)$$

This replicates an analogous method used to determine the moments of displacement propagators via analysis of q -space data [2, 3]. In the case of the fouling ROMs, signal is acquired (i) with the fluid stationary, in which case T_2 contrast results in a reduction in the 2nd moment as signal is lost from the biofilm regions, or (ii) under operational flowing conditions, in which case the 2nd moment increases as additional biofilm regions (and consequential stagnant zones) are established. This data is validated against measurements acquired at 2T; a sample data set is presented below in Figure 1.



This collective three moment approach can be used to isolate the location and extent of the fouling. Routine monitoring of the fouling extent at higher flowrates is also possible, simply via measurements of the total signal. This requires the use of remote signal excitation.

The moment analysis is also discussed in terms of its ability to measure interfacial tension via axi-symmetric drop shape analysis (ASDA) techniques.

References:

1. Graf von der Schulenburg, D.A., Holland, D.J., Paterson-Beedle, M., Macaskie, L.E., Gladden, L.F. and Johns, M.L., Spatially Resolved Quantification of Metal Ion Concentration in a Biofilm-mediated Ion Exchanger; *Biotech. and Bioeng.*, **99**(4), 821-829, (2008)
2. Scheven, U.M., Verganelakis, D., Harris R.J., Johns, M.L. and Gladden, L.F. (2005), Quantitative NMR measurements of pre-asymptotic dispersion in flow through porous media, *Physics of Fluids*, **17**, 117107.
3. Scheven, U.M. and Sen, P.N. (2002), Spatial and temporal coarse graining for dispersion in randomly packed spheres, *PRL*, **89**, 254501.

A new sequence for measuring NMR relaxation in flowing fluid

Deng Feng, Xiao Lizhi, Liao Guangzhi, Wu Yan, Xu Wei, He Chuanhang

State Key Laboratory of Petroleum Resources and Prospecting, China University of Petroleum, Beijing 102249, China

We present a pulse sequence for measuring NMR relaxation of flowing fluid, called DEFIR (Driven-Equilibrium Fast-Inversion-Recovery). The 2D functional relationship between the ratio of transverse relaxation time to longitudinal relaxation time of fluid (T_1/T_2) and T_1 distribution are obtained by means of DEFIR with only two one-dimensional measurements. Thus, the purpose of rapid measurement of relaxation characteristics for flowing fluid is achieved. A set of down-hole NMR fluid analysis system is designed and developed for the fluid measurement experiment and application research. The accuracy and practicability of DEFIR are demonstrated. This analysis system gives an important theoretical guide and technical support for instrument design and measurement method of flowing fluid.

An application method of viscous fluids component identification is proposed. The rotational correction time (τ_A) distribution can be used to infer the composition of viscous fluids, approximately proportional to the product of macroscopic viscosity and molecular volume. τ_A has certain functions with T_1 and T_2^4 , which in turn can obtained the correlation of T_1/T_2 and τ_A :

$$\frac{T_1}{T_2} = \frac{1}{2} \frac{5(1 + \omega^2 \tau_A^2)^{-1} + 2(1 + 4\omega^2 \tau_A^2)^{-1} + 3}{(1 + \omega^2 \tau_A^2)^{-1} + 4(1 + 4\omega^2 \tau_A^2)^{-1}},$$

here $\omega = 2\pi f$ where f is the ^1H frequency.

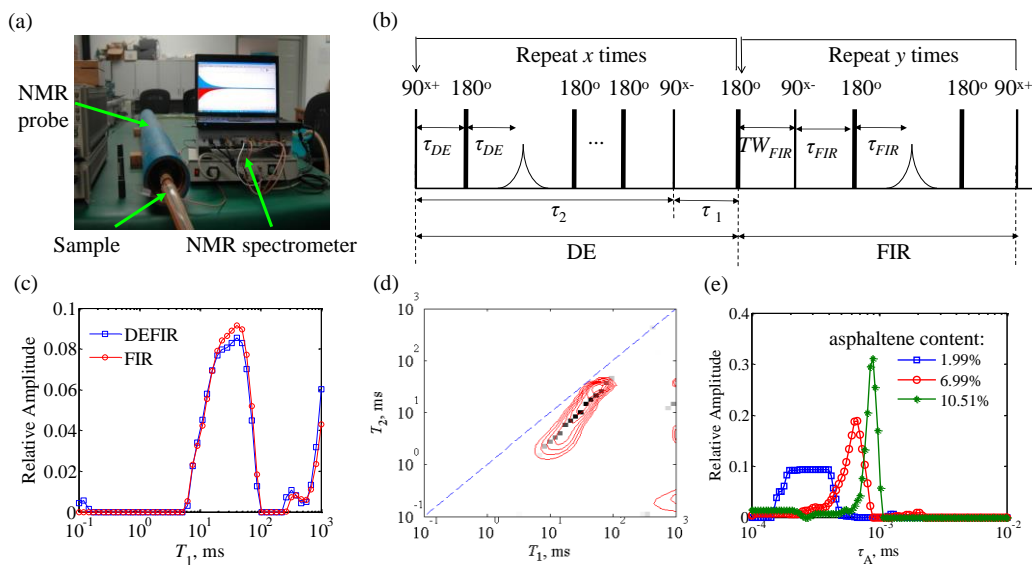


Fig.1: 2D NMR Relaxation Measurement in Flowing Fluid: (a) NMR fluid analysis system; (b) DEFIR pulse sequence; (c) T_1 maps of multi-component sample (crude oil); the red lines are static measurement result by T_1 -encoding pulse sequence, the gray solid line is DEFIR measurement result; (d) T_1 - T_2 map of multi-component sample;(e) τ_A distribution of the three crude oil samples with different asphaltene concentration.

References:

1. J. Mitchell, M. D. Hürlimann and E. J. Fordham. *J. Magn. Reson.*2009, 154:261-268
2. A. Caprihan, E. Fukushima. 1990,198:195-235
3. M. G. Prammer, J. C. Bouton, P. Masak, et al. US 20050017715A1. 2005-01-27
4. D. M. Wilson, and G. A. LaTorraca. Symposium of Society of Core Analysts. 1999, Paper 9923.

Displacement-relaxation correlations of biofilm growth in porous media

Sarah J. Vogt^{1,2*}, Alexis B. Sanderlin^{1,2}, Joseph D. Seymour^{1,2}, and Sarah L. Codd^{2,3}

¹Department of Chemical and Biological Engineering, Montana State University, Bozeman, MT, USA

²Center for Biofilm Engineering, Montana State University, Bozeman, MT, USA

³Department of Mechanical and Industrial Engineering, Montana State University, Bozeman, MT, USA

*Current address: School of Mechanical and Chemical Engineering, University of Western Australia, Perth, WA, Australia

In diverse growth environments, microorganisms including bacteria and algae attach to surfaces and grow within an excreted polymeric substance known as a biofilm. The biofilm is difficult to remove, providing potential positive applications such as bio-barriers to contain nuclear waste spills or as an additional way of plugging porous rock around carbon sequestration sites. Biofilm growth in porous media is difficult to study non-invasively due to the opaqueness and heterogeneity of the systems, and therefore realistic model simulations of biofilm growth kinetics and fluid dynamics are important tools for a range of industrial applications. The permeability of the biofilm matrix itself is currently an open question and an important parameter to quantify due to convective nutrient transport, if present, greatly enhancing biofilm growth kinetics in mass transfer limited systems; or if convective flow through the biofilm is not present, altering flow patterns due to increased fluid dynamic mixing and hydrodynamic dispersion caused by biofilm-clogged pores within the porous medium matrix [1].

Magnetic resonance displacement-relaxation correlation experiments [2, 3] were performed on fluid flow during *Bacillus mojavensis* biofilm growth in a model porous media of polystyrene beads [4]. A pulsed gradient stimulated echo (PGSTE) sequence was used to encode for displacement, followed by data acquisition of a CPMG pulse train to measure T_2 relaxation. The spin-spin T_2 magnetic relaxation distinguishes between the biofilm phase and bulk fluid phase due to water - biopolymer interactions in the biofilm. The propagator of displacement $P(Z,\Delta)$ encoded by the PGSTE sequence is separated into different T_2 components, thereby separating the flow dynamics of the biofilm phase from the bulk fluid phase and enabling a detailed analysis of both phases simultaneously within the same experiment (Figure 1). Within the displacement resolution of these experiments ($\pm 15.6 \mu\text{m}$, or $\pm 62.4 \mu\text{m/s}$ for Δ of 250 ms), no convective flow was measured through the biomass.

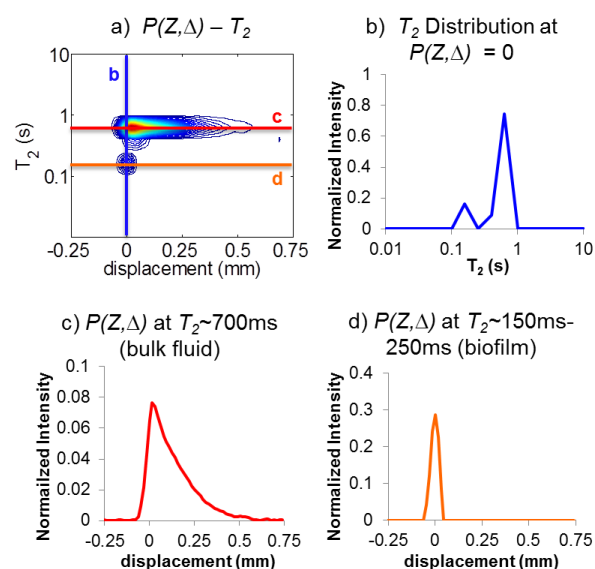


Figure 1. Propagator ($P(Z,\Delta)$)- T_2 data for $\Delta = 250$ ms and biofilm growth time of 30-33 hours.

References

1. Pintelon, T.R.R., C. Picioreanu, M.C.M. van Loosdrecht, and M.L. Johns, *Biotechnology and Bioengineering*, 2012. **109**(4): p. 1031-1042.
2. Windt, C.W., F.J. Vergeldt, and H. Van As, *Journal of Magnetic Resonance*, 2007. **185**(2): p. 230-239.
3. Burcaw, L.M., M.W. Hunter, and P.T. Callaghan, *Journal of Magnetic Resonance*, 2010. **205**(2): p. 209-215.
4. Vogt, S.J., A.B. Sanderlin, J.D. Seymour, and S.L. Codd, *Biotechnology and Bioengineering*, 2013. **110**(5): p. 1366-1375.

The influence of media pH and ionic strength on hydrogel formation and drug release from xanthan tablets

U. Mikac^a, A. Sepe^a, J. Kristl^b, and S. Baumgartner^b

^a Jožef Stefan Institute, Ljubljana, Slovenia, ^b Faculty of Pharmacy, University of Ljubljana, Ljubljana, Slovenia

Matrix tablets made of hydrophilic polymers like xanthan are widely used for controlled delivery of drugs. As medium penetrates the matrix, the outer surface of these tablets hydrate and swells, forming a hydrogel coat around the dry central core. This complex hydrogel coat around the dry central core regulates the penetration of body fluids into the tablet on one side and the drug release kinetics on the other¹. Therefore, the penetration of medium into the polymer tablet, the polymer swelling behaviour and the drug dissolution and diffusion out of the tablet are the key factors to understand the drug release mechanism from polymer matrices. Xanthan is an anionic poly-electrolyte that forms different complex secondary structures depending on environmental conditions. In solution the rigid helix-coil structure transforms into flexible coils whose stability and physical properties are strongly influenced by pH and the ionic environment². Since these parameters progressively change in the gastrointestinal tract, it is important to understand the swelling behaviour of as well as drug release from xanthan tablets under different conditions of pH and ionic strength.

In the study the hydrogel thicknesses of xanthan tablets containing different amount of Pentoxifylline drug were measured by combination of different MRI techniques³ in media with different pH and ionic strengths. The results were correlated with drug release studies. It was shown that the impact of the drug on the hydrogel thickness depends on the medium conditions at high enough drug amounts. The drug does not change the hydrogel thickness in water medium, whereas at lower pH the presence of the drug results in thinner hydrogel. The increased ionic strength also leads to formation of the thinner hydrogel layer, while the effect of increased ionic strength at low pH is very small. The drug release studies, on the other hand, show slower drug release for tablets with lower drug contents in media with high pH ($\text{pH} \geq 3$) and low ionic strength, i.e. in media where the hydrogel thickness was independent on the amount of drug in the tablet, while the release in media with low pH and/or high ionic strength was not affected by increased amount of the drug in the xanthan matrix. Different impacts of Pentoxifylline drug on the hydrogel thickness and drug release can be attributed to different hydrogel structures formed by different media and different drug-polymer interactions that can alter medium penetration and polymer chain mobility causing different swelling behaviour.

References:

1. M. Fukuda, N.A. Peppas, and J.W. McGinity, *Int. J. Pharm.* 310 (2006) 90.
2. M.M. Talukdar, A. Michoel, P. Rombaut, and R. Kinget, *Int. J. Pharm.* 129 (1996) 233.
3. U. Mikac, A. Sepe, J. Kristl, and S. Baumgartner, *J. Control Release*, 145 (2010) 247.

Magic-angle spinning of the q -vector in diffusion MRI

D. Topgaard

Division of Physical Chemistry, Center for Chemistry and Chemical Engineering, Lund University, P.O.Box 124, SE-22100 Lund, Sweden

Diffusion NMR and MRI measurements based on the classical PGSE experiment are commonly applied for determining pore sizes or the orientation of anisotropic pores. Many biologically and geologically relevant materials have pores covering a range of both sizes and orientations. For such materials, it is difficult to unambiguously extract information about size and orientation distributions, since the two effects are entangled in the standard PGSE experiment.

We have recently proposed the q -MAS PGSE sequence¹ (see Fig 1) as an efficient way of removing the influence of pore orientation on the experimental data. The design of the pulse sequence is inspired by magic-angle spinning (MAS) in solid-state NMR, utilizing the formal equivalence of the chemical shift and diffusion tensors, and the magnetic field and q -vectors. Provided that the signal from each distinct microscopic domain can be approximated as being Gaussian and described with a diffusion tensor, the q -MAS data can be interpreted as the Laplace transformation of the distribution of trace diffusivities for the ensemble of microscopic domains. This distribution is equivalent to the spectrum of isotropic chemical shifts obtained by MAS in solid-state NMR. Comparison of q -MAS and conventional PGSE data is a simple way of proving the presence of microscopic diffusion anisotropy.

Here, we define new parameters quantifying the diffusion anisotropy of the microscopic domains and their orientation dispersion, as well as introduce an analysis method with which they can be estimated from a combined set of q -MAS and conventional PGSE data.² The microscopic fractional anisotropy (μ FA) is defined in analogy with Basser's fractional anisotropy (FA).³ The value of μ FA is independent of the orientation distribution function, and is equal to FA if all domains have the same orientation. Comparison between μ FA and FA gives information about orientation dispersion. Implementation of q -MAS on clinical MR scanners is made possible through numeric optimization of the gradient modulation functions, yielding smooth waveforms that maximize the diffusion weighting for a given maximum gradient strength and sequence duration.⁴ We suggest that μ FA could replace FA as a measure of "white matter integrity" in studies of pathological conditions and normal brain development.

References:

1. S. Eriksson, S. Lasic, D. Topgaard, Isotropic diffusion weighting by magic-angle spinning of the q -vector in PGSE NMR, *J. Magn. Reson.* 226 (2013) 13-18.
2. S. Lasic, F. Szczepankiewicz, S. Eriksson, M. Nilsson, D. Topgaard, Quantification of microscopic fractional anisotropy (μ FA) by diffusion MRI and magic-angle spinning of the q -vector, Manuscript.
3. P.J. Basser, C. Pierpaoli, Microstructural and physiological features of tissues elucidated by quantitative-diffusion-tensor MRI, *J. Magn. Reson. B* 111 (1996) 209-219.
4. D. Topgaard, Isotropic diffusion weighting in PGSE NMR: Numerical optimization of the q -MAS PGSE sequence, *Microporous Mesoporous Mater.* 178 (2013) 60-63.

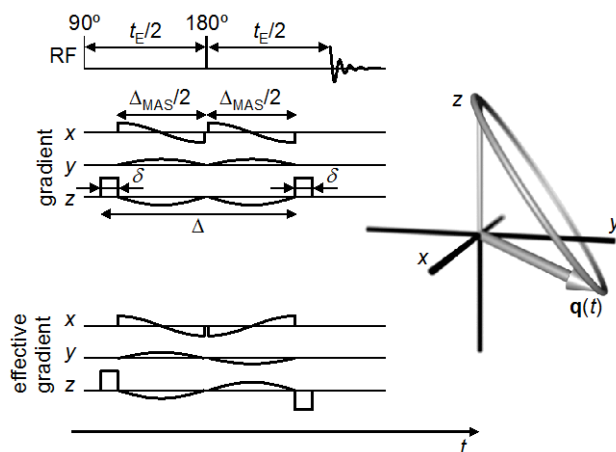


Fig. 1: Schematic of the q -MAS PGSE pulse sequence. Rectangular z -gradient pulses of duration δ and amplitude G rapidly increase and decrease the magnitude of the q -vector. The low-amplitude harmonically modulated gradients slowly rotate the q -vector around a lab-fixed axis. Isotropic diffusion weighting is achieved when the angle between the q -vector and the rotation axis equals the magic-angle 54.74° . The diffusion weighting b is identical to standard single-axis PGSE: $b = (\gamma G \delta)^2 (\Delta - \delta/3)$, where γ is the magnetogyric ratio.

Sizing of reverse micelles in microemulsions using NMR measurements of diffusion

S.J. Law, M.M. Britton,

Department of Chemistry, University of Birmingham, Edgbaston, Birmingham, UK

NMR diffusion measurements have been widely used to size and characterize micelles and emulsions,^{1,2} but there have been fewer studies sizing reverse micelles (RMs) in microemulsions. Traditionally, dynamic light scattering (DLS) has been used to measure the size distributions of RMs, however, this technique has a number of limitations. Here we propose an alternative method for studying and characterizing the size distribution of RMs by combining NMR measurements of diffusion with the inverse Laplace transform (ILT).³

Reverse micelles (w/o) are nano-sized water droplets surrounded by surfactant molecules in an organic continuous phase. They are of great interest, as they offer adaptable environments for chemical reactions, nanoparticle synthesis,⁴ as well as providing a model for biological systems.⁵ Knowledge of the RM size distribution is crucial in these applications.

For a range of AOT/octane/H₂O microemulsions, the self-diffusion coefficients (D) of RMs were determined using pulsed gradient stimulated echo (PGSTE) experiments and from these measurements, diffusion coefficient distributions, $G(D)$, were produced using the ILT. Size distributions were then produced using the Stokes-Einstein relation (eq 1)

$$D = k_B T / (6\pi \eta R_h). \quad (\text{eq 1})$$

This method was able to reproduce DLS measurements for RM sizes for a range of AOT/n-octane/H₂O microemulsions. The effect of the water to surfactant ratio (ω), volume droplet fraction (ϕ_d), temperature (Fig. 1) and the presence of additives were studied. By measuring the D of separate components in the microemulsion and applying the ILT, bimodal behavior and any compositional and hence structural changes may be probed.

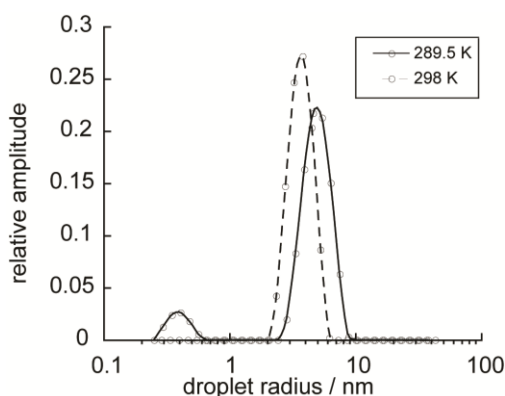


Fig. 1: Droplet size distributions for RM at $\omega = 15$ $\phi_d = 0.05$ in AOT/n-octane/H₂O microemulsion as a function of temperature.

1. O. Soderman and U. Olsson, *Micellar Solutions and Microemulsions*, eMagRes (2007)
2. O. Soderman, P. Stilbs and W.S Price, *NMR Studies of Surfactants*, *Con. Magn. Reson. A*, 23, (2004) 121
3. S.J.Law and M.M. Britton, *Langmuir*, 28 (2012) 11699
4. V. Uskokovic and M. Drogenik. *Surf. Rev. Lett.* 12 (2005) 239
5. N. Levinger, *Science*, 298 (2002) 1722

NMR responses in porous media with digital rock technique

Tianlin. An, Lizhi Xiao, Guangzhi Liao, Xin Li, Huabing. Liu, Zongfu, Zhang
 State Key Laboratory of Petroleum Resources and Prospecting,
 China University of Petroleum, Beijing, China

NMR response in porous media has been applied to characterize micro pore structure and morphology and to estimate the petrophysical parameters of rock samples. In this work, we present NMR relaxation characteristic in different pore structures, different fluid components, different rock properties and different wettability with digital core technology and simulation. By analyzing the influences of internal field gradients, surface relaxivity and restricted diffusion coefficient, the NMR responses in porous media were quantitatively characterized.

Diffusion and dephase effects were deduced based on Bloch-Torrey equation. Then the equations for apparent restricted diffusion coefficient, internal induced magnetic field and other critical quantities in porous media was inferred. Random packing and digital core models were employed to simulate the reservoir rocks. Monte Carlo Random Walk method was employed to represent the fluid molecules' diffusion and dephasing effects in porous media. Three-dimensional distribution of internal induced magnetic field and its gradients were quantitatively characterized with the equivalent magnetic dipole model. By using the particle rebounding trajectory tracking method, the restricted diffusion phenomenon was reproduced. Finally, the echo amplitudes were acquired and inverted into T_2 -D and T_2 -G spectrum.

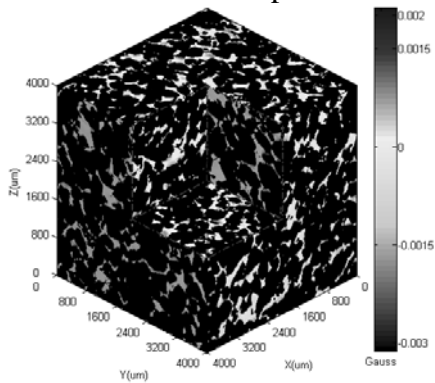


Fig. 1 (a) Distribution of induced magnetic field of Berea sandstone

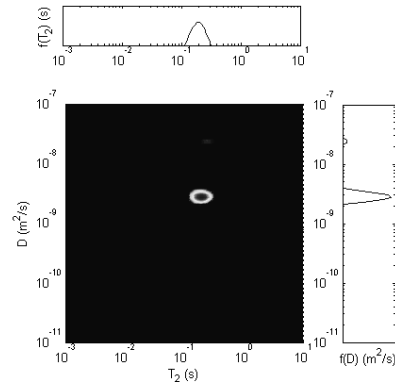


Fig. 1 (b) T_2 -D spectrum of Berea sandstone

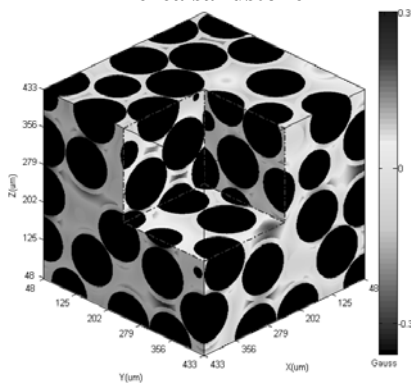


Fig. 2 (a) Distribution of induced magnetic field of oil-water saturated porous media

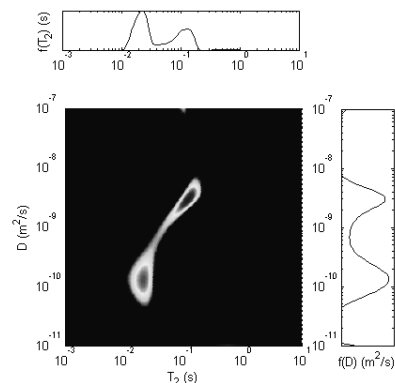


Fig. 2 (b) T_2 -D spectrum of porous media with $S_{water}=34\%$

References:

1. H. C. Torrey, Phys. Rev. 104 (1956) 563.
2. Y-Q. Song, Concepts in Magnetic Resonance. 18A (2003-2).
3. C. Arns, T. ALGhamdi and J. Y. Arns, New Journal of Physics. 13 015004 (2011).
4. T. An, L. Xiao, X. Li, et al. Science China, Physics, Mechanics & Astronomy. (in press)

TD-NMR, DOSY and MRI of chloroplasts?

Henk Van As, Erik Nonhebel, Shanthi Pagadala.

Laboratory of Biophysics and Wageningen NMR Centre, Wageningen University, Wageningen, The Netherlands

There is a strong perspective for an integrative approach combining different MRI parameters and additional (NMR or MRI) measurements to study the complex interplay between photosynthesis, evaporation, and sap transport (xylem and phloem, water and sugar) in plants. For such integrative studies we foresee combinations of (portable) NMR/MRI modules applied simultaneously at different positions to (organs) of a plant in combination with additional other (non-NMR/MRI) methods and MRI flowmetry, which has been applied very successful to study xylem and phloem sap transport¹.

Photosynthesis can be defined as the physico-chemical process by which photosynthetic organisms use light energy to drive the synthesis of organic compounds. The photosynthetic apparatus is housed in the thylakoid membranes in the chloroplasts, which are situated mainly in the leaf palisade and spongy cells. Photosynthetic activity rates are directly coupled to changes in chloroplast volumes and changes in thylakoid membrane composition and organization. Although chloroplast water amounts to around 20-25 % of the total leaf water, very limited NMR applications to study chloroplasts in relation to leaf water content have been published². Leaf water status has been studied using a portable, noninvasive unilateral NMR instrument in field conditions in different plants³. Although different T2 fractions (water pools?) were observed, no assignment to cell compartments/tissue types were reported.

Here we present results of ¹H high field DOSY- and low field TD-NMR of (isolated) chloroplasts and algae suspensions and chloroplasts in leaf disks and low field (portable) TD-NMR on intact leaves. We have tested if we can discriminate the chloroplast water pool and if changes in thylakoid membranes can be detected by changes in exchange kinetics over the thylakoid membranes (membrane permeability) and (restricted) diffusion behavior of the (bulk) chloroplast water and directly by observing the (thylakoid) membrane lipids.

In isolated chloroplast suspensions, water/proton exchange between water pools outside and inside the chloroplasts is fast, limiting the possibility to study restricted water diffusion and membrane permeability and to characterize the relaxation times of chloroplast water. Lipid diffusion, however, can be studied in isolated chloroplasts. Diffusion constants as low as $5 * 10^{-13}$ m²/s have been measured, in dependence of the diffusion labelling time. In algae, consisting for the largest amount of (intact) chloroplasts, chloroplast water could be easily discriminated from other water pools on the basis of (restricted) diffusion and relaxation behavior. In intact leaf disks water in chloroplasts can clearly be discriminated from other proton pools, among which lipid fractions can be observed. The latter is especially manifest in leaf disks of *Ficus benjamina*, which show ¹H spectra that are orientation dependent, and (lipid) resonances shifted from the water pool. For a better interpretation and assignment of the observed ¹H pools results of ¹H NMR diffusion measurements on low field (0.7 T) and higher field (7.2 T) as a function of leaf disk orientation were compared. In addition we have applied saturation transfer and D-T2 correlation experiments to measure the residence time of water and lipids in the different environments.

The results are discussed in view of possibilities to study chloroplast water and thylakoid membrane lipids by use of low field (portable) TD NMR in vivo by a NMR leaf sensor.

References:

1. H. Van As, J. van Duynhoven, J. Magn. Reson. 229 (2013) 25.
2. H. Van As, N. Homan, F.J. Vergeldt, C.W. Windt, Encycl. Magn. Reson. 1299 (2012).
3. D. Capitani, F. Brilli, L. Mannina, N. Proietti, F. Loreto, Plant Physiol. 149 (2009) 1638.

Poster Presentations

MR microscopy of organotypic hippocampal slice cultures: First steps to an *in vitro* approach for experimental epilepsy research

K. Göbel^a, R. Kamberger^b, J. Gerlach^c, O.G. Gruschke^b, J. Leupold^a, P. LeVan^a, D. von Elverfeldt^a, J.G. Korvink^b, C. Haas^c, J. Hennig^a

^aMedical Physics, Department of Radiology, University Medical Center Freiburg, Germany,

^bIMTEK, Laboratory of Simulation, University of Freiburg, Germany, ^cExperimental Epilepsy Research, Department of Neurosurgery, University Medical Center Freiburg, Germany

Organotypic hippocampal slice cultures (OHSC) are a well-established neuronal culture system that combines the advantages of cell culturing with a neuronal network tightly reflecting the *in vivo* state. They are frequently used to study morphological, molecular and electrophysiological changes associated with epilepsy¹. Our aim is to investigate these changes during epileptogenesis in OHSC, particularly using high spatial resolution MR microscopy which allows continuous monitoring near/at the cellular level^{2,3,4}. Novel screening methods with high spatial resolution will be imperative to detect new reliable epilepsy biomarkers and identify potential stimulation targets

First imaging trials were performed on a 9.4 T Bruker BioSpec small animal scanner (bore size = 20 cm, maximum gradient amplitude = 676 mT/m) using a custom-made phased-array microcoil⁵ (fig. 1) in receive mode, with a linearly polarized 1H coil in transmit mode.

A 7 T Bruker BioSpec small animal scanner using a mousehead two-element quadrature cryo coil was used as well. This coil is He-cooled to 26 K in order to improve the signal-to-noise ratio by a factor of about three.

Multi-slice gradient echo sequences were applied with: TR = 300 ms, TE = 7.9 ms, flip angle = 50°, resolution 20×20×200 μm³ obtained in 46min 43sec (fig. 2 A); and TR = 300 ms, TE = 7.7 ms, flip angle = 50°, resolution 16×18×150 μm³ obtained in 2h 8min (B). The neuronal structure was subsequently compared to optical microscopy of histologically stained cryosections (C and D); the laminar structure of hippocampal subfields is clearly visible.

Future relaxation measurements of T₁ and T₂ of fixed hippocampal samples will soon allow first trials in diffusion measurements. After setting up reliable protocols, we would like to examine *in vitro* slice cultures through MR microscopy.

References:

1. S. Tinnes et al., TIMP-1 inhibits the proteolytic processing of Reelin in experimental epilepsy, *FASEB J.* 27 (2013) 2545.
2. L. Harsan et al., In vivo Diffusion Tensor Magnetic Resonance Imaging and Fiber Tracking of the mouse brain, *NMR in Biomedicine* 23 (2010) 884.
3. N. Baxan et al., Microcoil-based MR phase imaging and manganese enhanced microscopy of glial tumor neurospheres with direct optical correlation, *Magn. Reson. Med.* 68 (2012) 86.
4. J. J. Flint et al., Magnetic resonance microscopy of human and porcine neurons and cellular processes, *NeuroImage* 60 (2012) 1404.
5. O.G. Gruschke et al., Lab on a chip phased-array MR multi-platform analysis system, *Lab Chip* 12 (2012) 495.

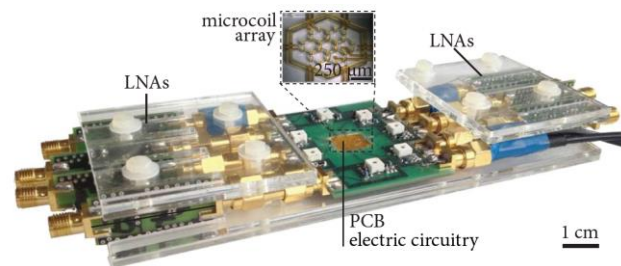


Fig. 1: Phased-array microcoil device illustrating the coil geometry with its seven overlapping coil elements

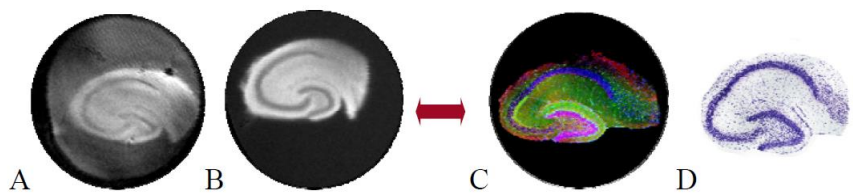


Fig. 2: Visualization of neuronal structures in a fixed OHSC using MR microscopy in comparison to optical microscopy of histologically stained cryosections. **A** MR Image (9.4 Tesla + custom-made phased-array microcoil) of a fixed OHSC; **B** MR Image (7 Tesla + Mousehead two-element quadrature cryo coil) of a fixed OHSC; **C** Immunohistochemical staining and **D** Nissl-stained cryosection of 20 μm thick OHSC

P02

Live Mice imaging with a 14.1T narrow-bore NMR magnet heading for *fMRI* by using an independent digital console and gradient probe

T. Haishi^a, *Y. Abe*^b, *K. Togashi*^a, *K. Kose*^c, *T. Hisatsune*^b

^a MRTechnology, Inc., ^b Departments of Integrated Biosciences, The University of Tokyo, Japan
^c Institute of Applied Physics, University of Tsukuba, Japan

Introduction

A mouse disease model in biomedical sciences is the global standard. In order to make use of MR imaging for the mice models of such as skin-tumor, liver, kidney, or the other big tissues, a compact permanent magnet MRI system⁽¹⁾ is a promising modality which shall be joined into their measurement series. However, are the very limited numbers of ultra-high field MRI (> 7T, > wide bore 89 mm ϕ) for mice able to support surely expanding demand for transgenic mouse models of e.g. brain sciences? In order to meet this demand, we have further developed a simple MRMICS⁽²⁾ method to utilize, standard narrow-bore NMR vertical-magnets, of which are 9,100⁽³⁾ installed NMR systems in the world-wide, to be a mouse brain's MR scanner part-timely and reproducibly.

An independent mouse MRI system and experiment

Figure 1(a) shows a developed mouse MRI system with an existing 14.1T NMR magnet. The digital MRI console⁽⁴⁾ has a PC (win7), digital transceiver (FPGA, rf converter & switch), rf transmitter (50W), gradient driver (+/-20V/20A). The probe head shown in fig. 1(b) has a three-axis gradient coil (ID/OD= 23/33 mm ϕ , 40 mT/m/A) and surface rf coil (15 mm ϕ). In order to investigate the imaging capability and BOLD⁽⁵⁾, C57BL/c (M, 3-6W) were imaged under injection-anesthetization by α -chloralose or Ketamine. Oxygen was supplied to the mice's atmosphere in flow rate from 0 to 500 mL/minute. These experiments kept animal's experimental regulation of the university department.

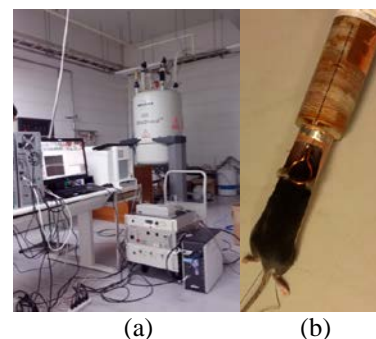


Fig. 1: 14.1T mouse MRI system.

Result and discussion

Figure 2(a, b) shows the imaging result ($T_{acq}=15\text{min}$, $T_{aqw}=5.12\text{ms}$), of mice (C57BL/c); (a) 3W, 3D-GRE, 1024×128^2 , TR/TE/FA = 60/6ms/90deg, $(110\mu\text{m})^3$; (b) 6W with suppressed oxygen flow, 3D-GRE, $256 \times 128 \times 32$, TR/TE/FA = 100/6.5ms/90 deg, $110 \times 110 \times 200 \mu\text{m}^3$. Fig.2 (a) has brighter signal intensity than that of (b), which has black lines on their cerebral cortex indicating blood oxygenation level dependency (BOLD).

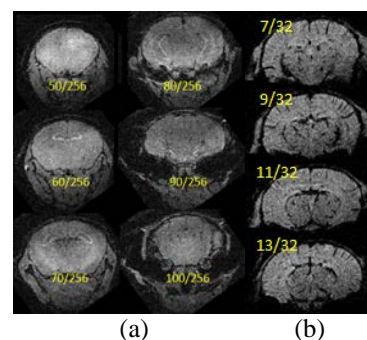


Fig. 2: 3D-GRE images at 14.1T indicating BOLD effect.

Conclusion

The live mice were imaged with the existing ^1H -600MHz NMR magnet and the developed MRI unit with the digital console and probe head with using 3D-GRE sequences. The NMR magnet had enough B_0 -homogeneity and the result promised mouse's *fMRI* with BOLD effect. This approach utilizing an existing NMR magnet with using the independent MRI unit is confirmed to be used as a mouse MR scanner at biomedical laboratories especially in brain and neuroscience.

References:

1. T Haishi et al, Development of a 1.0 T MR microscope using a Nd-Fe-B permanent magnet. MRI19, 875-880 (2001)
2. K. Kose et al, A Novel Approach to the MR microscope: MRMICS, April (1998), 6th ISMRM, Sydney.
3. S Tanaka, NMR spectrometer 9,100 installed, an article in Japanese, Superconductivity Web 21, ISTE, JUL (2001)
4. S Hashimoto et al, Rev. Sci. Instrum 83, 053702 (2012)
5. S. Ogawa et al, Proc. Natl. Acad. Sci. USA, Vol. 87, pp. 9868-9872, Dec (1990).

Mapping the pore size distribution of a glass microcapillary array phantom using d-PFG MRI

D. Benjamini^{a,b}, M. E. Komlosh^{a,c}, P. J. Basser^a, U. Nevo^b

^aSTBB, PPITS, NICHD, NIH, Bethesda, MD; ^bDepartment of Biomedical Engineering, The Iby and Aladar Fleischman Faculty of Engineering, Tel-Aviv University, Tel-Aviv, Israel. ^cCNRM, USUHS, Bethesda, MD, USA

Introduction: Noninvasive characterization of porous media is critical to many scientific and technical fields. Estimation of an empirical pore size distribution (PSD) has been demonstrated with single pulsed-field gradient (s-PFG) NMR in conjunction with solving an inverse linear problem.¹ In this case the solution depends on the degree of linear independence (degree of correlation between the different independent variables²) of the matrix that describes the set of linear equations. As the degree of multicollinearity rises, the solution becomes more ill-conditioned. Recently this linear approach was extended to include a second dimension in the parameter space using a double pulsed-field gradient (d-PFG) experiment.³ This 2-D method was shown to reduce multicollinearity and thus improve the stability and reliability of the estimated empirical PSD.³ Previously, this 2-D NMR method was performed on calibrated microcapillary PSD phantoms, resulting in accurate size distribution estimation.⁴ Here we present the first MRI implementation of this 2-D method, and report the successful estimation of the PSD map using a well-characterized phantom.

Methods: The PSD phantom is a glass capillary array (GCA)⁵ consisting of 3 different 2.5, 5, and 13.7 μm inner radii water-filled microcapillary wafers. d-PFG MRI experiments were performed on a 7T vertical-bore Bruker AVANCE III MR microimager. The acquisition parameters were: $\delta=1.65\text{ms}$, $\Delta=45\text{ms}$, $t_m=0$, 8 diffusion gradients ($G = 0-605 \text{ mTm}^{-1}$), 10 angles ($\varphi = 0-\pi$), $\text{TR}=5\text{s}$, $\text{TE}=7.75\text{ms}$ and spatial resolution = $0.242 \times 0.242 \times 1 \text{ mm}^3$. A total of 80 acquisitions were sufficient to obtain an accurate PSD in each voxel. The data was then fit to the 2-D linear PSD model.^{3,4}

Results: A sagittal proton density MRI of the phantom is presented in Fig. 1A. Different wafer-packs with different sizes are indicated, and the region of interest (ROI) for the PSD estimation is marked in blue. The estimated PSD is shown in Fig. 1B. The theoretical radii were verified by fitting the signal to the corresponding ROIs. The theoretical volumetric fractions were calculated from proton density MRI. Each theoretical distribution (blue) is known and presented on top of the estimated distribution (red). No regularization process or assumptions on the parametric form of the PSD are used. The obtained radii and their fractions are in very good agreement with the theory.

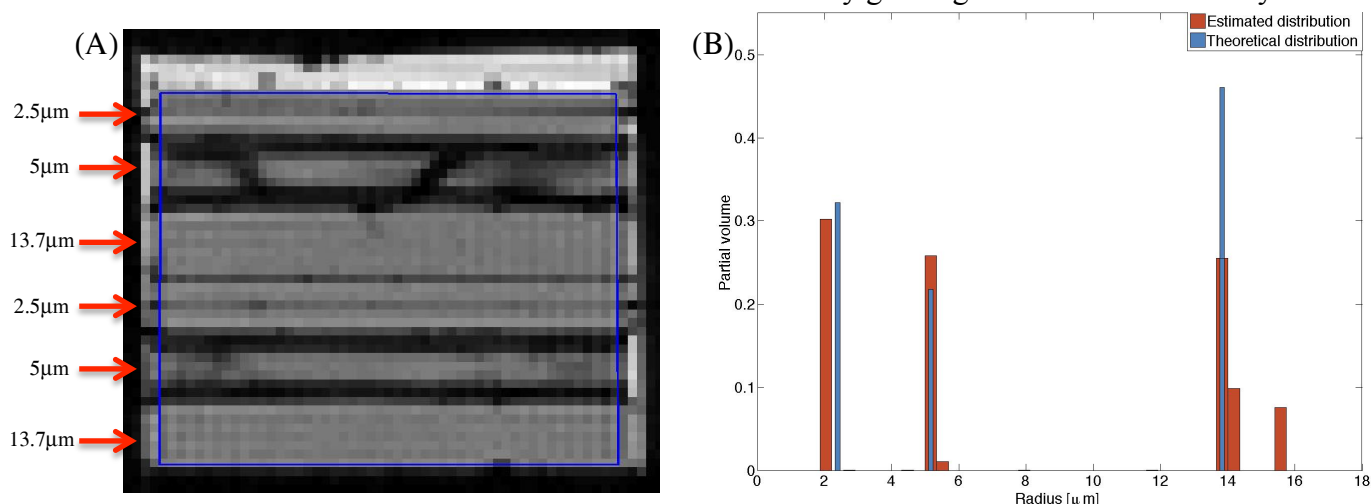


Fig. 1: (A) A proton density image of the GCA phantom. The different arrays are stacked and their size is indicated by red arrows. The ROI that was used to estimate the PSD is marked in blue. (B) The estimated (red) and theoretical (blue) PSD.

Reference: [1] K.G. Hollingsworth and M.L. Johns, *J. Colloid Interface Sci.*, 258 (2003) 383-389. [2] D.E. Farrar and R.R. Glauber, *Rev. Econ. Stat.*, 49 (1967) 92-107. [3] D. Benjamini et al., *J. Chem. Phys.*, 137 (2012) 224201. [4] D. Benjamini and U. Nevo, *J. Magn. Reson.*, 230 (2013) 198-204. [5] M.E. Komlosh et al., *J. Magn. Reson.*, 208 (2011) 128-135

MRI exploration of the low-density lipoprotein (LDL) transport in an artery model

*Clémentine Lesbats*¹, *Chunyu Jin*², *Sean P. Rigby*², *Thomas Meersmann*¹, *Dorothee P. Auer*³,
*Galina E. Pavlovskaya*¹

¹Sir Peter Mansfield Magnetic Resonance Centre, School of Clinical Sciences, ²Faculty of Engineering, ³Faculty of Medicine & Health Sciences, University of Nottingham, Nottingham, UK.

Background: Atherosclerosis is a medical condition caused by endothelial injury due to various factors [1]. The disease stays asymptomatic until the thickening of the artery wall significantly slows down blood flow. The injury is caused by LDL and monocyte penetration into the artery wall that can provoke inflammation, fibro-proliferation and necrosis, thereby inducing a protrusion of the plaque formed into the lumen of the artery. In theory, the concentration profiles of LDL across the arterial wall would correlate with variations in filtration velocities across this vessel wall. The aim of this study is to model LDL transport by measuring axial and transverse velocity profiles of a model suspension fluid in the “artery” wall model geometry using magnetic resonance imaging (MRI) velocimetry methods.

Material and methods: An artery geometric model is based upon a 3-fold magnification of the diameter of the carotid artery [2] (atherosclerosis occurs most frequently in this particular artery). The “artery wall” was initially modelled as a simple porous layer. However the complexity of the model was further developed to include a sandwiched layer of porous materials with different pore sizes and widths – we believe that this reflects more accurately the complex structure of the multi-layered artery wall. Pore sizes and widths of porous media used were also three times larger than the ones naturally present in human arterial blood vessels. The model fluid was a 30%(w/w) aqueous suspension of buoyant polystyrene spheres (16.2 microns) representing red blood cells. In addition, 5% of 50 nm particles were added to represent LDL in a concentration that matches the higher cholesterol limit in humans. The model fluid was flown through the model artery geometry such that the peak velocity corresponds to 30 cm/s.

All velocity measurements were performed with 9.4T microimaging Avance III Bruker system. Axial and transverse velocity fields were measured using spin-echo and stimulated echo MRI velocimetry protocols. Data processing and velocity calculations obtained through Prospa (v3.01, Magritek, Wellington); subsequent data analysis with IGOR Pro (v6.01, Wavemetrics, USA).

Results: The measured axial and transverse velocity profiles well reflected the non-Newtonian character of the model fluid used. At particular interest are the transverse velocity profiles at the boundary of the porous sandwiched wall. The obtained preliminary data sets a foundation for the future refinement of computer models, in particular when combined with clinical data.

Conclusion: Fluid mechanics studies with a comprehensive model of LDL accumulation within the arterial wall promise to offer unique insights into the underlying processes of atherosclerosis. The model may help to improve atherosclerosis pathophysiology and early non-invasive diagnosis.

References:

1. George, S.J., Johnson, J., 2010, *Atherosclerosis: Molecular and Cellular Mechanisms*, Wiley-Blackwell, Weinheim, 398p.
2. Limbu YR, Gurung G, Malla R, Rajbhandari R, Regmi SR (2006) *Assessment of carotid artery dimensions by ultrasound in non-smoker healthy adults of both sexes*. Nepal Medical College journal : NMCJ 8: 200-203.

Application of wavelet transform de-noising to MRI based on background noise estimation

Kang Liu^a, Ranhong Xie^a, Nian Wang^b, Yang Xia^b

^a State Key Laboratory of Petroleum Resources and Prospecting, China University of Petroleum (Beijing), Beijing 102249, China, ^b Department of Physics, Oakland University, Rochester, Michigan 48309, USA

The noise in the MRI magnitude data is Rician distributed, which depends on the noise level - distributing as Gaussian at high SNR and Rayleigh at low SNR. Since the noise level affects the performance of different image post-processing techniques, it's important to consider the noise properties while de-noising MRI data.

In this report, we presented the wavelet transform scheme for the purpose of noise reduction in MR images, which was based on a background noise estimation method. We firstly segmented the background part of the MRI data, and then used the background noise estimation method to calculate its noise level (which is usually Rayleigh distributed). The noise-level parameter was then used for the threshold setting in wavelet transform. A MRI model was first used to test the feasibility of this method. The method was then used to de-noise the data of cartilage (Figure 1) and rock core samples.

Figure 1b shows clearly the de-noising effect for an image without average, when it is compared to its original data (Figure 1a). The SNR of the de-noised image is higher than the image of the same sample with 32 averages (Figure 1c).

It is concluded that the proposed method can suppress the Rician noise in MRI data, and effectively preserve the edge and fine features of the specimens.

Acknowledgements

Ranhong Xie acknowledges the financial support of the National Natural Science Foundation of China (41272163). Y Xia is supported by NIH R01 grant (AR052353).

References

- [1] Nowak R D, IEEE Trans. Image Processing, 10:1408-19, 1999.
- [2] Aja-Fernández S et al., Magn. Reson. Imaging, 27:1397-409, 2009.
- [3] Zhou Dengwen, et al., Pattern Recognition Letters, 29(11): 1694-1697, 2008.
- [4] Wu ZQ, et al., Electronic Letter, 39(7): 603-5, 2003.

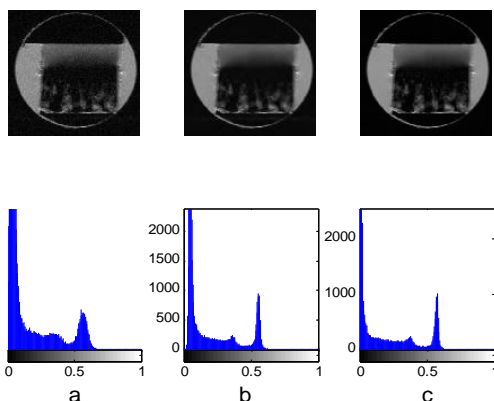


Figure 1 MRI of an articular cartilage sample. The images in the upper row are the original no-average image and its' denoised result, 32 times average. The lower are the gray-scale histograms of the upper row images respectively, which are calibrated into the range of 0 to 1.

MR microscopy in assessment of dental caries

L. Seršič^a, J. Vidmar^{a,b}, L. Nemeth^c, K. Cankar^b

^aJožef Stefan Institute, Ljubljana, Slovenia, ^bInstitute of Physiology, University of Ljubljana, Slovenia, ^cDepartment of Dental Diseases, University Medical Centre, Ljubljana, Slovenia

MRI of teeth *in vivo* is still relatively challenging and is therefore rarely used¹. However, MR microscopy studies of teeth *in vitro* show that MRI could have an important impact in dental diagnostics. It was already demonstrated that it is a powerful tool in analysis of root canal complex geometry². In this study, we demonstrate that MR microscopy can also be used to assess dental pulp response to caries and that it also enables caries grading according to the International Caries Detection and Assessment System (ICDAS). The assessment is based on caries induced changes of water mobility in dental pulp that can be detected by ADC mapping³.

Twenty six extracted teeth (mainly molars and premolars) of ICDAS scores 0 (intact tooth) to 6 (severe caries) were scanned on a 2.35 T MRI system using the high resolution 3D T1-w spin-echo method and the 3D DWI method. Before scanning, the teeth were coated by a dental impression material to prevent pulp desiccation and to enable a better visualization of hard dental tissue outline. The 3D T1-w images (matrix: 256 x 128 x 128, FOV: 30 x 15 x 15 mm³, TE/TR = 2.3/400 ms) were used for localization of demineralized hard dental tissues, while DW images of different *b* values (0, 132, 317 and 635 s/mm²) were used to calculate ADC maps of soft dental tissues (dental pulp).

Figure 1 shows T1-w MR images and corresponding ADC maps of two teeth, one intact (ICDAS 0) and one with severe caries (ICDAS 6). T1-w images clearly show demineralized dentin regions that were affected by caries which appear bright, while intact dentin gives no signal. Corresponding ADC maps show a significant difference in ADC values between an intact dental-pulp complex ($1.24 \pm 0.06 \cdot 10^{-9} \text{ m}^2/\text{s}$) and the complex affected by severe caries ($0.81 \pm 0.04 \cdot 10^{-9} \text{ m}^2/\text{s}$). The same analysis performed on other teeth of different ICDAS grades showed that there exists almost a perfect linear relationship between ICDAS grades and corresponding average ADC values of the dental-pulp complex. In addition to that, a relation between the demineralization depth and the average ADC of the dental-pulp complex was also found; i.e., increase in the demineralization depth for 1 mm yielded 0.7% decrease of the average ADC in the dental-pulp complex.

MRI enables reliable detection of caries lesions as well as their quantification based on diffusion properties of a dental-pulp complex. This feasibility *in vitro* study demonstrates a possible use of MR microscopy for *in vivo* assessment of caries.

References:

1. O. Tymofiyeva, K. Rottner, D. Gareis, J. Boldt, F. Schmid, M.A. Lopez, E.J. Richter and P.M. Jakob, *Concept Magn Reson B*, 33B (2008), 244-251.
2. D. Sustercic and I. Sersa, *Radiol Oncol*, 46 (2012), 1-7.
3. J. Vidmar, K. Cankar, L. Nemeth and I. Sersa, *NMR Biomed*, 25 (2012), 1056-1062.

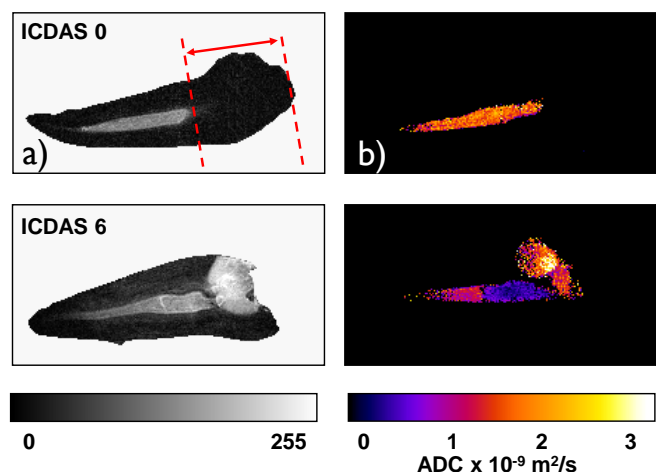


Fig. 1: analysis of the pulp chamber anatomy (a) and ADC mapping based discrimination between intact and decayed regions of the dental-pulp complex.

The dependences of multi-component T₂ measurement in cartilage and gel phantom on the imaging sequences and specimen solutions

Y. Xia, N. Wang

Departments of Physics, Oakland University, Rochester, MI 48309, USA

An accurate and faithful measurement of multi-component T₂ in biological tissue by either NMR or MRI is not trivial. In addition to the complex relaxation mechanism in tissue itself, the measurement can be influenced by many experimental factors. In this project, we investigated the influences of two factors related to the multi-component T₂ measurement in cartilage: (1) different pulse sequences (MSME, CPMG-SE); and (2) the influence of the bath solution (saline, PBS).

Methods: A Bruker AVANCE II 300 micro-imager was used to carry out the T₂ experiments using fresh canine cartilage-bone blocks and agar gel phantoms. NMR spectroscopy experiments used the standard CPMG sequence. μ MRI experiments used a commercial multi-slice, multi-echo (MSME) pulse sequence (only one slice was used in this study), as well as a CPMG magnetization-prepared spin-echo imaging sequence (termed as the CPMG-SE), both at three different transverse pixel resolutions (140 μ m, 70 μ m, and 35 μ m). The NNLS method was used to calculate the distribution profiles of T₂ relaxation times.

Results: The table on the right summarizes the μ MRI results of the gel samples, which is consistent with the NMR spectroscopy results of the gel (not shown). These data demonstrate unmistakably the potential uncleanness of the MSME sequence in the multi-component relaxation measurements. Fig 1a – 1d summarize the bulk T₂ results of cartilage in μ MRI when the tissue was soaked in saline. The influences of the two pulse sequences and the specimen orientations in the magnetic field are clear. As a comparison, Fig 1e – 1h show the same T₂ results of cartilage when the tissue was soaked in PBS. When the tissue was imaged by CPMG-SE, only a single T₂ component was observed at both 0° and 55° at all resolutions. When imaged by MSME, two components were observed at both 0° and 55° at all resolutions.

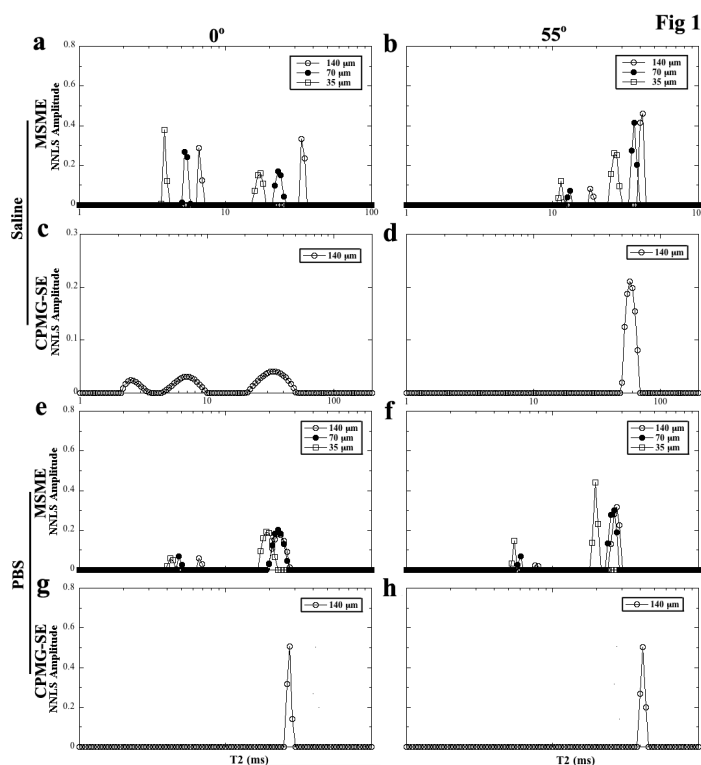
Discussion: The anisotropic T₂ in cartilage likely indicates the dipolar interaction-induced depth-dependency of relaxation at different structural zones of the collagen matrix in the tissue. The transition between the mono and multi-component in cartilage demands the caution in interpreting the multi-component relaxation results. Compared to the artificial multiple T₂ components by the MSME sequence, the CPMG-SE sequence is robust and reliable.

Acknowledgements: This project was funded by an R01 grant from NIH (AR 52353).

References:

(1) S. Zheng and Y. Xia, Magn Reson Imaging 28 (2010) 537; (2) N. Wang and Y. Xia, J Magn Reson 212 (2011) 124.

Pulse Sequence	Imaging Resolution					
	140 μ m		70 μ m		35 μ m	
	T ₂ (ms)	%	T ₂ (ms)	%	T ₂ (ms)	%
MSME	6.8 \pm 1.3	7.9 \pm 3.1	4.5 \pm 0.9	8.4 \pm 4.1	3.9 \pm 0.6	13.2 \pm 4.6
	39.4 \pm 2.8	92.1 \pm 3.4	31.3 \pm 1.8	91.6 \pm 5.3	21.5 \pm 3.0	86.8 \pm 5.8
CPMG-SE	78.4 \pm 4.0	100	78.0 \pm 3.7	100	77.9 \pm 4.6	100



***Operando* MR: Spatially-resolved NMR measurements of a fixed bed heterogeneous catalytic reaction**

L. Baker, M. P. Renshaw, M. Lutecki, M. D. Mantle, A. J. Sederman, L. F. Gladden

Department of Chemical Engineering & Biotechnology, University of Cambridge,
Pembroke Street, Cambridge CB2 3RA, UK

Fixed-bed heterogeneous catalysis is a complex, multi-step process requiring the simultaneous contacting of at least one fluid phase and a solid phase. When designing a reactor for such reactions, careful consideration of fluid dynamics, catalyst properties, thermal factors, transport properties of the fluids and reaction kinetics can result in a reactor with a high overall rate of conversion per unit volume, and high selectivity to the desired product. However, this design approach could be greatly enhanced by spatially-resolved information about these features such as the local rate of conversion at different parts of the catalyst bed, or local fluid diffusion characteristics. This kind of information could result in the design of more fixed bed catalytic reactors that are smaller, cheaper and better for the environment.

Four key features of NMR make it the ideal candidate to provide this information: it is a non-invasive, chemical-specific, motion-sensitive and spatially resolvable measurement technique. Recently we have commissioned a fixed-bed reactor capable of simulating industrially relevant conditions, and we have demonstrated this by examining the catalytic oligomerisation of ethene over a catalyst bed that was 45 mm high and 20 mm wide at 110 °C and 28.6 atm. 32 ^1H NMR chemical shift images (with spatial resolution in the vertical dimension) were acquired at different times during the 9 hour reaction. Figure 1 shows the two peaks that appear in the spectra resulting from this technique. The peak at ~ 5 ppm is from ^1H nuclei bonded to olefinic carbon atoms; the other peak arises from ^1H nuclei attached to aliphatic carbons. Figure 2 shows the relationship between the area under these two peaks and the vertical position of the spectra. From this information conclusions can be drawn about the spatial and temporal variations in the rate of conversion and selectivity of this oligomerisation reaction.

This work, therefore, introduces the potential of spatially-resolvable NMR techniques to characterise complex fixed-bed heterogeneous catalytic reactions.

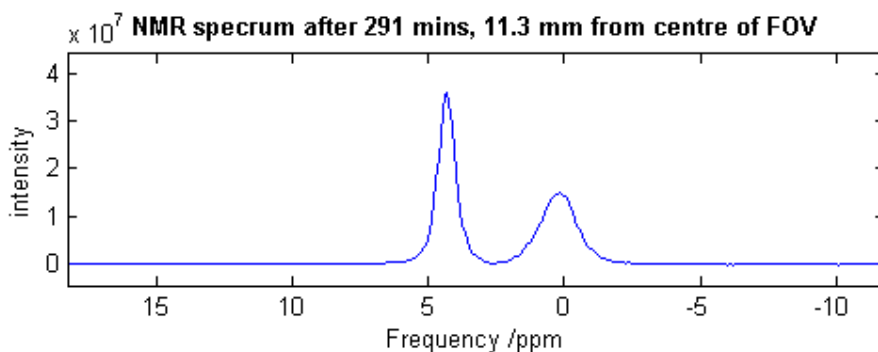


Figure 1: Typical ^1H NMR spectrum acquired from chemical shift imaging (CSI) experiment

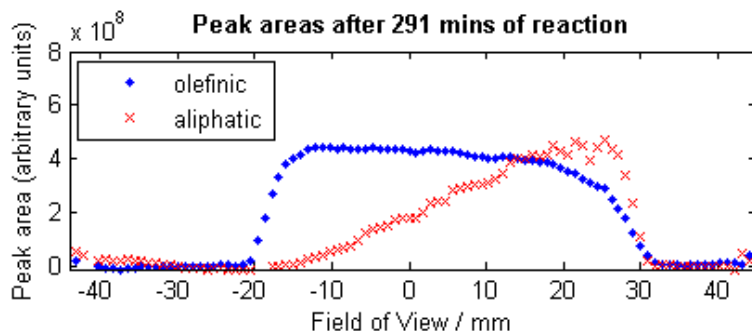


Figure 2: Graph depicting the variation of peak areas with distance from the top of the reactor (or whatever reference point you choose)

P09

In situ, real-time visualisation of electrochemistry using magnetic resonance imaging

Paul M. Bayley^{a}, Melanie M. Britton^b, Patrick C. Howlett^a, Alison J. Davenport^c and Maria Forsyth^a*

^a Institute for Frontier Materials, Deakin University, Victoria, 3125 Australia, ^b School of Chemistry, University of Birmingham, Birmingham, B15 2TT, UK, ^c School of Metallurgy and Materials, University of Birmingham, Birmingham, B15 2TT, UK, *Current address; Department of Chemistry, University of Cambridge, Cambridge, CB2 1EW, UK

The development of high-energy density batteries, fuel cells and other electrochemical devices expected to power society into the future would benefit from the unique, detailed, information provided by Magnetic Resonance Imaging (MRI). The use of MRI to study electrochemical systems has seen spurious interest from the research community, partly due to the problems inherent with strong magnetic fields. Our recent research into the feasibility of studying the electrolyte in a Zinc-air battery using MRI has yielded intriguing results. The data suggest that contrast on relaxation maps is the result of an electrochemical reaction and changes over time. The demonstration of this technique for such a device opens exciting opportunities to develop a greater theoretical understanding of the origin of the observed affects and optimisation of electrochemical devices in future. These results also have potentially concerning implications for clinical MRI.

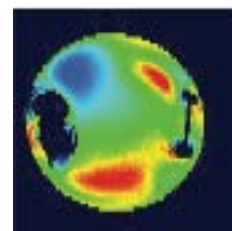


Fig. 1: Example of the features that evolve in a T_1 contrast image of the electrolyte during cell discharge.

Impact of salt on starch and gluten and on water migration in pasta studied with ^1H , ^{19}F , ^{23}Na and ^{35}Cl MRI/NMR

D. Bernin^{a,b}, T. Steglich^c, M. Röding^d, A. Moldin^e, M. Langton^g, D. Topgaard^h

^aApplied Surface Chemistry, Chalmers University of Technology, Gothenburg, Sweden, ^bSwedish NMR Center, Gothenburg University, Gothenburg, Sweden, ^cSIK – The Swedish Institute for Food and Biotechnology, Gothenburg, Sweden, ^dDepartment of Mathematical Statistics, Chalmers University of Technology and Gothenburg University, Gothenburg, Sweden, ^eLantmännen Cerealia, Järna, Sweden, ^gDepartment of Food Science, Swedish University of Agriculture Science, Uppsala, Sweden, ^hDivision of Physical Chemistry, Lund University, Lund, Sweden

Salt is added to food products for its flavor, texture and preservation. Sodium ions give the salty flavor, but can cause health problems if their consumption exceeds the reference daily intake of 1.5g¹. The rule for cooking pasta is to add 7g of sodium chloride to 1l water for every 100g of pasta². To minimize the sodium intake when eating pasta dishes, it is necessary to characterize the interactions of salt ions with starch or gluten and the impact of salt on cooking pasta.

The impact of sodium chloride on water migration was studied using ^1H relaxation imaging. Pasta with various starch and gluten contents were cooked inside the magnet and images were acquired in real time as a function of cooking time. Additionally, pasta was cooked in a sodium fluoride solution and the sodium and fluoride ion migration was monitored with ^{23}Na and ^{19}F imaging. Binding of sodium and chloride ions as well as exchange of fluoride ions between two sites ('free' and 'bound') in the presence of starch or gluten was verified with ^{23}Na and ^{35}Cl double-quantum filtered (DQF) and ^{19}F 2D exchange spectroscopy (EXSY), respectively.

In general, cooked pasta with high gluten content was characterized by an ungelatinized core compared to high starch content pasta for the same cooking time. The addition of sodium chloride seemed to slow down the water migration during cooking and thereby lengthening the cooking time. Fig. 1 shows representative T_2^* maps of pasta cooked in a sodium chloride solution. ^{23}Na and ^{19}F images revealed the fluoride and sodium ions in the water-containing regions of the pasta. The travelled distance of both ions differed depending on the composition of the pasta for the same cooking time. For high gluten content, both ions were still located at the edge of the pasta also after 16 min cooking time in contrast to high starch content, where the ions were distributed over the whole pasta. ^{19}F EXSY spectrum showed cross peaks indicating slow exchange of fluoride ions in the presence of gluten in contrast to starch. Binding of sodium and chloride ions to starch or gluten changed upon cooking.

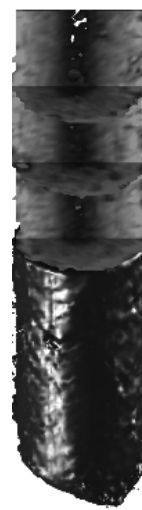


Fig. 1: Longitudinal and axial T_2^* maps (light gray > 15ms; dark gray < 2ms) with a 3D rendering of the relative water content of a pasta cooked in a sodium chloride solution. The ungelatinized core is seen in the middle of the pasta in dark gray.

Using salt for cooking pasta seemed to impact the water migration in pasta, particularly in pasta with high gluten content. Combining the results with the absolute ion concentration in cooked pasta, the composition of pasta may be tuned to minimize the daily sodium ion intake.

¹<http://www.efsa.europa.eu/en/ndatopics/docs/ndatolerableuil.pdf> (p.429-446)

²http://www.iso.org/iso/catalogue_detail?csnumber=13966

Taking magnetic resonance into industrial applications

T. Blythe^a, L.F. Gladden^a, J. Mitchell^a, A.J. Sederman^a, A. York^{a,b}, E.H. Stitt^b

^aDepartment of Chemical Engineering and Biotechnology, University of Cambridge, Cambridge CB2 3RA, UK

^bJohnson Matthey Catalysts, PO Box 1, Belasis Avenue, Billingham TS23 1LB, UK

Process rheometers, typically employed in online or inline configurations, are used in a wide range of industrial applications to examine the behaviour of fluids under shear conditions. Many of these rheometers are able to provide only one shear viscosity-shear rate data point in a single measurement and hence characterisation of rheology over a range of shear rates is time-consuming. Additionally, these process rheometers probe only bulk fluid behaviour and, whilst this is satisfactory for ‘normal’ fluids, it is not satisfactory for many of the ‘complex fluids’ encountered in industry. Complex fluids exhibit both liquid- and solid-like behaviour, with examples including slurries and emulsions. Under shear conditions, complex fluids may exhibit any number of complex flow phenomena and there is therefore a need to obtain real-time information about the flow field. The combination of existing rheometer geometries with flow visualisation techniques, including x-ray scattering and ultrasonic, allow for the identification of such phenomena. Magnetic Resonance (MR) offers a non-invasive, non-ionising and versatile method of flow visualisation.

Rheological characterisation across several decades of shear rate can be achieved using MR Imaging (MRI) velocimetry in ~10 minutes – substantially faster than conventional rheological studies. Work so far has considered two complementary methods allowing for the rheological characterisation of complex fluids; (i) rheoNMR and (ii) pipe flow. RheoNMR is concerned with contained-cell offline geometries including the Couette cell. A typical velocity image, acquired at high field (7 T), is shown in Fig. 1. The rheological characterisation of several Newtonian and non-Newtonian fluids has been performed using rheoNMR and the results were found to be in good agreement with values obtained using traditional methods. Pipe flow characterisation offers an online or inline technique. A combination of MRI velocimetry with pressure drop measurements has been implemented at intermediate field (2 T) and the accuracy of the rheological data was found to be within 5% in all cases. Both techniques therefore offer a fast, reliable and robust method of rheological characterisation with many advantages over traditional methods. All work so far has utilised super-conducting magnets and, despite the experimental advantages, there are very many disadvantages associated with their use. These disadvantages, which include a high cost and safety issues, prevent their use in industrial environments and, for this reason, this work aims to implement rheological characterisation at lower field strengths (<1 T).

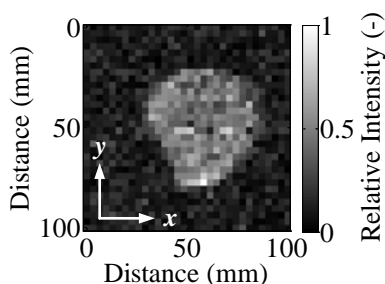


Fig. 2: 32 × 32 spin echo intensity image of a can of Red Bull clearly showing the air space above the liquid (bottom left) (85 min 20 s).

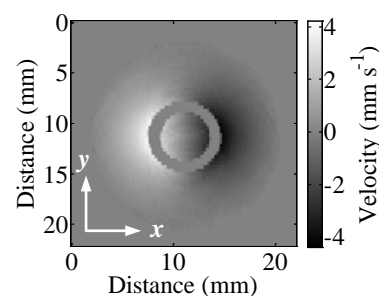


Fig. 1: A 128 × 64 pulsed gradient spin echo velocity image of water showing y-components of velocity at a Couette rotational frequency of 0.2 rev s⁻¹ (11 min 24 s).

An advantage associated with a reduction in field strength is an increase in the ability to probe fluids contained within metal containers¹. A feasibility study at Earth's field (~50 μT) has demonstrated that MR studies of fluids contained within metal containers, notably metal cans (~80 μm thickness), are possible. Fig. 2 shows the intensity image of a can of Red Bull. These initial experiments suggest that lower field MR has potential for the characterisation of process fluids in an industrial environment.

References:

1. Mößle, M., Han, S.-I., Myers, W. R., Lee, S.-K., Kelso, N., Hatridge, M., Pines, A. and Clarke, J., 2006, *Journal of Magnetic Resonance* **179**, 146-151.

Cross-validating magnetic resonance measurements of 3D cylindrical fluidized beds with predictions from a discrete element model

C. M. Boyce^a, D. J. Holland^a, S. A. Scott^b, J. S. Dennis^a

^aDepartment of Chemical Engineering and Biotechnology, University of Cambridge, UK

^bDepartment of Engineering, University of Cambridge, UK

A 3D cylindrical discrete element model combined with computational fluid dynamics (DEM-CFD) was developed to simulate fluid and particle dynamics in fluidized beds for direct comparison with magnetic resonance measurements. The discrete element model simulates the motion of each individual particle, using a combination of Newtonian and particle contact mechanics. Computational fluid dynamics using volume-averaged Navier-Stokes equations¹ were used to simulate gas flow, using the drag law of Beetstra *et al.*² to model fluid-particle interaction.

Time-averaged predictions of particle velocities using the DEM-CFD model were compared with the MR results of Holland *et al.*³ on the same bed. To understand how the acquisition and Fourier-space averaging process of MRI compares with other averaging processes, the predicted particle velocities were time-averaged in various ways. For direct comparison with MRI, in one average, outputs of particle positions from the DEM-CFD model were simulated as undergoing the same pulse sequence as used in the MR experiments. Figure 1 shows the cross-validation of MR measurements with DEM-CFD predictions for time-averaged particle velocity, as well as the comparison of the MR averaging process with other averaging techniques. The figure demonstrates that the MR-averaging procedure most closely matches a particle-based averaging procedure and is very different from a frame-based averaging procedure⁴.

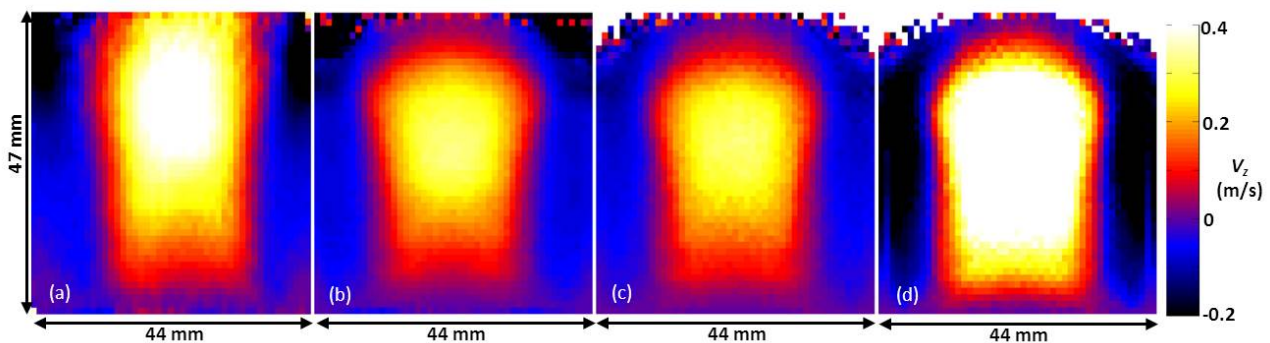


Fig. 1: Comparison of time-averaged particle velocities in a bubbling fluidized bed fluidized at $2 U_{mf}$: obtained from magnetic resonance imaging measurements (a), as well as DEM-CFD predictions processed using the full MR pulse sequence (b), a particle based average of particle velocities (c) and a frame-based average of particle velocities (d).

A further investigation examined the frequency of bubble formation and eruption as compared with the frequency of pressure oscillations in bubbling and slugging fluidized beds. 1-D FLASH images of particle distribution at the bottom and top of the bed obtained by Müller *et al.*⁵ were used to determine the rate of bubble formation and eruption experimentally. Horizontally-averaged voidage profiles at the bottom and top of the bed were used to determine the rate of bubble formation and eruption predicted by the DEM-CFD simulations. In both cases, frequencies of bubble formation and eruption were compared with the predicted frequencies of oscillations in pressure at the bottom of the bed. The DEM-CFD predictions cross-validated the MRI results, and both techniques showed a clear trend of the frequency of bubble eruption matching the frequency of pressure oscillations at the bottom of a slugging fluidized bed, for the bed sizes considered.

References:

1. T. B. Anderson, and R. Jackson, *Ind. Eng. Chem. Fund.* 6 (1967) 527.
2. R. Beetstra, M. A. van der Hoef, and J. A. M. Kuipers, *Chem. Eng. Sci.* 62 (2007) 246.
3. D. J. Holland, C. R. Müller, J. S. Dennis, L. F. Gladden, and A. J. Sederman, *Powder Technol.* 182 (2008) 171.
4. C. M. Boyce, D. J. Holland, S. A. Scott, and J. S. Dennis, *Ind. Eng. Chem. Res.* (Submitted).
5. Müller, C.R., Davidson, J.F., Dennis, J.S., Fennell, P.F., Gladden, L.F., Hayhurst, A.N., Mantle, M.D., Rees, A.C., Sederman, A.J. *Powder Technol.* 177 (2007) 87.

Effect of confinement on diffusion and dynamics of primary alcohols and non-ideal binary mixtures acetone-chloroform in mesoporous catalysts probed by PFG-NMR

Pierre Bräuer^a, Carmine D'Agostino^b, Mick Mantle^b, Lynn Gladden^b

^aDepartment of Chemical Engineering, Hamburg University of Technology, D-21073 Hamburg, Germany

^bDepartment of Chemical Engineering & Biotechnology, University of Cambridge, Pembroke Street, Cambridge, CB2 3RA, UK

In recent publications^{1,2} the diffusivity of bulk non-ideal binary mixtures acetone-chloroform and the molecular diffusion of organic liquids within mesoporous materials has been studied. Following up these previous works, this paper aims to elucidate the dynamics of acetone-chloroform mixtures confined in mesoporous materials as well as study the effect of confinement on the diffusion and hydrogen bonding network of a series of primary alcohols (methanol to 1-octanol) within the pore space for different mesoporous catalysts.

In this work, PFG-NMR was used to measure the self-diffusivity of the species in bulk liquid mixtures of acetone-chloroform as well as bulk liquid primary alcohols. The self-diffusive behaviour of both systems was then investigated in mesoporous supports and catalysts, namely TiO₂, Al₂O₃, and Pd/Al₂O₃. Measurements for acetone-chloroform binary mixtures were carried out over the full range of composition. For single liquid components, a set of primary alcohols with chain length ranging from C₁ to C₈ was studied in order to

assess the effect of the alkyl chain of the alcohol on the molecular self-diffusivity. The binary system acetone-chloroform showed an interesting behaviour. The deposition of Pd onto Al₂O₃ affects the physical structure of the pore network in terms of pore connectivity. In particular, the presence of Pd increases the tortuosity of the porous matrix, hence decreasing the diffusivity of guest molecules. Further, the presence of the porous media changes the relative translational dynamics of acetone with respect to chloroform as compared to the bulk liquid mixture.

The results on primary alcohols indicate that the length of the alkyl chain affects the translational dynamics of the alcohol molecules in the TiO₂ pores, which are seen to have a systematic enhanced diffusion behaviour as the carbon chain length increases, enhanced with respect to tortuosity of the porous matrix¹. This is thought to be due to the disruption of more extensive hydrogen bonding networks for the higher alcohols.

Knowledge of translational dynamics of liquids and solutions and how this is affected by molecular interactions within catalyst pores is crucial in order to design and optimise technological applications of porous solids or packed beds, such as heterogeneous catalysis and separation.

References:

1. C. D'Agostino et al., J. Phys. Chem. C. 2012, Bd. 116, 16, S. 8975-8982.
2. C. D'Agostino et al., Chem. Eng. Sci. 2013, Bd. 95, 0, S. 43-47.

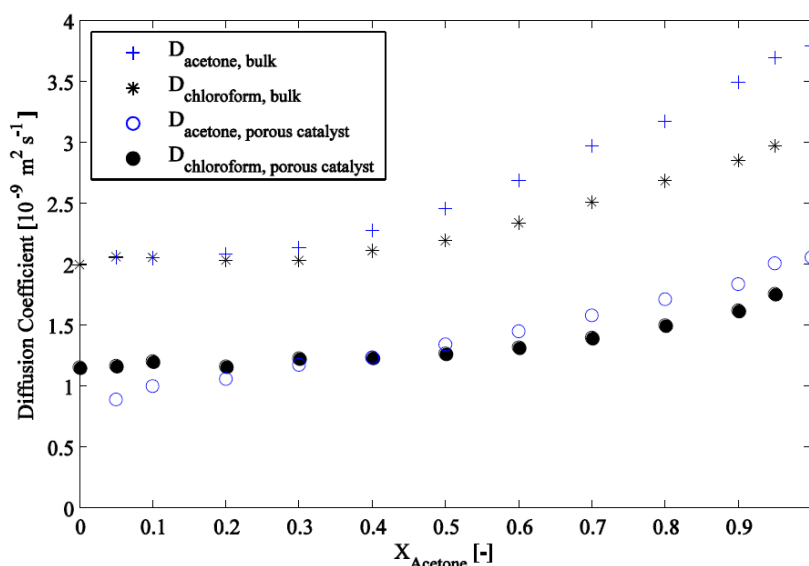


Fig. 1: Self-diffusion coefficients of acetone-chloroform mixtures as bulk liquid and liquid within a porous catalyst.

Direct multi-nuclear magnetic resonance imaging studies of controlled drug release

C. Chen, L. F. Gladden, M. D. Mantle

Department of Chemical Engineering and Biotechnology,
University of Cambridge, CB2 3RA, UK

The use of MRI as a tool in pharmaceutical dissolution research is now well established.¹ The majority of the studies have used ^1H MRI to acquire signals from water molecules within a pharmaceutical tablet during the dissolution process. In contrast, very few studies have investigated directly the behaviour of the active pharmaceutical ingredients (APIs), since the ^1H signal from API is normally obscured by the huge ^1H signal associated with the water based dissolution medium. ^{19}F is very promising candidate for API screening due to its close relevance in the pharmaceutical industry and its high sensitivity in MRI experiments.² Thus, MRI shows great potential in revealing the distribution and evolution of APIs under *in vitro* pharmacopeia dissolution conditions.³

This paper reports the first use of both ^{19}F and ^1H 2D slice selective imaging methods to examine simultaneously the behaviour of dissolution media ingress and API mobilization and egress in hydrogel tablets. Quantitative ^1H T_2 maps were acquired by T_2 preconditioned RARE pulse sequences.⁴ ^{19}F maps were acquired by FLASH pulse sequences with radial coverage of the k -space. The ^{19}F signal solely arises from the API dissolved in the hydrated gel layer. Figure 1(left) shows the co-registered ^1H water T_2 relaxation time and ^{19}F API spin density images. These can be uniquely used to monitor the mobilisation, dissolution and distribution of the hydrated API within the swelling polymeric matrix.

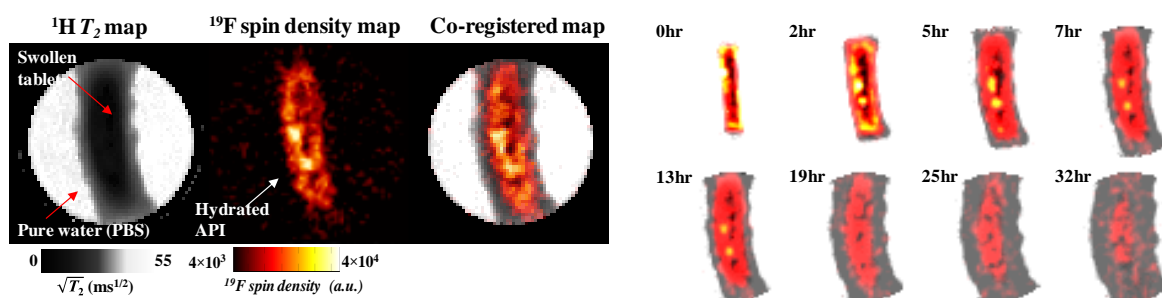


Figure 1. (left) Co-registration of quantitative ^1H T_2 images and ^{19}F API MR images from the tablet after 9 hours upon dissolution. (right) ^{19}F and ^1H co-registered maps at different hydration times.

Figure 1(right) shows the temporal evolution of the co-registered images of the same tablet. Inspection of figure 1(right) shows that the API remains within the gel layer once hydration of the solid tablet has occurred. After ~9 hours the rate of increase in size of the gel layer has “overtaken” that of the API mobilisation and a clear distinction between the API and gel layer is now visible where a significant proportion of the outer gel layer is now depleted with respect to the API. Co-registration of the ^1H and ^{19}F MRI enables the simultaneous visualization of drug egress and water ingress into the polymer matrix. This method presents a new way of understanding the detailed mechanisms of controlled drug release delivery devices.

References

1. Mantle, M.D., 2011. *Int J Pharm*, 417(1), pp. 173-195
2. Müller, K. et al. 2007. *Science*, 317(5846), pp. 1881-6
3. Zhang, Q. et al., 2011, *J Control Release*, 156(3), pp. 345-354
4. Chen, YY et al. 2010. *J Pharm Sci*, 99(8), pp. 3462-3472

P15

Nuclear magnetic resonance relaxometry in heterogeneous catalysis: New advances in understanding adsorption over solid catalyst surfaces

C. D'Agostino, J. Mitchell, M. D. Mantle, L. F. Gladden

Department of Chemical Engineering and Biotechnology, University of Cambridge,
Pembroke Street, Cambridge, CB2 3RA, UK

Nuclear magnetic resonance (NMR) relaxation times provide a unique probe of adsorbate/adsorbent interactions of liquids in porous materials. In the past decade, this method has been successfully used to characterise surface interactions of liquids, mostly water, in porous materials such as cement-based materials, plaster pastes, natural rocks and glasses. The technique is non-invasive, chemically selective, with generally short acquisition times of the experimental data. In recent years, we have been working intensively to extend the application of this technique to heterogeneous catalysis, where the interaction adsorbate/adsorbent plays a crucial role in the catalytic process.

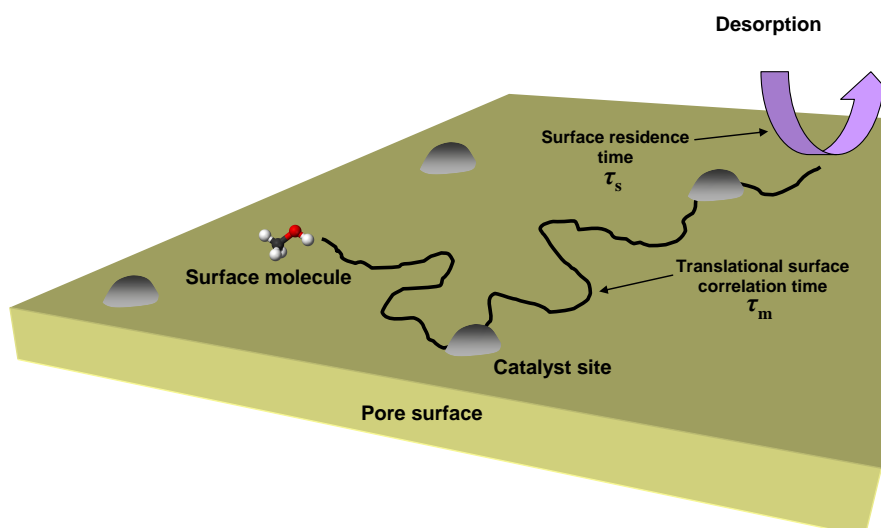


Fig. 1. Motion of adsorbed molecules over a heterogeneous catalyst pore surface.

In this work, we explore the first applications of the technique in the field of heterogeneous catalysis, focusing the attention on the investigation of several parameters that can influence the strength of surface interaction in porous catalysts, which ultimately affect catalytic activity, such as the effect of solvent composition, type of catalyst and support, metal loading and presence of product inhibition. We also show, experimentally and theoretically, that the ratio of the NMR relaxation times corresponds to a surface interaction energy, which is related to a translational surface correlation time, τ_m , and a surface residence time, τ_s , with a model surface depicted in Figure 1. The integration of NMR relaxometry with other characterisation tools will broaden our understanding of heterogeneous catalysis, allowing a more rational catalyst design and process optimisation, both on lab and industrial scale.

Monitoring of liquid reactions by low-field NMR spectroscopy

F. Dalitz^a, L. Kreckel^a, M. Maiwald^b, G. Guthausen^{a,c}

^aMVM, KIT, 76131 Karlsruhe, ^bProcess Analytics, BAM, 12489 Berlin, ^cITCP, KIT, 76131 Karlsruhe, Germany

Recent magnet development¹ allows nowadays also spectroscopic resolution at low magnetic fields. Compared to high field instrumentation, the resolution and the sensitivity are limited, but sufficient for identification and quantification of small molecules. The advantage of the permanent magnet based spectrometers is their size and robustness, allowing the applicability in rough industrial environments.^{2,3} With respect to an application in on-line reaction monitoring in terms of industrial process analytics, a by-pass has to be constructed and characterised.

Both, NMR and fluidic properties of the samples influence the acquired signal. Especially using a flow cell, flow and transport characteristics are of major importance for data interpretation. The flow field was calculated by numerical simulations and compared with MRI data. Additionally, the magnetisation build-up was studied as a function of volume flow rate. In addition to the expected dependence on the longitudinal relaxation time of the fluid, contributions of reverse flow within the flow cell due the cells' geometry were revealed.⁴

On the example of an esterification reaction, the contributions of flow to the NMR signal are calculated and considered during data processing, which reveals finally the kinetics of the reaction. Temperature dependent studies are also possible with the actual experimental setup, allowing the determination of the activation energy of the reaction.

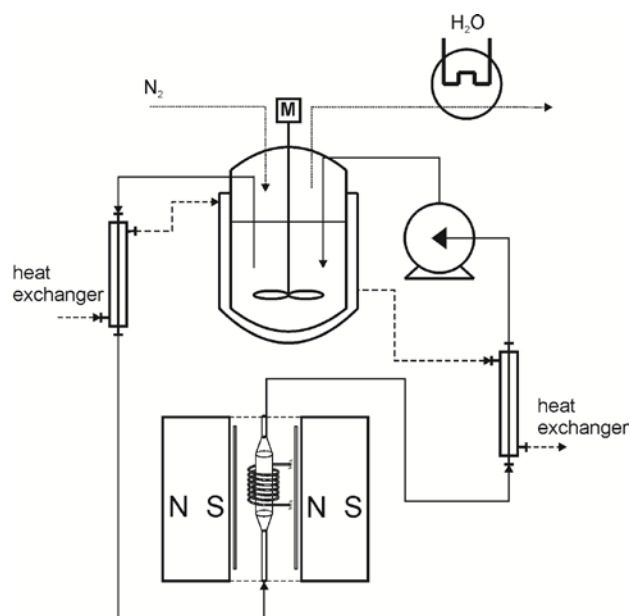


Fig. 1: Principle of the on-line process analytics in a by-pass by low-field NMR spectroscopy for reaction monitoring

References:

1. E. Danieli, J. Perlo, B. Blümich and F. Casanova, *Angew. Chem. Int. Edit.* 49 (2010) 4133.
2. A. Nordon, C. A. McGill and D. Littlejohn, *Analyst* 126 (2001) 260.
3. F. Dalitz, M. Cudaj, M. Maiwald and G. Guthausen, *Prog. NMR Spectr.* 60 (2012) 52.
4. F. Dalitz, M. Maiwald and G. Guthausen, *Chem. Eng. Sci.* 75 (2012) 318.

Ultra-short echo time magnetic resonance imaging in heterogeneous materials

H.T. Fabich^a, D.J. Holland^a, A.J. Sederman^a

^aDept. of Chemical Engineering and Biotechnology, University of Cambridge, UK

Fluidized bed reactors are a relatively new technology being used in many different industrial processes including fuel and polymer production. Fluidization refers to a fluid being forced through a bed of solid particles at a velocity that balances the force of the fluid and the weight of the particles. Fluidization is inherently difficult to study as its opacity rules out optical techniques. Recent advances in MRI have enabled characterization of 3D fluidized beds¹⁻³, however resolution and signal-to-noise ratio are limited by the short signal lifetime in these systems. Ultra short echo time (UTE) imaging is a technique that is used in medical imaging to measure material such as cartilage that have a short signal lifetime⁴⁻⁵. In this presentation we demonstrate the application of UTE to gas-fluidized beds. UTE will extend the range of particles that can be studied and increase the signal to noise ratio and resolution of ultra-fast imaging of fluidized beds.

UTE uses a half-Gaussian pulse for slice excitation in which the slice gradient and rf excitation are switched off together. Limitations of slew rate on the gradients mean that the gradients cannot switch off instantaneously. Instead, Variable Rate Selective Excitation (VERSE) is used to ramp the gradient and rf pulse off simultaneously⁶. Images are then acquired using a radial acquisition. This sequence requires a second excitation with the opposite sign for the slice selection gradient for each line in k-space. However, it permits a reduction in echo time of 1 ms or more.

In this presentation we combine UTE imaging with compressed sensing to reconstruct images in two and three dimensions with a minimum acquisition time. Figure 1 shows conventional and UTE images of a simple model system with a long T_2 to demonstrate the fidelity of the slice selection. The sample is poppy seeds and 10 mm glass beads. Both images have a spatial resolution of 0.2 mm. UTE imaging will have significant benefit for short T_2^* samples, where it will enable fast, low tip angle imaging.

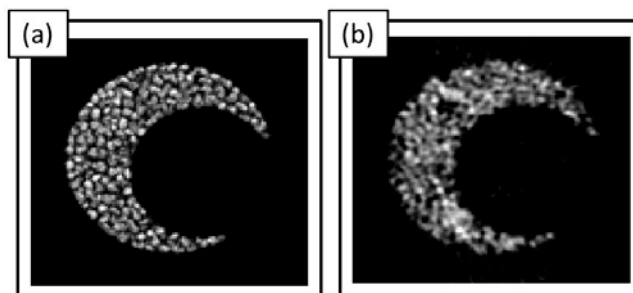


Fig 1: A 1 mm thick slice of a sample of 10 mm glass beads surrounded by poppy seeds is used to compare (a) a conventional spin echo imaging sequence and (b) a sparsely sampled UTE imaging sequence. The echo times in these images were (a) 1.7 ms and (b) 100 μ s. Data for (b) were collected via 64 radial spokes, each originating at the center of k-space. Each spoke was acquired with 256 points with a dwell time of 2.5 μ s.

References:

1. S. Harms, S. Stapf, and B. Blümich, Application of k- and q-space encoding NMR techniques on granular media in a 3D model fluidized bed reactor, *J. Magn. Reson.* 178 (2006) 308-317.
2. C.R. Müller, J.F. Davidson, J.S. Dennis, P.S. Fennell, L.F. Gladden, A.N. Hayhurst, M.D. Mantle, A.C. Rees, and A.J. Sederman, Real-Time Measurement of Bubbling Phenomena in a Three-Dimensional Gas-Fluidized Bed Using Ultrafast Magnetic Resonance Imaging *Phys. Rev. Lett.* 96 (2006) 154504.
3. D.J. Holland, C.R. Müller, J.F. Davidson, J.S. Dennis, L.F. Gladden, A.N. Hayhurst, M.D. Mantle, A.J. Sederman, Time-of-flight variant to image mixing of granular media in a 3D fluidized bed, *J. Magn. Reson.* 187 (2007) 199-204.
4. M.D. Robson, P.D. Gatehouse, M. Bydder, G.M. Bydder, Magnetic Resonance: An Introduction to Ultrashort TE (UTE) Imaging, *J. Comput. Assist. Tomogr.* 27(6) (2003) 825-846.
5. J. Du, M. Carl, M. Bydder, A. Takahashe, C.B. Chung, G.M. Bydder, Qualitative and quantitative ultrashort echo time (UTE) imaging of cortical bone, *J. Magn. Reson.* 207 (2010) 304-311.
6. B.A. Hargreaves, C.H. Cunningham, D.G. Nishimura, S.M. Conolly, Variable-Rate Selective Excitation for Rapid MRI Sequences, *Magn. Reson. Med.* 52 (2004) 590-597.

Arbitrary magnetic field gradient waveform correction using an impulse response based pre-equalization technique

Frédéric G. Goora^{a,b}, Bruce G. Colpitts^b, Bruce J. Balcom^a

^aMRI Centre, Department of Physics, University of New Brunswick, Fredericton, New Brunswick, Canada E3B 5A3, ^bDepartment of Electrical and Computer Engineering, University of New Brunswick, Fredericton, New Brunswick, Canada E3B 5A3

The application of time-varying magnetic fields (pulsed field gradients) required for spatial localization in magnetic resonance (MR) applications (such as imaging, pulsed gradient spin echo (PGSE) [1], and gradient enhanced spectroscopy [2]) result in the induction of eddy currents on conductive structures within the vicinity of the sample under investigation. These eddy currents typically result in undesired degradations of image quality for MRI applications. Their ubiquitous nature has resulted in the development of various approaches to characterize and minimize their impact on image quality.

A method that utilizes the magnetic field gradient waveform monitor method (MFGM) [3], [4] to directly measure the temporal evolution of the magnetic field gradient from a step-like input function and extracts the system impulse response. With the basic assumption that the gradient system is sufficiently linear and time invariant to permit system theory analysis, the impulse response is used to determine a pre-equalized (optimized) input waveform that provides the desired gradient response at the output of the system. An algorithm has been developed that calculates a pre-equalized waveform that is physically realizable and accounts for system limitations including system bandwidth, amplifier slew rate capabilities, and noise inherent in the initial measurement.

Significant improvements in magnetic field gradient waveform fidelity after pre-equalization have been achieved. A magnetic field gradient waveform before and after pre-equalization is shown in Fig. 1. This impulse-response based approach permits the determination of pre-equalized waveforms for arbitrary gradient output waveforms that are required for any magnetic resonance experiment and are applicable to any magnetic resonance scanner.

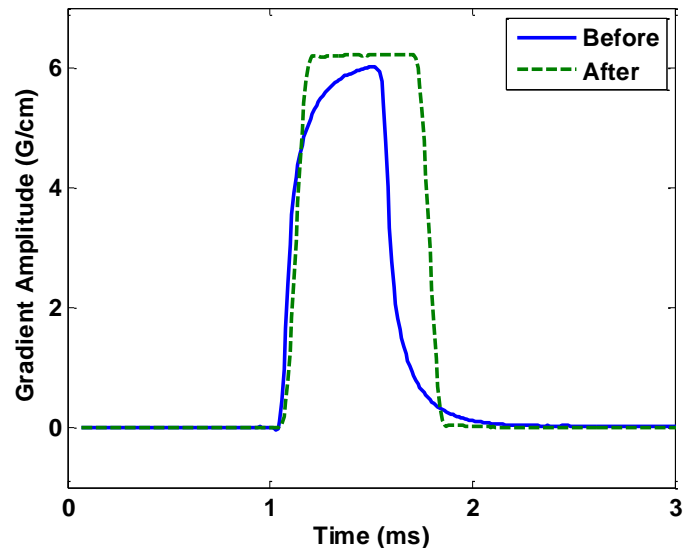


Fig. 1: Temporal evolution of a magnetic field gradient measured using MFGM before and after pre-equalization.

References:

- [1] W. S. Price, *NMR Studies of Translational Motion*. Cambridge: Cambridge University Press, 2009.
- [2] R. Hurd, "Gradient-enhanced spectroscopy," *J. Magn. Reson.*, vol. 87, no. 2, pp. 422–428, 1990.
- [3] H. Han, R. P. MacGregor, and B. J. Balcom, "Pure phase encode magnetic field gradient monitor," *J. Magn. Reson.*, vol. 201, no. 2, pp. 212–7, Dec. 2009.
- [4] H. Han, A. V. Ouriadov, E. Fordham, and B. J. Balcom, "Direct measurement of magnetic field gradient waveforms," *Concepts Magn. Reson., Part A*, vol. 36, no. 6, pp. 349–360, Nov. 2010.

NMR-diffusometry and relaxometry for the characterization of (double) emulsions in life science

R. Bernewitz^a, H. P. Schuchmann^a, G. Guthausen^b,
^aLVT, ^cITCP and IMVM, KIT, 76131 Karlsruhe, Germany

Double emulsions are of interest in life science and food processing due to their potential for fat reduction and encapsulation of active agents. They are often opaque, and dilution influences the system's equilibrium states. Non-destructive and non-invasive analytical tools are therefore to be developed for a comprehensive characterization. NMR methods are found to be well suited for this purpose and are exploited to give insight into geometry as well as into composition and molecular diffusion^[1, 2].

Two types of double emulsions were investigated: The water-in-oil-in-water emulsion (WOW) is studied with respect to droplet size distribution, dispersed phase ratio and release, i.e. coupling between phases. Diffusion phenomena and relaxation, involving spin labels, contribute to the understanding of these double emulsion types; via mathematical models the data can be processed quantitatively resulting in wanted measures of the systems.

OWO emulsions can be subject to similar measurements, requiring, however, a more detailed data analysis especially in the case of diffusion attenuation of PFG-NMR experiments. The geometric restriction leads to a less pronounced effect on the diffusion properties, therefore complicating the data processing step.

Results of both, relaxometry and diffusometry, and a differentiated picture of double emulsion system will be presented.

References:

1. J. P. Hindmarsh, J. Su, J. Flanagan, H. Singh, *Langmuir* 2005, 21, 9076.
2. M. L. Johns, K. G. Hollingsworth, *Prog. Nucl. Magn. Reson. Spectr.* 2007, 50, 51.

Uncovering supercritical CO₂ wood dewatering via interleaved ¹H-imaging and ¹³C-spectroscopy with real-time reconstruction

J. Fuchs^a, R. Meder^b, D. Sandquist^c, R.A. Franich^{c,d}, V.C. Behr^a

^aExperimental Physics 5, University of Würzburg, Germany; ^bCSIRO Plant Industry, St Lucia, Australia; ^cScion, Rotorua, New Zealand; ^dChemipreneur Limited, Rotorua, New Zealand

The Franich Process¹ describes wood dewatering by using supercritical CO₂. We measured wood samples in a pressure chamber using a 7T horizontal bore system and a double-tuned ¹H-¹³C resonator². The experimental setup allows varying the pressure and the ¹³C enrichment of the applied CO₂ in an MR-compatible autoclave as well as controlling the temperature, thereby enabling supercritical CO₂ (T_{crit} 31.1 °C, P_{crit} 7.3 MPa) to be formed *in situ* in contact with the wood. Keeping the sample volume at a constant temperature of 40°C and increasing the CO₂ pressure from 0.1 MPa to 20.0 MPa for several cycles (Fig. 2 bottom) greatly reduces the moisture content of the wood.

To monitor this process an interleaved ¹H-FLASH-imaging and ¹³C-spectroscopy sequence (as shown in Fig. 1) was utilized. The FLASH part acquires a proton image (Fig. 2 top left) of the dewatering wood every 3 seconds. The ¹³C part is a single global 90° pulse with an acquisition of the following carbon FID.

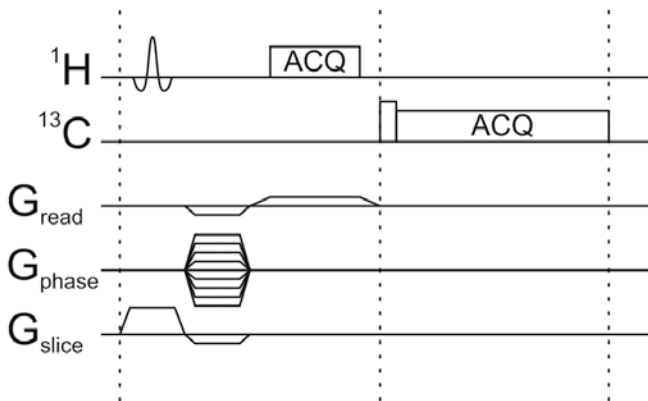


Fig. 1: Interleaved ¹H-FLASH and ¹³C-singlepulse sequence that was repeated continuously throughout the experiment.

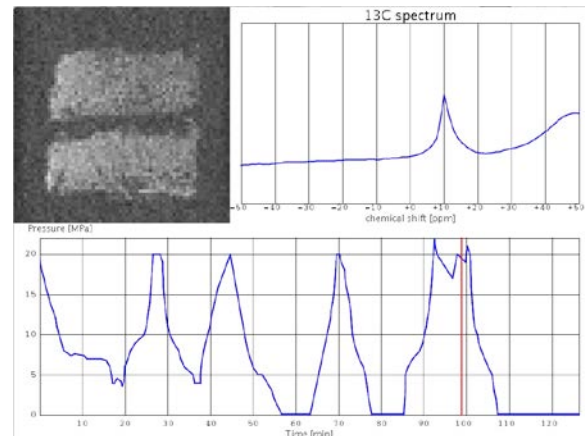


Fig. 2: Top: data displayed during interleaved measurements: left: ¹H image, right: ¹³C spectrum. Bottom: pressure readings during the consecutive cycles of the experiment.

Software was implemented to read the data from the spectrometer as it was acquired. The reconstruction software allows both the monitoring of the moisture content of the wood via a live proton image as well as observing the state of the carbon spectroscopically. In addition, signal averaging as well as exponential filtering (for the carbon spectrum) can be applied to the recorded data in order to adjust the reconstruction to the SNR of the individual measurement.

While usual NMR/MRI-experiments do not require on-the-fly reconstruction of the collected data, monitoring the wood dewatering in real-time allowed for adjustment of CO₂ pressure, temperature and ¹³CO₂ enrichment of the applied supercritical CO₂ according to the current state of the wood.

The resulting proton data provided insight into the mechanism of the wood dewatering process. The carbon data (Fig. 2 top right) served as a control for the pressure and measurement of the change of CO₂ during the experiments.

References:

1. R. A. Franich, S. S. Gallagher, H. W. Kroese, Improvements related to wood drying. WO2008/091163 (2008).
2. V. C. Behr *et al*, Concepts Magn. Reson. 43B (2013) 49-58.

Eddy currents reduction for an accessible mobile magnet

R. Kartäusch^a, D. Oppelt^b, T. Drießle^c, M. Ledwig^c, S. Wintzheimer^c, P. M. Jakob^{ab}, F. Fidler^a

^aResearch Center for Magnetic Resonance Bavaria e.V. Würzburg, Germany

^bDepartment of Experimental Physics 5, University Würzburg, Würzburg Germany

^cPure Devices GmbH, Würzburg Germany

Introduction An accessible mobile magnet offers the opportunity to measure plants in its natural surroundings. Conventional mobile magnets use iron pole shoes to increase the homogeneity of the static magnet field. Changing a magnet field gradient close to a conducting material induces eddy currents. We build a C-shaped magnet with non conducting pole shoes to minimize eddy currents.

Material/Methods

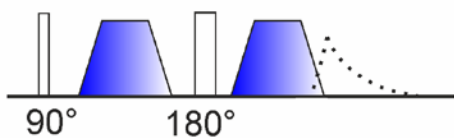


Fig. 1 Sketch of the SE sequence where a bpg (colored trapeze) is added to qualify the eddy currents.

The proposed magnet has been built with pole shoes made from non conducting ferrite materials. The C-shaped magnet has a gap of 20 mm delivering 0.42 T. The ferrite materials has a thickness of 10 mm. Additionally, an identical magnet with conventional pole shoes has been built. The magnets were equipped with a 3D gradient system and a foldable accessible coil. Eddy currents were measured by a SE sequence with bipolar gradient (bpg) (150 mT/m, ramp 100 μ s and 2 x 1 ms length) shown in Fig 1a. Repeating the measurement shows the influence of the remanence of the pole shoe on the gradients. A measurement without a bpg is acquired for comparison.

Results The eddy current reduction of the proposed magnet (Fig 2a) is a factor 24 compared with a conventional magnet (Fig 2b). The average percentage deviation between the signals with/without the bpg is 1.3% (ferrite) and 31% (iron).

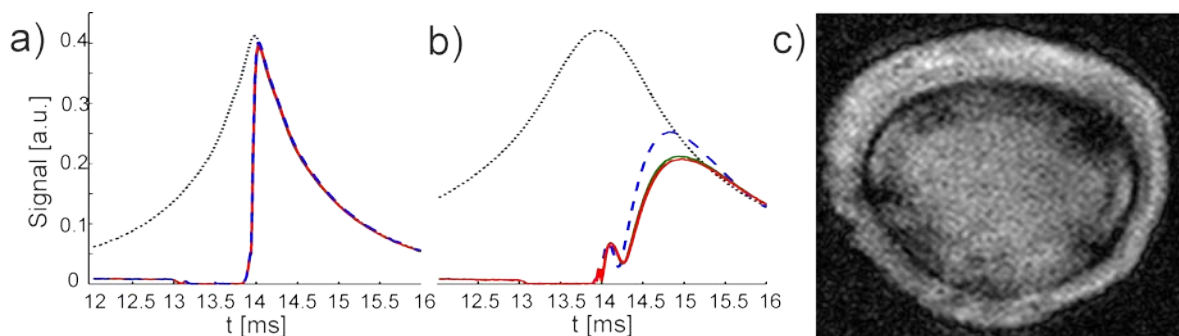


Fig. 2 a) Results of the SE measurement shown in Fig. 1a. The blue dashed line indicates the first measurement with the BPG, the straight red line shows the second and the black dotted line a measurement without a bpg. b) The same measurements for the magnet with iron pole shoes yields a strong influence of the eddy currents. c) Result of a TSE measurement of a tomato stem (10x10x3mm; 128x90; TF 30; TE 88 ms; measurement time: 5 min)

The eddy current reduction allows to use fast Turbo Spin Echo (TSE) sequences. Exemplary this is demonstrated on a tomato stem (Fig 2c).

Conclusion With the proposed system consisting of this accessible magnet fast high resolution imaging is demonstrated to be possible in vivo in plants. The virtually eddy current free magnet system allows to increase the effective gap size by removing the necessity of active shielded gradients for fast imaging sequences like TSE.

Combining NMR log and other logs evaluate shale formation

Dongliang Liao, Lizhi Xiao, Guangzhi Liao, Xin Li, Feng Deng, Xiaoling Zhang

State Key Laboratory of Petroleum Resources and Prospecting, China University of Petroleum, Beijing 102249, China

Formation porosity usually estimated by three-porosity logging curve or NMR log method. Due to the influence of TOC content and gas content, really porosity is difficult to calculate with three-porosity logging method in shale formations. The resistivity of shale formation not only effect by mineral and pore structure, also effect by TOC and gas content. Currently, there is no effective gas saturation interpretation model with resistivity log data in shale reservoir. Nuclear magnetic resonance core analysis is also difficult to estimate shale gas content accurately, due to the decreasing of the adsorption gas content as pressure reducing when the shale rock sample take from bottom to ground. Therefore shale formation must be evaluated in conjunction with multiple logs data¹.

NMR signal from shale formation is more sensitively effected factors by small pore size and kerogen in small pores compare to conventional formation. Molecular motion is restricted as restriction of geometric. Surface relaxation is enhanced as the existing of kerogen. Both of them decrease the NMR signals in shale formations. Pressure measurement in the laboratory can accurately measure shale formation porosity and fluid signal through a comparative study (T_2 -D) two-dimensional of NMR core experiments and NMR log example of shale formations, which shows the 2D-NMR log results would have corrected by experimental results² and the NMR logging data accurate evaluation formation porosity and bound fluid volume.

Well-logging responses are efficient comprehensive reflects of formation minerals, fluids and pore structures. Rock mineral types and content can be derived from ECS logs by using an optimized inversion algorithm which builds nonlinear weighted least squares objective function and combines one- and multi-dimensional search method³. Total porosity, effective porosity can be derived from NMR log. By combining of ECS, NMR and conventional logs (compensated sonic, compensated neutron, litho-density and resistivity), shale gas formation petrophysical parameters such as rock mineral volume, kerogen volume and saturation can be derived from similar inversion algorithm. Finally, permeability, free gas and absorbed gas volume can be evaluated with calibration of rock data.

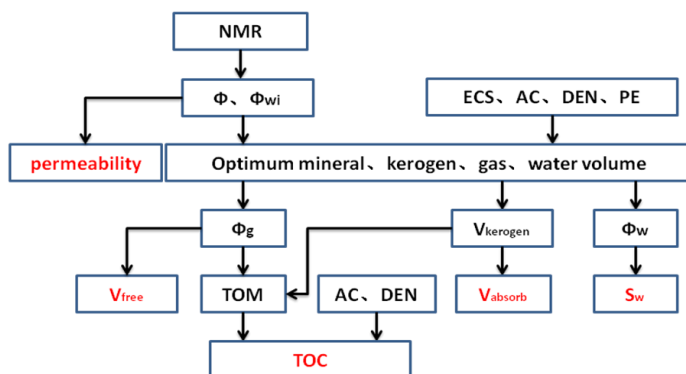


Fig.1 Flow chart of shale formation evaluation

Combining NMR log and other logs data

Φ: porosity

Φwi: bound fluid porosity

Φg: gas porosity

Vkerogen: Kerogen volume

Φw: water porosity

Vfree: Free gas volume

Vabsorb: Absorb gas volume

References:

1. John Quirein, Jim witkowsky, David Spain, et al. SPE Journal, 2010, September, 19-22
2. Cao Minh, C., Crary S., Zielinski L., et al. SPE Journal, 30 October-1 November 2012.
3. Yong S H. Dongying: University Of Petroleum Press,1995.

Noise reduction for an accessible mobile magnet

R. Kartäusch^a, D. Oppelt^b, T. Drießle^c, M. Ledwig^c, S. Wintzheimer^c, P. M. Jakob^{ab}, F. Fidler^a

^aResearch Center for Magnetic Resonance Bavaria e.V. Würzburg, Germany

^bDepartment of Experimental Physics 5, University Würzburg, Würzburg Germany

^cPure Devices GmbH, Würzburg Germany

Introduction An accessible mobile magnet offers the opportunity to measure plants in its natural surroundings. The main noise source in plant imaging is noise induced by the plant which typically acts like an antenna. Building an rf-shield around the plant is not always possible, we propose a novel gradiometer design with common mode rejection which cancel out the noise.

Material/Methods The proposed receiver coil is an accessible gradiometer coil. A specially designed symmetric tune and match network in combination with a high frequency transformer allows to suppress common mode signals in the gradiometer (Fig 1a). This common mode signals are induced by noise currents by the plant itself which transports noise from outside of the Faraday shield into the coil (Fig 1b). In contrast to this the MR-signal generates a voltage only in its corresponding coil segment. The noise cancelation is characterized by a snr measurement on a MR-phantom with an additional inserted antenna which is reproducible mimicking the plant. The snr has been measured with a SE sequence.

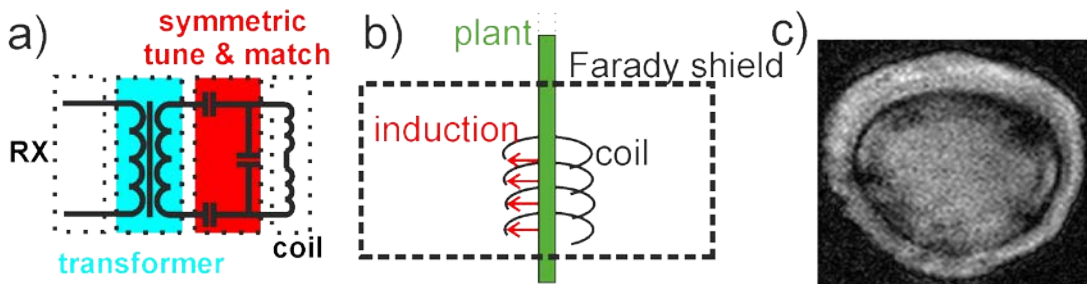


Fig. 1 a) Sketch of the SE sequence where a bpg (colored trapeze) is added to characterize the eddy currents. b) The plant acts like an antenna and induces the same noise level to the coil segments. c) The tuning circuit of the receive & transmit coil is drawn. The transformer and the symmetric tune cause a common-mode rejection.

Results The common mode rejection receiver coil compared with the coil without common mode rejection reduces the noise by a factor of 13 (Tab 1). The rejection nearly removes the complete noise induced by the antenna, the increase of the noise is approximately 17% in comparison to 1560%. With the proposed low noise receive system fast and high resolution imaging was possible with an accessible mobile MR system. Exemplary this is demonstrated on a tomato stem (Fig 1c).

Common mode rejection	SNR	Signal [a.u.]	Noise [a.u.]	Antenna inserted in phantom
No	$5.86 \cdot 10^5$	0.34	$0.58 \cdot 10^{-6}$	No
No	$0.36 \cdot 10^5$	0.33	$9.07 \cdot 10^{-6}$	Yes
Yes	$6.16 \cdot 10^5$	0.36	$0.58 \cdot 10^{-6}$	No
Yes	$5.06 \cdot 10^5$	0.34	$0.68 \cdot 10^{-6}$	Yes

Tab 1. SNR measurements with several configuration of the proposed receiver system demonstrating the operation of the common mode rejection.

Conclusion With the proposed noise rejection system fast high resolution imaging is demonstrated to be possible in vivo in plants. The noise cancelation strongly reduces the need for an rf-shield surrounding the plant. The high snr of the common rejection receive system allows acquiring high resolution images in reasonable time for in vivo plant imaging.

PFG NMR studies of CO₂ in metal-organic framework structures

*M. Lutecki^a, J. Canivet^b, C. Nieto^c, J. Perez Pelletero^d, N. Bats^c, M. Mantle^a, D. Farrusseng^b,
L. Gladden^a*

^a Department of Chemical Engineering and Biotechnology, Cambridge, UK, ^bIRCELYON, CNRS, Lyon, France ^cIFP, Physics and Analysis division, Solaize, France, ^dIFP, New Energy, Thermodynamic and Molecular Simulation Department, Rueil-Malmaison, France

Discovery of Metal-Organic Frameworks initiated a whole area of research dedicated to uncover promising applications for these materials. Due to their unique ordered hybrid organic-inorganic structure, presence of metal centres and high surface areas, MOFs soon were declared one of the most promising materials in the field of catalysis, gas storage and separation¹. Among those applications, CO₂ separation and capturing receives deserved attention, due to ever more restrictive regulations regarding emissions of greenhouse gases. Recently, the new solid, belonging to the class of ZIF materials (Zeolitic Imidazolate Frameworks) was synthesized and termed as SIM-1 (Substituted Imidazolate Material)². It is isostructural to ZIF-8; however, it has no group in position 2 of the imidazolate linkers, whereas it contains a methyl and an aldehyde in position 4 and 5. Subsequent permeation experiments showed that unlike ZIF-8, SIM-1 may be a promising candidate for CO₂ capture and separation from the gas fluxes³.

Herein, we report the results of PFG NMR experiments of CO₂ self-diffusing in both investigated structures. The measurements were carried out with four different samples, i.e., ZIF-8 (crystal size of ca. 5 μm), ZIF-8 (crystal size of ca. 50 μm), SIM-1 (crystal size of ca. 5 μm) and SIM-1 (extrudates). In order to measure the effective intracrystalline diffusion coefficient in porous media, a sufficiently big crystals needs to be investigated. The presence of intracrystalline component will depend on so called mean root square displacement $MSD = \sqrt{2D\Delta}$, where D is the diffusion coefficient and Δ is the diffusion time. The measurements were carried out at 20, 40 and 60 °C and with Pulsed Gradient Stimulated Echo (PGSTE) sequence for data acquisition.

In the case of MOFs with the crystal size of 5 μm, only intercrystalline diffusion (10^{-7} m²/s) was observed, as mean root square displacement is greater than the size of the crystals. With the larger crystals and extrudates it was possible to observe intracrystalline diffusion of CO₂ within both structures. The results showed that self diffusion coefficient of CO₂ over SIM-1 is about an order of magnitude lower than over ZIF-8 (10^{-11} vs. 10^{-10} m²/s) confirming stronger interactions of CO₂ with SIM-1 derived from adsorption experiments³. Calculated activation energies for diffusion were 5.2 and 15.4 kJ/mol for ZIF-8 and SIM-1 material, respectively. In the future, force field calculations will be conducted to compare the experimental and simulation results.

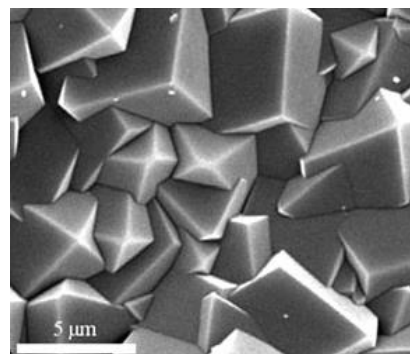


Fig. 1: SEM image of the surface of SIM-1 membrane.

References:

1. Metal-Organic Frameworks – Applications from Catalysis to Gas Storage, Wiley-VCH, 2011.
2. S. Aguado, J. Canivet, D. Farrusseng Chem. Commun 46 (2010) 7999
3. S. Aguado, C.-H. Nicolas, V. Moizan-Baslé, C. Nieto, H. Amrouche, N. Bats, N. Audebrand, D. Farrusseng New J. Chem. 35 (2011) 41.

Determining the role of grain roughness on evaporation from porous media with MRI

B. MacMillan^a, N. Shokri^b, and B.J. Balcom^a

^aMRI Research Centre, Department of Physics, University of New Brunswick, New Brunswick, Canada, ^bSchool of Chemical Engineering and Analytical Science, University of Manchester, Manchester, UK

The evaporation of absorbed fluids from porous materials is a critical phenomenon in many industrial and environmental applications, most notably the drying of food, wood, papers, and building materials, but also, on a larger scale, evaporation from land surfaces.

Such evaporation is a complex, often multi-stage, process. The drying of porous media is influenced by a variety of parameters including the distribution of pore sizes, the wettability of the grains, the structure and permeability of the porous media, atmospheric conditions, and the properties of the absorbed fluids.

The objective of this study was to investigate the effects of the shape, roughness and irregularities of the grains on the evaporation process from porous media. We tracked the moisture content in sand and glass beads with the Double Half-k (DHK) SPRITE imaging sequence¹ as water evaporated. These two particles share similar particle size distributions and average particle sizes but differ in surface roughness and grains shapes. Moisture content maps, e.g. figure 1, indicate marked differences in the respective evaporation processes.

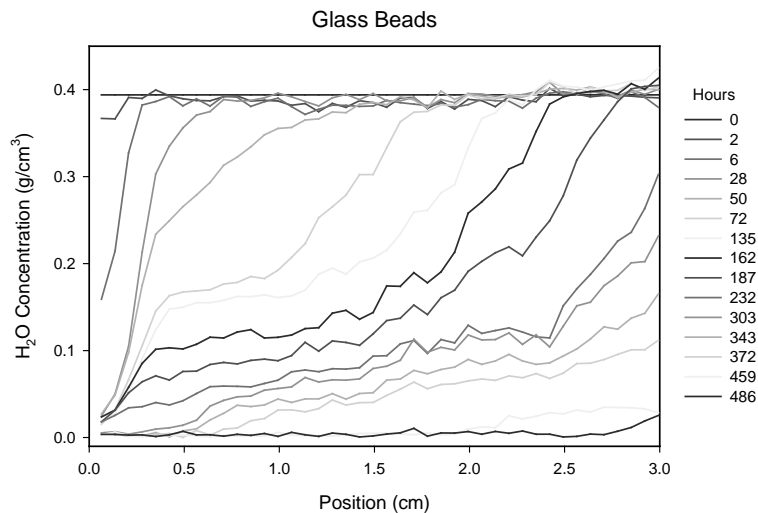


Fig. 1: Water content distribution during evaporation from glass beads. The legend indicates the elapsed time from the onset of the experiment.

References:

1. K. Deka, M.B. MacMillan, A.V. Ouriadov, I.V. Mastikhin, J.J. Young, P.M. Glover, G.R. Ziegler and B.J. Balcom, *J. Magn. Reson.* 178 (2006) 25.

Monitoring the drying stages of a porous medium by MRI and unilateral NMR

S. Merz^a, A. Pohlmeier^a, J. Vanderborgh^a, D. van Dusschoten^b, and H. Vereecken^a

^a Forschungszentrum Juelich, Institute of Bio- and Geosciences, Agrosphere Institute (IBG-3), Germany

^b Forschungszentrum Juelich, Institute of Bio- and Geosciences, Plant Sciences (IBG-2), Germany

Evaporation is a crucial process controlling water balance at the soil-atmosphere interface and can typically be divided into two stages. An initial regime (stage I) characterized by a high and constant evaporation rate, which is limited primarily by ambient conditions and where the evaporation front is at the porous medium surface. Below a critical water content capillary continuity to the surface ceases marking the onset of stage II. A new drying regime with lower evaporation rate arises and water transport is controlled by vapor diffusion in the porous medium through an increasing dry surface layer which constitutes an effective barrier for further evaporation [Shokri and Or, 2011]. Detailed understanding of conditions controlling the formation as well as the prediction of water transport through the dry layer are promoted by coupling theoretical considerations with experimental observations which requires a high resolution, non-invasive imaging technique. Our final goal is to investigate vertical profiles of moisture changes in the field by unilateral NMR, where the main challenge are the inherent fast T_2 times of natural soil matrices. Here, we present a laboratory study using a sand column under increasing drying conditions. The column was imaged by conventional MRI in a 4.7T vertical bore high field scanner by means of spin echo (SEMS) and single point imaging (SPI3D). Additionally, CPMG measurements were performed to monitor the T_2 distribution function over time. In parallel 1D moisture profiles were monitored by an open unilateral sensor (NMR-MOUSE) operating at 13.4 MHz resonance frequency using CPMG detection with $t_E = 0.1$ ms, $N_E = 1536$ and $N_S = 256$ with a step size of 2 mm for 9 steps (18 mm max. depth). Secondly, we compared and cross-validated MRI and unilateral sensor measurements using a soil physical model of coupled liquid and vapor phase flow as well as an analytical approach (Fig. 1). All methods could monitor uniformly decreasing moisture over a period of 47 days until the onset of stage II. Thereafter, a dry surface layer developed and a heterogeneous drying front receded into the soil as predicted by the theory. With the spin-echo method part of the MRI signal was decayed already during the first echo period but nevertheless, SEMS and 1D profiles agreed satisfactorily. It is remarkable that the onset of stage II coincided with the vanishing of the slowly decaying mode in the T_2 relaxation time distribution functions at about 200 ms which indicates that indeed the capillary continuity to the surface ceases at this point. Summarizing, we found that the unilateral NMR sensor is useful for detection of such processes in larger laboratory setups and shows promising potential for application in the field.

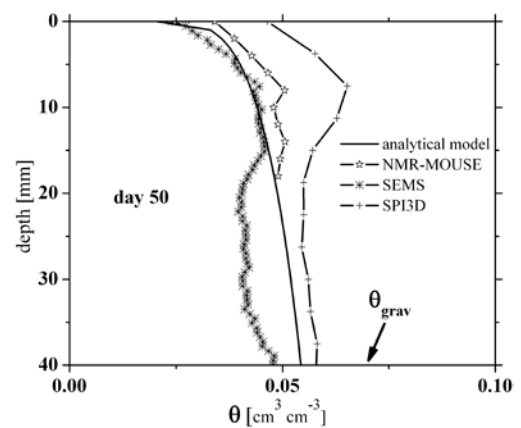


Fig.1: MRI and NMR MOUSE moisture profiles after 50 days, where the arrow represents the gravimetric water content of the complete column. The full line is the simulated result using the analytical approach at the end of stage I [Moghadas et al., 2013].

References:

1. Moghadas, D., K. Z. Jadoon, J. Vanderborgh, S. Lambot, and H. Vereecken (2013), Effects of Near Surface Soil Moisture Profiles During Evaporation on Far-Field Ground-Penetrating Radar Data: A Numerical Study, *Vadose Zone J.*, 1-11.
2. Shokri, N., and D. Or (2011), What determines drying rates at the onset of diffusion controlled stage-2 evaporation from porous media?, *Water Resour. Res.*, 47(9), W09513.

PFG-NMR Study of Tortuosity in Silicon Electrodes*Alison L Michan^a, Michal Leskes^a, Andy Sederman^b, Lynn Gladden^b and Clare P Grey^a*^aDepartment of Chemistry, University of Cambridge, UK, ^bDepartment of Chemical Engineering and Biotechnology, University of Cambridge, UK

Energy storage is critical for modern life and batteries are one method to store energy. Improvements in the form of increased safety, reduced cost, increased energy and power density, and longer life, would all benefit this technology and the average user. Performance of batteries is largely derived from the materials making up the battery and this study focuses on silicon composite electrode materials for use in lithium-ion batteries. These materials offer an improved energy density over traditional graphite electrodes. During electrochemical cycling, lithium ions diffuse through the electrolyte and pores of the silicon electrode. The size and distribution of the pores determines the ionic path through the electrode material. By measuring diffusion coefficients of nuclei contained in the electrolyte, the microstructure of the electrode can be probed. In our study we investigate the electrode microstructure accessible to the electrolyte using pulsed-field gradient nuclear magnetic resonance (PFG-NMR). The proton self-diffusion coefficients of DMC (dimethyl carbonate) saturated electrodes are compared with that of the free electrolyte and an apparent tortuosity is determined. During the process of repeated cycling, the tortuosity of the electrode is thought to increase in some systems as a result of decomposition products forming on the surfaces of the electrode. We expect the ionic transport, tortuosity, and electrode porosity, can be related to ageing mechanisms and can be probed using PFG-NMR.

Spatial resolution in low-field studies of oil recovery

J. Mitchell^{a,b}, J. Staniland^b, E.J. Fordham^b

^a Department of Chemical Engineering and Biotechnology, University of Cambridge, Cambridge CB2 3RA, UK

^b Schlumberger Gould Research, High Cross, Madingley Road, Cambridge CB3 0EL, UK

Magnetic resonance imaging (MRI) has been used extensively to elucidate displacement processes in porous media, such as oil recovery from reservoir rocks [1]. However, many of these imaging experiments were conducted on superconducting imaging magnets typically used for biomedical studies and operating at field strengths $B_0 > 1$ T. In petrophysics applications, low-field magnets operating at $B_0 = 50$ mT or less are routinely employed to provide (a) comparable experimental conditions to magnetic resonance well logging tools and (b) minimize the effects of magnetic susceptibility induced internal gradients that invalidate the archetypal T_2 measurement as an indicator of pore size or chemical (oil/brine) composition [2]. These low-field magnets have been used for laboratory characterization of bulk core-plug properties (porosity, saturation) for many years. However, the inherent poor signal-to-noise ratio (SNR) has traditionally ensured imaging experiments were prohibitively time consuming.

Developments in digital spectrometer design have enabled one-dimensional (1D) image profiles to be obtained on low-field systems with sufficient SNR per pixel to be useful. We have used a conventional multi-echo frequency encoded profiling pulse sequence [3] to obtain rapid T_2 maps from small core-plugs during the forced displacement of oil, enabling improved studies of enhanced oil recovery (EOR) chemical agents [4]. Example results from a brine and alkaline surfactant (AS) flood are shown in Fig. 1. The spatial information is critical in displacement studies employing short core-plugs (50 mm length) in order to obtain accurate oil saturations without the influence of end effects that would dominate bulk measurements in such samples. The inclusion of the T_2 dimension enables quantitative determination of both the oil and brine saturations from a single measurement.

By increasing the magnet field strength we retain the advantage of low-field for rock studies but are able to introduce sophisticated imaging protocols for fast 3D visualization of oil displacement due to the significant improvement in SNR. We will show some preliminary results indicative of the core-plug images available at slightly higher field strength.

References:

1. J. Mitchell et al., Magnetic resonance imaging in laboratory petrophysical core analysis, *Phys. Rep.* 526 (2013) 165.
2. J. Mitchell et al., Nuclear magnetic resonance relaxation and diffusion in the presence of internal gradients: the effect of magnetic field strength, *Phys. Rev. E* 81 (2010) 026101.
3. P. Majors et al., NMR imaging of immiscible displacements in porous media, *SPE Form. Eval.* (1997) 164.
4. J. Mitchell et al., Quantitative in situ enhanced oil recovery monitoring using nuclear magnetic resonance, *Transp. Porous Med.* 94 (2012) 683.

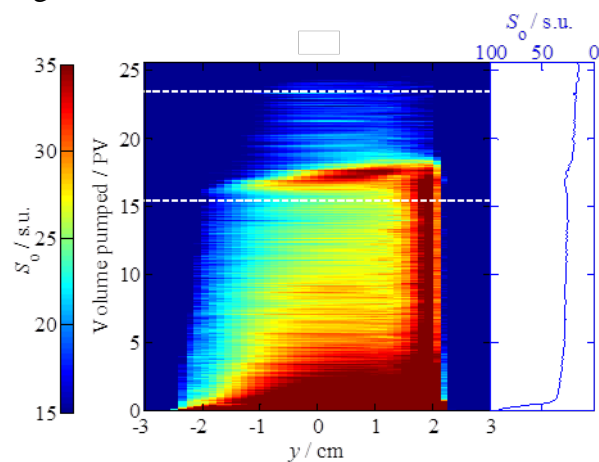


Fig. 1: Spatially resolved oil saturations in a limestone plug during forced displacement with brine and alkaline surfactant (between white dotted lines). Flow occurred from left to right at a realistic reservoir rate of 1 foot/day. The inlet face of the plug is at $y = -2.5$ cm and the outlet face is at $y = 2.5$ cm. Oil is trapped at the outlet face due to capillarity. On inject of AS solution, oil swept is forced through the rock causing the local saturation to increase in an “oil bank”. The AS solution is able to remove the oil trapped at the outlet and provides improved oil recovery compared to the brine flood.

PGSE pore microscopy

A. Mohoric^a, J. Stepišnik^{a,b}, B. Fritzing^c, U. Scheler^c

^aUniversity of Ljubljana, Slovenia, ^bJozef Stefan Institute, Slovenia, ^cLeibniz-Institut für Polymerforschung Dresden, Germany

Pulsed gradient spin echo¹ (PGSE) provides information about the size distribution of nanopores. This is demonstrated on a system of water trapped in a porous poly(amide)-6 (PA-6) membrane². Using the PGSE sequence with fixed gradient pulse width, but variable interval between pulses and by increasing the magnetic field gradient from zero to 11.6 T/m, we observed spin echo decay with small undulations. These “diffraction” patterns demonstrate the uselessness of the inverse-Laplace transform method to extract the pore size distribution.

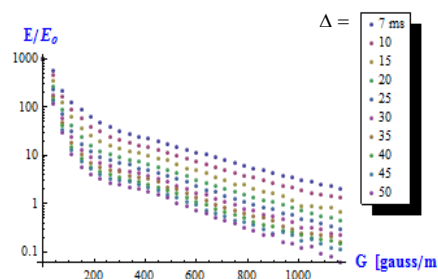


Fig. 1: PGSE of porous polyamide membrane soaked in water as a function of gradient measured at different diffusion times.

The diffusion propagator can be calculated by fitting normal distributions to q -space cosine Fourier transform of experimental data:

$$FT[E(q)](z) \approx \sum_p N_p \frac{1}{\sqrt{2\pi M_{2p}}} e^{-\frac{z^2}{2M_{2p}} \frac{\Delta + \delta}{T_{1p}}}$$

Second moments of the fitted normal distributions remain the same even if the interval between gradient pulses is changed. This is an indication of motion-narrowing regime, in which the second moments of propagators are proportional to the fourth power of pore sizes. In this way the pore size distribution is determined.

3-D plot in Fig. 2 shows the pore distribution as a function of the spin-relaxation and the pore radius, in which the share of spins in the pores with the radius (100 ± 10) nm (70%) prevails and pores with the radius (175 ± 30) nm are less abundant (20%). Water in these two types has identical spin relaxation $T_2 = (10 \pm 2)$ ms. Water in the pores with the radius of (282 ± 7) nm (5%) has a broader distribution of relaxation times, $T_2 = (14 \pm 5)$ ms.

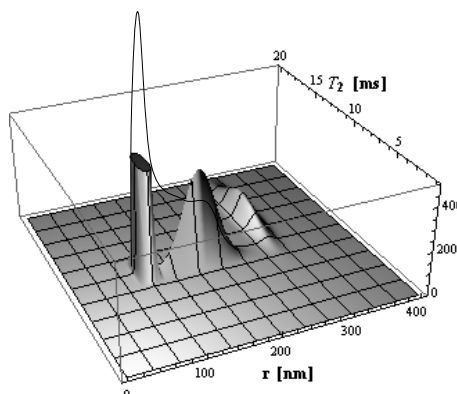


Fig. 2: The distribution of pores in a PA-6 membrane together with corresponding relaxation times.

References:

1. E. O. Stejskal and J. E. Tanner, J. Chem. Phys., 42 (1965) 288.
2. J. Meier-Haack, W. Lenk, S. Berwald, T. Rieser and K. Lunkwitz, Sep. Purif. Technol., 19 (2000) 199.
3. J. Stepišnik, Physica B 104 (1981) 350–64.
4. P.T. Callaghan, J. Stepišnik. Advances in Magnetic and Optical Resonance ed. Waren S. Waren, Vol. 19, p. 324-397, (1996), Academic Press.
5. J. Stepišnik, B. Fritzing, U. Scheler and A. Mohorič, EPL, 98 (2012) 57009.

Application of magnetic resonance velocimetry to investigate the transport phenomena of gas flow in a Diesel Particulate Filter

N.P. Ramskill^a, L.F. Gladden^a, A.P.E. York^b, A.J. Sederman^a

^a Department of Chemical Engineering and Biotechnology, University of Cambridge, UK

^b Johnson Matthey Technology Centre, Blounts Court, Sonning Common, UK

Internal combustion engines, whether they use petrol or diesel fuel, produce a number of species harmful to health and the environment. This work will focus on Diesel Particulate Filters (DPFs) which have been developed for the abatement of emissions from diesel engines. Within the present study magnetic resonance imaging (MRI) velocimetry has been used to non-invasively investigate the transport of the exhaust gas in DPFs. To date, the majority of the work on the fluid mechanics in DPFs has been computational modelling which has demonstrated that gas flow through the DPF will influence soot deposition within it. In turn, the soot deposition profile within the DPF channels has been shown to have a significant effect on the filter performance in terms of filtration efficiency, pressure drop and regeneration [1,2]. The data obtained from MRI velocimetry measurements will be used to enhance the understanding of transport phenomena in DPFs and validate the results of computational modelling.

Imaging of gases using MR techniques is challenging due to their low molecular density, typically three orders of magnitude lower than that of most liquids. In the present work, sulphur hexafluoride (SF_6) has been used as the NMR active gas as it has been shown that relative to other NMR active gases, SF_6 has properties that make it amenable to imaging such as high molecular density, high magnetogyric ratio, low self-diffusion coefficient and six ^{19}F atoms per molecule [3].

Images of the axial velocity component (v_z) have been acquired at different positions along the length of the DPF channel and a selection of images at four axial positions (P1-P4) along the length of the filter is shown below in Figure 1.

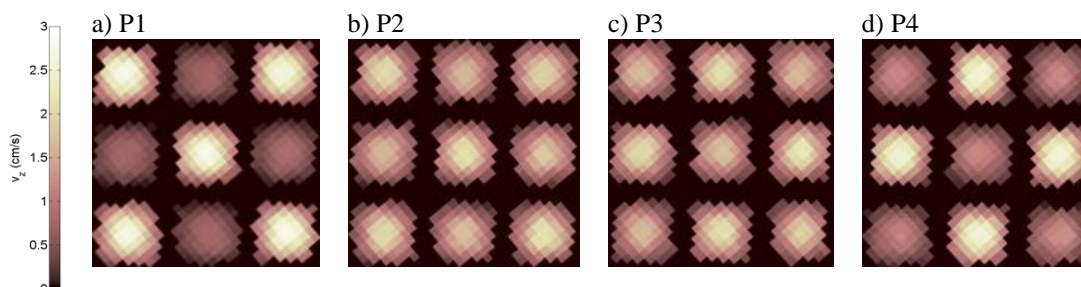


Fig. 1: Axial velocity (v_z) images acquired at different positions (P1-P4) along the length of the filter. The field of view in the read and phase directions was 18 mm and for a 128×128 matrix, the in-plane resolution was 0.14 mm/pixel in both directions. Inlet and outlet channels of the filter correspond to the high and low velocity regions in a) respectively.

Figure 1 shows that as the gas is forced through the permeable wall separating the inlet and outlet channels, the velocity in the former is reduced whilst, at the same time, increasing in the latter. Further analysis of the transport phenomena on the channel scale has been conducted in order to develop the understanding of how the gas flow fields within the filter influence the soot deposition profile along the length of the filter channel. These results will be presented with the poster.

References:

1. F. Piscaglia, A. Montorfano, A. Onorati, *Math. Comput. Model.* 52 (2010) 1133.
2. S. Bensaid, D. L. Marchisio, D. Fino, *Chem. Eng. Sci.* 65 (2010) 357.
3. M.H. Sankey, D.J. Holland, A.J. Sederman, L.F. Gladden, *J. Mag. Res.* 196 (2009) 142.

Spectroscopic dimension in MRI of materials with ultra short transverse relaxation times

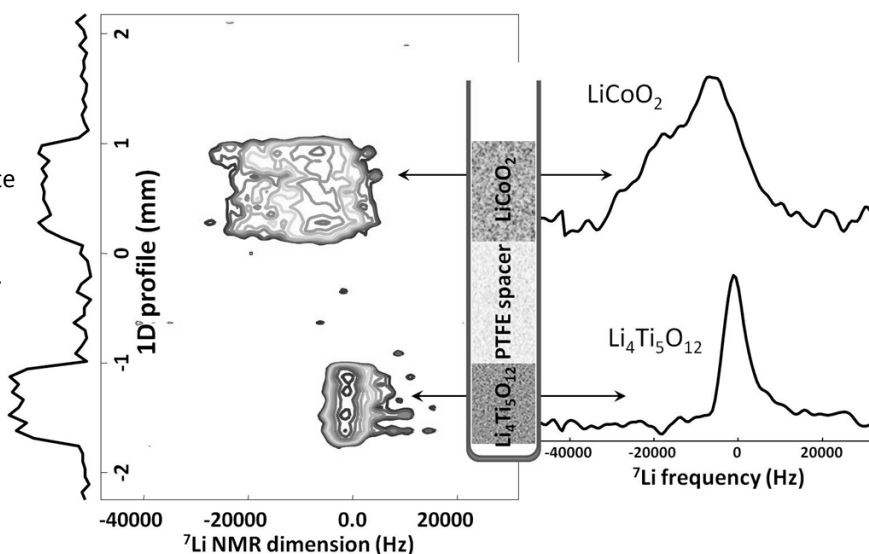
V. Sarou-Kanian^{a,b}, D. Massiot^{a,b}, C. Bessada^{a,b}

^a CNRS, UPR3079 CEMHTI, 1D av. de la Recherche Scientifique, 45071 Orléans, France

^b Université d'Orléans, Faculté des Sciences, av. du Parc Floral, BP 6749, 45067 Orléans, France

Magnetic resonance imaging of solid materials suffers from sensitivity and resolution losses because of anisotropic interactions (chemical shift, dipolar, quadrupolar) which may significantly broaden the line widths and affect the line shapes. This causes really short transverse relaxation times (T_2 or $T_2^* < \text{few hundreds of } \mu\text{s}$), such that classical MRI sequences using gradient and/or spin echoes become inefficient. To overcome this hindrance, numerous strategies has been proposed based on line-narrowing methods (multiple pulses¹, magic angle spinning²) and/or or using large gradient strengths (strong PFG³, stray field⁴). One of the most popular classes of MRI sequences dedicated to ultra short relaxation times is the single point imaging (SPI, also called constant time imaging), the general concept of which consists to sample the k-space by acquiring one single point with a pure phase encoding⁵. While images with relaxation contrasts (T_1 , T_2 , T_2^*) have been already obtained using SPI⁶, no investigation has been performed to correlate the image of a solid material with its spectroscopic dimension as it can be commonly seen for *in vivo* MRI (e.g. PRESS, STEAM). Here we propose a new SPI sequence allowing to increase the dimensionality of an image with its solid state NMR spectrum. 1D images of phantoms of solid materials with ultra short T_2^* caused by various interactions (chemical shift anisotropy, dipolar coupling...) and for different nuclei are presented.

Fig. 1: ^7Li 1D profile of lithium titanate and lithium cobalt oxide powders separated by a 1 mm PTFE spacer correlated with their NMR spectrum. Line widths and line positions give supplementary information on the chemical nature of the object.



References:

1. A. N.Garroway, J. Baum, M.G. Munowitz and A. Pines, J. Magn. Res. 60 (1984) 337.
2. D.G. Cory and W.S. Veeman, J. Phys. E 22 (1989) 180.
3. B.J. Balcom, R.P. Macgregor, S.D. Beyea, D.P. Green, R.L. Armstrong and T.W. Bremner, J. Magn. Res. A 123 (1996) 131.
4. J.A. Tang, G. Zhong, S. Dugar, J.A. Kitchen, Y. Yang and R. Fu, J. Magn. Res. 225 (2012) 93.
5. S. Emid and J.H.N. Creyghton, Physica B+C 128 (1985) 81.
6. S.D. Beyea, B.J. Balcom, P.J. Prado, A.R. Cross, C.B. Kennedy, R.L. Armstrong and T.W. Bremner, J. Magn. Res. 135 (1998) 156.

Using spatial resolution to enhance MR data interpretation of transport processes during gelation

Joseph D. Seymour^{a,b}, Matthew L. Sherick^{a,b}, Joshua M. Bray^c, Sarah J. Vogt^{a,d}, Varsha V. Rao^{a,b}, Jennifer R. Brown^a, Sarah L. Codd^{b,c}

^aDepartment of Chemical and Biological Engineering, Montana State University, Bozeman MT U.S.A., ^bCenter for Biofilm Engineering, Montana State University, Bozeman MT U.S.A.,

^cDepartment of Mechanical and Industrial Engineering, Montana State University, Bozeman MT U.S.A., ^dSchool of Mechanical and Chemical Engineering, University of Western Australia, Crawley, WA, Australia

Gelation processes have been studied rather extensively by magnetic resonance methods¹⁻⁴. Recently the formation of mesoscopic structures such as oriented capillaries⁴ have been investigated in greater detail using combinations of spatially and non-spatially resolved MR methods^{5,6}. These structures are of interest from the perspective of a fundamental understanding of the chemical physics of spontaneous structure formation and for applications in biotechnology and biomedicine such as tissue engineering⁷. MR measurement of the molecular dynamics during the gelation reaction provides unique data for characterizing mass transport during the structure formation in terms of phase transition thermodynamics such as spinodal decomposition⁸ and the diffusive versus convective dynamics of the reaction diffusion front⁹. The role of the biomolecular structure, such as acetylated and deacetylated forms of alginate molecules, in the formation of mesostructures and the information MR data provides on this role is considered. As an example of the type of information available from the MR data the coalescence of capillaries formed in a heterogeneous reaction-diffusion front gelation of 2% wt. algal alginate by 0.5 M CuCl₂ is shown in Fig.1. Such data can be directly compared to a modified coalescence model based on the Lifshitz-Slyozov-Wagner model for droplets¹⁰.

References:

1. K. Potter, T. A. Carpenter, L. D. Hall, *Carbohydrate Research* **1993**, 246, 43.
2. B. P. Hills, J. Godward, M. Debatty, L. Barras, C. P. Saturio, C. Ouwerx, *Magnetic Resonance in Chemistry* **2000**, 38, 719.
3. N. Nestle, R. Kimmich, *Magnetic Resonance Imaging* **1996**, 14, 905.
4. K. Potter, B. J. Balcom, T. A. Carpenter, L. D. Hall, *Carbohydrate Research* **1994**, 257, 117.
5. J.E. Maneval, D. Bernin, H.T. Fabich, J.D. Seymour and S.L. Codd, *Magnetic Resonance in Chemistry* **2011**, 49, 627.
6. H.T. Fabich, S.J. Vogt, M.L. Sherick, J.D. Seymour, J.R. Brown, M.J. Franklin and S.L. Codd, *Journal of Biotechnology* **2012**, 161 320.
7. A. Khademhosseini, J. P. Vacanti, R. Langer, *Scientific American*, **2009**, 300, 64
8. A. Onuki, S. Puri, *Physical Review E* **1999**, 59, R1331
9. N. A. Peppas, J. L. Sinclair, *Colloid and Polymer Science* **1983**, 261, 404.
10. A.J. Bray, *Advances in Physics* **2002**, 51, 481.

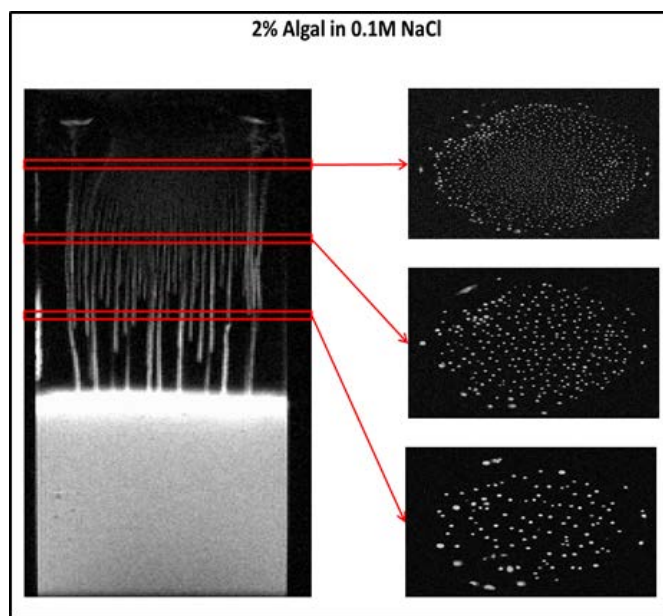


Fig. 1: MR images of 2% wt. algal alginate in 0.1M NaCl gelled by a diffusion-reaction front gelation process with 0.5M CuCl₂. Shown is a sagittal image with three corresponding axial slices. These images display capillary coalescence, as the capillaries become larger in size but fewer in number as the gel front moves downward. FOV: 20mm x 13mm (sagittal), 13mm x 13mm (axial), TE = 11 ms, Slice thickness = 0.5mm.

Spatially resolved relative permeability with simulated and experimental 1D NMR imaging

I. Shikhov, C.H. Arns

School of Petroleum Engineering, University of New South Wales, Sydney, Australia

In recent years low-field 1D MRI and NMR T_2 profiling have proven to be powerful tools of rock cores characterization. Being accompanied with centrifuge capillary drainage/imbibition experiments it is possible to significantly increase speed and improve the quality of constructed capillary curves (Chen and Balcom¹, 2005). Green², 2009 used Burdine and Brooks-Corey models to obtain relative permeability curves from capillary curves constructed with the aid of centrifugation and 1D MRI (intensity profiles).

Using a Magritek 2 MHz NMR Rock Core Analyzer and by applying RARE, a CPMG-style sequence (Rauschhuber & Hirasaki³, 2009), we attained T_2 -resolved profiles along the investigated outcrop cores. Measurements were performed on fully saturated and drained with centrifuge Mt. Gambier carbonate and Bentheimer sandstone core plugs. T_2 resolved profiles are then used to obtain log-mean T_2 values required for the SDR-based relative permeability correlation, k_r , suggested by AlGhamdi et al.⁴, 2012 (1):

$$k_{r\text{NMR}} = (S_w)^4 \cdot [T_{2\text{LM}}(S_w) / T_{2\text{LM}}(S_w=100\%)]^2 \quad (1)$$

The numerical part includes a simulation of a centrifuge capillary drainage experiment by applying corresponding morphological drainage transforms on high-resolution 3D tomograms. A random walk technique was then applied to simulate NMR T_2 responses. Distributions attained locally along the core length at 100% saturation and at a drained state are used to estimate relative permeability following equation (1).

It is well known, that low-field MRI suffers from the loss of short-time components of T_2 relaxation (up to few microseconds), while numerically we have no such a restriction. Comparison of numerically simulated and experimentally attained 1D MRI profiles enables evaluating the magnitude of this effect.

References:

1. Q. Chen and B.J. Balcom, Measurement of rock-core capillary pressure curves using a single-speed centrifuge and one-dimensional magnetic-resonance imaging, *J. Chem. Phys.*, 122 (2005), 214720.
2. D. Green, Extracting pore throat size and relative permeability from MRI based capillary pressure curves, *Int. Symp. of the Society of Core Analysts held in Noordwijk, The Netherlands, 27-30 September 2009*, SCA2009-46 (2009).
3. M. Rauschhuber and G. Hirasaki, Determination of saturation profiles via low-field NMR imaging, *Int. Symp. of the Society of Core Analysts held in Noordwijk, The Netherlands, 27-30 September 2009*, SCA2009-09 (2009).
4. T.M. AlGhamdi, C.H. Arns, and R.Y. Eyvazzadeh, Correlations between NMR relaxation response and relative permeability from tomographic reservoir rock images, *SPE Saudi Arabia Section Tech. Symp & Exhib. held in Al-Khobar, Saudi Arabia, 8-11 April 2012*, SPE160870 (2012).

The effect of swelling and annealing on the molecular mobility and phase composition of domains in Low Density Polyethylene

Y. Teymouri, R. Kwamen and B. Bluemich

Institut für Technische und Makromolekulare Chemie, RWTH Aachen University, Worringerweg 1,
D-52074 Aachen, Germany

The morphology of semi-crystalline polymers changes upon thermal annealing below the melting temperature [1]. This effect has extensively been studied by DSC and X-ray techniques [2]. When a semi-crystalline polymer is taken up by solvent, the solvent primarily enters the amorphous regions, which swell to accommodate the solvent. With time the morphology may change, for example, by solvent-induced crystallization, so that upon drying the polymer has a different nanoscopic structure. This change is essentially irreversible and has been investigated using the Flory-Huggins's model coupled with gravimetric measurements [3]. While DSC and XRD provide valuable information about crystalline domains the primary changes arise in the amorphous domains and the amorphous-crystalline interface [4] and are probed only indirectly by these methods.

In this work, the effects of swelling and thermal annealing on Low Density Polyethylene (LDPE) were investigated by transverse relaxation decays with the NMR-MOUSE in two separate experiments. First, LDPE samples were thermally annealed at 100° C and 90° C for different times. With increasing annealing the transverse magnetic relaxation times in the amorphous and interfacial phases decrease, reporting a decrease in mobility, which is accompanied by a shrinking population of these phases equivalent to increasing crystallinity. Second, LDPE samples were immersed in different organic solvents (Hexane, Toluene and Xylene) at room temperature for different swelling times and subsequently dried at room temperature until an equilibrium weight was reached. The NMR analysis showed that the chain mobility in amorphous and interfacial phases decreased due to solvent induced reordering of the polymer chains in the amorphous domains. Thus solvents and temperature effects on the morphology of semi-crystalline polymers are comparable in first order.

References:

1. C. Hedesiu, D. E. Demco, R. Kleppinger, A. Adams, B. Bluemich, K. Remerie, V. M. Litvinov, *Polymer* 48 (2007) 763-777.
2. S. Fakirov, E. W. Fischer, R. Hoffmann, G. F. Schmidt, *Polymer* 18 (1977) 1121-1129.
3. D. A. Blackadder, J. S. Keniry, *J. Appl. Polym. Sci.*, 16 (1972) 1261-1280.
4. N. Lutzow, A. Tihminlioglu, R. P. Danner, J. L. Duda, A. D. Haan, G. Warnier, J. M. Zielinski, *Polymer* 40 (1999) 2797-2803.

Motion effect in NMR well logging

S. Utsuzawa^a, C. Ryan^b, M. D. Hürlimann^b, H. Zhang^a, V. Jain^a, N. Heaton^a, and L. Zielinski^a,
^aSchlumberger Houston Formation Evaluation Center, ^bSchlumberger-Doll Research

NMR tools in the oilfield measure the relaxation times T_2 of nuclear spins in the formation, which may range from a fraction of a millisecond to several seconds. If the tool moves by a sizeable fraction of the excited slice width (which is typically of the order of 1 cm for downhole tools) during the time T_2 , the measurement of the corresponding relaxation time will be affected (Figure 1).

Figure 2 shows the example of motion effect observed during drilling operations. Two curves are the phase-corrected CPMG decay in a reaming (upper, with minimal motion effect) and drilling (lower, with significant motion effect) paths, respectively.

In this presentation, we will discuss the characteristics of the motion effect in downhole NMR applications, as well as the possible mitigation method. We will also discuss the implications for general NMR relaxometry where there is net relative displacement (other than diffusion) between the tool and the specimen.

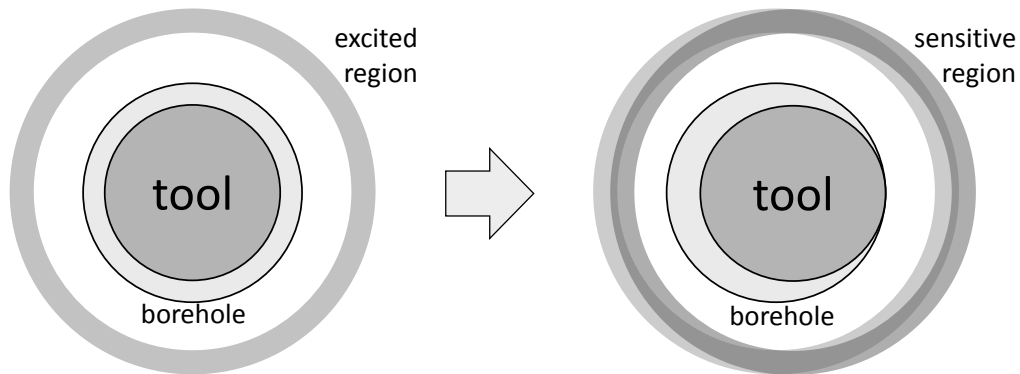


Figure 1. Lateral tool motion that causes motion effect in downhole NMR measurement.

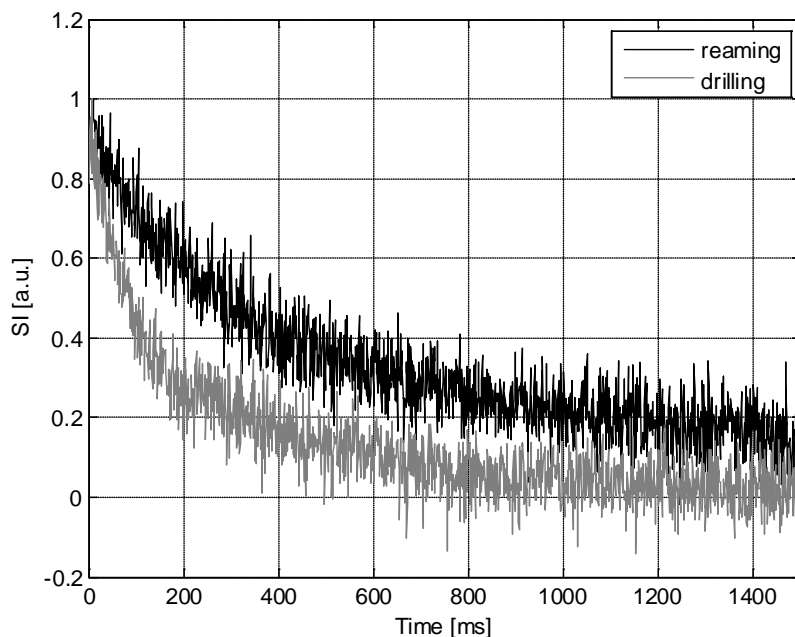


Figure 2. Example of motion effect observed during drilling operations. Two curves are the phase-corrected CPMG decay in a reaming (upper, with minimal motion effect) and drilling (lower, with significant motion effect) paths, respectively. In the drilling path, long T_2 component is distorted by severe tool motion.

Mapping of spin-density and -velocity in membranes

J. Vieß^a, D. Jaschtschuk^a, T. Fischer^b, E. Paciok^a, J.E. Wong^b, M. Wessling^b, B. Blümich^a

^aITMC, RWTH Aachen University, Aachen, Germany

^bChemical Process Engineering – AVT.CVT RWTH Aachen University, Aachen, Germany

In the last years the development of ceramic and polymeric membranes for ultra- and nanofiltration has been in the focus of research, because they can be used in a wide range, e.g. bioreactors and for desalination. However, membrane fouling is a major drawback for the lifespan of the membranes and constitutes a great challenge for membrane technologists.

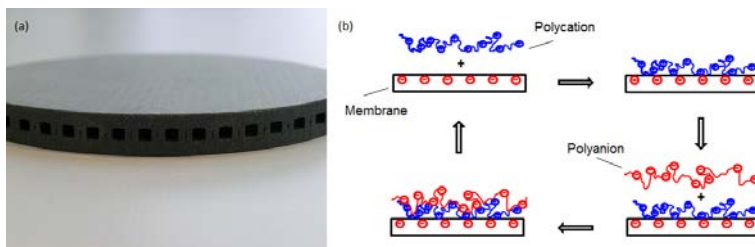


Fig. 1: (a) Virgin Silicon carbide membrane (heights: 6 mm); (b) Scheme of membrane coating, with which the membrane performance and – characteristics, such as polarity or pore size, can be tailored.

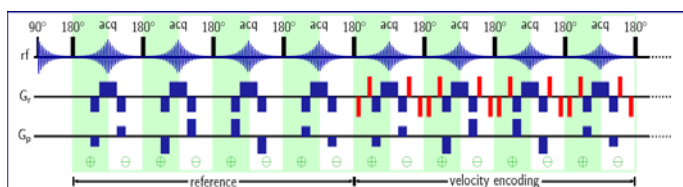


Fig. 2: FLIessen sequence; a RARE-based sequence, that allows to obtain a full 2D velocity map within one CPMG train

With *FLIessen*³ (*Flow Imaging Employing Single Shot Encoding*, Fig. 2) we analysed the spin density, the flow paths and the spin velocities in virgin and coated SiC-membranes (Fig. 1(a)) in a homemade pressure cell, when filtering pure water at different pump rates.

The results in Fig. 3 were measured on an empty pressure cell with a pump rate of 330 ml/h. Figure 3a shows a proton density map, whereas Fig. 3b shows a vector map of spin velocities.

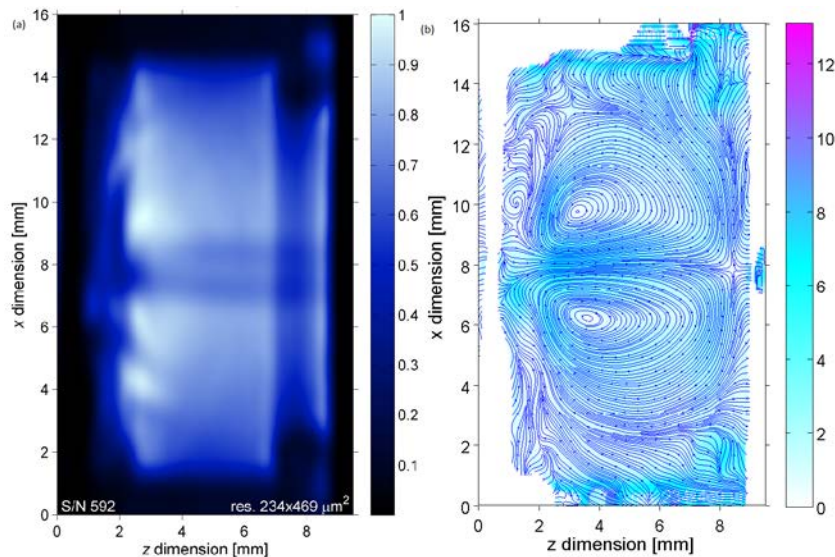


Fig. 3: Empty pressure cell when pumping water with a flux of 330 ml/h; (a) Normalized spin density map; (b) Velocity map with spin paths (both: FOV: 30 x 30 mm zoom on chamber, 128 x 64 pixels, resolution: 234 x 469 μm^2 , NS: 2, total measurement time: 8 sec.).

References:

1. G. Decher, *Science* **1997**, 277, 1232-1237.
2. T. Fischer, *Polyelectrolyte Membranes: From Microfiltration to Nanofiltration*, Aachen, Germany **2013**, not published.
3. A. Amar, B. Blümich, F. Casanova, *ChemPhysChem* **2010**, 11, 2630-2638.

Characterization of Mn doped Si nano particles designed as MRI contrast agents

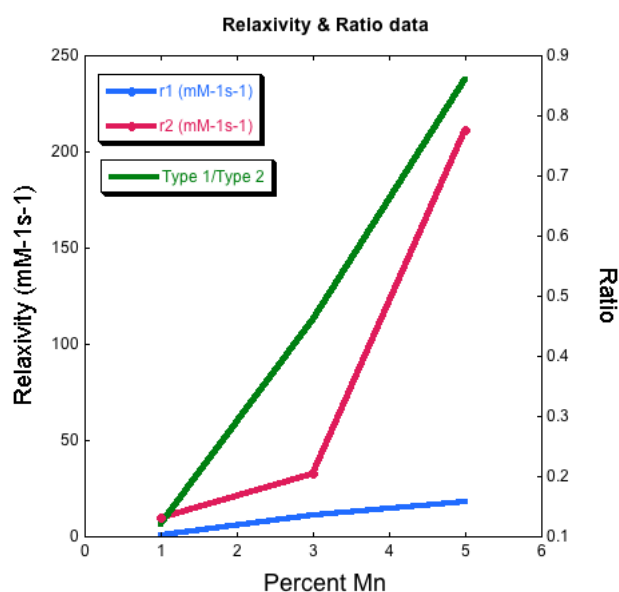
Tonya M. Atkins^a, Jeffrey H. Walton^b, Mani P. Singh^a, Oliver Janka^a, Angelique Y. Louiec, Susan M. Kauzlarich^a

^aDepartment of Chemistry, University of California, Davis California 95616, USA

^bUCD NMR Facility, University of California, Davis California 95616, USA

^cDepartment of Biomedical Engineering, University of California, Davis California 95616, USA

Water soluble poly(allylamine) manganese (Mn)-doped Si nanoparticles (SiMn NPs) have shown promise for biologically related applications. The NPs show both strong photoluminescence and the potential for magnetic resonance contrast imaging. Mn-doped Na_4Si_4 ($\text{Na}_4\text{Si}_{4-x}\text{Mn}_x$) was prepared using either Mn powder or Mn acetylacetonate ($\text{Mn}(\text{acac})_2$). $\text{Na}_4\text{Si}_{4-x}\text{Mn}_x$ prepared with $\text{Mn}(\text{acac})_2$ resulted in the highest concentrations (1, 3, and 5 percent) of Mn ($S=5/2$, $I=5/2$) in the Si NPs. Simulations of EPR spectroscopy data demonstrate that there are two types of Mn present. The ratio of type 1 to type 2 increases linearly with Mn concentration. Five percent doping also had a large amount of a spin 1/2 species that we identify as dangling Si bonds. T1 and T2 measurements vs concentration for each dopant level were measured to determine relaxivities r_1 and r_2 . Both relaxivities increase with dopant level with the r_2 dependence nonlinear and large at 5%. Possible explanations to account for the above observations include: 1) Mn preferentially occupies surface site in the nanoparticle, or 2) the dangling bonds in the 5% are sample are contributing significantly to the relaxivity. Determination will require further experiments.



Measurement of intra-particle chemical compositions in a trickle-bed reactor using an MRI-PLSR method

Q. Zheng, A. J. Sederman, L. F. Gladden

Department of chemical engineering and biotechnology, Cambridge, UK

A trickle-bed reactor (TBR) is a fixed bed reactor with liquid and gas flowing down concurrently and is widely used in chemical, petroleum and oil refining processes¹. Due to the complexity of hydrodynamics within a trickle-bed reactor, chemical compositions within the reactor distribute inhomogeneously. In addition, the mass transfer limitation between liquid inside and outside catalyst particles causes difference in the chemical compositions of inter- and intra-particle liquid. Measurement of intra-particle compositions during the process of chemical reactions within a trickle-bed reactor can provide unique information on mass transfer effects in reactors.

In this work, measurement of intra-particle chemical compositions within a trickle-bed reactor during hydrogenation of 1-octene was achieved by ¹³C chemical shift imaging (CSI) with spatial resolution along the length of the reactor (z direction). Data were acquired using a pulse sequence combining DEPT² and a phase encoding gradient along the z direction. Spectra were extracted from the CSI, to which a multivariate calibration method known as partial least squares regression (PLSR) was applied to predict the intra-particle compositions. The PLSR method has been widely employed to analyse spectroscopic data³. The PLSR method builds a relationship between the spectral data and the chemical compositions to be predicted in a compressed subspace of the original data set by extracting principal components of the original data.

MRI experiments were performed on a Bruker AV 400 spectrometer with a 9.4 T vertical magnet. A birdcage radio frequency (r.f.) coil of diameter 38 mm was used and dual-tuned for ¹H and ¹³C respectively. A glass reactor of 25 mm i.d. and 25 cm length was used for reaction experiment and was packed with 0.3 wt% Pd/Al₂O₃ catalyst (Johnson Matthey plc) to a height of 3 cm. Pure 1-octene and 50%/50% H₂ and N₂ mixture were flowed through the reactor as liquid and gas phase, respectively.

The PLSR model was tested with testing samples and the regression model can predict intra-particle compositions accurately with prediction error less than 1.5% (Table 1). The intra-particle compositions along the reactor were achieved using the joint technique of MRI and PLSR (Fig. 1b). From the local intra-particle compositions along the reactor, the accumulation of reaction product inside catalyst particles due to mass transfer limitation can be observed.

Table 1: PLSR prediction error for intra-particle compositions.

	1-octene	2-octene	n-octane
Prediction error/%	0.47	1.06	1.40

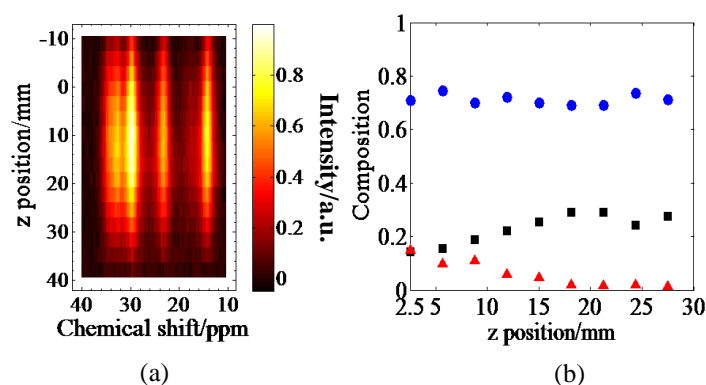


Fig. 1: Results for reaction experiment operated at liquid and gas flow rates of 1.07 ml/min and 30.07 ml/min, respectively. (a) The CSI of the reactor. The zero z position indicates the top of the catalyst layer. (b) Intra-particle composition profiles of 1-octene ●, n-octane ▲ and 2-octene ■ predicted with the PLSR method from the spectra extracted from the CSI.

References:

1. S. T. Sie and R. Krishna, *Rev. Chem. Eng.* 14 (1998) 203.
2. D. M. Doddrell, D. T. Pegg, M. R. Bendall, *J. Magn. Reson.* 48 (1982) 323.
3. S. Wold, M. Sjostrom, L. Eriksson, *Chemometr. Intell. Lab* 58 (2001) 109.

Bayesian Sphere Sizing for Food Foam Research

K. Ziovas^a, A.J. Sederman^a, M.D. Mantle^a, E.Hughes^b, C.Gehin-Delval^b

^aDepartment of Chemical Engineering and Biotechnology, University of Cambridge, UK

^bNestle Research Centre, Lausanne, Switzerland

The bubble or droplet size distribution (B/DSD) is an important characteristic for various commercial food products that can be classified either as foams or emulsions. The B/DSD can affect parameters like the shelf-life of a food product as well as the texture, appearance and taste. It is thus desirable to have a non-invasive, rapid measurement technique for the B/DSD.

Sphere sizing using Bayesian probability theory and NMR data has been developed recently¹. The main advantage of this method is the short experimental time required. It could be therefore used as a fast, non-invasive method for routine analysis in the food industry. The method makes use of standard Bayesian probability theory². A statistical model is first constructed through simulations where the model assumes randomly dispersed spheres and includes different types of sphere size distribution. This model ultimately generates likelihood functions, which describe statistically the intensity of the NMR k-space signal for a range of sphere sizes. By performing an NMR experiment on the sample of interest a single line in k-space can be acquired. The acquired data are compared to the statistical model and a probability estimation for the size distribution is subsequently calculated.

In this project different types of samples were studied. Initially, a model system was used. Glass ballotini were randomly dispersed in suspension in a Xanthan gum gel. The glass beads cover a range of diameters between 1.7 mm down to 100 μm . Xanthan gel was used because it is commonly found in commercial food products. Furthermore it produces a stable high-viscosity fluid allowing the glass beads to remain in suspensions for long periods of time (up to months). 1D-NMR k-space data were acquired using a Bruker Biospin DMX-300 MHz spectrometer. This poster shows that the Bayesian method gives accurate estimations of the glass beads diameters that compared well with optical image analysis. Aerated chocolate bars were chosen as suitable commercial food products for testing the combined NMR/Bayesian method. This product is solid at room temperature and maintains an internal foam structure. Figure 1 includes an optical image where the internal structure of the chocolate bar can be seen. 1D-NMR k-space data were acquired with a Bruker Biospin AV-85 MHz spectrometer and were subsequently analyzed with the Bayesian method.

Future work will focus on translating the high field NMR/Bayesian protocols to low-field NMR spectrometers with the ultimate goal of developing a rapid, non-invasive Bayesian /NMR approach to sphere sizing that can be used at the production line.

References:

1. D. J. Holland, A Bayesian approach to characterizing multi-phase flows using magnetic resonance: application to bubble flows, *JMR* 209 (2011) 83.
2. D. B. R. Andrew Gelman, John B Carlin and Hal S Stern, *Bayesian Data Analysis*, Second Edition, (2004).

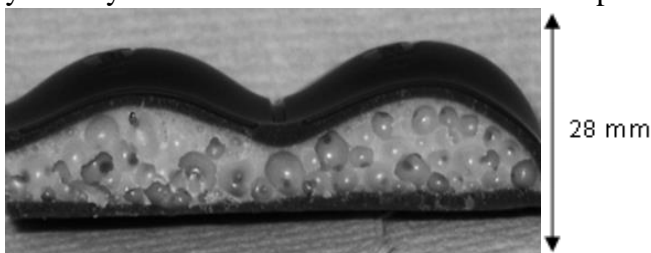


Fig. 1: An optical image from a commercial aerated chocolate bar. The bar has been cut vertically and the internal foam structure can be seen.

Portable NMR for practical analysis of ancient wall paintings

Wasif Zia, Tyler Meldrum, Bernhard Blümich

Institut für Technische und Makromolekulare Chemie (ITMC), RWTH Aachen University,
Germany

For almost a decade, single-sided NMR has been used to study objects of cultural heritage such as paintings¹, bones², ancient paper³ and frescoes⁴. The equipment is mobile and the measurement is non-invasive, making it suitable for on-site measurements of arbitrarily sized artifacts. We discuss measurement techniques for single-sided NMR in the context of ancient wall paintings by example of depth profiles that reveal the stratigraphy of the preparation layers supporting the painting. The translational mobility of residual water was also examined by measuring the self-diffusion coefficient at different depths across the wall in the Villa dei Papyri at Herculaneum, because moisture migration gives rise to surface damage. The self-diffusion coefficient of wall moisture also reports about differences in surface treatments for fresco conservation. We report the particular measurement procedures of mobile single-sided NMR that have been developed for the analysis of wall paintings.

References:

- 1.F. Presciutti, J. Perlo, F. Casanova, S. Glögler, C. Miliani, B. Blümich, B.G. Brunetti, A. Sgamellotti, Noninvasive nuclear magnetic resonance profiling of painting layers, *Appl. Phys. Lett.* 93 (2008) 033505-1 -3
- 2.F. Rühli, T. Böni, J. Perlo, F. Casanova, M. Baias, E. Egarter, B. Blümich, Non-invasive spatial tissue discrimination in ancient mummies and bones in situ by portable nuclear magnetic resonance, *J. Cultural Heritage* 8 (2007) 257-263
- 3.B. Blümich, S. Anferova, S. Sharma, A.L. Segre, C. Federici, Degradation of historical paper: nondestructive analysis by the NMR-MOUSE®, *J. Magn. Reson.* 161 (2003) 204–209
- 4.B. Blümich, A. Haber, F. Casanova, E. del Federico, V. Boardman, G. Wahl, A. Stilliano, L. Isolani, Noninvasive depth profiling of walls by portable nuclear magnetic resonance, *Anal. Bioanal. Chem.* 397 (2010) 3117-3125

Ultrafast in vivo imaging sequence for Bruker MRI systems

T. Roussel^a, A. Leftin^a, A. Seginer^a, L. Frydman^a

^aDepartment of Chemical Physics, Weizmann Institute of Science, Rehovot, 76100, Israel

Introduction

Reducing acquisition time is one of the most pressing challenge in Magnetic Resonance Imaging (MRI) research field. Recently, original ultrafast acquisition schemes have been proposed to collect the 2D NMR data within a single scan [1]. Since 2010, this concept is also applied for MRI giving birth to several ultrafast single-shot spatiotemporally encoded (SPEN) imaging sequences [2]. Besides important scan time reduction, SPEN experiments are especially robust regarding high-field artifacts such as B_0 inhomogeneities and susceptibility effects [3]. In this paper, we present a 2D SPEN method developed for Bruker MRI systems. The method includes a single-shot single-slice SPEN sequence with an online reconstruction, both of them fully integrated in Bruker Paravision.

Method

The 2D single-slice SPEN sequence is based on a spin-echo Echo Planar Imaging (EPI) scheme (Fig. 1). The SPEN excitation scheme starts with a 90° chirp pulse applied during a magnetic field gradient in order to perform the spatial encoding along the EPI phase encoding direction. The slice selection is performed with a standard three-lobed 180° sinc pulse. Fully refocused, SPEN signals are acquired using an EPI read-out detection scheme.

The sequence is fully integrated in Paravision as a “method”. As for other regular imaging sequences, the slice thickness, position and the FOV can be directly adjusted using the Geometry Editor (Fig. 2). Except for the chirp pulse attenuation, all the parameters are calculated automatically. The SPEN super-resolution image reconstruction [2] is also fully integrated in Paravision using Matlab Compiler Runtimes.

Results & Discussion

The method was installed and successfully tested on 3 Bruker Biospec MRI systems respectively equipped with a 4.7 T, 9.4 T and a 21.1 T widebore magnet. Ex-vivo



Fig. 3: Screen capture of the Image Display window after running a SPEN experiment on a rat brain acquired ex-vivo at 21.1 T.

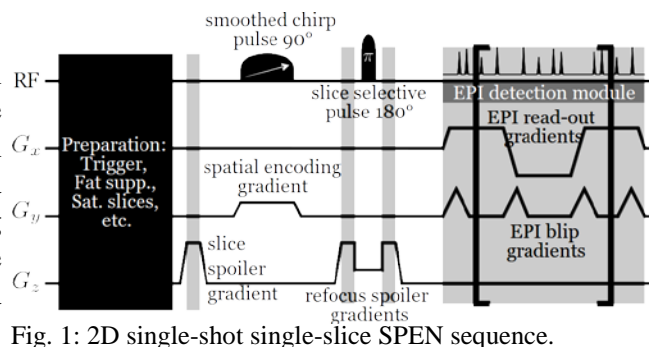


Fig. 1: 2D single-shot single-slice SPEN sequence.

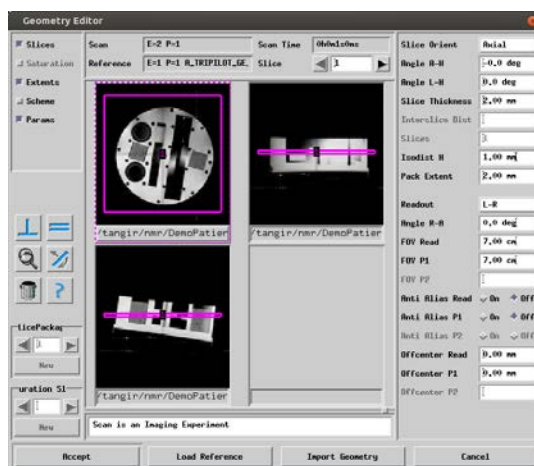


Fig. 2: Screen capture of the Geometry Editor graphical interface when adjusting the slice parameters for a SPEN scan.

single-shot SPEN experiments were performed on a rat brain at 21.1 T with the following parameters: 40 ms / 10 kHz spatial encoding, 15 x 15 mm FOV, 2 mm slice thickness, 100x100 points, TE=49 ms, 93 ms scan time. The reconstructed SPEN image is directly displayed in Paravision (Fig. 3).

References

1. L. Frydman, A. Lupulescu and T. Scherf, Principles and features of single-scan two-dimensional NMR spectroscopy, *J. Am. Chem. Soc.* 125 (2003) 9204–9217
2. N. Ben-Eliezer, M. Irani and L. Frydman, Super-resolved spatially encoded single-scan 2D MRI, *Magn. Reson. Med.* 63 (2010) 1594-1600
3. N. Ben-Eliezer, Y. Shrot and L. Frydman, High-definition, single-scan 2D MRI in inhomogeneous fields using spatial encoding methods, *Magn. Reson. Imaging* 28 (2010) 77-86

Compressed Sensing for the imaging of two-phase falling film flow

C. Schmaus, D.J. Holland, A.J. Sederman and L.F. Gladden

Department of Chemical Engineering and Biotechnology, University of Cambridge,
Pembroke Street, Cambridge CB2 3RA, UK

Multiphase flow processes are common across many areas of science and engineering, including oil recovery and chemical process design. Magnetic Resonance Imaging (MRI) can play an important role in gaining a detailed understanding of the flow characteristics and interaction between phases. However, MRI velocimetry studies of gas-liquid flows have often been limited to inferring information on the phase interaction from the behavior of the liquid phase, because the spin density of gases is three orders of magnitudes lower than that of liquids, which severely limits the signal-to-noise ratio. In this paper we discuss the application of Compressed Sensing (CS) to image both the gas and liquid velocities in a falling film system with co-current gas flow. CS is a novel approach to data sampling and image reconstruction, which allows the reduction of acquisition times by sampling fewer data points. Images acquired under violation of the Nyquist criterion can be reconstructed to high quality by nonlinear optimization.

Figure 1 shows some of the results obtained by applying CS to image a wavy falling film of polydimethylsiloxane (PDMS) on a vertical glass plate with a co-current flow of sulfur hexafluoride (SF_6). Falling films often serve as model systems for wavy flow and they provide a geometrically simple environment for the study of gas-liquid interfacial interactions. We will demonstrate: (i) excellent agreement of the liquid phase velocity profiles with the predictions of the Nusselt equation for laminar falling film flow¹; (ii) provide evidence for continuity of velocity across the gas-liquid interface; (iii) discuss how fluctuations in the two-phase flow can be detected on a timescale more than an order of magnitude below the acquisition time.

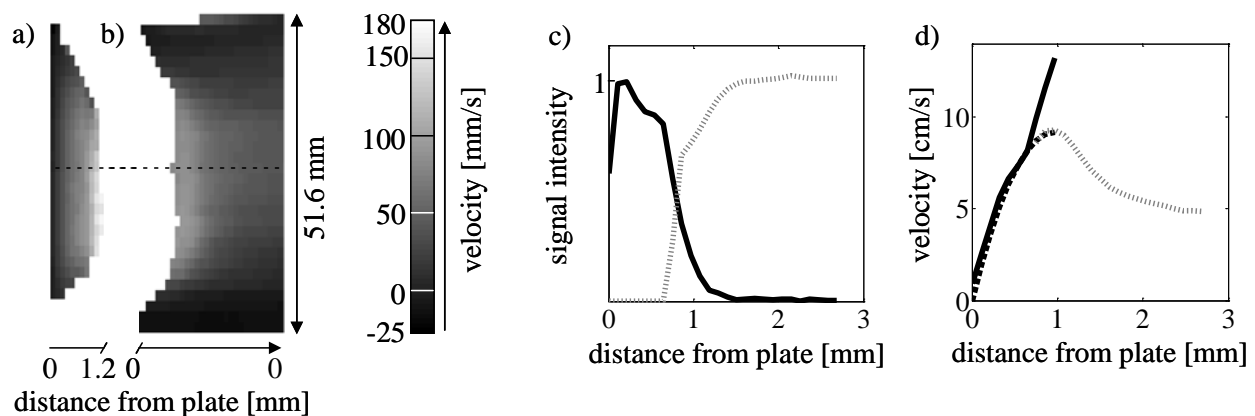


Fig. 1: a) Velocity map of wavy falling film flow of PDMS down a vertical glass plate at a flow rate of 3.1 ml/s; the liquid-solid interface is at the left side. b) Velocity map of the co-current flow of SF_6 at a pressure of 5 barg and a flow rate of 24.5 ml/s; Only the section directly adjacent to the liquid film is shown. c) Profile of the normalised signal intensity of PDMS (black) and SF_6 (grey, dashed) across the gas-liquid interface at the position indicated by the dotted line in Figure 1a and b. The region occupied by surface waves can be identified by the gradual decay of signal intensity towards the gas-liquid interface, which is caused by temporal fluctuations of the interface position on a time scale shorter than the image acquisition time. d) Profile of the velocity of PDMS (black) and SF_6 (grey, dashed) across the gas-liquid interface, demonstrating the continuity in velocity at the interface. The dashed black line shows the theoretical (Nusselt) velocity profiles within the liquid film.

Reference:

1. W. Nusselt, Die Oberflächenkondensation des Wasserdampfs, VDI Zeitung 60 (1916) 541.

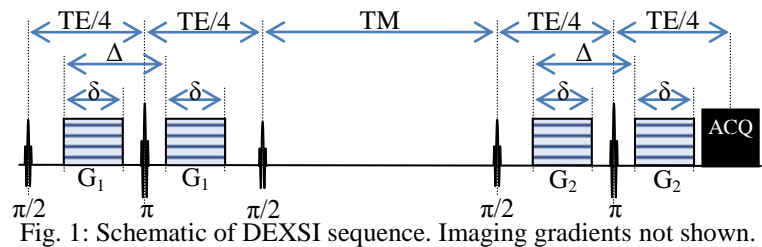
Diffusion-diffusion Exchange Spectroscopic Imaging (DEXSI) MRI in a rat corpus callosum

B. Siow^{a,b}, P.L. Hubbard^c, A. d'Esposito^b, M.F. Lythgoe^b, D.C. Alexander^a

^aMicrostructure Imaging Group, Centre for Medical Image Computing, UCL ^bCentre for Advanced Biomedical Imaging, UCL ^cCentre for Imaging Sciences, University of Manchester

Introduction: The permeability of membranes within tissue microstructure is abnormal in a number of pathologies, for example in cancer¹ and stroke². We adapt the Diffusion-diffusion Exchange Spectroscopy (DEXSY)^{3,4} NMR technique for MRI biological samples to quantify permeability. Previous studies that estimate permeability have adapted the Karger framework⁵ using biophysical models of tissue. An alternative, phenomenological approach, Filter Exchange Imaging (FEXI) has been used to quantify permeability in the human brain⁵. The FEXI study assumed a two site system and that the rate of exchange between sites was mono-exponential. A recent study suggests white matter can be better described by at least three compartments⁶. Diffusion-diffusion exchange techniques are inherently able to detect multiple diffusivities and thus the exchange of water between them. We demonstrate the first use of diffusion-diffusion exchange spectroscopy in an imaging application and, furthermore, the first use with biological tissue.

Methods: The DEXSI pulse sequence is shown in Fig 1. For this study, a single spin-echo readout was used and implemented on a 9.4T Agilent small bore scanner equipped with 1T/m gradients and 26mm r.f. volume coil. Diffusion gradients were aligned



perpendicular to axonal fibres in the mid-sagittal slice of the corpus callosum. 16x16 steps of G1 and G2 were taken (256 measurements in total). Parameters were: $\delta=5\text{ms}$, $\Delta=10\text{ms}$, $G_1=0$ to 0.7 T/m, $G_2=0$ to 0.7 T/m, $TM = 200\text{ms}$, TE was minimized, 12x24mm FoV, 128x128 matrix. A rat brain was perfused fixed and immersion fixed for 1 week in 4% aqueous formaldehyde from paraformaldehyde, then immersed in phosphate buffer solution for 1 week. The sample was immersed in perfluorosolv PFS-1 (Solvay Solexis) prior to scanning. Temperature was maintained at 18°C throughout the experiment. 2D diffusion spectra were generated using 2D inverse Laplace transform software⁷.

Results: An unweighted image of the mid-sagittal slice and 2D diffusion spectra of the corpus callosum are shown in Fig. 2&3 respectively. Peaks in the 2D diffusion spectrum are seen at $(D_1, D_2) \sim (3, 3)$ and $(2.5, 0.4) \times 10^{-10} \text{m}^2/\text{s}$. There are also corresponding peaks with very low diffusion constants.

Discussion: For the first time we have applied diffusion-diffusion exchange spectroscopy in an imaging application in biological tissue. Diffusion constants are consistent with fixed tissue at room temperature⁸. Future work will decrease total acquisition time by fast imaging and optimising the diffusion protocol⁹.

References: 1. Lätt J et al. NMR Biomed 22: 619–628 2. Nilsson M et al. Magn Reson Med, 69: 1572–1580 3. Qiao Y et al. J Chem Phys 122:214912 4. Hubbard PL et al. J Phys Chem B 110, 20781–20788. 5. Kärger J, Adv Coll Interf Sci 23, 129–148 6. Panagiotaki E et al. Neuroimage 59(3), 2241–2254 7. Godefroy S, Ryland B and Callaghan PT, Victoria University of Wellington, Wellington, New Zealand. Provided courtesy of Petrik Galvosas. 8. Alexander DC et al. NeuroImage 52, 1374–1389. 9. Alexander DC, Magn Reson Med 60, 439–448.

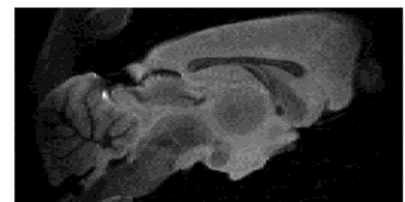


Fig. 2: Unweighted image of mid-sagittal slice

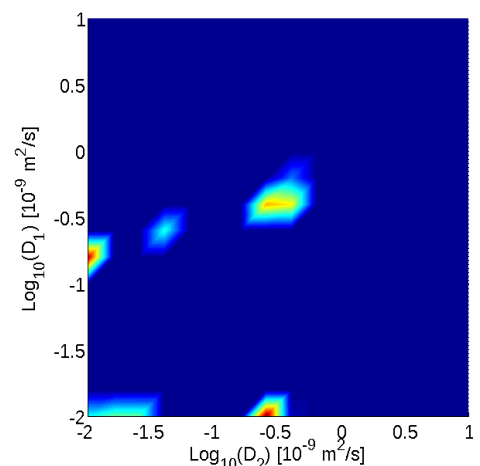


Fig. 3: 2D diffusion spectrum of rat corpus callosum

Diffusion time correlation experiment

Jeffrey Paulsen and Yi-Qiao Song

Schlumberger-Doll Research, Cambridge MA USA

Diffusion has long been used to probe molecular composition of fluids and micro-structure of porous media [1,2]. However, in practice and in particular for natural materials, both effects could be present together (further complicated by the distributions of pore sizes) making it difficult to identify fluid types and determine diffusion coefficient. One of the key characteristics of restricted diffusion is the apparent diffusion coefficient $D(\Delta)$ decreases as the diffusion time Δ increases. In contrast, bulk diffusion coefficient remain constant irrespective of the diffusion time used in the experiment.

The apparent diffusion coefficient (ADC) is defined by $\langle R(\Delta)^2 \rangle / 2\Delta$ where $\langle R(\Delta)^2 \rangle$ is the mean-squared molecular displacement over the time Δ . For bulk diffusion, since $R(\Delta)^2 = 2D_0\Delta$ (D_0 is the bulk diffusion constant), $D(\Delta)$ is a constant, independent of Δ . In the presence of restrictions, it is well-known that:

$$\frac{D(\Delta)}{D_0} \approx 1 - \frac{4}{9\sqrt{\pi}} \frac{S}{V_p} \sqrt{D_0\Delta}$$

where S/V_p is the surface-to-volume ratio of the porous material [3]. As a result, $D(\Delta)$ is a decreasing function, e.g. $D(\Delta) > D(2\Delta)$. In a plot of $D(\Delta)$ vs. $D(2\Delta)$, bulk diffusion signal would be on the diagonal line where restricted diffusion will be separated away from the diagonal line.

This paper analyzes the correlated diffusion process in a multiple-pulsed-field-gradient diffusion experiment and show that the diffusion dynamics can be decomposed into two orthogonal decay mechanisms and each is characterized by a different diffusion time. Based on this analysis we designed an experiment to obtain the correlation map of $D(\Delta)$ vs. $D(2\Delta)$. Experimental results (FIGURE 1) demonstrated a clear distinction between the two diffusion processes.

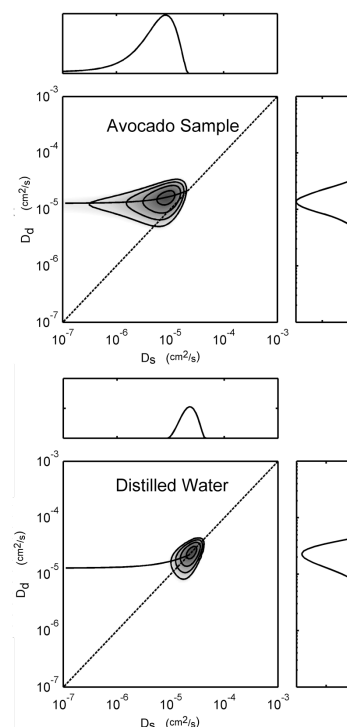


FIGURE 1. Experimental 2D diffusion time correlation spectra for bulk fluid and restricted diffusion in an Avocado sample. The peak for Avocado is significantly off the diagonal line demonstrating restricted diffusion.

References:

1. K. F. Morris and C. S. J. Jr. Diffusion-ordered two-dimensional nuclear magnetic resonance spectroscopy. *Journal of the American Chemical Society*, 114(8):3139–3141, 1992.
2. D. E. Woessner. NMR spin-echo self-diffusion measurements on fluids undergoing restricted diffusion. *J. Phys. Chem.*, 67:1365–1367, 1963.
3. P. P. Mitra, P. N. Sen, and L. M. Schwartz. Short-time behavior of the diffusion coefficient as a geometrical probe of porous media. *Phys. Rev. B*, 47:8565–8574, 1993.

Concentration mapping with MRI using compressed sensing

*E.von Harbou^a, H.T. Fabich^a, M. Benning^a, A.B. Taylor^a, Z. Qiao^a
A.J. Sederman^a, L.F. Gladden^a, D.J. Holland^a,*

^aDepartment of Chemical Engineering and Biotechnology, University of Cambridge, UK

Concentration maps of different chemical species can provide valuable information for many applications in chemical engineering. They can be used, for example, to study reaction and mass transfer phenomena in catalyst beds or along liquid-liquid interfaces. The acquisition time for multidimensional fully sampled concentration maps, however, may take several hours¹. Thus, we present a method for accelerating the acquisition of spatially resolved concentration maps by the use of compressed sensing (CS). This method reduces the duration of the experiments significantly and facilitates the investigation of phenomena that include concentration changes of different chemical species that take place within minutes.

CS enables the accurate reconstruction of an under-sampled signal by utilising the prior knowledge that the signal is compressible or sparse. Recently, it has been successfully applied to reduce the acquisition time of MR images² or MR velocity images³. When the chemical shift information is incorporated into the model used for the reconstruction, the chemical maps of different species can be directly recovered from the k -space data. Good results have been achieved in medical applications with this method for water and fat image separation⁴ but no quantitative concentration maps were retrieved. In this work, we applied CS reconstruction to resolve spatially and quantitatively the concentrations of different species in mixtures.

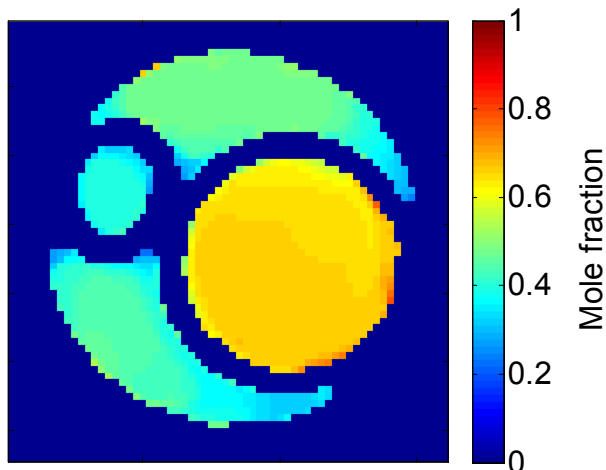


Fig. 1: Map showing the mole fraction of 1,4-dioxane in mixtures with cyclooctane in a phantom consisting of two cylinders contained within a 20 mm sample. The mole fraction of 1,4-dioxane in the small cylinder and the surrounding fluid is 0.42 mol/mol, and in the larger cylinder is 0.67 mol/mol.

A slice selective two-dimensional spin echo pulse sequence was used. The k -space sampling strategy followed a spiral design. To achieve a good coverage of k -space, typically eight spirals with different orientations were applied. Each spiral had a length of approximately 1.4 ms. Overall, 16 excitations (2 scans each) were required to obtain an image of 64 x 64 pixels.

The method was tested by acquiring concentration maps of binary and ternary mixtures in different phantom systems. Fig. 1 shows, as an example, the concentration map of 1,4-dioxane in mixtures with cyclooctane in a phantom consisting of two cylinders contained within a larger 20 mm diameter sample. The concentration in the smaller cylinder and the surrounding liquid was 0.42 mol/mol, whilst in the middle cylinder the concentration was

0.67 mol/mol. The measured and the expected concentrations show very good agreement. Typically, the relative mean error of the concentration (mole fraction) was below 3 %.

The presented method is a powerful tool for the fast acquisition of quantitative concentration maps that are valuable for the investigation of many phenomena in chemical engineering applications. Here we present a discussion of the strengths and limitations of this approach for quantifying chemical species in heterogeneous systems.

References:

1. B.A. Akpa, M.D. Mantel, A.J. Sederman, L.F. Gladden, *Chem. Commun.* (2005) 2741.
2. M. Lustig, D. Donoho, J.M. Pauly, *Magn. Reson. Med.* 58 (2007) 1182.
3. D.J. Holland, D.M. Malioutov, A. Blake, A.J. Sederman, L.F. Gladden, *J. Magn. Reson.* 203 (2010) 236.

Quantification of chemical composition using Bayesian NMR

Y. Wu^a, A. G. Wilson^b, D. J. Holland^a, M. D. Mantle^a, S. Nowozin^b, A. Blake^b, L. F. Gladden^a

^aDepartment of Chemical Engineering and Biotechnology, University of Cambridge, UK

^bMicrosoft Research Cambridge, UK

In many industrial and medical applications of NMR spectroscopy, the sensitivity is limited by low signal to noise ratio (SNR) or overlapping peaks. Further analysis can be complicated by variations in the baseline and difficulties in correctly phasing the signal. We introduce a Bayesian approach to infer chemical composition in mixtures directly from time domain NMR data. By incorporating prior information, the Bayesian model gives more quantitative estimates than the conventional Fourier transform (FT) spectra, especially under conditions of low SNR and peak overlap.

Time domain NMR data can be modeled as the sum of a quadrature free induction decay signal and Gaussian noise. The noise-free signal is parameterized as a sum of trigonometric functions weighted by amplitudes that correspond to the concentration of different chemicals. Uncertainty in the measurement arises in the form of Gaussian noise, therefore the entire signal can be modeled as a multivariate Gaussian distribution. It is therefore possible to analytically derive the posterior distribution for the amplitudes, which is used to infer the chemical composition. The model requires estimation of unknowns, including the frequencies and relaxation time constant. These unknown parameters are predicted by maximizing the marginal likelihood function.¹ The posterior over amplitudes is then estimated conditioned on such predictions. The final concentration probability distributions are acquired by sampling from the posterior over amplitudes.

We compare the performance of this general Bayesian NMR model with FT using ¹³C measurements of a binary mixture of butanone and cyclohexane. Figure 1 concentration estimates from the Bayesian NMR approach and those based on a conventional analysis of the peak area from the FT spectra. Figure 1 (a) shows a comparison of the error for concentrations > 10 %. The Bayesian results are more robust and accurate than conventional FT analysis, with smaller errors and error bars. For the low concentration mixtures in (b), FT suffers from peak overlap and tends to overestimate the concentration of the dilute species. However, the Bayesian method removes such bias and is able to distinguish the slight difference between concentrations.

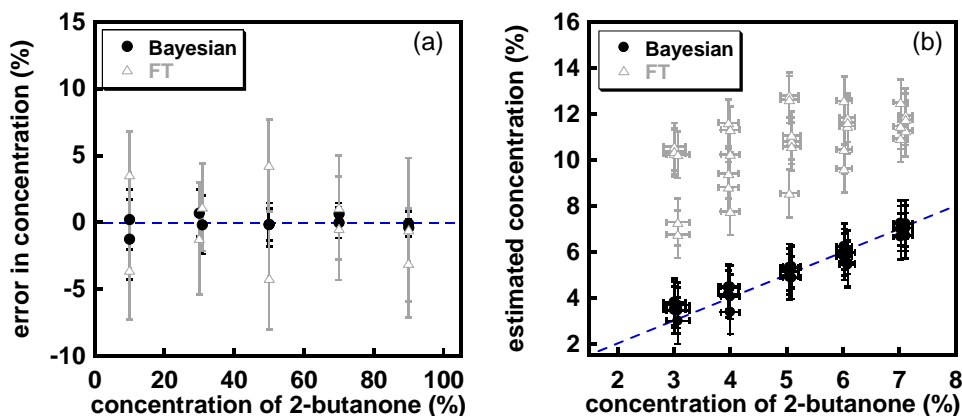


Fig. 1: Experimental comparison between the Bayesian NMR approach and the FT method. The data in each figure are acquired with the same noise level, which corresponds to a SNR of 4.5 for the lowest concentration in each figure. Error bars in y direction indicate the 95% credible region. The sample preparation errors are given as x direction error bars.

References:

1. M. F. Cardoso, R. L. Salcedo, and S. de Azevedo, *Comput. Chem. Eng.*, **20**, (1996) 1065.

***k*-t acceleration in pure phase encode MRI to monitor dynamic flooding processes in rock core plugs**

Dan Xiao^a, Bruce J. Balcom^a

^aMRI Research Center, Department of Physics, University of New Brunswick, Canada

In the study of petroleum reservoirs, and enhanced oil recovery, it is essential to understand the fluid interactions in the pore space which control the efficiency of petroleum recovery. Laboratory studies of rock core plugs permit better understanding of the porous media system. Conventional methods, such as effluent analysis and inflow-outflow methods, cannot provide spatially resolved information on fluid displacement and fluid interactions in the pore space. Pure phase encode MRI techniques, immune to susceptibility variations within the sample, have proven to be robust in their ability to generate quantitative images in porous media. However, the acquisition time is long with pure phase encoding as only one *k*-space point is typically acquired with each RF excitation, which limits the temporal resolution of the dynamic image series when monitoring flooding processes.

Spatiotemporal correlations can be exploited to undersample the *k*-t space data. The stacked frames/profiles can be well approximated by an image matrix with rank deficiency, which can be recovered by nonlinear nuclear norm minimization. The results of a low rank matrix completion technique were compared with *k*-t sparse compressed sensing.

These methods are demonstrated with one dimensional pure phase encode measurements of rock core plugs in laboratory study. 30% of the *k*-t space data points are sufficient for reconstructing good quality images with compressed sensing or low rank matrix recovery methods. This enables monitoring the dynamic process with a higher temporal resolution and/or a higher SNR. These methods can be easily extended to higher dimensionality MR imaging of dynamic rock core plugs flooding processes.

Noise reduction for NMR with regularization-heursure algorithm

Q. M. Xie^{a, b, c}, L. Z. Xiao^{a, b}, L. J. Cheng^{b, c}, J. F. Liu^{b, c}, G. Z. Liao^a, F. Deng^a

^a Key Laboratory of Resources Prospecting and Information Technology, China University of Petroleum, Beijing 102249, China, ^b Chongqing Shale Gas Research Centre of State Key Laboratory of Petroleum Resource and Prospecting, Chongqing Institute of Geology and Mineral Resources, Chongqing 400042, China, ^c Key Laboratory of Shale Gas Exploration, Ministry of Land and Resources, Chongqing Institute of Geology and Mineral Resources, Chongqing 400042, China

NMR logging is measured on the harsh conditions under high temperature and high pressure within the slice. The signal-to-noise ratio (SNR) is low influenced by the noise with complicated sources. Noise suppression is implemented with the proposed Regularization-Heursure (R-Heursure) aiming at the detail coefficients of wavelet decomposition. The selection of the regularization factor is related to the pore structure characteristics and raw SNR of NMR well logging data, which is just above noise statistics level and maintains the information of micro-pore as well. The optimal mother wavelet function, vanishing moment and decomposition level are selected by the principle of the maximum energy of correlative coefficients. The numerical simulation and NMR logging data processing show that SNR can be improved effectively with the proposed algorithm, the accurate information is provided for the reservoir evaluation, as the Fig .1.

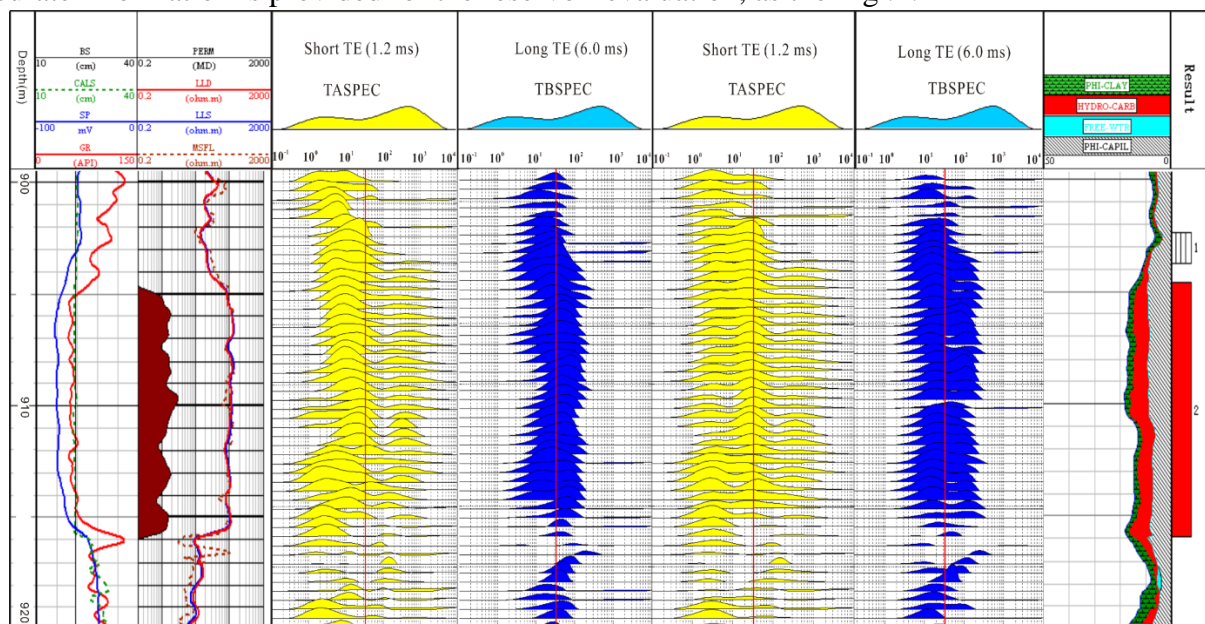


Fig. 1: De-noising results with R- Heursure algorithm for X well

References:

- [1] G. R. Coates, L. Z. Xiao, Prammer M G. NMR logging: principles and applications. Texas: Gulf Professional Publishing, 2000.
- [2] Q. M. Xie, L. Z. Xiao, G. Z. Liao. Application of SURE algorithm to echo train de-noising in low field NMR logging. Chinese J. Geophys., 2010, 53(11): 2776-2783.

Average bubble size estimation in an upward vertical bubbly flow at a low magnetic field (0.2 T)

Aidin Arbabi^a and Igor V. Mastikhin^a

^aUNB MRI Centre, Department of Physics, University of New Brunswick, Fredericton, New Brunswick, Canada E3B 5A3

When gas and liquid flow up a vertical tube, several flow patterns are possible¹: bubbly, slug, churn, and annular flows. In the bubbly flow, gaseous bubbles with various sizes are dispersed throughout the liquid phase. These bubbles are small compared to the diameter of the tube, and their shape is not significantly influenced by the tube walls². Regardless of its extensive applications in industries (e.g. sieve column), there is little theory available in the field due to the complexity, deformability, and compressibility of the phases. In this work, we studied different parameters of the bubbly flow including void fraction (i.e. volume of the liquid phase occupied by the gaseous phase), proton random motion (i.e. diffusion), and magnetic resonance (MR) spin-spin relaxation time at a low magnetic field of 0.2 Tesla. We, finally, calculated the average bubble size analytically.

The magnetic susceptibility difference between the water molecules and gaseous bubbles reduces the MR spin-spin relaxation time due to spins' diffusion through the internal gradients. Dharmakumar et. al.³ derived analytical expressions for stabilized microbubbles that relate the bubble-induced relaxation rates, average bubble radius, void fraction, and diffusion. A further analysis shows that measurement of relaxation rates at very short and very long evolution times can, in principle, yield the void fraction and average bubble size information.

The susceptibility-induced relaxation rate depends on the square of the magnetic field strength and is therefore very pronounced at high fields⁴. As most industry-based MR instruments operate at much lower fields, low-field studies of this effect represent an obvious practical interest.

Distilled water was doped by small amount of manganese sulfate (MnSO_4) to reduce the MR spin-lattice recovery time for a faster acquisition. We calculated void fraction from the amplitude of the MR free induction decay signal. The MR spin-spin relaxation time was measured from the standard CPMG pulse train for the stagnant water and bubbly flow at a wide range of echo times. We obtained diffusion information using the standard Pulsed Field Gradient Spin Echo pulse sequence, and studied diffusion as a function of the diffusion exchange time. All the measurements were performed for 3 different flow rates of the bubbly flow.

Finally, we calculated the average bubble size analytically using the newly developed approach and verified its accuracy with an independent optical method.

References:

- [1] D. Barnea, and L. Shemer, "Void fraction measurements in vertical slug flow: applications to slug characteristics and transition", *International Journal of Multiphase Flow*, 15 (1989), 495-504.
- [2] D. J. Nicklin, "Two-phase bubble flow", *Chemical Engineering Science*, 17 (1962), 693-702.
- [3] R. Dharmakumar, D. Plewes, G. Wright, "On the parameters affecting the sensitivity of MR measures of pressure with microbubbles", *Magnetic Resonance Med*, 47 (2002), 264-273.
- [4] A. Arbabi, I.V. Mastikhin, "Magnetic susceptibility based magnetic resonance estimation of micro-bubble size for the vertically upward bubbly flow", *Journal of Magnetic Resonance (JMR)*, 225 (2012), 36-45.

Multiphase flow validation using magnetic resonance imaging

O. Bartlett^a, A. Sederman^a, M. L. Johns^b

^a Department of Chemical Engineering, University of Cambridge, Cambridge, UK

^b School of Mechanical and Chemical Engineering, University of Western Australia

Magnetic resonance imaging (MRI) has long been employed as a non-invasive, chemically independent technique for flow imaging in non-field applications. However, flow imaging presents several challenges for high-velocity multiphase flows for a number of reasons, including loss of coherent signal due to increasing turbulence and washout effects.

For this project, a purely phase-encoded method known as single-point imaging (SPI)¹ was identified as suitable for high-velocity flow imaging due to a short time parameter t_p and a relative immunity to artefacts caused by B_0 field inhomogeneity and samples with short transverse relaxation times (T_2^*). Variants of this technique have previously been used for velocity imaging of rapid gas flows ($Re \leq 210,000$)² and horizontal bubbly flows³ with great success.

The SPI sequence was modified with the addition of velocity-encoding gradients and a slice-selective spin echo to minimise any residual B_0 artefacts. This modified SPI sequence was tested on a range of single- and two-phase flows. All vertical flow experiments were performed with a Bruker SWB-300 spectrometer operating at a 1H resonance frequency of 300 MHz. The flow was provided by a purpose-built air-water flow loop with an imaging section internal diameter of 50 mm.

The modified SPI sequence acquires data which is separated into modulus (intensity) and phase information. The phase images are converted to velocity maps, the intensity images can be used to quantitatively measure the phase volume fraction according to established correlations⁴.

In this presentation we give examples of the velocity maps and void fraction distributions for a range of single- and two-phase flow conditions with superficial velocities over 1 m s^{-1} (see Figure 1). When this data is combined to form weighted velocity maps, we compare the liquid flow rate determined from the SPI images to the flow rate measured using a turbine flow meter. The void distribution data is discussed with regards to the gas flow rate where applicable. The results are put into context as they pertain to multiphase flow metering to demonstrate the potential for this technique.

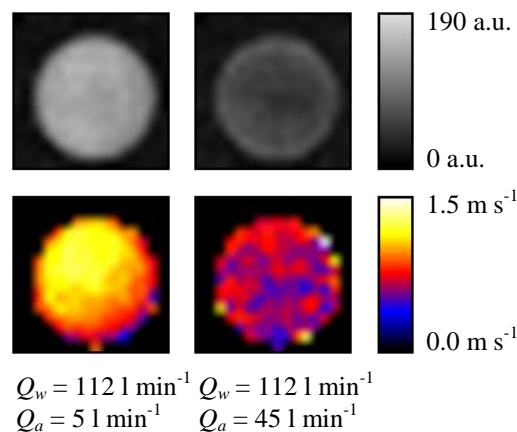


Figure 1. Examples of air-water flow images. TOP: intensity images, BOTTOM: weighted velocity maps. Gas flow rates given at standard conditions (20°C , 1 atm).

References:

1. S Emdin and J H N Creighton, High-resolution NMR imaging in solids, *Physica B+C* 128 (1985), pp 81-83.
2. B Newling, C P Poirier, Y Zhi, J A Rioux, A J Cristine, D Roach and B J Balcom, Velocity imaging of highly turbulent gas flow, *Phys. Rev. Letters* 93 (2004), number 15.
3. M Sankey, Z Yang, L F Gladden, M L Johns, D Lister and B Newling, SPRITE MRI of bubbly flow in a horizontal pipe, *J. Mag. Res.* 199 (2009), pp. 126-135.
4. G.F. Lynch and S.L. Segel, Direct measurement of the void fraction of a two-phase fluid by nuclear magnetic resonance, *Int. J. Heat Mass Transfer* 20 (1977), pp 7-14.

Shear-induced aggregation of bacterial-cellulose dispersions as viewed by rheo-NMR and PFG ^{19}F -NMR nanoprobe diffusometry

D.W. de Kort^{a,e}, G.J.W. Goudappel^{b,e}, Y. Mulla^a, A. Kuijk^b, S. Veen^b,

K.P. Velikov^{b,d}, F. Hoeben^{c,e}, H.M. Janssen^{c,e}, H. Van As^{a,e}, J.P.M. van Duynhoven^{a,b,e}

^aLaboratory of Biophysics, Wageningen University, ^bUnilever R&D, Vlaardingen, ^cSyMO-Chem, Eindhoven, ^dSoft Condensed Matter Group, Utrecht University, ^eTI-COAST, Amsterdam NL

Cellulose fibers have been exploited for the structuring and reinforcement of various products from polymer coatings to fast moving consumer goods. This structuring capacity can be enhanced when the fibers are finely dispersed as microfibrils with dimensions in the tens-of-nm range.¹ Under mild shear, cellulose microfibrils have a strong tendency to aggregate² due to Van der Waals and hydrogen bond driven interactions. Cellulose microfibril dispersions are therefore not thermodynamically stable; the only stabilization arising from steric constraints due to their entanglement, leading to gel formation. Microfibrillar cellulose dispersions can be stabilized by charging the microfibrils by chemical oxidation³ or by adsorbing with charged biopolymers, such as carboxymethyl cellulose (CMC)⁴. Here we studied the effect of low levels of CMC on microfibrillar network structure and shear-induced aggregation behavior. Bacterial cellulose was used as a model system, since it is readily available in microfibrillar form.

Due to the non-transparency of cellulose dispersions, the use of methods that rely on optical transparency is complicated. Therefore, we have used rheo-NMR for rheological, and PFG NMR nanoprobe diffusometry for non-invasive microstructural characterization.

A rheo-NMR setup at 300 MHz was used to measure flow profiles across the gap of a Couette cell. Without the addition of CMC, shear forces induce aggregation of cellulose microfibrils in a narrow zone near the rotating inner wall of the Couette cell (Fig. 1). The addition of only small amounts of CMC already changes this picture; a stable gel is formed which slips at both walls and does not flow until a yield stress is overcome; this yield stress is seen to decrease with cellulose concentration.

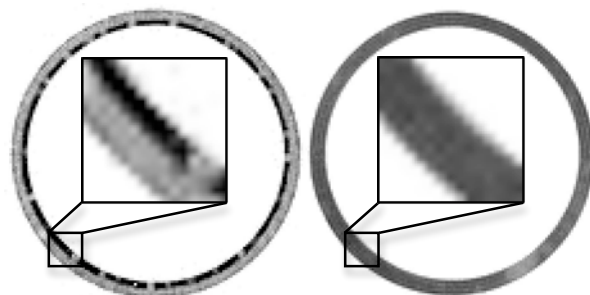


Fig. 1: T_2 -weighted cross section of a Couette device with sheared cellulose (left) and cellulose/CMC (right).

^{19}F -labeled, PEGylated dendrimers with a diameter of 7.5 nm (SyMO-Chem, Eindhoven) were deployed to probe the mesh size of cellulose microfibril networks. The ^{19}F label allowed for specific monitoring of the nanoprobe, without the need for suppression of background signals. A 1% w/w bacterial cellulose dispersion did not show an effect on the diffusion coefficient of these probes compared to the coefficient in water. After the addition of CMC, the diffusion coefficient did decrease, however. This can be attributed to more finely dispersed cellulose microfibrils over the available volume, since their aggregation is prevented by CMC. This explanation was supported by scanning electron microscopy (SEM).

In conclusion, addition of CMC to bacterial cellulose dispersions effectively prevents shear-induced microfibrillar aggregation. Rheo-NMR and nanoprobe diffusometry can be used to characterize these effects in a non-invasive manner; further work will focus on the dynamical aspects of the shear-induced aggregation process.

References:

1. Lavoine et al., Carbohydrate Polymers 90 (2012) 735–764
2. Saarikoski et al., Cellulose 19 (2012) 647–659
3. Saito et al., Biomacromolecules 8 (2007) 2485–2491
4. Pahimanolis et al., Cellulose 20 (2013) 1459–1468

Nanoprobe diffusometry in soft materials by frequency- and time-domain ^{19}F and ^1H NMR at low and high field strengths

D.W. de Kort^{a,d}, F.J.M. Hoeben^{c,d}, H.M. Janssen^{c,d}, J.P.M. van Duynhoven^{a,b,d}, H. Van As^{a,d}

^aWageningen NMR Centre & Laboratory of Biophysics, Wageningen University, ^bUnilever R&D, Vlaardingen, ^cSyMO-Chem, Eindhoven, ^dTI-COAST, Amsterdam, The Netherlands

Soft materials, such as entangled polymer solutions and gels, derive many of their macroscopic properties from the underlying nano- and mesoporous colloidal networks. An increasingly popular method for the non-invasive characterization of such structures is the use of diffusional nanoprobe with diameters in the 10^0 – 10^1 nanometer range. By using an appropriate model¹, it is possible to infer structural information about the network from the (time-dependent) self-diffusion coefficient. The approach has provided unique insights in the network structure of amongst others protein² and polysaccharide gels^{3,4}.

Here, the time-dependent diffusion coefficient of nanoprobe was assessed using PFG NMR. We designed and manufactured spherical and essentially monodisperse dendrimer particles with a diameter of 7.5 nm. PEGylation of the dendrimers reduced interactions with the matrix; hence, models of nanoprobe self-diffusion would only need to consider the obstruction effect of the network.

In order to prevent structural perturbation of the network, the nanoprobe had to be dosed at low levels. As a consequence, ^1H NMR observations were challenging, since a weak signal from the PEG groups had to be detected against a significant signal arising from the aqueous polymer matrix. To circumvent this, our nanoprobe were internally ^{19}F -labeled. Although this enabled background-free observation of nanoprobe diffusion, sensitivity was compromised due to an unfavorable intensity and faster relaxation of the ^{19}F label with respect to the ^1H signal of PEG.

We have explored the application scope of time and frequency domain diffusometric methods at low and high field strengths. In the time domain we made use of diffusion- T_2 -relaxation correlation spectroscopy (DRCOSY), whereas in the frequency domain, we used the diffusion ordered spectroscopy (DOSY). We used an aqueous 1% w/w xanthan gum solution as a model system and added 0.1% w/w nanoprobe.

At high field strength (7 T), nanoprobe self-diffusion could be easily monitored from a single ^{19}F signal in the frequency domain. ^1H frequency-domain DOSY experiments at the same field strength were more involved, because the water signal had to be suppressed and signals arising from the matrix could, in the spectral domain, overlap with the PEG signal. In this case, ^1H time-domain DRCOSY experiments

performed better in resolving the different signals. Remarkably, also at low field strength (0.7 T), self-diffusion of low levels of nanoprobe could be monitored using ^1H time-domain DRCOSY. Examples will be given of the different applications, based on the trade-offs between straightforward observation of a relatively weak ^{19}F signal and observation of the stronger ^1H PEG signal, requiring suppression of background signals, and between observation at high and low field strengths.

	time domain DRCOSY	frequency domain DOSY
high field 7 T	^1H	^{19}F (single line)
low field 0.7 T	^1H	×

Overview of the nanoprobe-diffusometry experiments

References:

1. L. Masaro, X.X. Zhu, *Prog. Polym. Sci.* 24 (1999) 731–775
2. S. Salami et al., *Food Hydrocolloids* 31 (2013) 248–255
3. D. Bernin et al., *Soft Matter* 7 (2011) 5711–7516
4. N. Lorén et al., *Biomacromolecules* 10 (2009) 275–284

Investigating fluctuations in wormlike micelles solutions with spectroscopic imaging and snap-shot GERVAIS velocimetry

B.S. Douglass, S. Kuczera, T.I. Brox, P. Galvosas

MacDiarmid Institute for Advanced Materials and Nanotechnology,
SCPS, Victoria University of Wellington, New Zealand

Wormlike micelles solutions are self-aggregating structures formed (usually) via some amphiphilicity within component molecules. The 'worms' in solution have the topology of simple 1D polymers, but are known for their exhibition of additional mechanical relaxation times due to breakage and recombination processes. Hence they are ideal as models for non-Newtonian viscoelastic materials¹. In particular, many display complex nonlinear behaviours such as shear-banding, in which a non-monotonic stress/strain-rate relationship leads to an instability in the flow, partitioning sheared fluids into two (possibly dynamic) bands of differing viscosity. The interplay between models of microscopic mechanisms and these phenomena is not yet fully resolved.

Velocity field measurements of deformational flows with magnetic resonance have become well established; previous works performed in our laboratory yield time resolution $\sim 1\text{fps}^2$, however the observed fluctuations of the interface between high- and low-shear-rate bands in cylindrical shearing geometries indicate faster experiments are needed to observe (1) slip-stick conditions of wall and fluid, (2) the transient responses of sheared fluids under commencement, cessation or variation in macroscopic deformational conditions, and (3) the spatiotemporal nature of fluctuations in the shape and position of shear bands with accuracy. To that end we are using a rapid echo-planar imaging pulse program component to quickly capture 2D k -space data of PGSE velocity-encoded fluids (snap-shot-GERVAIS³) under shear, thereby achieving full 3D velocity images within $\sim 100\text{ms}$, and potentially more rapidly should fewer components of the velocity vector be required.

In combination with this velocity imaging to show results in the three scenarios mentioned, we utilise an additional tool in the rheo-NMR toolbox, the simultaneous application of deuterium NMR spectroscopy (through use of a dual channel coil) to such interesting samples as wormlike micelles solutions. ^2H NMR imaging is particularly useful in investigating alignment and orientation⁴, and its use in wormlike micelles solutions in flow situations can aid in correlating the microscopic stress, structure and dynamics with the macroscopic evolution of flow patterns and instabilities gained with fast proton NMR velocimetry.

References:

1. H. Rehage and H. Hoffmann, *Mol. Phys.* 74(5) (1991) 933.
2. K.W. Feindel and P.T. Callaghan, *Rheol. Acta* 49(10) (2010) 1003.
3. A.B Taylor *et al.*, *J. Magn. Reson.* 204 (2010) 266.
4. M. Klinkenberg, P. Blümmler and B. Blümich, *J. Magn. Reson., Ser. A*, 119 (1996) 197.

Microscopic fractional anisotropy with q -MAS PGSE

Stefanie Eriksson^a, Samo Lasic^b, Daniel Topgaard^a

^aPhysical Chemistry, Lund University, P.O.B. 124, SE-22100 Lund, Sweden; ^bColloidal Resource AB, Lund, Sweden

Pulsed field gradient NMR can be used to monitor water self-diffusion and can give structural information such as pore size, permeability and anisotropy for a wide range of porous materials. The presence of microscopic anisotropy in macroscopically isotropic materials gives a characteristic curvature to the signal attenuation curve retrieved with a pulsed gradient spin echo (PGSE) experiment¹. The shape of the signal attenuation curve can be approximated to the Laplace transform of the probability distribution of the of the apparent diffusion coefficients², $P(D)$. Similar curvatures can arise in purely isotropic systems due to restricted diffusion in polydisperse pores. This will give a dispersion of the apparent diffusion coefficients.

The q -MAS PGSE³ is a technique that applies modulated gradients in three orthogonal directions to effectively spin the q -vector at the magic angle around a fixed axis in a laboratory frame, forming a cone shape after one rotation. The q -MAS has been demonstrated to effectively reveal the presence of microscopic anisotropy in macroscopically anisotropic materials. The pulse sequence provides the isotropic average of the diffusion coefficient and removes anisotropic contributions to $P(D)$. At the same time it preserves information of pore size dispersion. This method is independent of orientation dispersion, of the micro domains that display the anisotropic diffusion.

Here we present a method to quantify the microscopic anisotropy by comparing the isotropic diffusion weighting given by the q -MAS and the non-isotropic weighting given by a standard PGSE experiment. The non-isotropic diffusion weighting was done in 15 non-collinear gradient directions and arithmetically averaged over all directions in order to mimic a uniform orientation dispersion of micro domains. We introduce a new parameter that we call μFA , which represents the fractional anisotropic diffusion on a sub-voxel scale. This is in analogy to the standard fractional anisotropy parameter⁴ that quantifies the fractional anisotropic diffusion on a scale of the imaging voxel. Experiments on lamellar liquid crystals show good agreement to the theoretical value of the μFA of the diffusion in between plates in such structure.

The μFA parameter can give a new type of imaging contrast that can reveal structural information on a sub-voxel level.

References:

1. P. T Callaghan and O. Söderman, J Phys Chem 87 (1983) 1737-1744
2. C. S Johnson Jr., Prog Nucl Magn Reson Spectrosc 34 (1999) 203–256
3. S. Eriksson, S. Lasic and D. Topgaard. J Magn Reson 226 (2013) 13–18
4. P. J. Basser and C Pierpaoli J Magn Reson B 111 (1996) 209-219

Following transport of contrast agent particle in sand and soil column

*P. Faure^a, E. Michel^b, S. Rodts^a, S. Sammartino^b,
P. Guillet^c, M. Neugodova^b, A. Polidoric, S. Neveu^d*

^a Université Paris-Est, Lab. Navier (UMR8205, ENPC-IFSTTAR-CNRS), Champs-sur-Marne, France ; ^b Lab. EMMAH (UMR1114 INRA-UAPV), Avignon, France ; ^c Lab. de chimie bioorganique et systèmes amphiphiles, (UMR5247 IBMM), Avignon, France ; ^d Lab. PECSA, Université Paris 6, France

The capability to predict the fate in the soil of colloidal particles is of paramount importance as such particles can often carry adsorbed pollutant towards the groundwater or be themselves pollutants. Magnetic Resonance techniques permit to determine spatially resolved soil water content with imaging, or to estimate water distribution in soil microstructure as a function of pore size with relaxometry. It is also possible to follow water transfers in porous media (sand or soil) with profile imaging and to evaluate colloidal particle concentration with contrast agent using. The ferrimagnetic nanoparticles provided an important contrast for NMR imaging and relaxometry. This allowed us to determine displacement of the particles in the porous media.

With the aim of comparing their transport properties, in both saturated sand columns and repacked soil cores, we synthesized maghemite nanoparticles and stabilized them by adsorbing either ionic species onto their surface or neutral poly(ethylene-glycol) chains. NMR studies were performed on a vertical imaging spectrometer DBX 24/80 from Bruker operating at 0.5T (20MHz proton), which is equipped with a proton birdcage radio frequency coil of 20cm inner diameter for experiment on column, and with a minispec Bruker with 10mm diameter tube for agent contrast analysis effect on signal and for evaluating adsorption. We used global relaxation measurements (T_1 with IR and T_2 with CPMG sequences) to calibrate effect of particles on NMR signal, and double spin echo sequence and T_1 profile sequence to observe and calculate the contrast agent concentration for transport experiments.

With the two methods, we obtain concentration profile of particles in function of time (Fig. 1). Profiles spin-echo and T_1 allow good measurements of concentration in contrast agents for sand but for soil is more complicated, due to adsorption contrast agents in soil. Adsorption kinetic and impact on relaxation of contrast agent adsorbed has been evaluated.

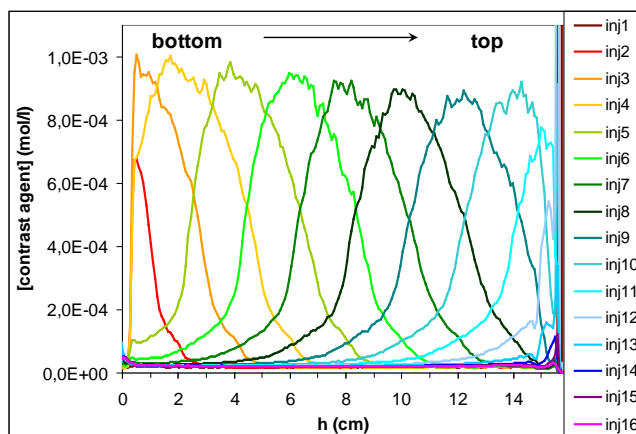


Fig. 1: Sand column with initial concentration of contrast agent: 10^{-3} mol/L. Concentration profile in contrast agent obtained with T_1 profile.

References:

1. P F. Faure, E Michel, S Sammartino, and C Doussan. Magnetic resonance imaging and relaxometry as tools to investigate water distribution in soils. AIP Conference Proceedings, Volume 1330 (MRPM10), p69 (2011)
2. Keating, K., and R. Knight, (2007) A Laboratory study to determine the effects of iron-oxides on proton NMR measurements. Geophysics, 72(1);
3. T R. Bryar, C J. Daughney, R J. Knight. Paramagnetic Effects of Iron(III) Species on Nuclear Magnetic Relaxation of Fluid Protons in Porous Media. J MAGN RESON , vol. 142, pp. 74-85 (2000);
4. Ramanan, Holmes Sloan and Phoenix, Environmental Science&Technology (2011);
5. Haber-Pohlmeier, Bechtold, Stapf and Pohlmeier, Valdose Zone J9 (2010)

Magnetic resonance imaging of local flow velocity profiles in biofilm carriers from waste water treatment

M. Herrling^a, G. Guthausen^b, H. Horn^a, S. Lackner^a

^aDepartment of Chemical Engineering and Process Engineering, Chair of Water Chemistry and Water Technology, Karlsruhe Institute of Technology, Engler-Bunte-Ring 1, 76131 Karlsruhe, Germany, ^bDepartment of Chemical Engineering and Process Engineering, Institute for Mechanical Process Engineering and Mechanics, Karlsruhe Institute of Technology, Adenauerring 20b, 76131 Karlsruhe, Germany

Biofilms are the most successful way of life on earth, which is formed by attachment of microorganisms (MOs) to surfaces. Being omnipresent in natural as well as in technical systems, biofilms show various structures with smooth, rough, fluffy, porous or compact texture¹. Besides traditional activated sludge systems, biofilms attached on carrier materials are of great interest to biological waste water treatment. For nitrogen removal, biofilm carriers are used in so called Moving Bed Biofilm Reactors (MBBRs) where the carriers are circulated by aeration or stirring to achieve high efficiency². It is well known that presence and the structure of biofilms influence the local flow field and mass transport of e.g. substrate¹. Therefore, we investigated the fluid-structure interactions of real biofilms from technical processes for a better understanding of the flow conditions and the substrate transport in MBBRs by means of Magnetic Resonance Imaging (MRI). In comparison, other studies mainly refer to pure cultures in idealized flow systems^{3,4}. MRI proves to be the ideal tool for non-destructive accurate imaging of living biological samples and has a strong potential in biofilm research.

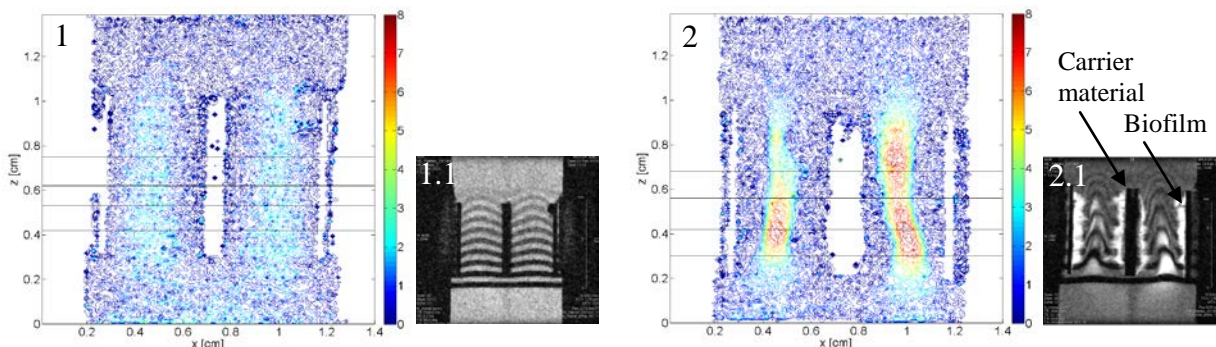


Fig. 1: Local flow velocity measurements in sagittal cuts: flow phase contrast images (FLOW PC) on a biofilm carrier (1) without biofilm and (2) with biofilm in tap water. The applied flow rate was 0.42 mm/s in flow direction (z -direction). The vertical color bar encodes the flow velocity v_z in mm/s. Figures (1.1) and (2.1) represent multi slice multi echo images of the same scenario where the displacement of the saturation stripes over time is proportional to the local flow velocity.

The spatially resolved flow velocity maps show a significant increase of the local flow velocities in the carrier due to the presence of the biofilm; see Figure 1, (1) and (2). The same applies to scenarios with higher applied flow rates. Furthermore, increasing local flow velocities result in higher shear stress and a compression of the boundary layer on the liquid-biofilm interface which favors the mass transport into the biofilm. This is expected to lead to a better performance of the biofilm carriers. However, the irregular geometry of the carrier material and heterogeneous biofilm morphologies are a challenge for the numerical image processing with the aim of reconstruction of shear and flow fields.

References:

1. H. Odegaard, *Water Sci. Techn.* 53 (2006) 17.
2. T.R. Neu & J.R. Lawrence, *Microbial glyco-biology*, Elsevier, San Diego, (2009) 735.
3. B. Manz et al., *Biotechnol. Bioeng.* 84 (2003) 424.
4. J. D. Seymour et al., *J. Magn. Reson.* 167 (2004) 322.

New method for down-hole two-NMR fluid analysis

Sijia Jiang, Lizhi Xiao, Guangzhi Liao, Yan Wu, Jiangjie Zhao*
 State Key Laboratory of Petroleum Resources and Prospecting
 China University of Petroleum, Beijing 102249, China

In general, conventional methods of measuring T_1 needs a long waiting time and the sample should keep static. However, the down-hole fluid always be polarized when it flows in the NMR fluid analyzer. So, the analyzer could measure T_1 continuously and quickly with the use of saturation-recovery or inversion-recovery method. The main application of T_1 is to estimate the contamination levels of mud-filtrate and to identify the fluid type.

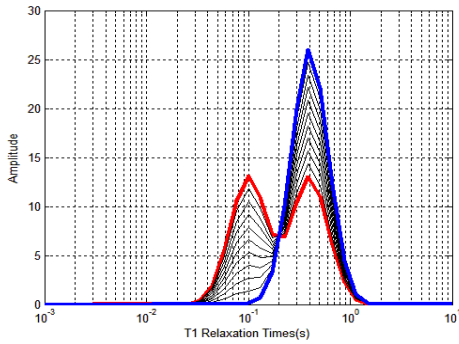


Fig-1: T_1 distributions for simulated data used in mixing-model validation.

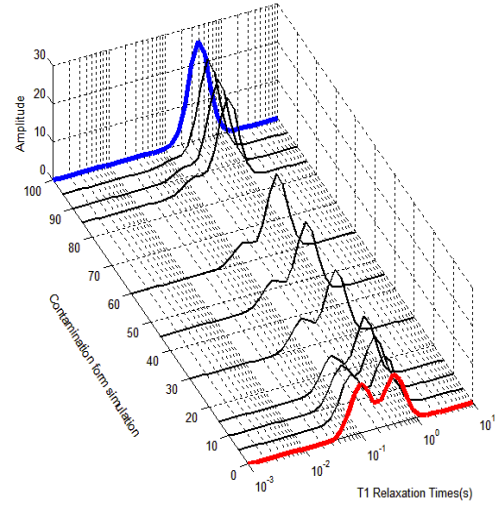


Fig-2: Simulated data of T_1 distributions with contamination from Fig-1

Visual Point-and-Click, Cutoff Value and Log-Mean Diffusion (D_{LM}) approach are employed to analyze the down-hole fluid quantitatively. According to the T_2 -D map, we will acquire the value of fluid saturation, gas-oil ratio, viscosity accurately with suited analysis method.

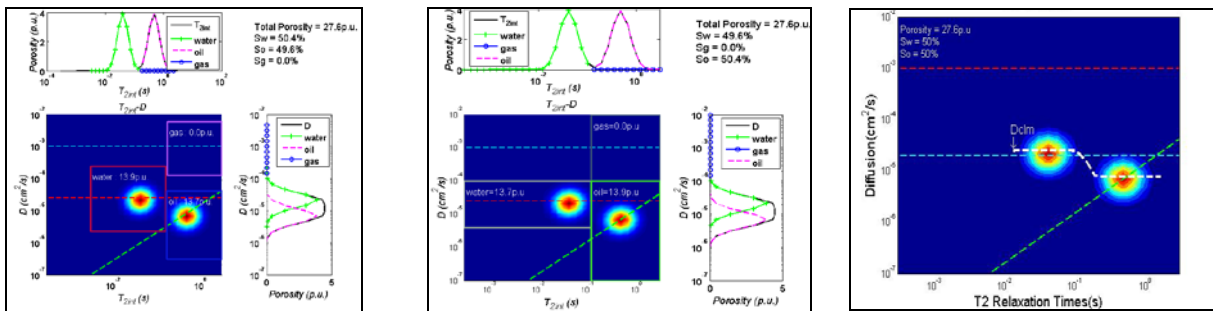


Fig-3: Three methods: a) Visual Point-and-Click, b) Cutoff Value, c) D_{LM} to calculate the down-hole fluid

References:

1. Ridvan Akkurt and Carl-Magnus Fransson, SPE. Sep 26-29(2004).
2. Chanh Cao Minh and Nick Heaton , SPE. Oct 5-8(2003).

Fast RARE velocimetry for curved flow in Couette geometry

Stefan Kuczera, Timothy Brox, Bradley Douglass and Petrik Galvosas

MacDiarmid Institute for Advanced Materials and Nanotechnology, Victoria University of Wellington, SCPS, Wellington, New Zealand

The properties of liquids under shear flow in Couette geometries is of wide interest in many fields like soft matter research or rheology. In particular quantitative information on the velocity field of the liquid trapped in the gap is of great importance for the study of local effects. Amongst several techniques such as particle imaging velocimetry (PIV), ultrasonic speckle velocimetry (USV) or optical methods, NMR has been extensively used to reveal the flow properties of Taylor vortices [1] and the flow behaviour of complex fluids [2] in this geometry. The non-invasiveness, e.g. no need of tracer particles, and the intrinsic 3-dimensional nature are factors that may make NMR preferential in many cases. Yet one of the challenges for NMR velocimetry is to strive for spatial and temporal resolution. This has led to the development of more sophisticated pulse sequences, that allow the acquisition of a multidimensional flow field within the order of seconds down to a few tens of milliseconds. However these techniques require a careful choice of acquisition parameters and thorough data analysis.

Here we want to address problems arising from a PGSE-RARE (pulsed gradient spin echo - rapid acquisition with relaxation enhancement) sequence that can generate a 2D velocity map of a complex fluid sheared in a cylindrical Couette geometry within 1-2 seconds with a spatial resolution of about 100 μm across the gap of the cell (s. Fig. 1). The experimental conditions in question are displacements that exceed the voxel size due to the curved nature of the flow, the appropriate choice of k -space sampling, slice thicknesses to minimise averaging effects and outflow. A recent study using PGSE-RARE has revealed anomalous lever rule behaviour for banded flow of a complex fluid in this geometry [3], which was controversially discussed even more recently [4]. A detailed experimental study supplemented by numerical calculations will be presented to clarify the situation and yield methods to correct velocity measurements for artifacts in post processing.

The obtained results will help to improve the understanding of measurements under similar conditions and further establish NMR velocimetry as an important experimental tool in soft matter research. Additionally using the example of the PGSE-RARE sequence the potentials of NMR velocimetry will be compared to other techniques.

References:

1. K. Kose, "Spatial mapping of velocity power spectra in Taylor–Couette flow using ultrafast NMR imaging", *Phys. Rev. Lett.* 72, 1467 (1994)
2. P. Callaghan, "Rheo-NMR: A New Window on the Rheology of Complex Fluids", *eMagRes*, 2007
3. K. Feindel and P. Callaghan, "Anomalous shear banding: multidimensional dynamics under fluctuating slip conditions", *Rheologica Acta*, vol. 49, pp. 1003–1013, 2010.
4. M. Fardin et al, "Shear-banding in surfactant wormlike micelles: elastic instabilities and wall slip", *Soft Matter*, vol. 103, 2012.

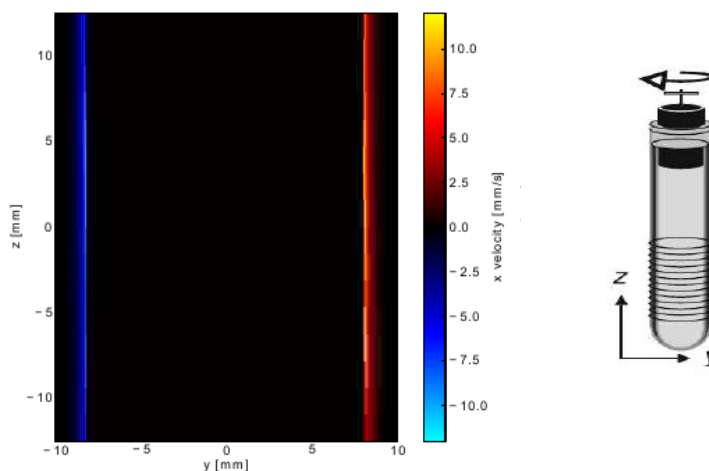


Fig. 1: 2D velocity field of a complex fluid under shear (left) in a Couette geometry (right) captured with a PGSE-RARE sequence. Effects due to a certain voxel size and fluid displacement during acquisition have to be considered in data interpretation, as artifacts can appear under certain conditions.

Characterization of oilfield emulsion using nuclear magnetic resonance

Nicholas N. A. Ling, Eric F. May, Einar O. Fridjonsson, Michael L. Johns

Fluid Science Division, Centre for Energy, School of Mechanical and Chemical Engineering,
University of Western Australia

Water-in-crude oil emulsions are problematic in a range of contexts regards oil production. Existing emulsion breaking technologies, typically employing chemicals and/or heat, are time consuming and often ineffective. Essential to screening and future development of emulsion breaking strategies is rapid, accurate measurements of the evolving emulsion droplet size distributions. This is particularly difficult for existing technologies when applied to concentrated emulsions. Here we present recent developments with respect to the use of bench-top nuclear magnetic resonance (NMR) pulsed field gradient (PFG) measurements to provide such a measurement capacity.

Specifically we detail measurements using a 1T permanent magnet system that retains chemical shift information allowing for unambiguous detection of the droplet water phase NMR signal. We outline the use of the discrepancy principle¹ to invert the PFG attenuation data to provide the droplet size distribution and show how it can be employed to detect any systematic errors in the procedure/system employed. We also demonstrate the application of flow-compensated PFG for emulsion droplet sizing² adapted for application on the 1T magnet. This is used to correct for velocity effects due to slight (0.7°) gradient misalignment. Finally we discuss developments with respect to accurate emulsion sizing under flowing conditions.

In terms of applications, we consider the use of physical emulsion inversion to o/w emulsions, which are more easily separated. We quantify the emulsion structure and droplet size distribution as the physical inversion point is approached via droplet phase addition and compare with conceptual models in the literature.

References:

1. K. G. Hollingsworth and M. L. Johns, Measurement of emulsion droplet sizes using PFG NMR and regularisation methods, *J. Colloid Interface Sci.* 258 (2003) 383.
2. M. L. Johns and L. F. Gladden, Sizing emulsion droplets under flowing conditions using Magnetic Resonance methods, *J. Magn. Reson.* 154 (2002) 142.

Investigating the molecular behaviour of ionic liquids using magnetic resonance

C. F. Smith, M. M. Britton

School of Chemistry, University of Birmingham, Edgbaston, Birmingham, B15 2TT, UK

Ionic liquids have a range of properties, such as high thermal stability, wide electrochemical window and ability to solvate a wide variety of compounds, which make them ideal as media for nanoparticle suspensions¹. Ionic liquid suspensions have been used in electroplating of metals² and as electrolytes in solar cells³. Investigation of the flow properties of these systems can give an insight into their underlying molecular behaviour and help improve their use as suspensions^{4,5}. The addition of nanoparticles to ionic liquids has previously been observed to change the flow properties of the system, such as forming shear thickening colloidal suspensions⁵.

Expanding on previous studies⁶, a range of suspensions of hydrophilic silica nanoparticles in the ionic liquid 1-butyl-3-methylimidazolium chloride, $[C_4mim][BF_4]$, have been investigated. It has been observed that changing concentrations of silica nanoparticles affects the rheology of the system. NMR techniques, such as velocimetry, have been used to investigate the system further. Figure 1 shows the radial velocity profile for $[C_4mim][BF_4]$ at different rotation rates, ω . This was generated from velocity measurements of $[C_4mim][BF_4]$ in a Couette cell. These measurements have enabled a more in depth understanding of how the silica nanoparticles interact with the ionic liquid.

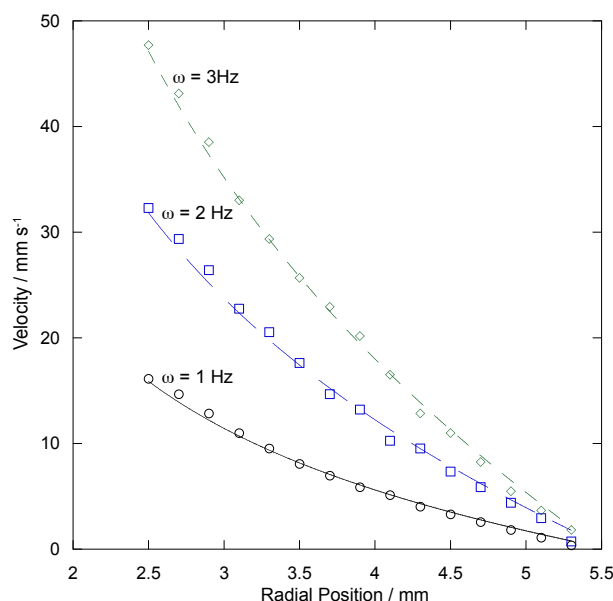


Fig. 1: Radial velocity profile for $[C_4mim][BF_4]$, showing fits from the power law equation at different velocities, ω , which gave an average value of the power law exponent, $n = 1$ indicating Newtonian behaviour.

References:

1. M. Freemantle, *An Introduction to ionic liquids*, RSC Pub.: Cambridge, UK (2010).
2. A. P. Abbott, F. Qiu, H. M. A. Abood, M. R. Ali, K. S. Ryder, *Phys. Chem. Chem. Phys.* 13 (2010) 1862.
3. A. Noda, K. Hayamizu and M. Watanabe, *J. of Phys. Chem. B*, 105 (2001) 4603.
4. K. Ueno, S. Imaizumi, K. Hata, M. Watanabe, *Langmuir*, 25 (2009) 825.
5. G. L. Burrell, N. F. Dunlop, F. Separovic, *Soft Matter*, 6 (2010) 2080.
6. J. Novak and M. M. Britton, *Soft Matter*, 9 (2013) 2730.

Measurement of transport and reaction in vortical flows using magnetic resonance

A. Vallatos, M. M. Britton,

School of Chemistry, University of Birmingham, Birmingham, B15 2TT, UK

An integrated approach combining magnetic resonance (MR) techniques with modelling has been used to study transport and reaction in stationary and travelling Taylor vortices. This work explores the coupling of an autocatalytic reaction with 3D vortical flows¹ produced in a Couette cell. Understanding this coupling is of interest in various fields from chemical engineering or biology. In particular, the interplay between micro-mixing and the transport of chemical signals has an important role in defining the nature and stability of spatial self-organisation in combustion, plankton blooming and biological morphogenesis.

Flow and molecular displacements, within stationary and translating vortices, were characterised using a combination of MR velocity and diffusion mapping (Fig.1a) with MR molecular displacement experiments (propagators). A model based on MR experimental data was developed to simulate molecular displacements (Fig.1b) and provide quantitative information on micro-mixing and long time-scale axial dispersion². Simulations of molecular displacements allowed to link molecular transport with the propagation of chemical waves travelling through vortical flows. MR imaging of chemical waves (Fig.1c) was shown to compare well with molecular displacement simulations, providing with a means for characterising the coupling of flow and chemistry in reactive flow systems.

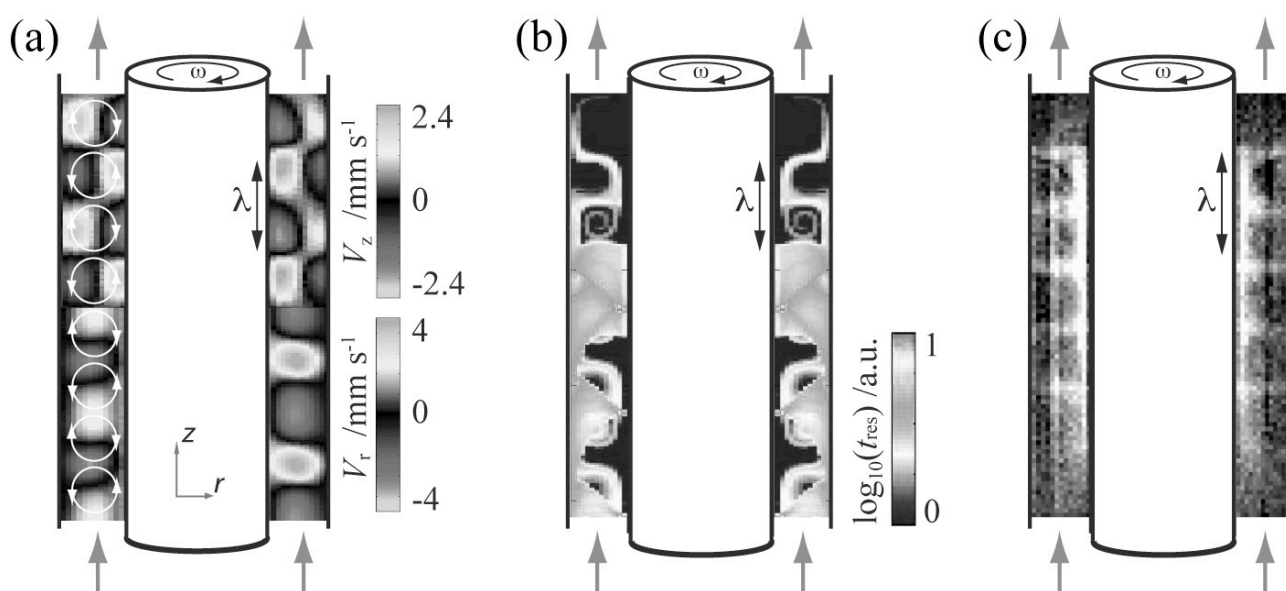


Fig. 1: (a) Velocity maps of traveling vortices in the axial (V_z) and radial (V_r) direction. (b) Molecular displacement map in the reference frame of the traveling vortices. (c) MR image of chemical wave propagation in traveling vortices. The bright regions indicate a high concentration of Mn^{3+} and the dark regions indicate a high concentration of Mn^{2+} . The arrows show the flow direction.

References:

1. A. Vallatos, R. D. Evans, A. F. Taylor and M. M. Britton, *Chaos* 23 (2013) 023115.
2. A. Vallatos, M. C. T. Wilson, A. F. Taylor and M. M. Britton, *Europhys. Lett.* 99 (2012) 68001

Density-Driven Fingering during Brine-Water Miscible Displacement in Two Inclining Porous Media Layers by Magnetic Resonance Image

Ruina Xu^{a,b}, Rong Li^a, Andy Sederman^b, Lynn Gladden^b, Peixue Jiang^a

^a Department of Thermal Engineering, Key Laboratory for Thermal Science and Power Engineering of Ministry of Education, Beijing Key Laboratory of CO₂ Utilization and Reduction Technology, Tsinghua University, Beijing 100084, China

^b Dept. of Chemical Engineering and Biotechnology, University of Cambridge, Cambridge, CB2 3RA, UK

Density-driven flows arise in many practical applications like waste repository management, petroleum engineering and geothermal energy exploration. The stability of such flows is known to depend on the density, viscosity, velocity, dispersion and the medium heterogeneity. The objective of this paper is to study the effect of the density of driven fluid on the fingering stability, to understand the spatial-temporal change of concentration inside the mixing zone quantify and to investigate the incline interface effect on the density-driven fingering and stability. Meanwhile, CFD (Computational Fluid Dynamics) was used to analyze the influence of buoyancy and heterogeneity effects on flow stability.

Magnetic resonance imaging techniques were used to measure the concentration distribution inside the mixing zone. The experimental test samples used were porous media with two layers of different permeability as shown in Fig.1. The sample inside the NMR was saturated with 3% KCl brine solution first and then displaced by the freshwater which was pumped into the samples with various flow rates. Fresh water and KCl solutions were selected as a pair of miscible working fluids to analysis density-driven fingering effects whilst excluding the viscosity changing effect. In order to obtain contrast in the MRI measurements the brine was doped with a contrast agent, Gd³⁺, to reduce the T_1 relaxation time such that the bulk and injected fluids could be differentiated. The unstable stratification of a dense fluid overlaying a lighter fluid (also known as Rayleigh-Taylor fingering) and the influence of interface shapes and injection parameters was obtained in this experimental study. Figure 2 shows the brine concentration in sample S1 when the injection rate was 5 ml/min. Water migration pathways are different because of the competition between the buoyancy and the viscosity resistance.

Numerical simulations to model the experimental studies were completed using commercial Computational Fluid Dynamics (CFD) software Ansys Fluent 13. The comparison between experimental and numerical results, shown in Fig. 3, shows that numerical method neglecting pore scale heterogeneity was able to capture the flow and mass transfer information on a layer-averaged scale, while the detail of flow instability which strongly depends on the perturbation of pore scale heterogeneity was not observed in numerical results although that was captured by the MR experiments clearly. The geometry of the interface between two layers influences the layer scale flow and the mass transfer is significantly dominated by the competition of buoyancy forces and layer scale heterogeneity.

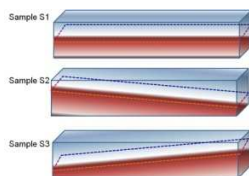


Fig. 1 The test samples: Upper layer is packed beds ($d_p=0.4-0.6$ mm), porosity=0.36, $K_1=1.49 \times 10^{-10}$ m⁻², bottom layer is packed beds ($d_p=1-1.2$ mm), porosity=0.38, $K_2=5.01 \times 10^{-10}$ m⁻²

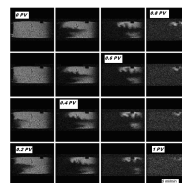


Fig. 2 The saltwater concentration in sample S1 when the injection rate was 5 ml/min

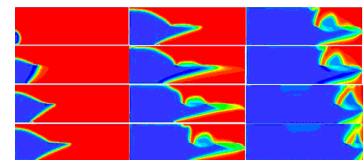


Fig.3 Numerical prediction result in sample S1 when the injection rate was 5 ml/min

Spatially resolved D - T_2 correlation NMR of porous media

Y. Zhang, B. Blümich,

Institut für Technische und Makromolekulare Chemie, RWTH Aachen University, Germany

Within the past decade, 2D Laplace nuclear magnetic resonance (NMR) has been developed to analyze pore geometry and diffusion of fluids in porous media on the pore scale.^{1,2} This study focuses on spatially resolved D - T_2 correlation techniques to access the information contained in pixels of similar contrast by pixel summation of experimental data from porous samples. D - T_2 correlation maps are measured in inhomogeneous fields by diffusion encoding with a modified stimulated echo employing anti-phase pulsed field gradient pairs to cancel the effect of background gradients³ and CPMG (Carr-Purcell-Meiboom-Gill) detection of the relaxation signal. Such D - T_2 maps can simply be acquired with spatial resolution by combining the 2D correlation NMR schemes with back-projection imaging and rotating these from acquisition to acquisition to subsequently reconstruct D - T_2 correlation maps in each pixel. The scheme has been tested on different samples, including glass-bead packs, mortar and a heterogeneous porous ceramic. First a high-resolution image of the sample is acquired, which delineates different sample regions. Then a low-resolution image is acquired with a D - T_2 map in each pixel. The D - T_2 from pixels corresponding to regions with similar contrast in the high-resolution image are averaged and analyzed for pore-scale heterogeneity associated with the contrast in the high-resolution image.

References:

1. L. Monteilhet, J.-P. Korb, J. Mitchell, P.J. McDonald, Observation of exchange of micropore water in cement pastes by two-dimensional T_2 - T_2 nuclear magnetic resonance relaxometry, *Physical Review E* 74 (2006) 061404.
2. M.D. Hürlimann,^a L. Venkataramanan, C. Flaum, The diffusion-spin relaxation time distribution function as an experimental probe to characterize fluid mixtures in porous media, *J. Chem. Phys.* 117 (2002) 10223.
3. R. M. Cotts, M. J. R. Hoch, T. Sun, and J. T. Markert, Pulsed field gradient stimulated echo methods for improved NMR diffusion measurements in heterogeneous systems, *J. Magn. Reson.* 83 (1989) 252 .

Accelerating Imaging with a Unilateral NMR Scanner

E. Bergman¹, A. Liberman¹, Y. Sarda¹, A. Yeredor², U. Nevo¹

¹Department of Biomedical Engineering, ²Department of Electrical Engineering, the Iby and Aladar Fleischman Faculty of Engineering, Tel-Aviv University

Introduction Unilateral NMR devices are currently not applied routinely for imaging. The inhomogeneity of B_0 in these scanners [1] forces the use of the relatively slow Single Point Imaging (SPI) schemes and results in a poor SNR and long averaging times. Reducing the scan duration is thus a key factor in facilitating the use of this affordable and portable technology for imaging applications. We suggest two complementary approaches to accelerate imaging times: (1) Improving the SNR of the acquired MR signal with a novel statistical signal-processing method which exploits the redundancy in the acquired MR signal and the noise characteristics via Least Square estimation approach. (2) A Fast Spin Echo (FSE) sequence which was especially modified for imaging with a unilateral scanner and overcomes the basic restriction posed by SPI.

Methods: *1. Slice selective Image reconstruction with the estimation approach* - In the presence of the constant gradient, the acquired echo is not only phase-encoded by gradients in the lateral directions (x,y) [2], but also frequency encoded (z direction) during acquisition. Since the excited slices are very thin we assume that image can be approximated as: $I(x, y, z) \approx I(x, y) \cdot I(z)$. The phase encoded coefficient, $\alpha + i\beta$, can thus be estimated at every phase encoding step, by minimizing:

$$J(\alpha, \beta, \underline{a}) = \left[Y - \begin{pmatrix} h_r & -h_i \\ h_i & h_r \end{pmatrix} \cdot \begin{pmatrix} \alpha \\ \beta \end{pmatrix} \cdot \underline{a} \right]^T C^{-1} \left[Y - \begin{pmatrix} h_r & -h_i \\ h_i & h_r \end{pmatrix} \cdot \begin{pmatrix} \alpha \\ \beta \end{pmatrix} \cdot \underline{a} \right]$$

Here the frequency encoded echo (h) is evaluated independently in a short measurement with no planar encoding. \underline{a} is a vector of echoes amplitudes, Y is the measured data and C is the model error covariance matrix, derived from the measurements of noise in-between excitations periods at each encoding step.

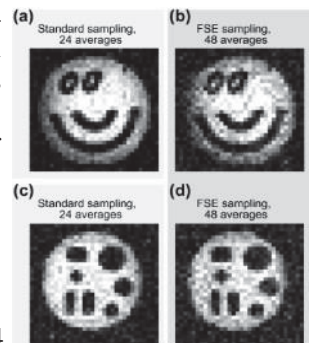
2. Fast Spin Echo (FSE)- FSE was implemented with differential phase encoding by applying two consecutive gradient 'blips' per k-point phase-shift, with no rephasing. The use of short gradient 'blips' allowed the use of short TE. Within the N-echoes train, the first coefficient was encoded based on the integration of the first M echoes, and the second coefficient of the remaining $N - M - 2$ echoes. M was calculated by demanding equal energy for both parts of the FID, given a pre-measured T2. An extended 4-step phase cycling scheme was employed to gather all four components of the pre-blip and post-blip magnetization. This was done by alternating the orthogonal direction of the post-blip π pulses.

Results Three circular shaped phantoms were scanned with the NMR-MOUSE. Images were reconstructed with the weighted (WLS) and non-weighted LS estimation and compared to a conventional reconstruction via the MSE criterion with respect to gold standard images (Table 1). The results show significant improvement in the quality of the images in all experiments. Fig. 1 presents the FSE imaging results: an FSE scan with 48 averaging repetitions (Fig. 1b for phantom A, Fig. 1d for phantom B) is compared to a standard scan with 24 averaging repetitions (Fig. 1a for phantom A, Fig. 1c for phantom B) resulting in an equal scan time. FSE is thus feasible in a unilateral NMR.

	Error-Improvement (%) = $100 \left(1 - \frac{MSE(I_{est})}{MSE(I_{conv})} \right)$					
	Phantom A		Phantom B		Phantom C	
	LS	WLS	LS	WLS	LS	WLS
Experiment 1	18%	19%	9%	29%	17%	22%
Experiment 2	17%	36%	21%	24%	17%	19%
Experiment 3	11%	26%	16%	22%	10%	23%

Table 1: The error-improvement of the LS and WLS estimations from scans of phantoms A, B and C, with three experiments for each

Fig. 1: FSE experiment results with phantoms A (left) and phantom B



References [1] Blumich, B. *et al.* Prog. Nuc. Mag. Res. Spec.2008. [2] Perlo, J. *et al.* JMR 2004

The new application of low-field NMR technology in petroleum evaluation

Qing Cai^a, Yingli Zhang^a, Yi Yang^a, Peiqiang Yang^a,

^aNiumag Company, Suzhou 215163, China

In recent years, more and more exploration and development of unconventional oil and gas storage Unconventional reservoir is prominently characterized by nanometer scale pores and non-Darcy flow, which determines its differences compared with the conventional reservoir, such as oil or gas, distribution, accumulation mechanism, and drilling or production technology, etc. So, the conventional NMR technology can not satisfy with the reservoir demands. So we change the hardware and methods to develop new applications in petroleum exploration field using low-field NMR technology.

1. Nanometer Scale Calibration

Low-field NMR technology has higher resolution and can detect approximately 2nm scale pores.



Fig. 1: MicroMR-CL NMR analysis system

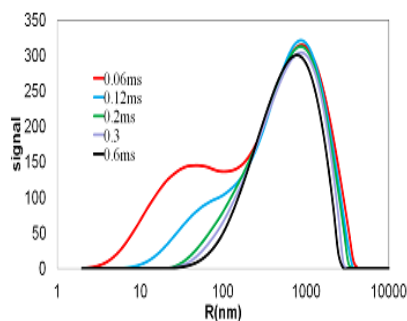


Fig. 2: Shows the effect of different TE values on the nanoscale pore

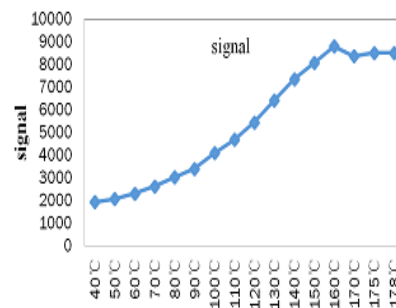


Fig. 3: Shows the signal of different temperature

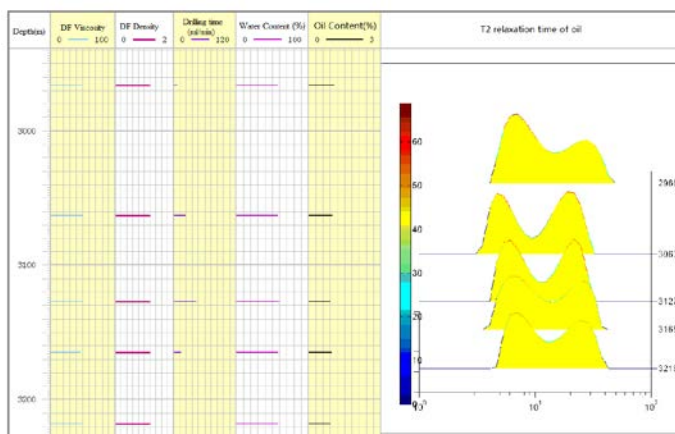


Fig. 4: Shows the oil and water content on different depths

2. Heavy Oil in Nanometer Pore Calibration

The more temperature increasing, the more signal get and the T2 relaxation time increasing.

3. Drilling Fluid Testing

Using Low-field NMR technology can test the oil and water content of drilling fluid, and has higher precision. These methods provide valuable complements to the existing mud logging series, and can be used to improve oil layer finding ratio and evaluation precision ratio

Biofilm detection using low field magnetic resonance

*Catherine M. Kirkland^a, Randy Hiebert^a, Elliot Grunewald^b, Dave Walsh^b, Joseph D. Seymour^a,
Sarah L. Codd^a*

^aCenter for Biofilm Engineering, Montana State University, Bozeman, USA

^bVista Clara, Seattle, USA

This research addresses the challenges associated with in-situ monitoring and mapping of the geochemical and microbial activity central to bioremediation of subsurface contaminants. Remediation efforts often include growth and maintenance of a biofilm mat to contain or degrade chemical contaminants [1]. Previous research with geophysical remediation methods have indicated that nuclear magnetic resonance (NMR) is sensitive to the biogeochemical processes associated with remediation—biofilm growth (location and density of biofilm or biofouling) [2] and biofilm induced iron redox reactions which change the contaminants to an insoluble form in the subsurface [3]. Previous research conducted at MSU has shown that the Vista Clara low-field NMR spectrometer, can detect the presence of biopolymers in laboratory samples of both high and low susceptibility geological materials by measuring T_2 relaxation times [4].

This research addresses the challenges associated with in-situ monitoring and mapping of the geochemical and microbial activity central to bioremediation of subsurface contaminants. The bioreactor is on a larger scale than the previous work and uses a novel radial flow design to simulate biofilm growth around a well bore. It is difficult, however, to monitor the establishment and growth of the subsurface biofilm over space and time, making it challenging to measure the effectiveness of the remediation efforts in a cost effective and non-destructive manner.

This research focusses on the development of a new phase of low-cost NMR instrumentation that will support 1) in-situ monitoring over space and time and 2) NMR measurement and interpretation methods to allow better monitoring of biofilm growth and geochemical remediation processes in the subsurface. Successful development of this new phase of NMR instrumentation has the potential to reduce the cost and improve the efficacy of monitoring subsurface remediation efforts.

References:

- [1] Cunningham, A.; Sharp, R. R.; Hiebert, R.; James, G., Subsurface biofilm barriers for the containment and remediation of contaminated groundwater. *Bioremediation* 2003, 7, 151-164.
- [2] S.L. Codd, S.J. Vogt, J.A. Hornemann, A.J. Phillips, J.E. Maneval, K.R. Romanenko, L. Hansen, A.B. Cunningham, J.D. Seymour, "NMR Relaxation Measurements of Biofouling in Model and Geological Porous Media." *Organic Geochemistry* 42: 965–971 (2011)
- [3] Keating, K., R. Knight, and K. Tufano, "Nuclear magnetic resonance relaxation measurements as a means of monitoring iron mineralization processes." *Geophysical Research Letters*, 35,L19405, doi10.1029/2008GL035225. (2008)
- [4] Sanderlin, A. B., S. J. Vogt, E. Grunewald, B. A. Bergin, S. L. Codd, "Biofilm detection in natural unconsolidated porous media using a low-field magnetic resonance system." *Environmental Science and Technology*. (DOI: 10.1021/es3040686) 2012

Motion effects and corrections of NMR scanning measurement

Deng Feng, Xiao Lizhi, Liao Guangzhi, Liu Huabing, An Tianlin, Jia Zijian

State Key Laboratory of Petroleum Resources and Prospecting, China University of Petroleum, Beijing 102249, China

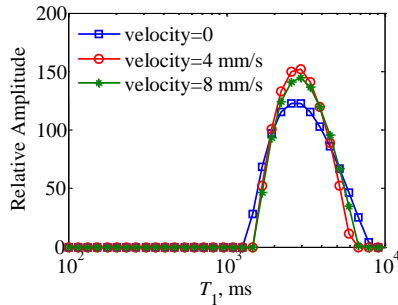
NMR measurement at motion gets more and more important¹. Movement speed will affect both polarization and echo acquisition processes during an NMR experiment². Keeping the instrument moving, a part of the sample is not fully polarized when it enter into the magnet, whereas the other part was fully polarized. This discrepancy caused a part of the polarization to be incomplete. In the echo acquisition process, a part of the magnetization vector was not tipped into X-Y plane by a 90° pulse, whereas the other part of the magnetization vector was done. This discrepancy caused the signal acquisition to be incomplete. These process can be expressed as:

$$M_i = \phi S_i H_{1,i} \{1 - \exp[-T_w (\frac{1}{T_{1,i}} + X_v)]\}, ECHO = \sum_{i=1}^n M_i \exp[-t(\frac{1}{T_{2,i}} + Y_v)],$$

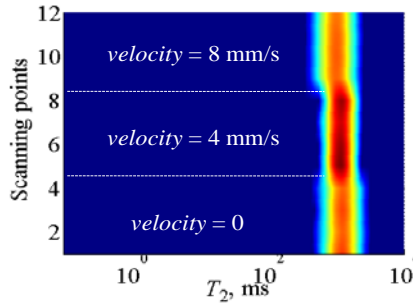
where X_v and Y_v represent motion effects of the polarization and echo acquisition processes, respectively.

A new method for motion corrections of NMR data³ based on quantitative analysis of motion effects on polarization and echo acquisition, is proposed. A set of multi-functional NMR scanning system is independently designed and developed to verify the theoretical analysis. Presented experiments demonstrate that the theoretical and experimental results matches very well.

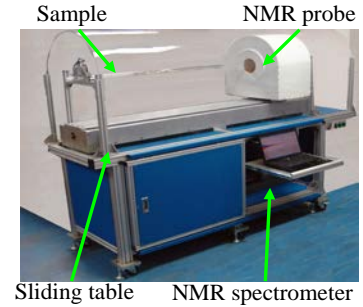
(a) T_1 maps (before correction)



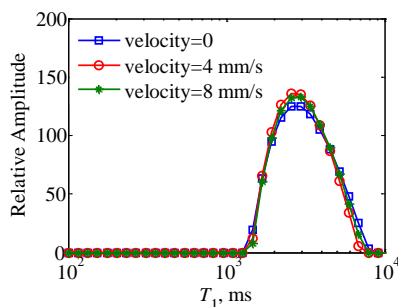
(c) T_2 maps (before correction)



(e) NMR scanning system



(b) T_1 maps (after correction)



(d) T_2 maps (after correction)

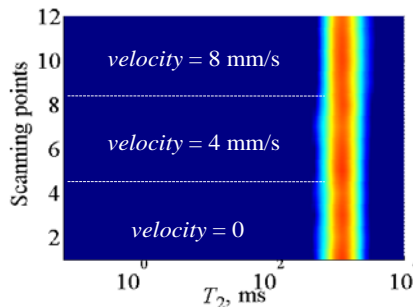


Fig.1:NMR scanning measurement and motion correction:(a) and (c) are T_1 and T_2 maps with variable motion velocity, $TW=3000$ ms, sample is distilled water (b) and (d) results of the motion correction on (a) and (c); (e) is the photo of NMR scanning system.

References:

1. G. R. Coates, L. Z. Xiao, M. G. Prammer. Texas: Gulf Professional Publishing, 2000
2. C. M. Edwards. SPWLA's 38th Annual Logging Symposium, Houston, June 1997
3. C. M. Chanh, L. Jack, C. Steven, N. B. Henry. U.S. 2012/0025820 A1, 2012

The Mini-MOUSE – a miniaturized NMR sensor

D. Oligschläger^a, S. Glögler^b, J. Watzlaw^c, B. Blümich^b

^aInstitut für Technische und Makromolekulare Chemie, RWTH Aachen Germany

^bUniversity of California, Los Angeles, USA

^cInstitut für Werkstoffe der Elektrotechnik, RWTH Aachen, Germany

The Mini-MOUSE, a miniaturized version of the NMR-MOUSE[®] has been built from four 2 x 2 x 2 cm³ Neodymium permanent-magnet cubes, positioned on an iron yoke. They are combined with a stacked-microcoil in quadratic shape and an edge length of 4 mm (Fig. 1 a, b). The sensitive slice is located 800 μm above the microcoil, enabling the possibility to record depth profiles by shifting the sensitive slice through a given sample with the help of a positioning device. The maximum achievable resolution is about 8 μm. The sensor has a gradient of 53.6 T/m and its SNR (Signal-to-noise-ratio, normalized to pulse length and coil size) is 1.8 times higher than the SNR of a standard PM5.

The micro-coil enables the use of very short echo times, such as 16 μs. Short echo times are of benefit by analyzing materials with very short relaxation times like polymers, concrete and paintings. Considering a CPMG experiment, short echo times are of high benefit due to a higher number of data points compared to an experiment using longer echo times, which consequently increases the information for short relaxation components.

The Mini-MOUSE has been employed in measurements of polymer samples, such as HDPE with two different grades of crystallinity and Nylon (Fig. 2). Given the small size of the micro-coil, a single grain of polymer can be measured. Different crystallinity grades can be distinguished. Moreover car-polish samples and human skin were analyzed with the Mini-MOUSE. The w-profile reveals different layers (plastic, grounding and two polish layers) of the car-polish sample (Fig. 3).

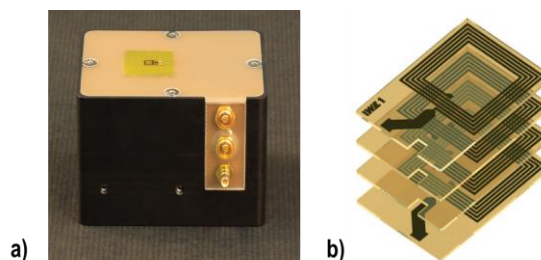


Fig. 1: a) Picture of the Mini-MOUSE. The magnet assembly, as well as the NMR-circuit are included in a housing which can be mounted on a manual or motor lift to enable depth-profiling. b) Scheme of the stacked micro-coil used with the Mini-MOUSE sensor.

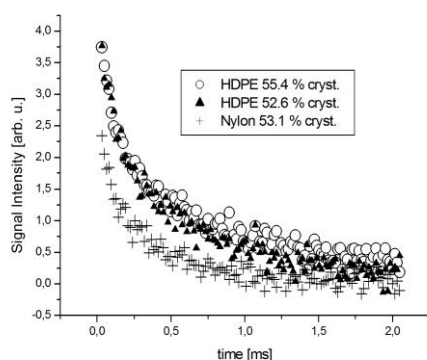


Fig. 2: CPMG measurements of single grains of HDPE and Nylon, measured with the Mini-MOUSE using an echo time of 16 μs.

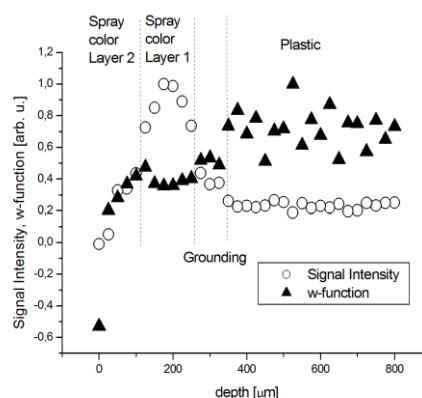


Fig. 3: Depth profile of a car polish sample. Different layers of polish, the grounding and the ground material can be distinguished in the w-profile.

References:

1. B. Blümich, P. Blümmler, G. Eidmann, A. Guthausen, R. Haken, U. Schmitz, K. Saito, G. Zimmer, *Magn. Reson. Imaging*, 16 (1998) 479-484.
2. J. Watzlaw, S. Glögler, B. Blümich, W. Mokwa, U. Schnakenberg, *J. Magn. Reson.*, 230 (2013) 176-185.

Inverse Laplace transform strategies suitable to inhomogeneous NMR magnet systems.

M. N. d' Eurydice^a, P. Galvosas^a.

^a School of Chemical and Physical Sciences – Victoria University of Wellington – New Zealand

One sided NMR devices have become a very powerful tool in order to perform low field NMR diffusion and relaxation analysis. These analysis are very useful in the industry environment when evaluating the quality and quantity of Hydrogen based materials, besides distinguishing the content proportions of different phases in the samples. Several techniques have been developed over the last decade in order to take advantage of the characteristics of these devices, increasing their applicability to many different fields¹⁻³.

In order to determine diffusion coefficients of fluids in different environments, this work uses a pulse sequence combining spin echo and CPMG experiments (SGSE-CPMG)⁴, where the first echo time is varied in each subsequent measurement to record a two-dimensional data set. Data processing is based on a two step inverse Laplace transformation. The first processes the set of CPMG decays to obtain a set of T_2 distributions, which is used to corrected for T_2 relaxation during the first stage of the pulse sequence responsible for measuring the diffusion coefficients. Subsequently, the second determines the diffusion coefficient distribution using the T_2 corrected data set in conjunction with a customized kernel, based on the results of a standard sample. As a result, this novel procedure enables the determination of $D \times T_2$ correlation maps even using the inhomogeneous magnetic field provided by the MOLE⁵ magnet array, Fig. 1(a) and (b), without requiring pulsed field gradients.

This technique can be used for the determination of proportional content of fluid mixtures as well as to explore diffusion of fluids in porous host systems using one sided NMR devices.

The experiments were performed using the Kea2 spectrometer⁶ and the Mobile Lateral Explore, Fig. 1(a) and (b). Using water+CuSO₄ and kitchen oil as standard samples, the determination of proportional content was tested artificially, Fig. 1(c) and (d), in order to show the efficiency of the method.

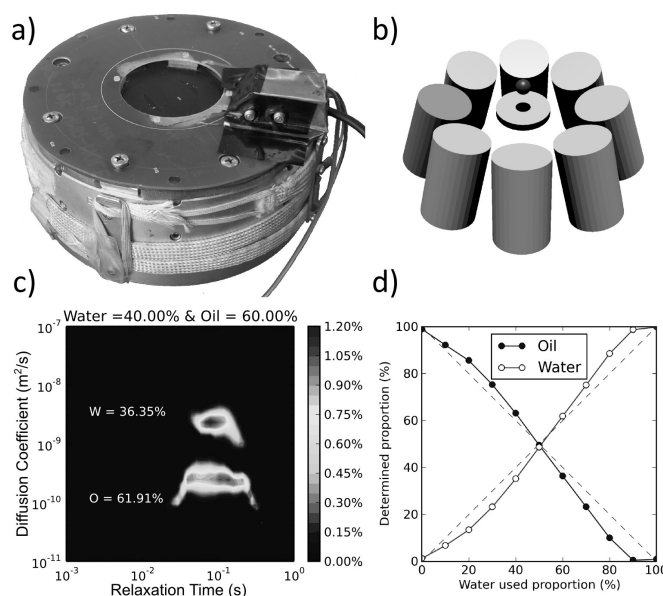


Fig. 1 - The Mobile Lateral Explorer, a) MOLE NMR, which is constituted by a b) permanent magnet array. c) $D \times T_2$ correlation map of different concentration of water and oil signals composed artificially. d) Determination of water and oil content for different proportions.

References:

1. B. Blümich, J. Perlo, and F. Casanova, *Progress in Nuclear Magnetic Resonance Spectroscopy*, 52 (2008) 197.
2. E. Veliyulin, C. van der Zwaag, W. Burk, and U. Erikson *Journal of Science of Food Agriculture*. 85 (2005) 1299.
3. I. G. Aursand, et al, *Journal of Agriculture Food Chemistry*. 57 1 (2009) 46.
4. D. G. Rata, F. Casanova, J. Perlo, D. E. Demco, and B. Blümich, *Journal of Magnetic Resonance*, 180 (2006) 229.
5. B. Manz, A. Coy, R. Dykstra, C. Eccles, M. Hunter, B. Parkinson & P. Callaghan, *Journal of Magnetic Resonance*, 183(1) (2006) 25
6. <http://www.magritek.com/>

Study of NMR responses in particle packing models

Wei Xu, Lizhi Xiao, Guangzhi Liao, Feng Deng, Zongfu Zhang, Jiajie Cheng

China State Key Laboratory of Petroleum Resources and Prospecting

China University of Petroleum, Beijing 102249, China

The internal magnetic gradients induced by susceptibility contrast in the porous media usually destroy the homogeneity of background field, thus affect the NMR measurements. For analyzing characteristics and influence factors of internal gradients, the dipole field method¹ is performed on the calculation of local magnetic field gradients from different particle packing models². The effective gradient, which represents the volumetrically weighted average of internal gradients, is proposed. At last, the NMR responses and T_2 - D and T_2 - G maps of different models are simulated via combination of random walk³ algorithm and dipole field method. The simulated results are matched with real measurements, which demonstrate that the methods used in this paper are suitable for the numerical simulation of NMR responses from particle packing models. The effective gradient is valid in the monodisperse packing model and the polydisperse packing model with good sorting.

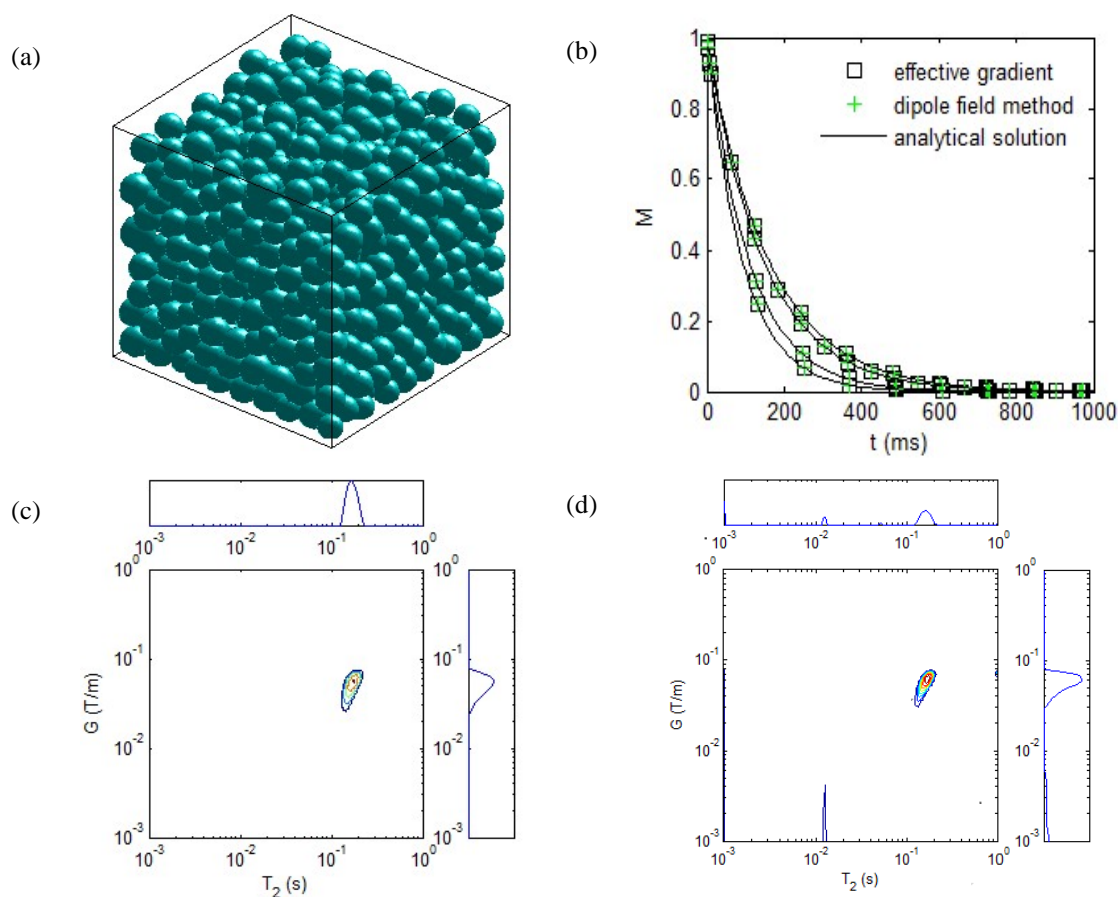


Fig. 1: (a) polydisperse random packing model; (b) simulated echo trains; (c) simulated T_2 - G map; (d) experiment results;

References:

1. P. N. Sen, S. Axelrod. J Appl Phys. 86(1999)4548.
2. D. He, N. N. Ekere, L. Cai. Phys. Rev. E. 60(1999) 7098.
3. E. Toumelin, C. Torres-Verdín, B. Q. Sun et al. J. Magn. Reson. 188(2007) 83.

Determining structural anisotropy of biological tissues using two-dimensional DDCOSY NMR

F. Zong, M. N. d' Eurydice, P. Galvosas

MacDiarmid Institute for Advanced Materials and Nanotechnology, School of Chemical and Physical Sciences, Faculty of Sciences, Victoria University of Wellington, New Zealand

As cancer leads to increasing mortality worldwide, early detection is essential to patient survival. Contrast agents are commonly applied in hospital to enhance T_1 or T_2 divergence between healthy and cancerous tissues. However, this method is invasive, expensive and time-consuming and may not be tolerated by some patients. On the other hand, it is noticeable that the diffusivity of fluids in tissues may be anisotropic. Diffusion Tensor Imaging (DTI) is suited to evaluate Fractional Anisotropy (FA) from the diffusion tensor eigenvalues in each pixel^{1,2}, which has larger contrast than Relative Anisotropy (RA) and the Apparent Diffusion Coefficients (ADC)³. FA was found to degrade by a factor of 3 with the exacerbation of cyst in normal tissues¹, which makes it a candidate for robust early cancer detection without contrast agents.

Anisotropic structures has been studied by two-dimensional NMR Diffusion-Diffusion COrrrelation Spectroscopy (DDCOSY)^{3,4,5}, providing a promising approach for obtaining similar parameters as compared to DTI. To this extend DDCOSY experiments were performed on bulk water, water in 20 μm diameter aligned capillaries and in biological tissue. After data processing, isotropic features for the bulk water can be identified by diagonal peaks as shown in Fig.1 (a). On the contrary, anisotropic features can be distinguished by off-diagonal peaks due to the presence of oriented structures (capillaries) as seen in Fig.1 (b). Furthermore, for preliminarily testing the feasibility of DDCOSY before using human tissues, carrot was chosen as it is widely available and used as an anisotropic biological phantom⁷, leading to the distribution in Fig.1(c). Subsequently, the eigenvalues can be extracted from the orthogonal apparent diffusion coefficients D_1 and D_2 , thus the ratio of D_1 and D_2 (regarding the simplified ellipsoid model of the diffusion tensor⁸) can be calculated as an indicator of the anisotropy for tissue characterization. All the experiments were performed on Avance 400MHz Bruker spectrometer.

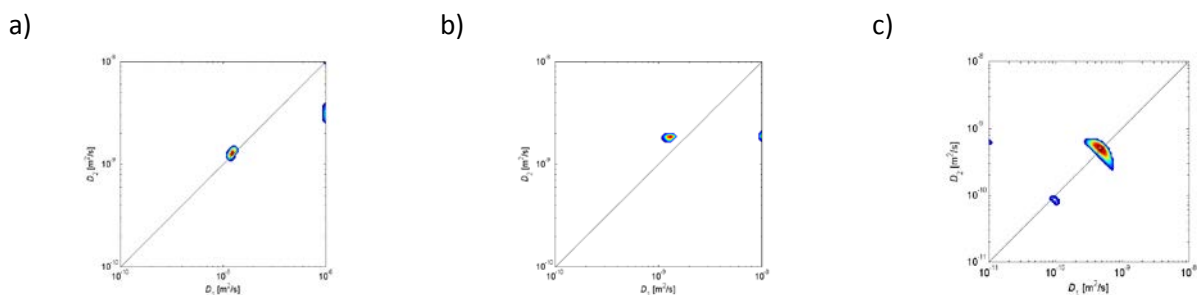


Fig. 1 D-D correlation map under three scenarios: a) Isotropic diffusion; b) Macroscopic anisotropic diffusion in 20 μm diameter capillaries; c) Macroscopic isotropic with microscopic anisotropic diffusion.

References:

- [1] S.C. Partridge, R.S. Murthy, A. Ziadloo, et al. *Magnetic Resonance Imaging*, 28 (2010) 320
- [2] C. Beaulieu. *NMR in Biomedicine* 15(2002) 435
- [3] P. Galvosas, and P. T. Callaghan, *Comptes Rendus Physique*, 11 (2010) 172
- [4] N. Spindler, Forschungszentrum Jülich GmbH, Jülich, 2011
- [5] P.T. Callaghan, Oxford University Press, New York, 2011
- [6] C. Beaulieu, P. S. Allen. *Magnetic Resonance in Medicine*, 31(1994) 394
- [7] D. Güllmar, T. Jaap, M. E. Bellemann, et al. *Biomedical Engineering* 47(2002) 420.
- [8] K.M. Hasan, A.L Alexander, and P.A. Narayana. *Magnetic Resonance in Medicine*, 51(2004) 413

Measuring Soil Moisture with Slim-line Logging NMR Tool

B. Guo, J. Perlo, S.Haber-Pohlmeier, B. Blümich

Institut für Makromolekulare Chemie, RWTH Aachen University, Germany

Soils are recognized as an important factor for the food production and for the balance in many ecosystems. As a powerful technology, Nuclear magnetic resonance (NMR) could detect the hydrogen nuclei contained in the water between soils, which can determine the soil moisture directly. And compared with conventional methods, such as electrical and acoustic methods, NMR is more accurate and non-invasive. The design and use of a first-generation Slim-Line Logging (SLL) NMR tool for measuring water content in the vadose zone at shallow penetration depths had been reported earlier [1]. Recently a second-generation SLL NMR tool has been developed that reaches a penetration depth of 20 mm measured from the outer wall of the pipe without compromising sensitivity [2].

In this case, a model soil is studied with the second-generation SLL NMR tool to demonstrate that the sensor can follow the dynamics of outflow, imbibition and migration of a moisture front. An outflow experiment is carried out in a 2 m dual-column composed of an external and an internal tube of 20 cm and 7 cm diameter, respectively. The space between them was filled with the model soil initially saturated with water. The SLL tool is fixed at certain position inside the internal tube, to monitor the content variations of bound water, mobile water and total water. Then hydraulic conductivity and hydraulic head can be calculated from the curve of water content vs. time using Richards equation. Finally, T_1 - T_2 and D - T_2 experiments are carried out in glass beads with two different sizes, the water distribution in unsaturated situation, such as soil, would be studied in these experiments.

References:

1. O. Sucre, A. Pohlmeier, A. Miniere and B. Blümich, *Journal of Hydrology*, 406 (2011) 30-38.
2. J. Perlo, E. Danieli, J. Perlo, B. Blümich and F. Casanova, *Journal of Magnetic Resonance*, 233 (2013) 74-79.

Unilateral Magnet with solenoid RF probe for magnetic resonance analysis of core plugs

Pan Guo^{a,b}, Juan C. Garc ía-Naranjo^{a,c}, Florin Marica^a, Guangzhi Liao^a, Bruce J. Balcom^a

^aMRI Research Centre, Physics Department, University of New Brunswick, Canada

^bState Key Laboratory of Power Transmission Equipment & System Security and New Technology, Chongqing University, Chongqing, China

^cCentre of Medical Biophysics, Universidad de Oriente, Patricio Lumumba S/N, Santiago de Cuba, Cuba

Magnetic Resonance has a long history of applications in the petroleum area [1], and two general classes of experiments and instruments can be distinguished. The first class involves downhole NMR tools [2], and the second class is a benchtop measurement [3].

A new approach for the second class of measurements, employing a unilateral magnet (2.25MHz) with a solenoid (see Fig.1a) as the RF probe is presented. A three-magnet array, with a homogeneous spot and an extended constant gradient, were employed separately. This approach avoids signal from the near surface region of the core plug, which is affected by cutting tools and may not produce reliable information. Core plugs (see Fig.1b) of different lengths and diameters can be measured employing solenoids of different diameters as the RF probe.

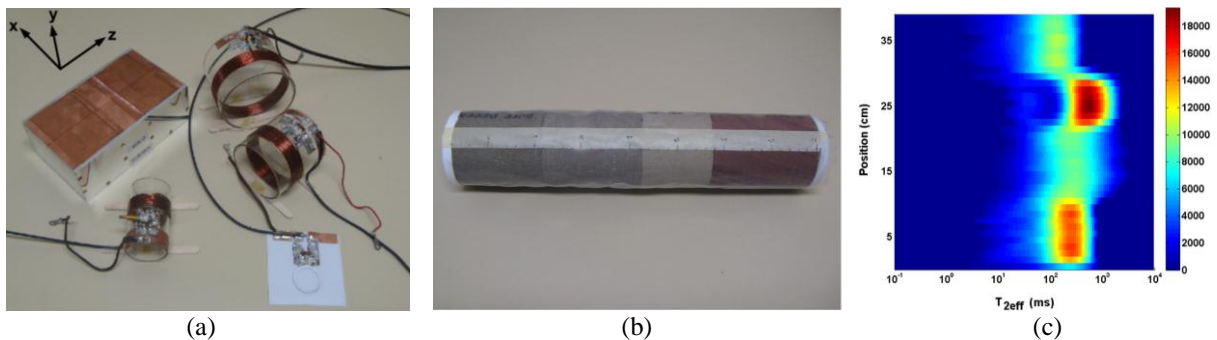


Fig. 1: (a) Three magnet array with homogeneous spot, surface coil (3 cm diameter) and solenoid RF probes of 4.2 cm, 7 cm and 9 cm diameters. (b) Composite sample of 3.5" diameter created from individual core plugs of different brine saturated rocks. From left to right Berea, Indiana Limestone, Bentheimer and Nugget sandstone core plugs held together with a heat shrink tube and two Teflon end caps. (c) T_{2eff} distributions of the composite core plug sample.

The result has shown that the three-magnet array is a very simple and reliable tool for core plug analysis. Porosity and T_{2eff} profiles as well as T_{2ff} distributions (see Fig.1c) have been obtained. The solenoid, easy to build and more sensitive, is a much better RF probe than the surface coil to explore deeper layers inside the sample. Even though the three-magnet array with an extended constant gradient reduces the size of the measurement spot and therefore reduces the SNR, it is a reasonable option for exploring very deep layers inside the core plug if one employs a solenoid RF probe. The three-magnet array unilateral magnet instrument with solenoidal RF probes is also able to monitor displacement processes in core plug samples.

References:

1. J. A. Jackson, L.J. Burnett, J. F. Harmon, Remote (inside-out) NMR. III. Detection of nuclear magnetic resonance in a remotely produced region of homogeneous magnetic field, *J. Magn. Reson.* 41, 411–421, 1980.
2. R. L. Kleinberg, NMR measurement of petrophysical properties, *Conc. Magn. Reson.*, Vol. 13(6), 404–406, 2001.
3. S. Anferova, V. Anferov, J. Arnold, E. Talnishnikh, M.A. Voda, K. Kupferschl äger, P. Blümner, C. Clauser, B. Blümich, Improved Halbach Sensor for NMR Scanning of Drill Cores, *Magn. Reson. Imag.* 25, 474-480, 2007.

A novel three-cylinder array NMR sensor with homogeneous spot or extended constant gradient

Pan Guo^{a,b}, Juan C. Garc ía-Naranjo^{a,c}, Bruce J. Balcom^a

^aMRI Research Centre, Physics Department, University of New Brunswick, Canada

^bState Key Laboratory of Power Transmission Equipment & System Security and New Technology, Chongqing University, Chongqing, China

^cCentre of Medical Biophysics, Universidad de Oriente, Patricio Lumumba S/N, Santiago de Cuba, Cuba

The inside-out NMR concept, developed in the oil industry [1], means the magnet is surrounded by the object and the magnetic field is open. As boreholes have a circular cross-section, the suitable sensitive volume of the NMR sensor should have the shape of a hollow cylinder.

A new inside-out magnet (three-cylinder array) is presented in this work (Fig.1a). This approach combines the toroidal symmetry proposed by Jackson [2] with advantages of the three-magnet array idea introduced by Marble [3] and Garcia [4]. The three-magnet array has proved both analytically and practically that two external magnet blocks and one central magnet block, magnetized along the same direction, can generate a homogeneous spot and an extended constant gradient in an external volume by varying the position of the central magnet. This design (see Fig1.b) changes the sensitive volume to 3D (toroidal spot around the magnet) by changing the magnet from blocks to cylinders. A similar magnet structure has been published by Perlo et al [5].

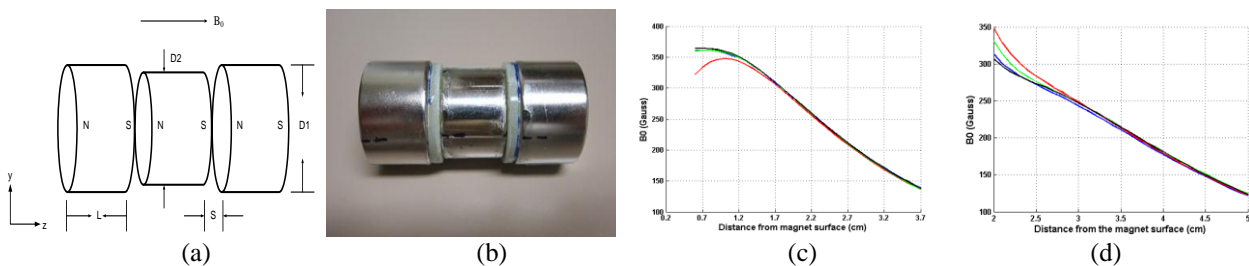


Fig. 1: (a) Illustrations of three-cylinder array. (b) A photo of the three-cylinder array. (c) and (d) are magnetic field distribution on radial direction at 0, 90, 180, 270 degrees for homogeneous spot and extended constant gradient respectively.

The homogeneous field (1.5 MHz for ^1H) of the magnet extends on its radial direction and axial direction for a certain distance (see Fig.1c). A configuration with extended constant gradient (see Fig.1d) can also be achieved (40 Gauss/cm) by changing the thickness of the spacers between external and central cylinders. A saddle coil is placed between the external magnets to generate a RF field B_1 orthogonal to the static magnetic field B_0 . Despite the light weight (200 g) and the small size (2.54 cm in diameter and 6 cm in length), the sensor possesses a relatively good sensitivity. A better homogeneity along the radial direction will be achieved by employing high quality magnets.

References:

1. B.Blumich; J.Perlo; F.Casanova. Mobile single-sided NMR. *Progress in NMR Spectroscopy*. 2008, 52, 197-269.
2. J. A. Jackson, L.J. Burnett, J. F. Harmon, Remote (inside-out) NMR. III. Detection of nuclear magnetic resonance in a remotely produced region of homogeneous magnetic field, *J. Magn. Reson.* 41, 411–421, 1980.
3. A.E.Marble; I.V.Mastikhin; B.G.Clopitts; B.J.Balcom. A compact permanent magnet array with a remote homogeneous field. *J. Magn. Reson.* 2007, 186, 100-104.
4. J. C. Garc ía-Naranjo, I. V. Mastikhin, B. G. Colpitts, B. J. Balcom, A unilateral magnet with an extended constant magnetic field gradient, *J. Magn. Reson.* 207, 337- 344, 2010.
5. J. Perlo, E. Danieli, Juan Perlo, B. Blümich, F. Casanova. Optimized slim-line logging NMR tool to measure soil moisture in situ. *J. Magn. Reson.* 2013, 233, 74-79.

Green coffee bean quality studied by single-sided NMR

E. Hughes^a, B. Folmer^b, A. Rodriguez^b

^aNestle Research Centre, Lausanne, Switzerland

^bNespresso, Lausanne, Switzerland

The in-cup quality of coffee depends on many parameters such as the botanical variety, harvest and post harvest practices, drying, transporting and storing of the green coffee beans as well as the roasting, grinding, packing and extraction of the coffee. When selecting green beans, the quality of the coffee can be judged partly on the flavor potential that the bean brings, partly by the external appearance of the beans and partly by their physical properties such as density, moisture and bean size. Most quality driving factors are defined by the variety, harvesting and post harvesting practices. Density and moisture variations however may lead to a more brittle, porous structure of the beans and impact coffee quality during the drying phase as well as during transport and storage.

We have used a low-field single-sided NMR (ACT Aachen) and the permanent gradient present to measure the diffusion properties of the oil within a series of green coffee bean samples to identify structural changes as a function of post harvest storage. The results show that this technique can clearly identify changes in pore structure as a function of differences in storage conditions. The changes observed in the diffusion data have been interpreted as a change in the closed porosity of the green beans due to the different storage regimes investigated.

Portable NMR sensor for crude oil analysis

Zijian Jia, Lizhi Xiao, Feng Deng, Guangzhi Liao, Baosong Wu

State Key Laboratory of Petroleum Resources and Prospecting, China University of Petroleum, Beijing 102249, China

Portable equipment for nuclear magnetic resonance is becoming increasingly attractive in a variety of applications. In this work we present a portable sensor for both relaxation and diffusion measurements on fluid and rock plugs (Fig.1a). It is 150 mm length and 50 mm radius. The magnet system is composed of three cylindrical sections. Two separate RF coils are placed in the center of the magnet ($B_0=0.47\text{T}$, a proton(^1H) resonance frequency of 20MHz). The sensitive volume can be divided into an interior, homogeneous region and an exterior gradient region. The field in the fringe volume can be approximated as a single field gradient value G_0 (Fig.1a). Two separate radio frequency coils are used for pulse transmission and echo reception. The one for pulse transmission is solenoid coil and the other is saddle coil (Fig.1a). The SNR is improved with the design.

The portable NMR sensor is employed to determine the fluid composition of oil. Crude oils are complex mixtures of molecules with a broad range of sizes and chemical properties. Relaxation and diffusion measurements with low field NMR have become powerful tools for the study of such fluids. Fluid composition affects both the NMR relaxation behavior and the translational diffusion property. For alkane molecules are a significant fraction of the composition in many crude oils, we use alkane model to represent crude oil. In mixture of alkane, $T_{2,i}$ relaxation and diffusion coefficient D_i for component i have a relationship with chain length N_i and average chain length \bar{N} .

$$D_i = A\bar{N}^{-\alpha} N_i^\beta T_{2,i}$$

For mixtures of alkanes at room temperature and atmospheric pressure, the prefactor $A=5.2 \times 10^{-10} \text{m}^2/\text{s}^2$ and the exponent $\alpha \approx 0.48$, $\beta \approx 0.6$. The T_2 -D map (Fig.1b) is inferred from T_2 distribution (Fig.1c). The effects of asphaltene and aromatics in crude oil is discussed lately. A correction equation will be proposed for heavy oil in the near future. By analysing the relationship, compositions of crude oil are estimated from measured T_2 -D maps. Details will be discussed subsequently.

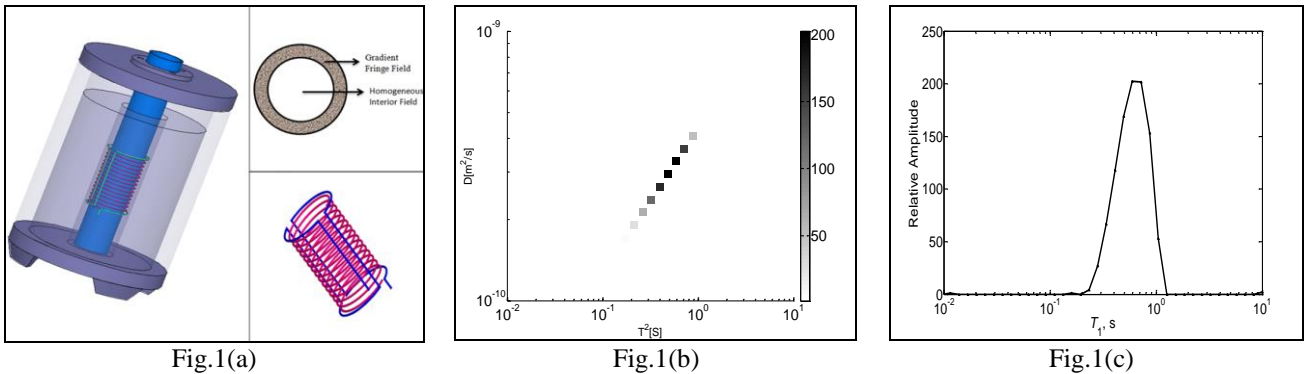


Fig.1: (a) The schematic diagram of Mobile Magnetic Resonance Sensor (b) T_2 -D maps is inferred from T_2 distribution (c) Simulation T_2 distribution of light oil

References:

1. B. Blumich, F. Casanova, S. Appelt, Chemical Physics Letters 477 (2009) 231 - 240
2. M. D. Hürlimann, Appl. Magn. Reson. 25, 651-660 (2004)
3. D. E. Freed, M. D. Hürlimann, C. R. Physique 11 (2010) 181 - 191.
4. C.W. Windt, H. Soltner, D. Dusschoten, P. Blümler, J. M. Resonance 208 (2011) 27 - 33

Diffusion effects on contrast in profile NMR on liquid samples – a survey of experiences and some general criteria

N. Nestlé^a, F. Quero^a, N. Tissier^a, J. Antony^b, E.H. Hardy^c, M. Bencsik^d

^aBASF SE Ludwigshafen, Germany, ^bEscuela de Química, Universidad de Costa Rica, San José, ^cIMVM, KIT, Karlsruhe, Germany, ^dNottingham Trent University, UK

NMR profiling offers an attractive geometry for studies of drying processes. At the same time, the NMR behaviour of fast-diffusion components is affected by the strong background gradient intrinsic to the profile NMR method. Like that, the diffusive effect on apparent transverse relaxation for highly mobile components will dominate over actual relaxation even in a CPMG sequence with very short pulse spacing.

Our contribution will review experiences made in drying experiments with different types of originally liquid samples and the development of a drying setup with well-defined conditions that can be used in order to provide identical drying environments in several experimental techniques (see figure 1). Special attention will be paid to the development of the contrast with time in the different types of samples (see figure 2 for a typical set of profile data on a drying polymer dispersion) and ways to discriminate different components in the sample will be discussed.

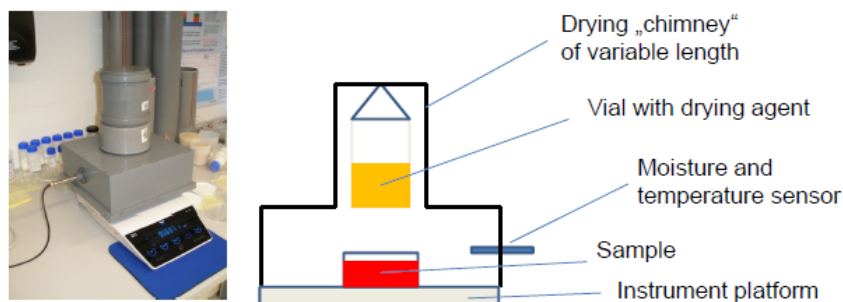


Figure 1 Drying chamber (on analytical balance) and schematic representation

Based on these findings and the basic relationships governing diffusion and relaxation effects, a range of criteria for available contrasts in different types of samples will be derived. Furthermore, the manifestation of different contrasts in simple evaluation procedures for profile NMR such as cumulative binning will be discussed.

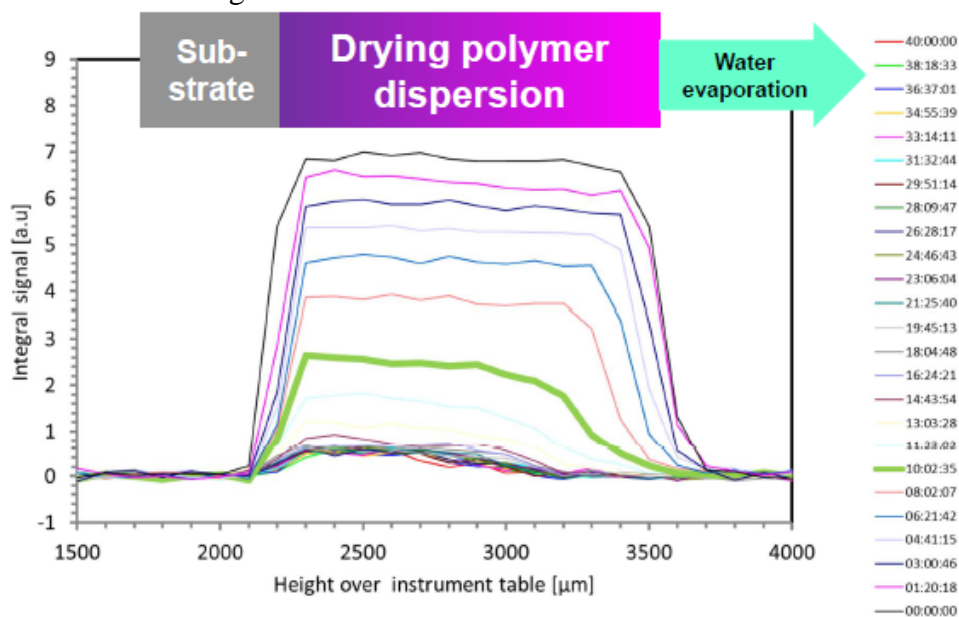


Figure 2 Profile data set for a drying polymer dispersion over 40 h

In situ living tree measurements using a 0.2 T permanent magnet

Y. Terada, A. Fukita, S. Moriwaki, and K. Kose

Institute of Applied Physics, University of Tsukuba, Ibaraki, Japan

In situ MRI measurements of a living tree offer the opportunity to investigate water distribution and flow in relation to the tree physiology. Although there are outstanding technological advancements in plant MRI, only few trials have been reported on *in situ* measurements of living trees in outdoors [1,2]. Here we develop an MRI system with an open-access 0.2 T permanent magnet to visualize water transport in an intact tree, and investigate how it correlates with environmental indicators such as solar radiation, humidity, and temperatures.

Figure 1(a) shows a picture of our MRI system. The system consists of a 0.2 T with a 16 cm gap permanent magnet (NEOMAX Engineering, 520 kg), planar gradient coil set, solenoid RF probe (7 cm in diameter, 6 cm long, 12 turn), and MRI console. The field homogeneity was high (34.6 ppm over $20 \times 20 \times 12 \text{ cm}^3$ DEV). The magnet, gradient coil set, RF probe, and other electronics were waterproofed by a box made of acrylic plates. The magnet temperature was kept almost constant by silicon heaters and heat insulators ($\sim 0.1^\circ\text{C}$ change against the air temperature change of 10°C), and the typical field drift was $< 100 \text{ Hz/h}$. The efficiency for z (defined as the B_0 direction), x (defined as the vertical direction), and y gradients was, 0.262, 0.676, 0.123 G/cm/A, respectively. The magnet was placed such that a Zelkova serrate was located through the center of the magnet gap. A part of the trunk at 40 cm above ground was measured using 2D spin echo sequences with motion probing gradients along the trunk. The ADC maps were calculated from diffusion weighed (DW) images with different b values ($b = 0, 31, 126, 283, 503, \text{ and } 637 \text{ mm}^2/\text{s}$).

Figure 1(b) shows an example of DW images of the trunk at 5:19 a.m. The signal-to-ratio is high enough to visualize anatomical structures. Figure 1(c) shows examples of ADC maps calculated from DW images obtained at different times (5:19 a.m. and 11:59 a.m.). The diurnal changes of the ADC values for different parts were correlated with environmental indicators (Fig. 1(d)). These results show clear differences in ADC values (and thus in water flow) both between times and tree parts. Our system is a useful tool for *in situ* and real-time tree measurements in outdoors for a long time (whole day to several months).

References: 1. T. Kimura, Y. Geya, Y. Terada, K. Kose, T. Haishi, H. Gemma, Y. Sekozawa, Development of a mobile magnetic resonance imaging system for outdoor tree measurements, Rev. Sci. Instrum. 82 (2011) 053704.
2. M. Jones, P.S. Aptaker, J. Cox, B.A. Gardiner, P.J. McDonald, A transportable magnetic resonance imaging system for in situ measurements of living trees: The Tree Hugger, J. Magn. Reson. 218 (2012) 133.

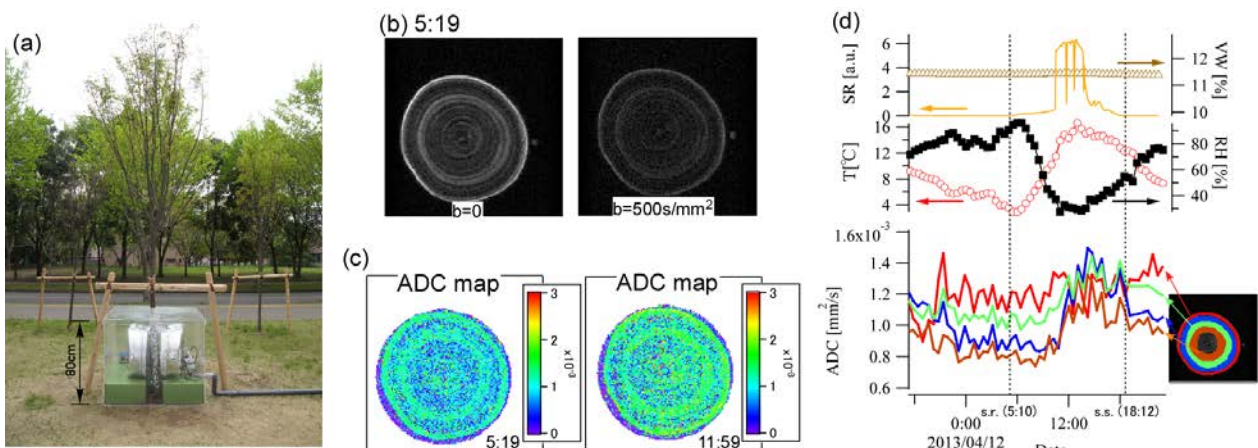


Fig. 1: (a) Outdoor MRI using a 0.2 T open permanent magnet. (b) Spin echo and diffusion weighted ($b = 503 \text{ s/mm}^2$) images of Zelkova serrata. TE = 50 ms, TR = 1.2 s, 128×128 , FOV = 10 cm \times 10 cm, slice thickness = 2 cm, NEX = 2, pixel bandwidth = 195 Hz. (c) ADC maps for 5:19 a.m. and 11:59 a.m. (d) Diurnal changes of ADC, solar radiation (SR), volume water content (VW), outdoor air temperature (T), and relative humidity (RH). ADC values are averaged over areas drawn with the same colors as in an inset figure. Sun rise (s.r.) and sun set (s.s) times were 5:10 and 18:12, respectively.

Research on the hydrogen index of flowing fluid in downhole NMR fluid analysis laboratory

Wu Baosong, Xiao Lizhi, Wu Yan, Liao Guangzhi

State Key Laboratory of Petroleum Resources and Prospecting, China University of
Petroleum, Beijing 102249, China

Downhole nuclear magnetic resonance (NMR) fluid analysis laboratory can evaluate fluid information in real time with reservoir conditions at a depth of several thousand meters. In the initial stage, the flow fluids run through the probe and then into the borehole. In order to obtain the properties of reservoir fluid, spin–lattice relaxation time (T_1) of flowing fluid with SR sequences has been measured. In this process, the hydrogen index (HI) could be obtained from different formation, such as flushed zone, invaded zone and undisturbed zone.

The HI is defined as the hydrogen density compared to the reference fluid of water at room temperature and atmospheric conditions. The parameter HI is necessary to accurately determine porosity from wireline NMR logging. The estimated value of HI can be obtained from charts or empirical equations¹. But downhole NMR fluid analysis laboratory can provide exact HI for the correction of porosity.

$$\Phi_{NMR} = \Phi_t * HI$$

Where Φ_t is the true porosity. Φ_{NMR} is the NMR porosity obtained from wireline or LWD (logging while drilling) NMR logging. That is to say, different logging data should be combined together in order to get Φ_t .

Based on the analytic model for double coils, this paper has studied T_1 measurement of flowing fluid^{2,3} (Fig.1). The probe is considered to be relative motion while fluid is relatively static in this model. From NMR mechanism and signal detection, the effects of flow fluid on the NMR measurement have been studied, and then HI has been calculated. The flow rate (v) and polarization will affect the calculation of HI. There are four kinds of cases which were discussed in detail: 1) $v < V$, and completely polarized; 2) $v > V$ (the critical rate), and completely polarized; 3) $v < V$, and partially polarized; 4) $v > V$, and partially polarized.

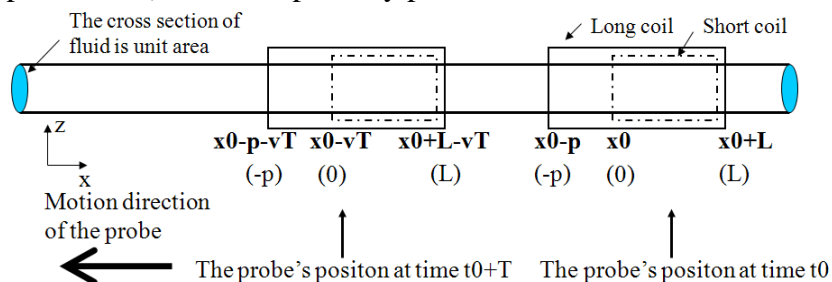


Fig. 1: The analytic model represents double coils probe's position at time t_0 and t_0+T , respectively.

References:

1. Coates G. R., Xiao L. Z., Prammer M. G. Texas: Gulf Professional Publishing, 2000.
2. Akkurt R. Effect of motion in pulsed NMR logging: (PHD's thesis), 1990.
3. Akkurt R. System and methods for T_1 -based logging. U.S. Patent, US7755354B2, 2010.

Detection of adulteration in olive oil with profile NMR sensors

Zheng. Xu^a, Robert H. Morris^b, Martin. Bencsik^b, Michael I. Newton^b

^aSchool of Electrical Engineering, Chongqing University, China ^bSchool of Science and Technology, Nottingham Trent University, UK

Introduction:

The detection of adulteration in edible oils is a concern in the food industry, especially for high priced olive oils. Some cheaper oils, such as sunflower oil or red palm oil, are usually used as the adulterants. This paper presents an NMR method to detect the adulterations in olive oil. The measurements were firstly undertaken on a *Profile NMR-MOUSE*[®], where rapid detection of adulterations can be performed without opening the bottle by measuring the T_2 relaxation and diffusion behaviors. As the sensitive volume of the NMR MOUSE is not always remote enough to probe inside specific bottles, a tailored portable NMR sensor with V-shape structure was designed.

Experiments on the *Profile NMR-MOUSE*[®]:

(1) One-dimensional T_2 distribution

Olive and sunflower oils mixed with different percentages were measured. The CPMG sequence was employed to record the ^1H transverse relaxation decay curves. The curves are obtained with the inverse Laplace transformation for one dimensional T_2 distribution analysis¹. Fig.1 demonstrates that sunflower oil clearly results in the T_2 distribution's second peak's contribution increase.

(2) Diffusion

Sunflower and red palm oils mixed with different percentages were measured. The SGSE sequence² was employed. Fig.2 shows that the sunflower oil has a faster diffusion behavior.

The V-shape structure NMR sensor:

The magnet structure is constructed with two NdFeB magnets, steel yoke, and a pair of steel wedge-shims. The angle of the yoke, and the angle of the wedge-shims are numerically optimized with Maxwell 3D software to make the B_0 field uniform. At the centre of the sensitive volume, the strength of the field is $\sim 0.23\text{T}$, and in the vertical direction the field has an approximate constant gradient of 8.6 T/m . The direction of the polarizing field is shown with a black arrow in Fig.1. A plane RF coil is used to generate the B_1 field and detect the echoes.

Conclusion:

A new detection method of adulterations in olive oil based on NMR measurements was introduced. Its effectiveness was demonstrated on the *Profile NMR-MOUSE*[®]. A tailored portable NMR sensor was designed and more tests on this sensor will be undertaken in future work to further assess its enhanced performance.

References:

1. F. Casanova, J. Perlo, B. Blümich, Single-Sided NMR. Springer, (2011) 57-82.
2. D.G.Rata, F.Casanova, J.Perlo, D.E.Demco, B.Blumich. Self-diffusion measurements by a mobile single-sided NMR sensor with improved magnetic field gradient. Journal of magnetic resonance. 180 (2006) 229-235.

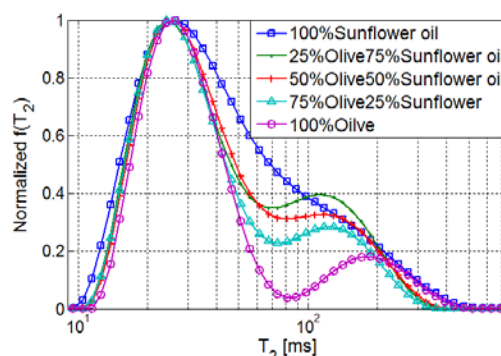


Fig.1: 1D T_2 distribution of oils

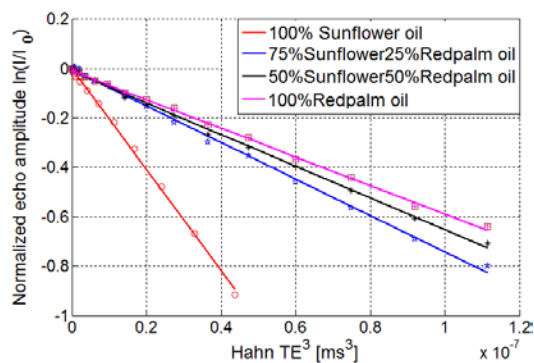


Fig.2: Diffusion lines

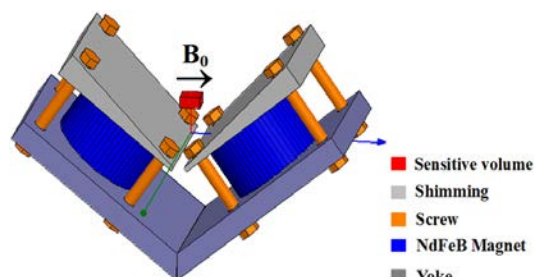


Fig.3: Structure of the magnet

A portable NMR sensor used for assessing the aging status of the silicone rubber insulator

Zheng. Xu, Shujie Zhao

School of Electrical Engineering, Chongqing University, China

Introduction:

The silicone rubber insulator is widely used in the power system. Its aging assessment is very important for the reliability of the power supply. This paper presents a portable low-field NMR sensor with a ‘clamp’ structure to detect the aging status of the insulator. By measuring the insulator’s transverse relaxation behavior, its aging status can be quantified with the T_2 parameter.

Hardware:

Two *NdFeB* magnet disks are placed in a SN-SN arrangement to build a B_0 field between them. A plane figure ‘8’ RF coil is fixed on the surface of one magnet. The insulator’s shed can be clamped by the two magnet disks. The strength of B_0 field in the centre of the sensitive volume is 217.5mT (a resonance frequency of 9.26MHz for 1H).

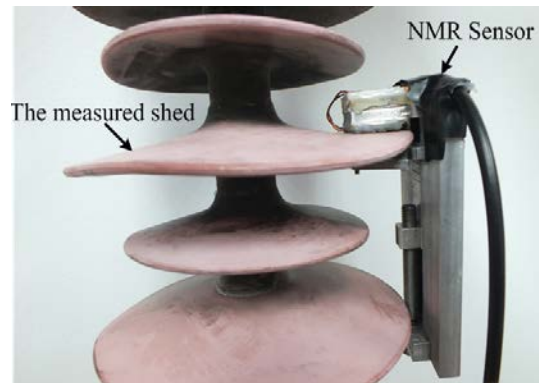


Fig.1: NMR sensor

Experimental details:

Three silicone rubber insulators with different service times of 0 year (new insulator), 2 years, and 5 years in the same power line were measured. The CPMG sequence was employed to record the 1H transverse relaxation decay curves. The curves are performed with the inverse Laplace transformation¹ for one dimensional T_2 distribution analysis. The insulator’s relative permittivity was also measured to compare with the NMR measurements’ results.

Results:

Fig.2 demonstrates a comparison between relative permittivity and transverse relaxation time ($T_{2\text{ long mean}}$). As the service time increasing, the relative permittivity decreases almost at a constant gradient, while $T_{2\text{ long mean}}$ decreases faster than the relative permittivity. The result indicates that $T_{2\text{ long mean}}$ is more sensitive to the aging status of the insulator.

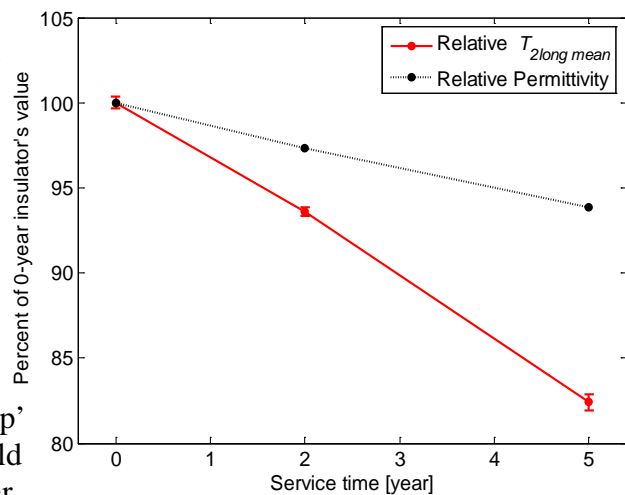


Fig.2: Comparison between the relative permittivity and transverse relaxation time for insulators with different service time.

Conclusion:

A portable NMR sensor with a ‘clamp’ structure was constructed for noninvasively in-field measurement of the aging status of silicone rubber insulators. It shows that the $T_{2\text{ long mean}}$ relaxation time decreases as the aging level increasing, so $T_{2\text{ long mean}}$ can be used as an index of the aging status of the silicone rubber insulator.

References:

1. F. Casanova, J. Perlo, B. Blümich, Single-Sided NMR. Springer, (2011) 57-82.

Development of a combined NMR and vibrational spectroscopic system for heterogeneous catalysis

Jules Camp^a, James McGregor^b, Mick Mantle^a, Andrew York^c

^aDepartment of Chemical Engineering & Biotechnology, University of Cambridge; ^bDepartment of Chemical and Biological Engineering, University of Sheffield; ^cJohnson Matthey Technology Centre, Sonning Common.

Research in catalysis places an increasing importance on studying materials during the catalytic reaction itself, i.e. *in situ* and/or *operando*. This allows observed changes in catalyst structure to be related to catalyst activity and selectivity, and hence to derive structure-performance relationships. However, in most cases the application of multiple techniques is required to develop a complete understanding of a catalytic system. An extension of this principle is to use a combined spectroscopic method, where two techniques are applied simultaneously. The advantage of this approach is the guarantee that the results obtained are from the same catalyst sample, under identical reaction conditions. Recent advances in this area include the combination of MAS NMR with UV/Vis spectroscopy¹ and a combined Raman, UV/Vis and ATR-FTIR set-up². NMR and Raman spectroscopies can probe both the reactants/products and the catalyst itself, hence combining these methods has the potential to provide significant insights into catalytic reaction mechanisms.

The technical challenge of combining two spectroscopic techniques involves the modification of a Bruker 7 mm MAS solid state probe, together with rotors and its air drive system, to incorporate a Raman spectroscopic probe, whilst still ensuring sufficient signal is obtained to acquire information-rich Raman spectra.

Initial, independent Raman and NMR studies of catalytic metathesis, demonstrate that the combined apparatus should provide valuable data in both homogeneous and heterogeneous catalysis. The combined system is then subsequently utilised for Grubbs' catalysed 1-hexene self metathesis, with the results compared to the independent techniques. This type of system perfectly demonstrates the ability of ¹³C NMR to follow the course of the reaction by monitoring the unsaturated region of the spectrum (Fig. 1); Raman measurements are taken simultaneously and are able to record reaction progress to confirm reaction progress. Thereafter heterogeneously catalysed hydrocarbon conversion reactions, namely *n*-pentane isomerisations using sulfated zirconia catalysts, are investigated. This is an extension of the homogeneously catalysed reaction; in this case the NMR can monitor reactant consumption/product evolution, as before, while Raman spectroscopy can probe the solid catalyst for changes throughout to give an insight into the catalytic mechanism.

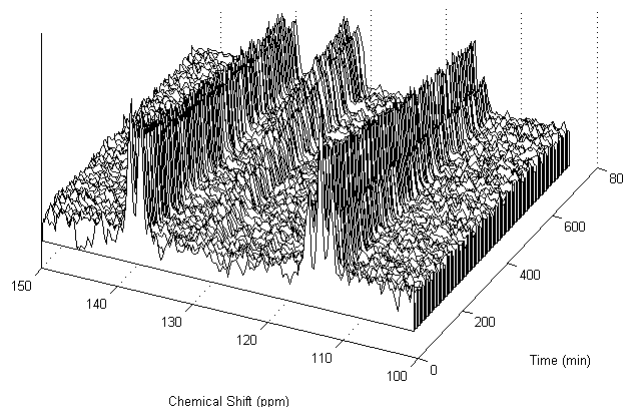


Fig. 1: ¹³C NMR stacked plot of the Grubbs' catalysed, self metathesis of 1-hexene in the C=C region. Reactant consumption is observed through the decrease in peaks at 117 and 139 ppm, corresponding to the C=C in hexene; product evolution is detected by the increase in the peak at 131 ppm, corresponding to the C=C in the product 5-decene.

References:

1. Hunger, M., *Chem Comm*, **2004**, 5, 584-585.
2. Brukner, A., *Chem Comm*, **2005**, 13, 1761-1763.

***Operando* MR: Pore condensation in porous media at elevated temperature and pressure**

M. P. Renshaw^a, S. T. Roberts^a, B. S. Akpa^b, M. Lutecki^a, M. D. Mantle^a, J. McGregor^c, A. J. Sederman^a, L. F. Gladden^a

^a Department of Chemical Engineering & Biotechnology, University of Cambridge, Pembroke St., Cambridge CB2 3RA, UK

^b Department of Chemical Engineering, University of Illinois at Chicago, 810 S Clinton St, Chicago, IL 60607, USA

^c Department of Chemical and Biological Engineering, University of Sheffield, Portobello Street, Sheffield S1 3J, UK

The ability to perform *operando* studies of fixed-bed heterogeneous catalytic systems has long been a goal of catalysis research; Magnetic Resonance (MR) methods, being non-invasive and non-destructive, are ideal for this purpose¹. However, until recently, the processes studied using MR have been performed under mild conditions (typically < 5 atm and < 200 °C). We have commissioned a fixed-bed reactor, compatible with operation inside a superconducting magnet, which can be operated up to a temperature of 350 °C and a pressure of 31 atm whilst simultaneously performing MR experiments (Fig. 1).

To demonstrate its capability we have studied the effect of confinement in mesopores on the vapour-liquid phase change of cyclohexane to elucidate pore filling and emptying mechanisms. The understanding of confinement effects, particularly at realistic reaction conditions, is an important consideration in heterogeneous catalysis.

Isothermal (150 °C and 188 °C) vapour-liquid phase change cycles of cyclohexane in a bed of titania pellets were conducted. ¹H spin density images reveal changes in pore saturation of the pellets as the phase boundary is crossed. Pore confinement effects are exhibited, as liquid remains within the pores after bulk liquid has vaporised. Pore saturation during the evaporation-condensation cycles exhibits hysteresis, demonstrating the differences between the filling and emptying mechanisms in these systems. The data are analogous to N₂ adsorption isotherms that characterise pore diameter and surface area, but are conducted for a relevant species at realistic conditions.

Data from these MR images, in conjunction with ¹H *T*₁ and *T*₂ relaxation time measurements and pulsed field gradient diffusion measurements, are used to assess the mechanism of pore filling and emptying in addition to revealing information about the formation of liquid films.

This work shows the capability to visualise porous media inside a catalytic reactor under realistic operating conditions through MR imaging whilst gaining information on pore filling mechanisms. The use of the reactor is also being applied to heterogeneous catalytic reactions.

References:

1. L. F. Gladden *et al.*, *Adv. Catal.* **50** (2006) 1.



Fig. 1: *Operando* MR reactor capable of 31 atm and 350 °C in up- or down-flow modes of operation whilst inside an NMR magnet.

MR microscopy using a high T_c superconducting bulk magnet

D. Tamada^{a,b,c}, *T. Nakamura*^{b,c}, *K. Kose*^b

^aResearch Fellow of Japan Society for Promotion of Science, ^bInstitute of Applied Physics, University of Tsukuba, Tsukuba, Ibaraki, Japan, ^cRIKEN, Wako, Saitama, Japan

A high critical temperature (T_c) superconducting bulk magnet, which acts like a permanent magnet by trapping an external magnetic field and can produce a stable and strong magnetic field like a conventional superconducting magnet, is a novel magnet for MRI [1]. However, there is a restriction in sample size because the magnet bore diameter is limited due to difficulty in obtaining a large single domain crystal. Therefore, the major application of the bulk magnet is MR microscopy. In such case, it requires the long signal averaging time to achieve high SNR because the signal intensity is proportional to voxel volume. In this study, we developed a compressed sensing approach [2], which can shorten the scan time without image quality degradation.

The MRI system we used consists of a superconducting bulk magnet, a 3-axis gradient coil set, an RF coil, and an MRI console. The bulk magnet comprised six annular superconductors (60 mm OD, 28 mm ID, 20 mm high, $T_c = 93\text{K}$) made of c-axis oriented single-domain $\text{EuBa}_2\text{Cu}_3\text{O}_y$ crystals. The room temperature bore diameter of the magnet was 23 mm. The bulk magnet was magnetized at 4.74 T by using a field cooling method with a conventional superconducting NMR magnet (JMTC-300/89, JASTEC, Kobe, Japan, $B_0 = 4.74\text{ T}$) as shown in Fig.1(b) to achieve homogeneous magnetic field of the magnet. The RF coil (Fig.1c) was a solenoid coil with 0.4 mm copper wire (6 mm diameter, 6 mm length, 4 turns). The MR image was reconstructed using the compressed sensing algorithm. We used the fast composite splitting algorithm [3] with an undersampled data using a Cartesian trajectory with random phase encoding. MR images of a biological sample (*Phytolacca americana*) were acquired using fully sampled (2 NEX, scan time = 3.6 hour) and randomly undersampled (10 NEX, reduction factor = 5, scan time = 3.6 hour) 3D spine echo sequences (image matrix = 256^3 , voxel size = $(50\mu\text{m})^3$, TR/TE = 100/10 ms).

The microstructure of an MR image reconstructed from the fully sampled k-space data (2 NEX) was not clear due to noise (SNR = 5.2). On the other hand, the background noise was suppressed (SNR = 25.3) by using the CS reconstruction shown in Fig. 1(d). These results clearly demonstrate that the SNR per unit time in microimaging was improved significantly by using the CS reconstruction.

In conclusion, we succeeded to acquire MR images with high resolution of $(50\mu\text{m})^3$ by using the compressed sensing technique, demonstrating the usefulness of the bulk magnet for MR microscopy.

References: [1]. K. Ogawa, et al., Appl. Phys. Lett., **98**, 23 (2011) 234101, [2]. M. Lustig, et al., Magn. Reson. Med., **58**, 6 (2007) 1182, [3]. J. Huang, et al., Med. Imag. Anal., **15** (2011) 670

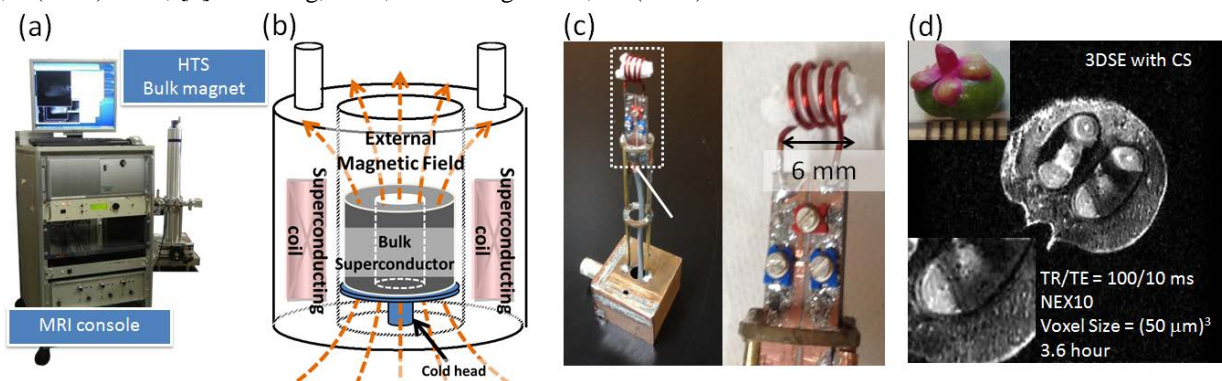


Fig. 1. (a) The MR microscope using the HTS superconducting bulk magnet. (b) Overview of magnetization process. (c) A solenoid RF coil (inner diameter = 6 mm, length = 6 mm). (d) An MR image of a biological sample (*Phytolacca Americana*) reconstructed from undersampled k-space data with the CS reconstruction.

Probe design of slim downhole NMR fluid analyzer

Jiangjie Zhao, Lizhi Xiao*, Baosong Wu, Guangzhi Liao, Sijia Jiang

State Key Laboratory of Petroleum Resources and Prospecting

China University of Petroleum, Beijing 102249, China

Downhole NMR fluid analyzer is a very important tool for identifying fluids timely by measuring relaxation times T_1 , T_2 and diffusion coefficient D at reservoir conditions. However, the large size of the existing probes obstructs the application in the slim borehole. Polarization section and measurement section are normally fixed in the probe, which will affect the polarization for fluids with a wide range of T_1 or flow velocity.

In this paper, we present optimal designs focus on decreasing the diameter and whole length of the probe. The interval between the magnet and the magnetically permeable steel shell is filled with aluminum, and adjust the thickness of aluminum to shorten the probe diameter and keep the magnet with enough thickness. The interval between the polarization section and the measurement section is filled with air to speed up the magnetization attenuation of over-polarized fluids, and the length of the air section can be changed to meet the polarization for fluids whose T_1 or flow velocity vary in a large range. Simulation and experimental results demonstrate the beneficial of the design.

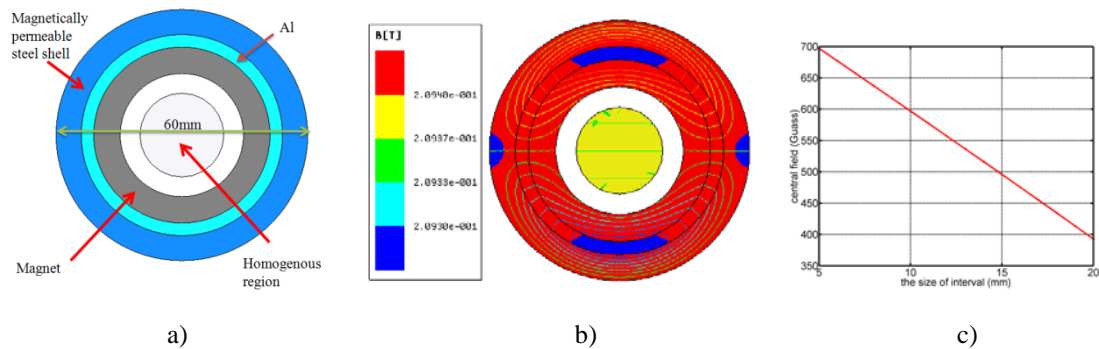


Fig. 1: The cross section of the polarization section (a); magnetic field(b); the relationship between aluminum thickness and central magnet field(c)

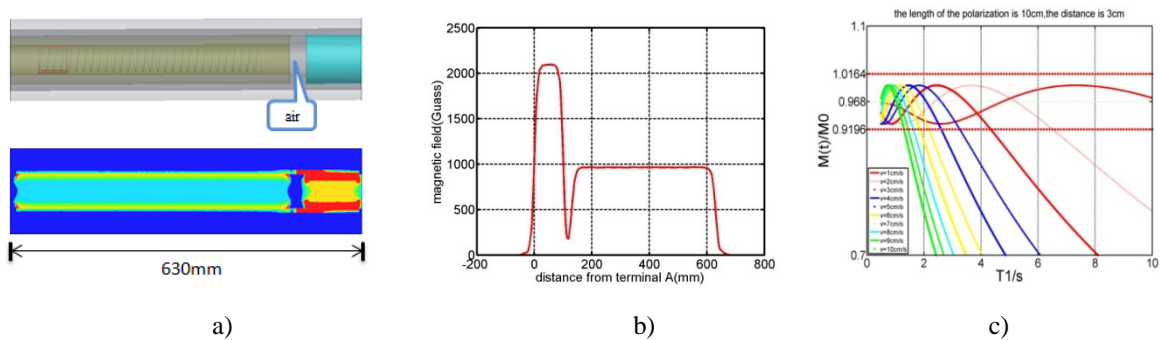


Fig. 2: The overall structure of e probe (a) ; axial magnetic field(b); the polarization effect for different fluids(c)

References:

1. M. G. Prammer, J. Bouton and P. Masak,US,20050017715A1, 2005-01-27.
2. B. S. Wu, L. Z. Xiao L, Petroleum Science. 1(2012)38-45

Class D RF amplifier with amplitude modulation for 17 MHz NMR MOUSE sensor

J. Zhen^a, R. Dykstra^a, C. Eccles^b, G. Gouws^a

^aSchool of Engineering and Computer Science, VUW; ^b Magritek Ltd, New Zealand

Class D amplifiers are known for their excellent power efficiency^{1,2,3,4} and are now used extensively for audio applications^{5,6,7}. Due to the switching speed limitations of power MOSFET devices, Class D amplifiers typically operate under 1MHz. With the recent availability of some new high speed and high power MOSFET devices in the market, it is now possible to develop Class D RF amplifiers that operate up to 20MHz thus making them viable for mobile low frequency NMR applications.

Higher frequency Class D amplifiers are normally operated in a resonant mode with a constant amplitude output. Here we demonstrate a Class D amplifier operating at 17MHz and working with an NMR MOUSE Sensor⁸. With some intelligent switching control, amplitude modulation is also possible. A prototype has been built on a 4-layer PCB with an area of 40cm², output power is 10W as required by the MOUSE sensor. Test results show the class D amplifier is operating well at 17MHz with fast turn on and turn off times, producing constant amplitude pulses as short as 2μs, and is able to run long CPMG experiments with tens of thousands of echoes.

References:

1. H.Koizumi, T.Suetsugu, etl, Class DE High-Efficiency Tuned Power Amplifier, IEEE Transactions on Circuits and Systems-I, VOL.43, NO.1, JAN.1996, pg 51.
2. M. Albulet, RF Power Amplifiers, Noble Publishing Corporation, Atlanta, GA. 2001.
3. M.K. Kazimierczuk, RF Power Amplifiers, John Wiley & Sons, West Sussex. 2008
4. A.Grebennikov, N.O. Sokal, Switchmode RF Power Amplifiers, Elsevier Inc, MA. 2007.
5. M. Berkhout, An Integrated 200-W Class-D Audio Amplifier, IEEE Journal of Solid-State Circuits, VOL.38, NO.7, JULY 2003. pg 1198.
6. Jr. W. Marshall Leach, Introduction to Electroacoustics and Audio Amplifier Design, Kendall Hunt Publishing; 3rd ed. 2008.
7. B. Cordell, Designing Audio Power Amplifiers, McGraw Hill. 2011.
8. G. Eidmann, R. Savelsberg, P. Blümmler, B. Blümich; The NMR MOUSE: A Mobile Universal Surface Explorer , J. Magn. Reson. A , 122, (1996) 104 – 109.

3D water and lipid MR-microscopy of rape seed germination dynamics

E. Munz^{a,b}, J. Fuchs^{a,b}, L. Borisjuk^b, P. Jakob^{a,c}

^a Department of Experimental Physics 5, University of Würzburg, Würzburg, Germany

^b Leibniz Institute of Plant Genetics and Crop Plant Research, Gatersleben, Germany

^c MRB Research Center for Magnetic-Resonance-Bavaria, Würzburg, Germany

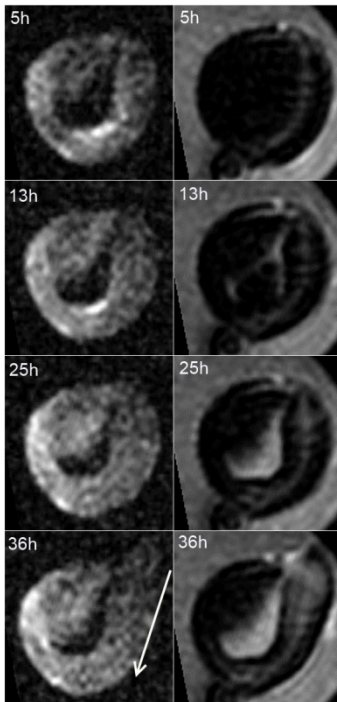


Fig. 1: MRI of the single seed after imbibition: different states of germination and associated distributions of lipid (left) and water (right). The lipid gradient in the root (arrow) is clearly visible (36hrs).

Introduction: Germination of seed is essential for successful agriculture. While the water uptake activates the process, the lipid acts as a vital source of energy during germination, however little is known about mechanisms governing this process under in vivo condition. In this contribution a method is presented for the simultaneous in vivo monitoring of both water and lipids as seen in [1].

Subjects and Methods: For acquisition of high-resolution images, we used a 3D Spin-Echo-Sequence (TR=250 ms, TE=7.794 ms, Matrix 256 x 64 x 64, Resolution 94 μm isotropic) on a Bruker 17.6 T AVANCE 750 WB spectrometer. We interleaved the acquisition of water and lipid datasets using chemical shift selective pulses to capture both dynamics at once [2]. The rape-seed was placed in a 5 mm glass tube containing agar-gel for water-supply and furthermore minimization of displacement during the experiment. Each dataset was acquired within $T_a=17:04$ min, providing an adequate resolution in time. By measuring 128 repetitions we could observe the germination process within the first 36.5 hours after imbibition. The resulting datasets were averaged using a sliding-window algorithm.

Results and Discussion: The seed's shape is visible due to the bright background. The spatially-resolved process of water uptake and the distribution of lipid in the seed are shown in Fig. 1. In the germinating root a distinct lipid gradient (arrow) is visible. In Fig. 2 the uptake of water and the decomposition of lipid in the seed are depicted. The selected ROI accounts for the seed's enlargement due to the water absorption within the first four hours after imbibition. A direct correlation between lipid consumption and water inflow is not detectable. This contribution shows, that the propagation of water in the seed is split in different phases while the metabolization of lipid is a constant procedure.

Conclusion: The results demonstrate the potential of 4D MR-microscopy to track the dynamics of water and lipid in germinating seeds. In contrast to conventional histological/analytic protocols, which are highly invasive, we are able to correlate the change in water and lipid content spatially and temporally in a single seed over a long period of time.

References:

1. V.V.Terskikh, *Planta* (2005), 221 : 17-27;
2. J. Fuchs, *Plant Physiology* (2013), 161 : 583-593

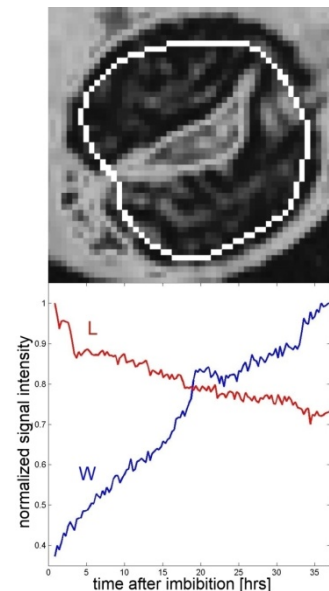


Fig. 2: Selected ROI in rape seed (water image, 36h) and normalized intensity of water and lipid over time.

NMR-microscopy of glass laminates

P. Offer^a, J. Vieß^a, M. Auth^a, B. Blümich^a

^aInstitut für Technische und Makromolekulare Chemie, RWTH Aachen University, 52074 Aachen, Germany.

Initial low-field studies of glass laminates with an NMR-MOUSE[®][2] revealed the presence of a proton gradient across the laminate layer (*B*-axis in Fig. 1, left image), which results from the production process.[3] The laminate is waterglass, a solution of sodium meta silicates.

The solid sodium silicate layer gives rise to a broadened water signal in the ¹H NMR spectrum corresponding to a *T*₂ of about 1.2 ms. In the gradient fields the apparent *T*₂ and *T*₂^{*} are further shortened, so that imaging studies challenge the technical limits of the NMR hardware. Nevertheless, the proton density gradient across the laminate layer could be assigned to concentration gradients of the waterglass components with the help of Chemical Shift Imaging (CSI).

At ambient temperature useful images could only be acquired using the zero time encoding sequence (ZTE). However, no proton gradient was detected. At 60 °C the spectral line width narrowed from one line with 6.40 ppm FWHM at room temperature to two lines with 0.47 ppm FWHM and 0.62 ppm FWHM for the -OH protons and -CH/-CH₂ protons, respectively.

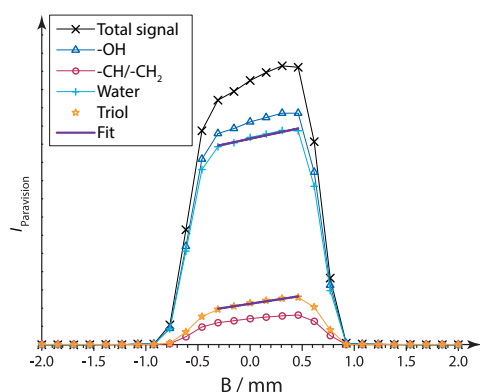


Fig. 2: Intensity plot for a horizontal profile centered in the middle of the waterglass layer depicted in Fig. 1 (right) obtained by CSI. The intensity for the -OH-peaks and -CH/-CH₂-peaks was determined by integration of the peaks. Under the assumption that every proton yields the same signal intensity the gradients for H₂O and triol can be calculated.

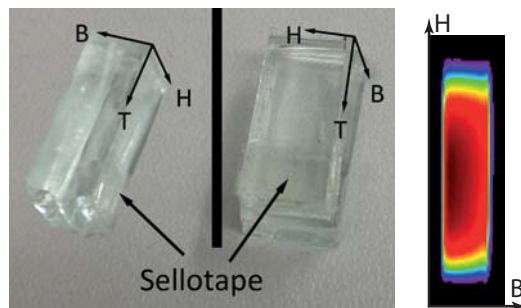


Fig. 1: Photo of the measured sodium silicate glass sample, which is embedded in-between two regular window glasses (left). ¹H-MGE-image (multi gradient echo) of the sodium silicate layer (right). Intensity losses at the top and bottom of the image result from birdcage resonator *B*₁-inhomogeneities.^[1]

Accordingly the concentration gradients across the laminate layer for water and a known triol could be determined by CSI.^[4]

It is evident that even though the absolute density gradient of the triol is smaller than the density gradient of water, the normalized density gradient of the triol is larger: The ratio of the slopes of the linearly fitted data points in Fig. 2 is $m_{\text{H}_2\text{O}} / m_{\text{triol}} = 1.39$. The ratio of the slopes for the individually baseline corrected, normalized and fitted water/triol density gradients (not depicted) is $m_{\text{H}_2\text{O, norm}} / m_{\text{triol, norm}} = 0.31$. With respect to the diffusion coefficients the opposite result would be anticipated. This effect can be explained by taking into account a slow cooling process. While the mobility of water molecules is still high the mobility of the triol molecules is too low. This enables concentration equalization for the water molecules during the cooling process.

References:

- [1] M. A. Voda, Dissertation: *Advances in Studying Order and Dynamics in Condensed Matter by NMR*, Aachen 2006.
- [2] J. Perlo, F. Casanova, B. Blümich, *Journal of Magnetic Resonance* **2005**, 176, 64-70.
- [3] J. Vieß, Preliminary report: *Kernmagnetische Resonanz zur Messung von Wasserglasschichten*, Aachen, **2012**, not published.
- [4] M. Auth, *Personal communication*, Receipients: P. Offer, J. Vieß, **2013**.

Quantitative ultra-fast MRI of powder dispersion

Y. Peng^a, M.D. Mantle^a, A.J. Sederman^a, M. Ramaioli^b, E. Hughes^b, L.F. Gladden^a,

^aDepartment of Chemical Engineering and Biotechnology, University of Cambridge, UK

^bNestlé Research Centre, 1000 Lausanne 26, Switzerland

The process of uniformly distributing a solid in a liquid is a physical phenomenon known as powder dispersion. It is of interest across many applications: the dispersion of pigments and powders is key to achieving consistency in paints and drug tablets, whilst the problem of how to disperse and dissolve powders in the reconstitution of dehydrated food stuff is a practical problem for the food industry on a daily basis. Thus finding the fastest way to achieve a uniform dispersion and dissolution is of central importance. Magnetic Resonance Imaging (MRI) offers a non-invasive multidimensional imaging technique for this study of dispersion, where a liquid jet is up-injected into a dry static bed of poppy seeds. The interaction of the powder and the liquid within such a system is visually observed for the first time.

A 1D gradient-echo profiling sequence was used to initially study a liquid jet injected into a full cell of liquid, but a loss of total signal intensity by up to 25% once injection started was observed. The development of a velocity compensated profiling sequence confirmed this loss of signal was due to undesired first moment phase in the system. The loss of the total signal was contained to ~5% by velocity compensation. With a temporal resolution of up to 300 frames per second, the initial penetration of the powder bed by the liquid jet can be accurately quantified with respect to the initial imbibition velocity ($v_{z,imb}$) and the liquid content of the cell over time.

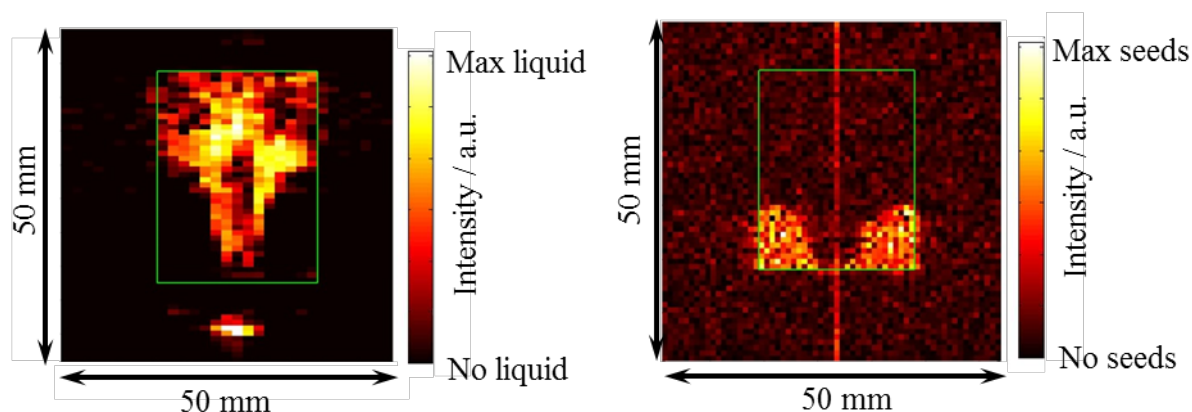


Fig. 1: Left: Liquid imaging still of the central vertical slice of a dispersion experiment showing the liquid jet rising from the bottom of the dispersion cell (green boundary) in a plume, the poppy seeds are not seen. Right: Powder imaging still from the central vertical slice of a dispersion experiment showing the regions of static powder in the dispersion cell, note the liquid jet is not seen.

Figure 1 shows sub-millimeter resolution 2D velocity compensated FLASH (Fast Low-Angle Shot) for liquid imaging and RARE (Rapid Acquisition with Relaxation Enhancement) for powder imaging at a temporal resolution of 10 and 2 frames per second respectively. From the liquid imaging, the behaviour of the liquid within the dispersion cell is observed. The powder imaging allows regions of static powder to be traced during the liquid injection.

The MRI results show that two different dispersion regimes can be observed: *jetting* and *lifting*. The formation of a liquid jet in the center of the powder bed is the prevailing regime at: (i) lower powder filling levels of the dispersion cell; (ii) higher liquid injection flow rates and (iii) lower liquid contact angles. A number quantitative *descriptors* of powder dispersion were extracted from the MRI data including: the jetting angle (θ_j) from the 2D liquid imaging data; the initial imbibition velocity ($v_{z,imb}$) from the 1D profiling sequence; the static solid fraction (\hat{A}) at equilibrium and the bed rise velocity ($v_{z,rise}$) from the 2D powder imaging data.

Viable isolated white matter: Microstructural MRI investigations at physiological temperature

S.Richardson^{1,2}, B.Siow^{1,2}, E.Panagiotaki², T.Schneider³, M.F.Lythgoe¹, D.C.Alexander²

¹UCL Centre for Advanced Biomedical Imaging, Division of Medicine, University College London, UK, ²Centre for Medical Image Computing, Dept of Computer Science, University College London, London, UK, ³Institute of Neurology, University College London, London, UK

Introduction: We take detailed diffusion magnetic resonance imaging (dMRI) measurements from viable isolated tissue (VIT) and fit a hierarchy of multi-compartment models to extract microstructural information from the tissue. This data is compared to electron microscopy (EM) data. We have previously developed and validated an MRI compatible chamber to maintain isolated white matter in a structurally and functionally viable and stable condition for 10 hours¹.

Methods: A rat optic nerve (σ SD) was maintained in our VIT chamber at 36.5°C. A multi-b-value 256 measurement dMRI dataset was acquired from the tissue. MR experiments were performed using a 9.4T Agilent VNMRs system, scan duration: 7h. The open source Camino diffusion MRI tool kit² was used to fit a set of multi-compartment signal models (32 models) from³ to the dMRI data. Feret radius measurements (ImageJ) were taken from EM and used to acquire ground truth information from the nerve.

Results: Ranking of fitted models (using Bayesian information criterion) ranked three compartment models highest. In the terminology of³: Zeppelin models outranked Tensor and Ball (hindered compartment - f_1) while Stick models outranked Cylinder models (restricted compartment - f_2). Astrosticks ranked highest as descriptors of the isotropic restricted compartment - f_3 . [Table 1](#) shows parameters estimates from a selection of the best and worst ranking models. [Table 2](#) shows EM measured ground truth data.

Models	Ranking	Best Parameter Estimates										
		S_0	f_1	f_2	f_3	d_1	$d_{\perp 1}$	$d_{\perp 2}$	θ	ϕ	R	α
ZeppelinStickAstrosticks	1	0.99	0.60	0.22	0.18	2157	635	-	-0.04	-15	-	-
ZeppelinCylinderAstrosticks	4	0.99	0.60	0.22	0.17	2143	622	-	0.05	-6.1	1.2	-
TensorStickAstrosticks	10	0.99	0.59	0.22	0.19	2200	771	347	0.04	-6.1	-	-0.93
BallStick	27	1.0	0.74	0.26	-	1699	-	-	0.12	0.19	-	-
DT	32	0.94	1.0	-	-	1606	67	61	0.02	0.23	-	2.5

Table 1: Fitted parameters from a selection of models: three of the highest and two of the lowest BIC ranked models. The volume fractions for each compartment (1, 2 and 3) are denoted f_1 , f_2 and f_3 respectively. The units for the diffusivities (d_1 , $d_{\perp 1}$, $d_{\perp 2}$) are in $\mu\text{m}^2/\text{s}$, for the radii (R) μm and the angles (θ , ϕ , α) are in radians.

Intra Axonal	Glial Cells and Extra Cellular	Myelin	Axon Radius (μm)
0.359	0.440	0.201	0.870

Table 2: Ground truth area fractions from electron micrographs covering ~ 1500 axons, total areas are scaled to equal 1.

Discussion: Parameter estimates from the top ten ranking models are similar and differ greatly from the worst fitting models. This data suggests that selecting the appropriate tissue model for the sample under investigation is important. EM myelin area fraction correlates well with the restricted compartment (f_3) estimates, intra axonal space fraction (f_1) and axon radius (R) are over estimated by the best fitting models. The ‘intra axonal’ volume fraction (f_1) may include signal from the glial cells or extra axonal space.

Conclusion: The VIT maintenance device used here is demonstrated to be a useful tool for investigation of microstructural parameters in viable white matter at physiological temperature. Complex multi compartment models can be fit to detailed high SNR data sets to extract parameters relevant to the underlying microstructure in mammalian white matter.

Selected References:

- Richardson S. A viable isolated tissue system. Magn. Reson. Med. 2012:E-pub.
- Cook P. Camino: Open-Source Diffusion-MRI Reconstruction and Processing. 14th ISMRM.2006. p2759.
- Panagiotaki E. Compartment models of the diffusion MR signal in brain white matter. NeuroImage 2012;59:2241.

Investigation of apple parenchyma microstructure using MRI multi-exponential T_2 relaxation and microporosity measurements

Guillaume Winisdorffer^{a,b,c}, Maja Musse^{a,b}, Stéphane Quellec^{a,b}, Marie-Françoise Devaux^c, Marc Lahaye^c, François Mariette^{a,b}

^aIRSTEA, TERE, France; ^bUniversité européenne de Bretagne; ^cINRA, UR1268 BIA, France

INTRODUCTION: Quantitative Magnetic Resonance Imaging is an appropriate non-destructive tool to study fruit microstructure [1]. Recent developments [2] allow accessing spatially resolved multi-exponential relaxation of water protons in intact fruit, providing insights on water status and distribution at the subcellular level. Microporosity distribution in fruit tissues can also be estimated by MRI [3], offering additional information about gas distribution.

For the first time, MRI multi-exponential T_2 and apparent microporosity were used to investigate the effects of fruit heterogeneity and cell size for different apple cultivars. The MRI data were related to histological measurements. The general objective was to provide a multi-scale approach for apple tissue characterization.

MATERIAL & METHODS: Experiments were performed 2 weeks after harvest on Granny Smith, Ariane, Fuji apples and an experimental cultivar (EC). Apples were calibrated as 3 groups: c1, about 120 cm³, c2 about 180 cm³ and c3, about 290 cm³. MRI measurements were carried out on a 1.5T MRI scanner (Avanto, Siemens). The 5-mm median planes of fruit were imaged with a pixel size = 1.19 mm² and a TR = 10 s. T_2 was obtained from a 512-echoes MSE sequence with "TE = 7.1 ms. T_2^* , used with T_2 for microporosity estimation, was obtained from GE sequences with TE₁ = 2.77 ms and "TE = 1.61 ms. Cell size distribution was estimated on same samples from macrovision images using an erosion/dilation method [4].

RESULTS: Apple T_2 decay was well fitted by a tri-exponential decay curve with T_2 about 15-26 ms, 85-135 ms and 360-550 ms and associated relative intensities about 10, 20 and 70 %, respectively. The study of parenchyma heterogeneity revealed that from outer (near the cuticle) to inner (near the core) regions, relaxation times decreased up to 20% and subcellular water distribution was slightly different. In contrast, microporosity was shown to increase of up to 28 % (see Fig. 1).

T_2 measurements of Fuji apples of calibers c1 and c3 showed variations for the longest vacuolar T_2 component from 423 ± 25 ms to 469 ± 20 ms, respectively. Cell size distributions, obtained by macrovision, showed larger cells in big apples thus linking cell size to T_2 relaxation time. Microporosity increased from 33 ± 3% for small fruits to 39 ± 2 % for big apples. Differences between cultivars of the same caliber were observed. For example, EC had higher porosity and lower relaxation times and Granny Smith had a less heterogeneous parenchyma than other cultivars.

Size-contrasted fruits permitted to highlight cell size influence on multi- T_2 relaxation time. In apple cortex, T_2 relaxation time increased with distance to the core even if apparent microporosity increased. Finally, this work showed that MRI can differentiate apple cultivars according to their T_2 and microporosity spatial distribution.

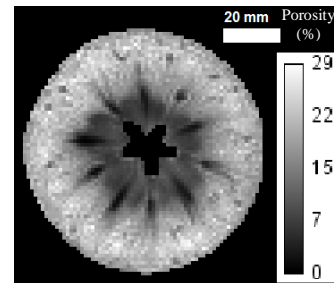


Fig. 1: apparent porosity map of Fuji (c3) apple

References

- [1] Van As, H. and J. van Duynhoven, Journal of Magnetic Resonance, 2013. **229**: p. 25-34..
- [2] Adriaensen H, et al, Magnetic Resonance Imaging, 2013.
- [3] Musse, M., et al., Magnetic Resonance Imaging, 2010. **28**(10): p. 1525-34
- [4] Devaux, M.-F., et al., Postharvest Biology and Technology, 2008. **47**(2): p. 199-209

Dynamic nuclear polarization at 9.2 T

V. Denysenkov, P. Neugebauer, J. Krummenacker, T. Prisner

Institute of Physical and Theoretical Chemistry and Center of Biomolecular Magnetic Resonance,
Goethe University Frankfurt, Germany

We could show for the first time that dynamic nuclear polarization in liquid solutions allows enhancing proton NMR signals by up to a factor of ~ 93 ^{1,2}. To achieve an effective MW excitation of the liquid sample without excessive heating of the liquid a double resonance structure for the electron and nuclear spin (260 GHz/ 400 MHz) has been developed, that allows for up to 200 nl of liquid sample places on the flat mirror of a Fabry-Perot resonator³. Potential applications of this method to magnetic resonance microscopy and magnetic resonance imaging will be discussed⁴.

References:

1. M.J. Prandolini, V.P. Denysenkov, M. Gafurov, B. Endeward & T. Prisner; High-Field Dynamic Nuclear Polarization in Aqueous Solutions, *J.Am.Chem.Soc.*, 131 (2009), 6090
2. P. Neugebauer, J. Krummenacker, V. Denysenkov, G. Parigi, C. Luchinat & T. Prisner Liquid state DNP of water at 9.2 T: an experimental access to saturation *Phys. Chem. Chem. Phys.*, 15 (2013), 6049
3. V. Denysenkov, & T. Prisner; Liquid State Dynamic Nuclear Polarization Probe with Fabry-Perot Resonator at 9.2 Tesla *J.Magn.Reson.*, 217 (2012), 1
4. J. Krummenacker, V. Denysenkov, M. Terekhov, L. Schreiber & T. Prisner; DNP in MRI: An in-bore approach at 1,5 T, *J.Magn.Reson.*, 215 (2012), 94-99

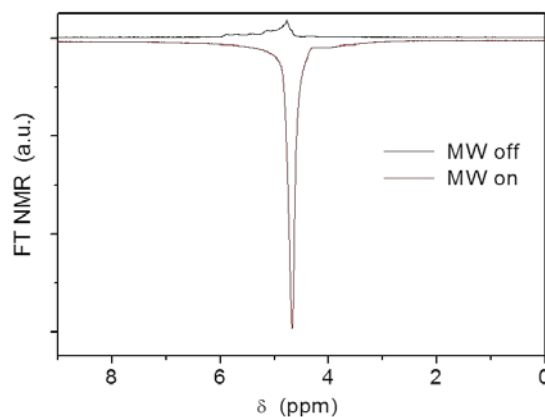


Fig. 1: Dynamic nuclear polarization of a liquid solution of TEMPOL (40 mM) in water at room temperature. The positive signal corresponds to the proton NMR signal without application of MW irradiation; the negative enhanced signal corresponds to the Overhauser DNP enhanced signal under irradiation with 2 W of MW at 260 GHz frequency.

Simulation of NMR response based on digital rock images

Jiajie. Cheng, Lizhi. Xiao^{}, Guangzhi. Liao*

State Key Laboratory of Petroleum Resource and Prospecting
China University of Petroleum, Beijing 102249, China

NMR technology is widely used in formation evaluation and petrophysics study. The study of the response characteristics of NMR in pore-scale model contributes to understanding its response mechanism. Digital images which reveal complex pore structures of rocks can be used to analyze the influences of different lithologies, different pore structures and different fluid components on NMR response.

Three dimensional (3D) digital rock images are obtained by X-ray scanning experiment (micro-CT). Alternatively, they are reconstructed from two dimensional (2D) thin sections using multiple-point statistics method. Monte Carlo random walk algorithm is used to describe the random motion of fluid molecules in pore space. The magnetization decay is simulated under a magnetic field gradient with CPMG pulse sequence. The influence of voxelized representations of rocks on simulation results is considered. Based on 3D digital rock images, Monte Carlo random walk method is used to simulate the magnetization decay. T_2 distributions are obtained with inversion method. The simulation results are verified by experimental measurements. Combined digital rock images, the influences of surface relaxivity, fluid diffusion coefficient, magnetic field gradient and inter-echo spacing on NMR response are analyzed. The simulation results in reconstructed images are similar to those in micro-CT images, which suggests that pore-scale NMR simulation can be taken as a validation for the method to reconstruct porous media.

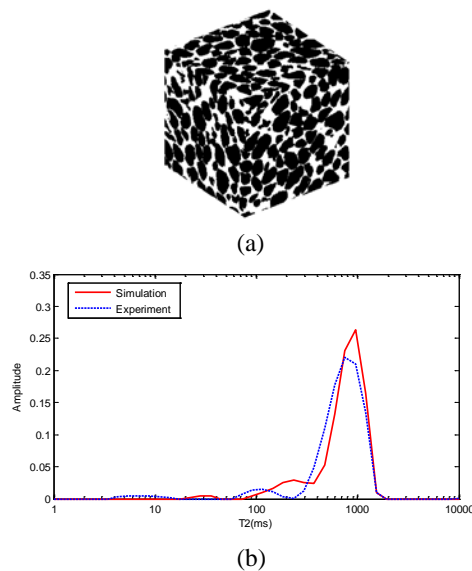


Fig. 1: Simulation result in micro-CT image.
(a)Micro-CT image; (b)Comparison result.

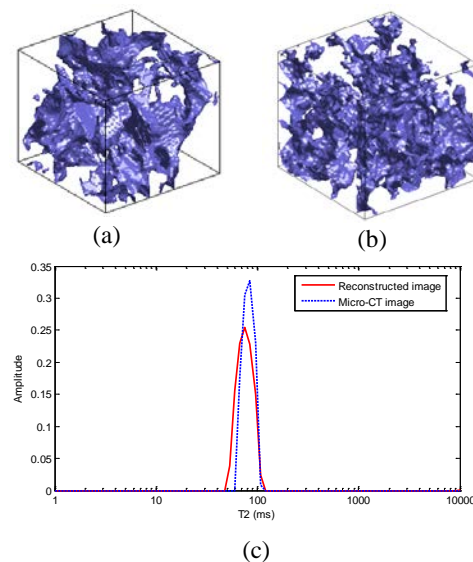


Fig. 2: Simulation result in reconstructed image. (a)Micro-CT image; (b)Reconstructed image; (c)Comparison result.

References:

1. G. Jin, C. Torres-Verdín, E. Toumelin, J. Magn. Reson., 200 (2009):313-320.
2. O. Talabi, S. Alsayari, S. Iglauer, et al., J. Petrol. Sci. Eng., 67 (2009):168–178.
3. H. Okabe, M. Blunt, Phys. Rev. E, 70 (2004) 066135.

Accelerated aging of plasticized PVC studied by NMR microscopy

*Rance Kwamen, Geovani Dal-Ri Junior, Bernhard Blümich, and Alina Adams,
ITMC, RWTH Aachen University, 52056 Aachen, Germany*

Plasticized PVC is one of the most important technical polymer materials with applications ranging from industry to medicine. With increasing service time and under accelerated conditions the material ages, for example by exposure to high temperature or by contact with organic solvents. Plasticizer may migrate out of the sample, and this is accompanied by a change in the thermal and mechanical properties. Characterising the speed of plasticizer loss with the aging time, understanding which factors govern the process, and studying how the polymer matrix itself is affected are the key topics for the design of new kinds of plasticizers with improved properties.

Usually, the loss of plasticizer in PVC is extensively investigated mainly based on gravimetric and chromatographic methods. These methods give indirect information about the changes in PVC itself, and they are mainly restricted to samples with well-defined geometries and dimensions. Additionally, with these methods it is not possible to spatially discriminate the plasticizer loss in the material. However, such information would be of great importance because studies based on mechanical measurements suggest that the deterioration of the mechanical properties seems to be related not only to the amount of the plasticizer inside a PVC plate but also to its distribution across its thickness.

In this work, we apply ^1H relaxation measurements performed using unilateral NMR to monitor the aging of plasticized PVC plates under three different conditions: when subjected to elevated temperature and in contact with *n*-hexane and deuterated chloroform. By taking advantage of the strong and uniform gradient of the NMR sensor, we obtain for the first time direct information about the changes that the polymer and the plasticizer suffer upon aging at various depths across the polymer plate.

For thermally aged samples, the loss of plasticizer is homogeneous across the whole plate thickness, and the NMR results correlate well with the changes in weight. For samples in contact with solvent, the plasticizer is lost much faster due ingress of solvent into the polymer plate. In this case, we can clearly demonstrate that a quantification of plasticizer loss based on changes in weight leads to wrong results as a part of the solvent taken up is trapped inside the sample even after drying and therefore contributes to the measured weight. This result is also supported by ^1H and ^{13}C solid state NMR measurements performed under magic angle sample spinning. The observed characteristics are in good agreement with published studies on similar samples.

Application of adaptive compressed sensing algorithm to echo train de-noising in low field NMR logging

Yuanfeng Lian, Guangzhi Liao

Departments of Geophysics and Information Engineering, China University of Petroleum, Beijing Campus (CUP), Beijing 102249, China

In NMR logging, the echo train is vulnerable to noise and the amplitude is very weak. It is critical to improve the signal-noise-ratio of echo train. A novel denoising algorithm—Adaptive Basis CS algorithm, which is based on minimizing the rank of an accumulated matrix, whose eigenvectors approximate the optimal basis sparsely representing the original echo train. Based on the theory of matrix completion, the original signal from its random projections under the observation that the constructed accumulated matrix is of low rank according to noise coefficient. Compared to traditional algorithm, the proposed method efficiently improves the SNR quality and provide more precise porosity for the fluid analysis of formation.

Keywords Nuclear Magnetic Resonance, Echo De-noising, Compressed Sensing (CS), SVD Inversion, Spare Representation.

Identify heavy oil combining NMR and conventional logs

Yan Wu, Lizhi Xiao, Guangzhi Liao, Wensheng Wu*
 State Key Laboratory of Petroleum Resources and Prospecting
 China University of Petroleum, Beijing 102249, China

The T_2 distribution of oil in the formation can be estimated with NMR logging, then oil viscosity which is an important parameter in the reservoir evaluation can be calculated based on the distribution with some empirical methods. In heavy oil reservoir, it is difficult to estimate the T_2 distribution of oil by one dimensional method, which often overlaps with bound fluid. Because of the limit of acquisition parameters in NMR logging and rapid decay of short T_2 components, a broadening response usually appears in the diffusion dimension of T_2 - D map. It is hard to distinguish heavy oil and bound fluid with NMR data solely, which will be difficult to calculate viscosity.

This paper we present a method which combines NMR and conventional logs to identify heavy oil. As for 1D method, this article adopts MRF method combining with simulated annealing (SA) method to distinguish fluid typing. The SA method is mainly used to estimate the parameters of fluid model which required in MRF processing (Fig. 1). As for 2D method, this article adopts conventional logging results as a constraint condition to distinguish fluid typing (Fig. 2).

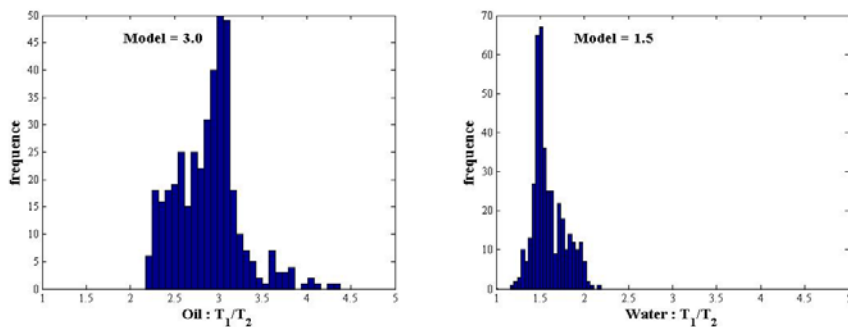


Fig. 1: Histogram of T_1/T_2 in MRF method calculated by simulated annealing

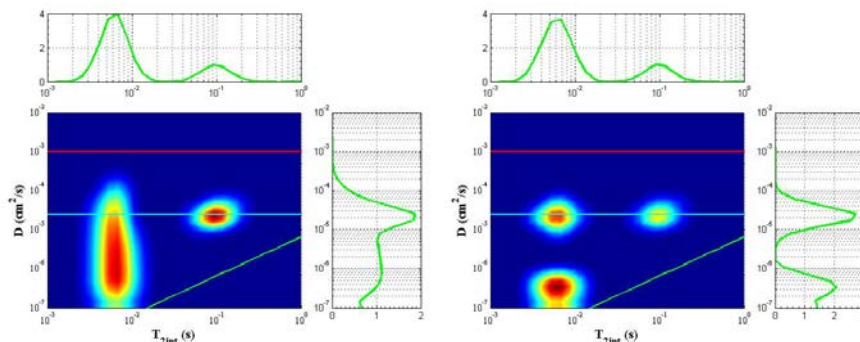


Fig. 2: T_2 - D map with conventional inversion method (left) and T_2 - D map with same method constrained by conventional logging data (right)

References:

1. Freedman R, Sezginer A, Flaum M, et al. SPE Annual Technical Conference and Exhibition, 2000, SPE 63214.
2. Heaton N J, Minh C, Kovats J, et al. SPE Annual Technical Conference and Exhibition, 2004, SPE 90564.
3. Al-Yaarubi A, Al-Bulushi N, Al Mjeni R. SPE Heavy Oil Conference Canada, 2012, SPE 157596.
4. Heaton N, Lavigne J, Bachman H N et al. SPWLA 53th Annual Logging Symposium, 2012.

Restricted k -space sampling in pure phase encode MRI

D. Xiao^a, B. Balcom^a

^aMRI Research Center, Department of Physics, University of New Brunswick, Canada

In the study of rock core plugs with multidimensional MRI, the samples are of a regular cylindrical shape that yields well defined intensity distributions in reciprocal space. The high intensity k -space points are concentrated in the central region and in specific peripheral regions. A large proportion of the k -space points have signal intensities that are below the noise level. These points can be zero-filled instead of being collected experimentally. k -space sampling patterns that collect regions of high intensity signal while neglecting low intensity regions can be naturally applied to a wide variety of pure phase encoding measurements, such as T_2 mapping SESPI¹, hybrid-SESPI and SPRITE², since all imaging dimensions can be under-sampled. These ideas also apply for conventional frequency encoding. With a shorter acquisition time, as fewer experimental data points are required, the RF and gradient duty cycles are reduced, while the image SNR is improved.

Restricted sampling data acquisition patterns are based on high intensity regions in the model k -space, to ensure the coverage of high intensity points in the reciprocal space of realistic samples. These patterns, with the remaining points set to zero, upon Fourier transformation, yield good quality images with acceptable blurring. The slightly blurred images from restricted sampling reveal more clearly the intermediate scale sample structure that is more desirable, in many porous media studies, than the pixel scale variations which are largely affected by noise. The restricted sampling data acquisition provides a viable alternate to compressed sensing, in select samples, with dramatically simplified data processing. In this lecture, I will discuss the merits of restricted k -space sampling versus compressed sensing in applications such as rock core plugs.

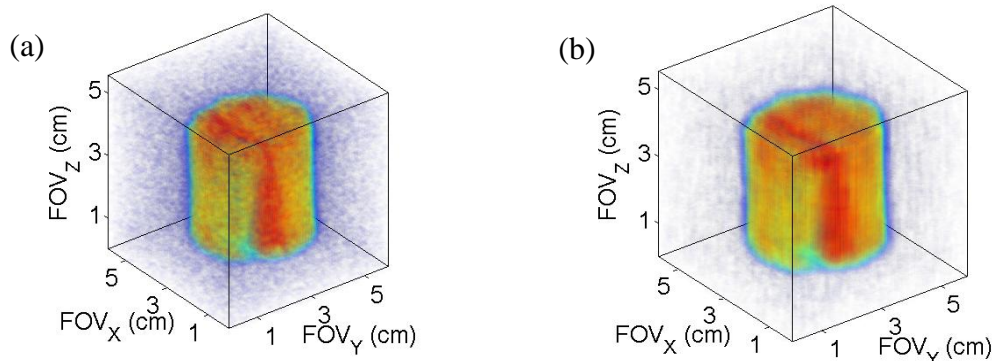


Figure 1. (a) Conical SPRITE with 39 cones. (b) Restricted sampling SPRITE with 10% of k -space points.

References:

1. D. Xiao and B. J. Balcom, Two-dimensional T_2 distribution mapping in rock core plugs with optimal k -space sampling. *JMR* (2012) 220, 70-78.
2. D. Xiao and B. J. Balcom, Restricted k -space sampling in pure phase encode MRI of rock core plugs. *JMR* (2013) 231, 126-132.

List of Posters by Number and Topic

	Presenter	Title of Abstract
P01	Göbel, Katharina	MR microscopy of organotypic hippocampal slice cultures: First steps to an in vitro approach for experimental epilepsy research
P02	Hasihi, Tomoyuki	Live mice imaging with a 14.1T narrow-bore NMR magnet heading for <i>f</i> MRI by using an independent digital console and gradient probe
P03	Komlosh, Michal	Mapping the pore size distribution of a glass microcapillary array phantom using d-PFG MRI
P04	Lesbats, Clémentine	MRI exploration of the low-density lipoprotein (LDL) transport in an artery model
P05	Liu, Kang	Application of wavelet transform de-noising to MRI based on background noise estimation
P06	Sersa, Igor	MR microscopy in assessment of dental caries
P07	Xia, Yang	The dependences of multi-component T2 measurement in cartilage and gel phantom on the imaging sequences and specimen solutions
P08	Baker, Luke	<i>Operando</i> MR: Spatially-resolved NMR measurements of fixed bed heterogeneous catalytic reaction
P09	Bayley, Paul	In situ, real-time visualisation of electrochemistry using magnetic resonance imaging
P10	Bernin, Diana	Impact of salt on starch and gluten and on water migration in pasta studied with ¹ H, ¹⁹ F, ²³ Na and ³⁵ Cl MRI/NMR
P11	Blythe, Thomas	Taking magnetic resonance into industrial applications
P12	Boyce, Christopher	Cross-validating magnetic resonance measurements of 3D cylindrical fluidized beds with predictions from a discrete element model
P13	Bräuer, Pierre	Effect of confinement on diffusion and dynamics of primary alcohols and non-ideal binary mixtures acetone-chloroform in mesoporous catalysts probed by PFG-NMR
P14	Chen, Chen	Direct multi-nuclear magnetic resonance imaging studies of controlled drug release
P15	D'Agostino, Carmine	Nuclear magnetic resonance relaxometry in heterogeneous catalysis: New advances in understanding adsorption over solid catalyst surfaces
P16	Dalitz, Franz	Monitoring of liquid reactions by low-field NMR spectroscopy
P17	Fabich, Hilary	Ultra-short echo time magnetic resonance imaging in heterogeneous materials
P18	Goora, Frederic	Arbitrary magnetic field gradient waveform correction using an impulse response based pre-equalization technique
P19	Guthausen, Gisela	NMR-diffusometry and relaxometry for the characterization of (double) emulsions in life science
P20	Kampf, Thomas	Uncovering supercritical CO ₂ wood dewatering via interleaved ¹ H- imaging and ¹³ C-spectroscopy with real-time reconstruction

- P21 Kartaeusch, Ralf Eddy currents reduction for an accessible mobile magnet
- P22 Liao, Dongliang Combining NMR log and other logs evaluate shale formation
- P23 Kartaeusch, Ralf Noise reduction for an accessible mobile magnet
- P24 Lutecki, Michal PFG NMR Studies of CO₂ in metal -organic framework structures
- P25 MacMillan, Bryce Determining the role of grain roughness on evaporation from porous media with MRI
- P26 Merz, Steffen Monitoring the drying stages of a porous medium by MRI and unilateral NMR
- P27 Michan, Alison PFG-NMR study of tortuosity in silicon electrodes
- P28 Mitchell, Jonathan Spatial resolution in low-field studies of oil recovery
- P29 Mohoric, Ales PGSE pore microscopy
- P30 Ramskill, Nicholas Application of magnetic resonance velocimetry to investigate the transport phenomena of gas flow in a Diesel Particulate Filter
- P31 Sarou-Kanian, Vincent Spectroscopic dimension in MRI of materials with ultra short transverse relaxation times
- P32 Seymour, Joseph Using Spatial Resolution to Enhance MR Data Interpretation of Transport Processes during Gelation
- P33 Shikhov, Igor Spatially resolved relative permeability with simulated and experimental 1D NMR imaging
- P34 Teymouri, Yadollah The effect of swelling and annealing on the molecular mobility and phase composition of domains in Low Density Polyethylene
- P35 Utsuzawa, Shin Motion effect in NMR well logging
- P36 Vieß, Jochen Mapping of spin-density and -velocity in membranes
- P37 Walton, Jeffrey Characterization of Mn doped Si nano particles designed as MRI contrast agents
- P38 Zheng, Qingyuan Measurement of intra-particle chemical compositions in a trickle-bed reactor using an MRI-PLSR method
- P39 Ziovas, Kostas Bayesian sphere sizing for food foam research
- P40 Blümich, Bernhard Portable NMR for practical analysis of ancient wall paintings
- P41 Roussel, Tangi Ultrafast in vivo imaging sequence for Bruker MRI
- P42 Schmaus, Christine Compressed Sensing for the imaging of two-phase falling film flow
- P43 Siow, Bernard Diffusion-diffusion Exchange Spectroscopic Imaging (DEXSI) MRI in a rat corpus callosum
- P44 Song, Yi-Qiao Diffusion time correlation experiment
- P45 Qiao, Zhi Concentration mapping with MRI using compressed sensing
- P46 Wu, Yuting Quantification of chemical composition using Bayesian NMR

- P47 Xiao, Dan *k*-t acceleration in pure phase encode MRI to monitor dynamic flooding processes in rock core plugs
- P48 Xie, Qingming Noise reduction for NMR with regularization-heursure algorithm
- P49 Arbabi, Aidin Average bubble size estimation in an upward vertical bubbly flow at a low magnetic field (0.2 T)
- P50 Bartlett, Oliver Multiphase flow validation using magnetic resonance imaging
- P51 de Kort, Daan Shear-induced aggregation of bacterial-cellulose dispersions as viewed by rheo-NMR and PFG ¹⁹F-NMR nanoprobe diffusometry
- P52 de Kort, Daan Nanoprobe diffusometry in soft materials by frequency- and time-domain ¹⁹F and ¹H NMR at low and high field strengths
- P53 Douglass, Bradley Investigating fluctuations in wormlike micelles solutions with spectroscopic imaging and snap-shot GERVAIS velocimetry
- P54 Eriksson, Stefanie Microscopic fractional anisotropy with *q*-MAS PGSE
- P55 Faure, Pamela Following transport of contrast agent particle in sand and soil column
- P56 Herrling, Maria Magnetic resonance imaging of local flow velocity profiles in biofilm carriers from waste water treatment
- P57 Jiang, Sijia New method for down-hole two-MNR fluid analysis
- P58 Kuczera, Stefan Fast RARE velocimetry for curved flow in Couette geometry
- P59 Ling, Nicholas Characterization of oilfield emulsion using nuclear magnetic resonance
- P60 Smith, Catherine Investigating the molecular behaviour of ionic liquids using magnetic resonance
- P61 Vallatos, Antoine Measurement of transport and reaction in vortical flows using magnetic resonance
- P62 Xu, Ruina Density-driven Fingering during brine-water miscible displacement in two inclining porous media layers by magnetic resonance image
- P63 Zhang, Yan Spatially resolved D-T₂ correlation NMR of porous media
- P64 Bergman, Elad Accelerating imaging with a unilateral NMR scanner
- P65 Cai, Qing The new application of low-field NMR technology in petroleum evaluation
- P66 Codd, Sarah Biofilm detection using low field magnetic resonance
- P67 Deng, Feng Motion effects and corrections of NMR scanning measurement
- P69 Oligschläger, Dirk The Mini-MOUSE - a miniaturized NMR sensor
- P70 Galvosas, Petrik Inverse Laplace transform strategies suitable to inhomogeneous NMR magnet systems
- P71 Guangzhi Liao Study of NMR responses in particle packing models
- P72 Galvosas, Petrik Determining structural anisotropy of biological tissues using two-dimensional DDCOSY NMR
- P73 Guo, Baoxin Measuring soil moisture with slim-line logging NMR tool

- P74 Guo, Pan Unilateral magnet with solenoid RF probe for magnetic resonance analysis of core plugs
- P75 Guo, Pan A novel three-cylinder array NMR sensor with homogeneous spot or extended constant gradient
- P76 Hughes, Eric Green coffee bean quality studied by single-sided NMR
- P77 Jia, Zijian Portable NMR sensor for crude oil analysis
- P78 Nestle, Nikolaus Diffusion effects on contrast in profile NMR on liquid samples - a survey of experiences and some general criteria
- P79 Terada, Yasuhiko *In situ* living tree measurements using a 0.2 T permanent magnet
- P80 Wu, Boasong Research on the hydrogen index of flowing fluid in downhole NMR fluid analysis laboratory
- P81 Xu, Zheng Detecton of adulteration in olive oil with profile NMR sensors
- P82 Xu, Zheng A portable NMR sensor used for assessing the aging status of the silicone rubber insulator
- P83 Camp, Jules Development of a combined NMR and vibrational spectroscopic system for heterogeneous catalysis
- P84 Renshaw, Matthew *Operando* MR: Pore condensation in porous media at elevated temperature and pressure
- P85 Tamada, Daiki MR microscopy using a high T_c superconducting bulk magnet
- P86 Zhao, Jiangjie Probe design of slim downhole NMR fluid analyzer
- P87 Zhen, John Class D RF amplifier with amplitude modulation for 17 MHz NMR MOUSE sensor
- P88 Munz, Eberhard 3D water and lipid MR-microscopy of rape seed germination dynamics
- P89 Offer, Patrick NMR-microscopy of glass laminates
- P90 Peng, Yunan Quantitative ultra-fast MRI of powder dispersion
- P91 Richardson, Simon Viable isolated white matter: Microstructural MRI investigations at physiological temperature
- P92 Winisdorffer, Guillaume Investigation of apple parenchyma microstructure using MRI multi-exponential T2 relaxation and microporosity measurements
- P93 Prisner, Thomas Dynamic nuclear polarization at 9.2 T
- P94 Cheng, Jiajie Simulation of NMR response based on digital rock images
- P95 Kwamen, Rance Accelerated aging of plasticized PVC studied by NMR microscopy
- P96 Lian, Yuanfeng Application of adaptive compressed sensing algorithm to echo train de-noising in low field NMR logging
- P97 Wu, Yan Identify heavy oil combining NMR and conventional logs
- P98 Xiao, Dan Restricted k -space sampling in pure phase encode MRI

List of Posters by Author

Presenter	Title of Abstract	
Arbabi, Aidin	Average bubble size estimation in an upward vertical bubbly flow at a low magnetic field (0.2 T)	P49
Baker, Luke	<i>Operando</i> MR: Spatially-resolved NMR measurements of fixed bed heterogeneous catalytic reaction	P08
Bartlett, Oliver	Multiphase flow validation using magnetic resonance imaging	P50
Bayley, Paul	In situ, real-time visualisation of electrochemistry using magnetic resonance imaging	P09
Bergman, Elad	Accelerating imaging with a unilateral NMR scanner	P64
Bernin, Diana	Impact of salt on starch and gluten and on water migration in pasta studied with ^1H , ^{19}F , ^{23}Na and ^{35}Cl MRI/NMR	P10
Blümich, Bernhard	Portable NMR for practical analysis of ancient wall paintings	P40
Blythe, Thomas	Taking magnetic resonance into industrial applications	P11
Boyce, Christopher	Cross-validating magnetic resonance measurements of 3D cylindrical fluidized beds with predictions from a discrete element model	P12
Bräuer, Pierre	Effect of confinement on diffusion and dynamics of primary alcohols and non-ideal binary mixtures acetone-chloroform in	P13
Cai, Qing	The new application of low-field NMR technology in petroleum evaluation	P65
Camp, Jules	Development of a combined NMR and vibrational spectroscopic system for heterogeneous catalysis	P83
Chen, Chen	Direct multi-nuclear magnetic resonance imaging studies of controlled drug release	P14
Cheng, Jiajie	Simulation of NMR response based on digital rock images	P94
Codd, Sarah	Biofilm detection using low field magnetic resonance	P66
D'Agostino,	Nuclear magnetic resonance relaxometry in heterogeneous	P15
Dalitz, Franz	Monitoring of liquid reactions by low-field NMR spectroscopy	P16
de Kort, Daan	Shear-induced aggregation of bacterial-cellulose dispersions as viewed by rheo-NMR and PFG ^{19}F -NMR nanoprobe diffusometry	P51
de Kort, Daan	Nanoprobe diffusometry in soft materials by frequency- and time-domain ^{19}F and ^1H NMR at low and high field strengths	P52
Deng, Feng	Motion effects and corrections of NMR scanning measurement	P67
Douglass, Bradley	Investigating fluctuations in wormlike micelles solutions with spectroscopic imaging and snap-shot GERVAIS velocimetry	P53
Eriksson, Stefanie	Microscopic fractional anisotropy with q -MAS PGSE	P54
Fabich, Hilary	Ultra-short echo time magnetic resonance imaging in heterogeneous materials	P17

Faure, Pamela	Following transport of contrast agent particle in sand and soil column	P55
Galvosas, Petrik	Inverse Laplace transform strategies suitable to inhomogeneous NMR magnet systems	P70
Galvosas, Petrik	Determining structural anisotropy of biological tissues using two-dimensional DDCOSY NMR	P72
Göbel, Katharina	MR microscopy of organotypic hippocampal slice cultures: First steps to an in vitro approach for experimental epilepsy research	P01
Goora, Frederic	Arbitrary magnetic field gradient waveform correction using an impulse response based pre-equalization technique	P18
Guangzhi Liao	Study of NMR responses in particle packing models	P71
Guo, Baoxin	Measuring soil moisture with slim-line logging NMR tool	P73
Guo, Pan	Unilateral magnet with solenoid RF probe for magnetic resonance analysis of core plugs	P74
Guo, Pan	A novel three-cylinder array NMR sensor with homogeneous spot or extended constant gradient	P75
Guthausen, Gisela	NMR-diffusometry and relaxometry for the characterization of (double) emulsions in life science	P19
Hasihi, Tomoyuki	Live mice imaging with a 14.1T narrow-bore NMR magnet heading for <i>f</i> MRI by using an independent digital console and gradient	P02
Herrling, Maria	Magnetic resonance imaging of local flow velocity profiles in biofilm carriers from waste water treatment	P56
Hughes, Eric	Green coffee bean quality studied by single-sided NMR	P76
Jia, Zijian	Portable NMR sensor for crude oil analysis	P77
Jiang, Sijia	New method for down-hole two-MNR fluid analysis	P57
Kampf, Thomas	Uncovering supercritical CO ₂ wood dewatering via interleaved ¹ H-	P20
Kartaeusch, Ralf	Eddy currents reduction for an accessible mobile magnet	P21
Kartaeusch,	Noise reduction for an accessible mobile magnet	P23
Komlosh, Michal	Mapping the pore size distribution of a glass microcapillary array phantom using d-PFG MRI	P03
Kuczera, Stefan	Fast RARE velocimetry for curved flow in Couette geometry	P58
Kwamen, Rance	Accelerated aging of plasticized PVC studied by NMR microscopy	P95
Lesbats,	MRI exploration of the low-density lipoprotein (LDL) transport in an	P04
Lian, Yuanfeng	Application of adaptive compressed sensing algorithm to echo	P96
Liao, Dongliang	Combining NMR log and other logs evaluate shale formation	P22
Ling, Nicholas	Characterization of oilfield emulsion using nuclear magnetic resonance	P59
Liu, Kang	Application of wavelet transform de-noising to MRI based on background noise estimation	P05
Lutecki, Michal	PFG NMR Studies of CO ₂ in metal -organic framework structures	P24

MacMillan, Bryce	Determining the role of grain roughness on evaporation from porous media with MRI	P25
Merz, Steffen	Monitoring the drying stages of a porous medium by MRI and unilateral NMR	P26
Michan, Alison	PGF-NMR study of tortuosity in silicon electrodes	P27
Mitchell, Jonathan	Spatial resolution in low-field studies of oil recovery	P28
Mohoric, Ales	PGSE pore microscopy	P29
Munz, Eberhard	3D water and lipid MR-microscopy of rape seed germination dynamics	P88
Nestle, Nikolaus	Diffusion effects on contrast in profile NMR on liquid samples - a survey of experiences and some general criteria	P78
Offer, Patrick	NMR-microscopy of glass laminates	P89
Oligschläger, Dirk	The Mini-MOUSE - a miniaturized NMR sensor	P69
Peng, Yunan	Quantitative ultra-fast MRI of powder dispersion	P90
Prisner, Thomas	Dynamic nuclear polarization at 9.2 T	P93
Qiao, Zhi	Concentration mapping with MRI using compressed sensing	P45
Ramskill,	Application of magnetic resonance velocimetry to investigate	P30
Renshaw,	<i>Operando</i> MR: Pore condensation in porous media at elevated	P84
Richardson, Simon	Viable isolated white matter: Microstructural MRI investigations at physiological temperature	P91
Roussel, Tangi	Ultrafast in vivo imaging sequence for Bruker MRI	P41
Sarou-Kanian,	Spectroscopic dimension in MRI of materials with ultra short	P31
Schmaus, Christine	Compressed Sensing for the imaging of two-phase falling film flow	P42
Sersa, Igor	MR microscopy in assessment of dental caries	P06
Seymour, Joseph	Using Spatial Resolution to Enhance MR Data Interpretation of Transport Processes during Gelation	P32
Shikhov, Igor	Spatially resolved relative permeability with simulated and experimental 1D NMR imaging	P33
Siow, Bernard	Diffusion-diffusion Exchange Spectroscopic Imaging (DEXSI) MRI in a	P43
Smith, Catherine	Investigating the molecular behaviour of ionic liquids using magnetic resonance	P60
Song, Yi-Qiao	Diffusion time correlation experiment	P44
Tamada, Daiki	MR microscopy using a high T_c superconducting bulk magnet	P85
Terada, Yasuhiko	<i>In situ</i> living tree measurements using a 0.2 T permanent magnet	P79
Teymouri, Yadollah	The effect of swelling and annealing on the molecular mobility and phase composition of domains in Low Density Polyethylene	P34
Utsuzawa, Shin	Motion effect in NMR well logging	P35
Vallatos, Antoine	Measurement of transport and reaction in vortical flows using magnetic resonance	P61
Vieß, Jochen	Mapping of spin-density and -velocity in membranes	P36

Walton, Jeffrey	Characterization of Mn doped Si nano particles designed as MRI contrast agents	P37
Winisdorffer, Guillaume	Investigation of apple parenchyma microstructure using MRI multi-exponential T2 relaxation and microporosity measurements	P92
Wu, Boasong	Research on the hydrogen index of flowing fluid in downhole NMR fluid analysis laboratory	P80
Wu, Yan	Identify heavy oil combining NMR and conventional logs	P97
Wu, Yuting	Quantification of chemical composition using Bayesian NMR	P46
Xia, Yang	The dependences of multi-component T2 measurement in cartilage and gel phantom on the imaging sequences and specimen solutions	P07
Xiao, Dan	k - t acceleration in pure phase encode MRI to monitor dynamic flooding processes in rock core plugs	P47
Xiao, Dan	Restricted k -space sampling in pure phase encode MRI	P98
Xie, Qingming	Noise reduction for NMR with regularization-heursure algorithm	P48
Xu, Ruina	Density-driven Fingering during brine-water miscible displacement in two inclining porous media layers by magnetic resonance image	P62
Xu, Zheng	Detecton of adulteration in olive oil with profile NMR sensors	P81
Xu, Zheng	A portable NMR sensor used for assessing the aging status of the silicone rubber insulator	P82
Zhang, Yan	Spatially resolved D-T ₂ correlation NMR of porous media	P63
Zhao, Jiangjie	Probe design of slim downhole NMR fluid analyzer	P86
Zhen, John	Class D RF amplifier with amplitude modulation for 17 MHz NMR MOUSE sensor	P87
Zheng,	Measurement of intra-particle chemical compositions in a trickle-	P38
Ziovas, Kostas	Bayesian sphere sizing for food foam research	P39

Author Index

Abe, Y.	P2	Blümler, P.	O21
Adair, A.	O32	Blythe, T.	P11
Adams, A.	P95	Borisjuk, L.	P88
Adegbite, O.	O32	Boyce, C. M.	P12
Alexander, D. C.	O14, P91, P43	Bräuer, P.	P13
Allen, D.	O29	Bray, J. M.	Y15, P32
Alonso, J.	O2	Britton, M. M.	P9, O26, O38, P60, P61
Altobelli, S. A.	O9		
An, T.	O39	Brown, J. R.	P32
Anferov, V.	P68	Brox, T. I.	O25, P53, P58
Anferova, S.	P68	Cai, Q.	P65
Antony, J.	P78	Camp, J.	P83
Arbabi, A.	P49	Canivet, J.	P24
Arns, C. H.	O30, P33	Cankar, K.	P6
Atchinson, D. A.	O16	Casanova, F.	O12
Atkins, T. M.	P37	Cehin-Delval, C.	P39
Atkinson, K. D.	O4	Chen, C.	P14
Auer, D. P.	P4	Cheng, J.	P94, P71
Auth, M.	P89	Cheng, L. J.	P48
Baker, L.	P8	Chuanhang, H.	O34
Balcom, B. J.	O3, P18, P74, P75, P25, O32, P47, P98	Ciobanu, L.	O27
		Codd, S. L.	Y15, Edu2, P66, Y11, P32, O35
Barskiy, D. A.	O5	Colpitts, B. G.	P18
Bartlett, O.	P50	Creber, S. A.	O33
Basser, P. J.	P3	d 'Esposito, A.	P43
Bats, N.	P24	D'Agostino, C.	P13, P15
Baumgartner, S.	O36	Dalitz, F.	P16
Bayley, P. M.	P9	Dal-Ri Jr., G.	P95
Beech, J.	O29	Danieli, E.	O12
Behr, V. C.	P20, O1	Davenport, A. J.	P9
Beloil, J-C.	Y13	de Kort, D. W.	P51, P52
Bencsik, M.	P78, P81	Decoville, M.	Y13
Benjamini, D.	P3	Deng, F.	P68, P71, P77, P22, P48
Benning, M.	O29, Y14, P45		
Bergman, E.	P64	Dennis, J. S.	P12
Bernewitz, R.	P19	Denysenkov, V.	O6/P93
Bernin, D.	P10	d'Eurydice, M. N.	O11, P70, P72
Bessada, C.	P31	Devaux, M.	P92
Blake, A.	P46	Dorkes, A. C.	O18
Blümich, B.	P40, O12, P69, P73, P95, P89, Y16, P34, P36, P63	Douglass, B. S.	O25, P53, P58
		Drießle, T.	P21, P23
		Duckett, S. B.	O4

Dykstra, R.	P87	Guo, P.	P74, P75
Eccles, C.	P87	Guthausen, G.	P16, P19, P56
Eriksson, S.	P54	Haas, C.	P1
Fabich, H. T.	P17, P45	Haase, A.	O13
Farrusseng, D.	P24	Haber, A.	YI6
Faure, P.	P55	Haber-Pohlmeier, S.	P73
Feng, D.	O34, P67	Haishi, T.	P2, O8
Fidler, F.	P21, P23, O1	Hall, I. P.	O18
Fischer, R.	O25	Hardy, E. H.	P78
Fischer, T.	P36	Heaton, N.	P35
Folmer, B.	P76	Heil, W.	O21
Fordham, E. J.	P28	Hennig, J.	O24
Forsyth, M.	P9	Herrling, M.	P56
Franich, R. A.	P20	Hertel, S. A.	YI2
Fridjonsson, E. O.	YI1, O33, P59	Hiebert, R.	P66
Fritzing, B.	P29	Highton, L. A. R.	O4
Frydman, L.	Plen1, P41	Hisatsune, T.	P2
Fuchs, J.	P20, P88	Hoeben, F.	P51
Fukita, A.	P79	Hoeben, F. J. M.	P52
Fukushima, E.	O9	Holland, D. J.	O29, P12, P17, P42, P46
Galvosas, P.	O25, P53, O11, P70, P72, YI2, P58	Horn, H.	P56
Garcia-Naranjo, J. C.	P74, P75	Howlett, P. C.	P9
Geffroy, F.	O27	Huabing, L.	P67
Gerlach, J.	P1	Hubbard, P. L.	P43
Gibson, A.	O14	Hughes, E.	P76, P90, P39
Gladden, L. F.	P8, O29, P11, P13, P14, P15, P24, P27, P90, P30, P84, P42, YI4, P46, P62, P38	Hughes-Riley, T.	O18
Glöggler, S.	P69	Hugon, C.	O2
Göbel, K.	P1	Hunter, M.	YI2
Goora, F. G.	P18, O32	Hürlimann, M. D.	O10, P35
Goudappel, G. J. W.	P51	Jain, V.	P35
Gouws, G.	P87	Jakob, P.	O28
Green, G. G. R.	O4	Jakob, P. M.	P21, P23, P88, O1
Green, R. A.	O4	Janka, O.	P37
Grey, C. P.	O22, P27	Janssen, H. M.	P51, P52
Grunewald, E.	P66	Jaschtschuk, D.	P36
Gruschke, O.G.	P1	Jelescu, I. O.	O27
Guangzhi, L.	O34, P67	Jia, Z.	P77
Guiga, A.	O2	Jiang, P.	P62
Guillet, P.	P55	Jiang, S.	P57, P86
Guo, B.	P73	Jin, C.	P4
		Johns, M. L.	P50, YI1, O33, P59
		Joudiou, N.	YI3
		Kamberger, R.	P1

Karpuk, S.	O21	Lilburn, D. M. L.	O18
Kartäusch, R.	P21, P23	Ling, N. N. A.	P59
Kasthurirangan, S.	O16	Liu, H.	O39, P68, O11
Katz, Y.	O31	Liu, J. F.	P48
Kauzlarich, M.	P37	Liu, K.	P5
Keeler, J.	Edu1	Lizhi, X.	O34, P67
Kersemans, V.	O29	Lloyd, L. S.	O4
Kirkland, C. M.	P66	Lother, S.	O1
Kittler, W.	O25	Louat, F.	YI3
Kleinnijenhuis, M.	O19	Louie, A. Y.	P37
Komlosh, M. E.	P3	Lutecki, M.	P8, P24, P84
Koptyug, I. V.	O5	Lythgoe, M. F.	P91, P43
Koroleva, V. D. M.	O10	MacMillan, B.	P25
Korvink, J. G.	P1, O24	Maiwald, M.	P16
Kose, K.	P2, O8, P85, P79	Mandal, S.	O10, O23
Kovtunov, K. V.	O5	Mantle, M. D.	P8, O29, P13, P83, P14, P15, P24, P90, P84, P46, P39
Kreckel, L.	P16		
Kristl, J.	O36		
Krummenacker, J.	O6/P93		
Kuczera, S.	O25, P53, P58	Marica, F.	P74
Kuijk, A.	P51	Mariette, F.	P92
Kullmann, W. H.	O1	Massiot, D.	P31
Kwamen, R.	P95, P34	Mastikhin, I. V.	P49
Lackner, S.	P56	Mattea, C.	O20
Lahaye, M.	P92	May, E. F.	P59
Langton, M.	P10	McDowell, A. F.	O9
Lasic, S.	P54	McGregor, J.	P83, P84
Law, S. J.	O38	Meder, R.	P20
Le Bihan, D.	O27	Meersmann, T.	P4, O7
Ledwig, M.	P21, P23	Meldrum, T.	P40
Leftin, A.	P41	Même, S.	YI3
Lesbats, C.	P4	Merz, S.	P26
Leskes, M.	P27	Mewis, R. E.	O4
Leupold, J.	P1	Meyer, C. H.	Edu3
LeVan, P.	P1	Michan, A. L..	P27
Levitt, M. H.	Edu4	Michel, E.	P55
Li, R.	P62	Mikac, U.	O36
Li, X.	O39, P22	Mitchell, J.	P11, P15, P28
Lian, Y.	P96	Mohoric, A.	P29
Liao, D.	P22	Moldin, A.	P10
Liao, G.	O39, P94, P71, P74, P77, P57, P96, P22, P80, P97, P86	Moriwaki, S.	P79
		Morris, P. G.	O18
		Morris, R. H.	P81
		Mulla, Y.	P51
Liao, G. Z.	P48	Munz, E.	P88
Liberman, A.	P64	Musse, M.	P92

Nakamura, T.	P85	Roussel, T.	P41
Nemeth, L.	P6	Rückert, M. A.	O1
Nestle, N.	P78	Ryan, C.	P35
Neugebauer, P.	O6/P93	Sakellariou, D.	O2
Neugodova, M.	P55	Salnikov, O. G.	O5
Neveu, S.	P55	Sammartino, S.	P55
Nevo, U.	P64, O31, P3	Sanderlin, A. B.	O35
Newling, B.	O32	Sandquist, D.	P20
Newton, M. I.	P81	Sarda, Y.	P64
Nieto, C.	P24	Sarou-Kanian, V.	Y13, P31
Nikiel, A.	O21	Scheler, U.	P29
Nonhebel, E.	O40	Schmaus, C.	P42
Norris, D.	O19	Schneider, T.	P91
Nowozin, S.	P46	Schönlieb, C.	O29
Offer, P.	P89	Schuchmann, H. P.	P19
Oligschläger, D.	P69	Scott, S. A.	P12
Oppelt, D.	P21, P23	Sederman, A. J.	P8, P50, P11, P17, P27, P90, P30, P84, P42, Y14, P62, P38, P39
Paciok, E.	Y16, P36		
Pagadala, S.	O40		
Panagiotaki, E.	P91		
Paulsen, J.	P44	Seginer, A.	P41
Pauly, J. M.	O17	Sepe, A.	O36
Pavlovskaya, G. E.	P4, O18, O7	Sepehrband, F.	O16
Peng, Y.	P90	Serša, I.	P6
Perez Pelletero, J.	P24	Seymour, J. D.	Y15, P66, Y11, P32, O35
Perlo, J.	O12, P73		
Pohlmeier, A.	P26	Shaw, D. E.	O18
Polidoric, A.	P55	Sherick, M. L.	P32
Pope, J. M.	O16	Shikhov, I.	O30, P33
Prisner, T.	O6/P93	Shokri, N.	P25
Proverbio, A.	O14	Singh, M. P.	P37
Prüssmann, K.	Plen2	Siow, B.	O14, P91, P43
Quellec, S.	P92	Six, J. S.	O18, O7
Quero, F.	P78	Skovpin, I. V.	O5
Ramaioli, M.	P90	Smart, S.	O29
Ramskill, N. P.	P30	Smith, C. F.	P60
Rao, V. V.	P32	Soleilhavoup, A.	O2
Renshaw, M. P.	P8, P84	Song, Y.	O10, O23, P44
Repetto, M.	O21	Staniland, J.	P28
Richardson, S.	P91	Stapf, S.	O20
Rigby, S. P.	P4	Steglich, T.	P10
Roberts, S. T.	P84	Stepisnik, J.	P29
Röding, M.	P10	Stitt, E. H.	P11
Rodriguez, A.	P76	Stupic, K. F.	O18, O7
Rodts, S.	P55	Tamada, D.	P85
Rössler, E.	O20	Tayler, A. B.	Y14, P45

Terada, Y.	O8, P79	Xiao, L.	O39, P94, P68,
Teymouri, Y.	P34		P71, P77, P57,
Tianlin, A.	P67		P22, P80, P97,
Tissier, N.	P78		P48, P86
Togashi, K.	P2	Xie, Q. M.	P48
Topgaard, D.	P10, P54, O37	Xie, R.	P5
Tullney, K.	O21	Xu, R.	P62
Utsuzawa, S.	P35	Xu, W.	P71
Valkonen, T.	O29	Xu, Z.	P81, P82
Vallatos, A.	P61	Yan, W.	O34
Van As, H.	P51, P52, O40	Yang, P.	P65
van Cappellen van Walsum, A.	O19	Yang, Y.	P65
Van Dusschoten, D.	P26	Yeredor, A.	P64
van Duynhoven, J. P. M.	P51, P52	York, A. P. E.	P11, P83, P30
Van Landeghem, M.	YI6	Zhang, H.	P35, O19
Vanderborgh, J.	P26	Zhang, T. Z.	O9
Veen, S.	P51	Zhang, X.	P22
Velikov, K. P.	P51	Zhang, Y.	P65, P63
Vereecken, H.	P26	Zhang, Z.	O39, P71
Verkicharla, P. K.	O16	Zhao, J.	P57, P86
Vidmar, J.	P6	Zhao, S.	P82
Vieß, J.	P89, P36	Zhen, J.	P87
Vogel, P.	O1	Zheng, Q.	P38
Vogt, S. J.	O33, P32, O35	Zhivonitko, V. V.	O5
von Elverfeldt, D.	P1	Zia, W.	P40
von Harbou, E.	P45	Zielinski, L.	P35
Walsh, D.	P66	Zijian, J.	P67
Walton, J. H.	P37	Ziovas, K.	P39
Wang, N.	P5, O15, P7	Zong, F.	P68, P72
Warren, W. S.	Plen3		
Watzlaw, J.	P69		
Wei, X.	O34		
Wessling, M.	P36		
Wiedermann, D.	O19		
Wilson, A. G.	P46		
Winisdorffer, G.	P92		
Wintzheimer, S.	P21, P23		
Wong, J. E.	P36		
Wu, B.	P77, P80, P86		
Wu, W.	P97		
Wu, Y.	P57, P80, P97, P46		
Xia, Y.	P5, O15, P7		
Xiao, D.	P47, P98		

List of Delegates

Mohamed **Ainte**, MRRC, University of Cambridge, UK, E-mail: ma601@cam.ac.uk

Belinda **Akpa**, University of Illinois at Chicago, USA, E-mail: belinda.akpa@gmail.com

Daniel **Alexander**, University College London, UK, E-mail: d.alexander@cs.ucl.ac.uk

Stephen **Altobelli**, ABQMR, USA, E-mail: salto@nmr.org

Matthias **Appel**, Shell International E&P, USA, E-mail: matthias.appel@shell.com

Peter **Aptaker**, Lapiacian Ltd, UK, E-mail: psa@laplacian.co.uk

Aidin **Arbabi**, University of New Brunswick, Canada, E-mail: aidin.arbabi@unb.ca

Christoph **Arns**, University of New South Wales, Australia, E-mail: c.arns@unsw.edu.au

Luke **Baker**, MRRC, University of Cambridge, UK, E-mail: lb550@cam.ac.uk

Bruce **Balcom**, University of New Brunswick, Canada, E-mail: bjb@unb.ca

Bhim Bahadur **Bam**, ENI SpA, E & P Division, Italy, E-mail: bhim.bam@eni.com

Oliver **Bartlett**, MRRC, University of Cambridge, UK, E-mail: ob268@cam.ac.uk

Paul **Bayley**, University of Cambridge, UK, E-mail: pmb57@cam.ac.uk

Martin **Benning**, MRRC, University of Cambridge, UK, E-mail: mb941@cam.ac.uk

Elad **Bergman**, Tel Aviv University, Israel, E-mail: elad.bergman@gmail.com

Diana **Bernin**, Swedish NMR Center, Sweden, E-mail: diana.bernin@gu.se

Bernhard **Blümich**, RWTH Aachen University, Germany, E-mail: bluemich@itmc.rwth-aachen.de

Peter **Blümmler**, University of Mainz, Germany, E-mail: bluemler@uni-mainz.de

Thomas **Blythe**, MRRC, University of Cambridge, UK, E-mail: tb483@cam.ac.uk

Céline **Boutin**, CEA, France, E-mail: celine.boutin@cea.fr

Christopher **Boyce**, MRRC, University of Cambridge, UK, E-mail: cmb206@cam.ac.uk

Joshua **Bray**, Montana State University, USA, E-mail: joshua.bray@coe.montana.edu

Melanie **Britton**, University of Birmingham, UK, E-mail: m.m.britton@bham.ac.uk

Timothy **Brox**, Victoria University of Wellington, New Zealand, E-mail: tim.brox@vuw.ac.nz

Pierre **Bräuer**, MRRC, University of Cambridge, UK, E-mail: pierre.braeuer@googlemail.com

Qing **Cai**, Niumag Company, China, E-mail: cq2565096@163.com

Jules **Camp**, MRRC, University of Cambridge, UK, E-mail: [jcyj2@cam.ac.uk](mailto:jcj2@cam.ac.uk)

Chen **Chen**, MRRC, University of Cambridge, UK, E-mail: charliechen0322@gmail.com

Luisa **Ciobanu**, Neurospin/CEA, France, E-mail: luisa.ciobanu@cea.fr

Sarah **Codd**, Montana State University, USA, E-mail: scodd@coe.montana.edu

Andrew **Coy**, Magritek, New Zealand, E-mail: andrew@magritek.com

Franz **Dalitz**, Karlsruhe Institute of Technology, Germany, E-mail: franz.dalitz@kit.edu

Ernesto **Danieli**, RWTH Aachen University, Germany, E-mail: danieli@itmc.rwth-aachen.de

Daan **de Kort**, Wageningen University, The Netherlands, E-mail: daan.dekort@wur.nl

Feng **Deng**, China University of Petroleum, China, E-mail: dengfeng0719@hotmail.com

Bradley **Douglass**, Victoria University of Wellington, New Zealand, E-mail: Bradley.Douglass@vuw.ac.nz

Toni **Driessle**, Pure Devices GmbH, Germany, E-mail: ajs40@cam.ac.uk

Simon **Duckett**, University of York, UK, E-mail: simon.duckett@york.ac.uk

Robin **Dykstra**, Victoria University of Wellington, New Zealand, E-mail: robin.dykstra@vuw.ac.nz

Stefanie **Eriksson**, Lund University, Sweden, E-mail: stefanie.eriksson@fkem1.lu.se

Hilary **Fabich**, MRRC, University of Cambridge, UK, E-mail: htf21@cam.ac.uk

Paméla **Faure**, Univeristé Paris-Est, France, E-mail: pamela.faure@ifsttar.fr

Michelle **Flückiger**, Wiley VCH Verlag GmbH & Co KGaA, Germany, E-mail: chemphyschem@wiley-vch.de

Einar **Fridjonsson**, University of Western Australia, Australia, E-mail: einar.fridjonsson@uwa.edu.au

Lucio **Frydman**, Weizmann Institute of Sciences, Israel, E-mail: lucio.frydman@weizmann.ac.il

Eiichi **Fukushima**, ABQMR, USA, E-mail: eiichi@abqmr.com

Petrik **Galvosas**, Victoria University of Wellington, New Zealand, E-mail: petrik.galvosas@vuw.ac.nz

Lynn **Gladden**, MRRC, University of Cambridge, UK, E-mail: lfg1@cam.ac.uk

Katharina **Göbel**, University Medical Center Freiburg, Germany, E-mail: katharina.goebel@uniklinik-freiburg.de

Fred **Goora**, University of New Brunswick, Canada, E-mail: f.goora@unb.ca

Gert-Jan **Goudappel**, Unilever R&D, The Netherlands, E-mail: gert-jan.goudappel@unilever.com

Derrick **Green**, Green Imaging Technologies, Canada, E-mail: Derrick.Green@GreenImaging.com

Clare **Grey**, University of Cambridge, UK, E-mail: cpg27@cam.ac.uk

Dieter **Gross**, Bruker Biospin GmbH, Germany, E-mail: Dieter.Gross@Bruker-Biospin.de

Oliver **Gruschke**, University of Freiburg, Germany, E-mail: oliver.gruschke@imtek.uni-freiburg.de

Baoxin **Guo**, RWTH Aachen, ITMC, Germany, E-mail: Guo@itmc.rwth-aachen.de

Pan **Guo**, University of New Brunswick, Canada, E-mail: b904h@unb.ca

Gisela **Guthausen**, Karlsruhe Institute of Technology, Germany, E-mail: gisela.guthausen@kit.edu

Axel **Haase**, Technical University Munich, Germany, E-mail: axel.haase@tum.de

Tomoyuki **Haishi**, MRT Technology Inc, Japan, E-mail: haishi@mrtechnology.co.jp

Jürgen **Hennig**, University Medical Center Freiburg, Germany, E-mail: juergen.hennig@uniklinik-freiburg.de

Maria Pia **Herrling**, Karlsruhe Institute of Technology, Germany, E-mail: maria.herrling@kit.edu

Stefan **Hertel**, Victoria University of Wellington, New Zealand, E-mail: stefan.hertel@vuw.ac.nz

Daniel **Holland**, MRRC, University of Cambridge, UK, E-mail: djh79@cam.ac.uk

Eric **Hughes**, Durham University, UK, E-mail: erichughesabc@gmail.com

Martin **Hurlimann**, Schlumberger, USA, E-mail: hurlimann@slb.com

Peter **Jakob**, University of Würzburg, Germany, E-mail: Peter.Jakob@physik.uni-wuerzburg.de

Zijian **Jia**, China University of Petroleum, China, E-mail: jjazijian111@gmail.com

Zhao **Jiangjie**, China University of Petroleum, China, E-mail: zhaojiangjie100@163.com

Michael **Johns**, University of Western Australia, Australia, E-mail: michael.johns@uwa.edu.au

Barry **Jones**, Oxford Instruments Magnetic Resonance, UK, E-mail: barry.jones@oxinst.com

Nicholas **Joudiou**, CNRS, France, E-mail: nicolas.joudiou@cns-orleans.fr

Robert **Kamberger**, University of Freiburg, IMTEK, Germany,
E-mail: robert.kamberger@imtek.uni-freiburg.de

Thomas **Kampf**, University of Würzburg, Germany, E-mail: thomas.kampf@physik.uni-wuerzburg.de

Ralf **Kartäusch**, MRB Research Center, Germany, E-mail: ralf.kartaesch@physik.uni-wuerzburg.de

Yaniv **Katz**, Tel Aviv University, Israel, E-mail: yanivkatz86@gmail.com

James **Keeler**, University of Cambridge, UK, E-mail: jhk10@cam.ac.uk

Jürgen **Kolz**, Magritek GmbH, Germany, E-mail: juergen@magritek.com

Michal **Komlosh**, Uniformed Services, USA, E-mail: komloshm@yahoo.com

Igor **Koptyug**, International Tomography Center, SB, RAS, Russia, E-mail: koptyug@tomo.nsc.ru

Katsumi **Kose**, University of Tsukuba, Japan, E-mail: kose@bk.tsukuba.ac.jp

Stefan **Kuczera**, Victoria University of Wellington, New Zealand, E-mail: stefan.kuczera@vuw.ac.nz

Markus **Küppers**, RWTH Aachen, ITMC, Germany, E-mail: kueppers@itmc.rwth-aachen.de

Susan **Law**, University of Birmingham, UK, E-mail: sjl609@bham.ac.uk

Clementine **Lesbats**, University of Nottingham, UK, E-mail: msxcl1@nottingham.ac.uk

Malcolm **Levitt**, University of Southampton, UK, E-mail: mhl@soton.ac.uk

Guangzhi **Liao**, China University of Petroleum, China, E-mail: liaoquangzhi@cup.edu.cn

Dongliang **Liao**, China University of Petroleum, China, E-mail: liaodl.sripe@sinopec.com

Nicholas **Ling**, University of Western Australia, Australia, E-mail: lingn01@student.uwa.edu.au

Kang **Liu**, China University of Petroleum, China, E-mail: wendaoguangli@163.com

Michal **Lutecki**, MRRC, University of Cambridge, UK, E-mail: ml572@cam.ac.uk

Bryce **MacMillan**, University of New Brunswick, Canada, E-mail: Bryce@unb.ca

Mick **Mantle**, MRRC, University of Cambridge, UK, E-mail: mdm20@cam.ac.uk

Bertram **Manz**, Magritek Limited, New Zealand, E-mail: bertram@magritek.com

Thomas **Meersmann**, University of Nottingham, UK, E-mail: thomas.Meersmann@nottingham.ac.uk

Steffen **Merz**, IBG-3, Germany, E-mail: s.merz@fz-juelich.de

Craig **Meyer**, University of Virginia, USA, E-mail: cmeyer@virginia.edu

Alison **Michan**, University of Cambridge, UK, E-mail: alm77@cam.ac.uk

Urša **Mikac**, Jozef Stefan Institute, Slovenia, E-mail: urska.mikac@ijs.si

Jonathan **Mitchell**, MRRC, University of Cambridge, UK, E-mail: jm600@cam.ac.uk

Alex **Mohoric**, University of Ljubljana, Slovenia, E-mail: ales.mohoric@fmf.uni-lj.si

Eberhard **Munz**, University of Würzburg, Germany, E-mail: amunz@physik.uni-wuerzburg.de

Nikolaus **Nestle**, BASF SE, Germany, E-mail: nikolaus.nestle@basf.com

Benedict **Newling**, University of New Brunswick, Canada, E-mail: bnewling@unb.ca

Thomas **Oerther**, Bruker Biospin GmbH, Germany, E-mail: Thomas.Oerther@Bruker-Biospin.de

Patrick **Offer**, RWTH Aachen, ITMC, Germany, E-mail: offer@itmc.rwth-aachen.de

Dirk **Oligschläher**, RWTH Aachen, ITMC, Germany, E-mail: oligschlaeger@itmc.rwth-aachen.de

Eva **Paciok**, RWTH Aachen, ITMC, Germany, E-mail: paciok@itmc.rwth-aachen.de

John **Pauly**, Stanford University, USA, E-mail: pauly@stanford.edu

Galina **Pavlovskaya**, University of Nottingham, UK, E-mail: Galina.Pavlovskaya@nottingham.ac.uk

Yunan **Peng**, MRRC, University of Cambridge, UK, E-mail: yp229@cam.ac.uk

James **Pope**, Queensland University of Technology, Australia, E-mail: j.pope@qut.edu.au

Thomas **Prisner**, University of Frankfurt, Germany, E-mail: Prisner@Chemie.Uni-Frankfurt.de

Alessandro **Proverbio**, University College London, UK, E-mail: alessandro.proverbio.09@ucl.ac.uk

Klaas **Prüssmann**, University of Zürich, Switzerland, E-mail: pruessmann@biomed.ee.ethz.ch

Zhi (George) **Qiao**, MRRC, University of Cambridge, UK, E-mail: zq211@cam.ac.uk

Nicholas **Ramskill**, MRRC, University of Cambridge, UK, E-mail: npr24@cam.ac.uk

Jean Pierre **Renou**, INRA, France, E-mail: jean-pierre.renou@clermont.inra.fr

Matthew **Renshaw**, MRRC, University of Cambridge, UK, E-mail: mpr34@cam.ac.uk

Simon **Richardson**, University College London, UK, E-mail: simon.richardson.09@ucl.ac.uk

Scott **Riley**, Tecmag Inc, USA, E-mail: sriley@tecmag.com

Ian **Robertson**, Oxford Instruments, UK, E-mail: ian.robertson@oxinst.com

Tangi **Roussel**, Weizmann Institute of Sciences, Israel, E-mail: tangi.roussel@weizmann.ac.il

Dimitrios **Sakellariou**, CEA Saclay, France, E-mail: dsakellariou@cea.fr

Vincent **Sarou-Kanian**, CNRS-CEMHTI, France, E-mail: sarou@cnrs-orleans.fr

Christine **Schmaus**, MRRC, University of Cambridge, UK, E-mail: cs587@cam.ac.uk

Andy **Sederman**, MRRC, University of Cambridge, UK, E-mail: ajs40@cam.ac.uk

Igor **Sersa**, Jozef Stefan Institute, Slovenia, E-mail: igor.sersa@ijs.si

Joseph **Seymour**, Montana State University, USA, E-mail: jseymour@coe.montana.edu

Igor **Shikhov**, University of New South Wales, Australia, E-mail: igor.shikhov@student.unsw.edu.au

Matsyendra Nath **Shukla**, University of Glasgow, UK, E-mail: MatsyendraNath.Shukla@glasgow.ac.uk

Jiang **Sijia**, China University of Petroleum, China, E-mail: jsj0925@126.com

Bernard **Siow**, University College London, UK, E-mail: b.siow@ucl.ac.uk

Joseph **Six**, University of Nottingham, UK, E-mail: msxjs@nottingham.ac.uk

Catherine **Smith**, University of Birmingham, UK, E-mail: cxs800@bham.ac.uk

Po-Wah **So**, King's College London, UK, E-mail: po-wah.so@kcl.ac.uk

Yi-Qiao **Song**, Schlumberger, USA, E-mail: ysong@slb.com

Siegfried **Stapf**, TU Ilmenau, Germany, E-mail: siefried.stapf@tu-ilmenau.de

Daiki **Tamada**, University of Tsukuba, Japan, E-mail: daiki.tamada@gmail.com

Alexander **Taylor**, MRRC, University of Cambridge, UK, E-mail: abt31@cam.ac.uk

David **Taylor**, M R Solutions Ltd, UK, E-mail: david.taylor@mrsolutions.co.uk

Yasuhiko **Terada**, University of Tsukuba, Japan, E-mail: terada@bk.tsukuba.ac.jp

Yadollah **Teymouri**, RWTH Aachen, ITMC, Germany, E-mail: Teymouri@itmc.rwth-aachen.de

Daniel **Topgaard**, Lund University, Sweden, E-mail: daniel.topgaard@fkem1.lu.se

Shin **Utsuzawa**, Schlumberger, USA, E-mail: sutsuzawa@slb.com

Antoine **Vallatos**, University of Birmingham, UK, E-mail: axv982@bham.ac.uk

Henk **Van As**, Wageningen University, The Netherlands, E-mail: henk.vanas@wur.nl

Jochen **Vieß**, RWTH Aachen University, Germany, E-mail: Viess@itmc.rwth-aachen.de

Anna **Vilter**, University of Würzburg, Germany, E-mail: avilter@physik.uni-wuerzburg.de

Patrick **Vogel**, University of Würzburg, Germany, E-mail: Patrick.Vogel@physik.uni-wuerzburg.de

Sarah **Vogt**, University of Western Australia, Australia, E-mail: sarah.vogt@uwa.edu.au

Jeffrey **Walton**, University of California, USA, E-mail: jhwalton@ucdavis.edu

Warren S **Warren**, Duke University, USA, E-mail: warren.warren@duke.edu

Ian **Wilkes**, Whitford Ltd, UK, E-mail: iwilkes@whitfordww.com

Guillaume **Winisdorffer**, IRSTEA, France, E-mail: g.winisdorffer@irstea.fr

Baosong **Wu**, China University of Petroleum, China, E-mail: wu_baosong@sohu.com

Wensheng **Wu**, China University of Petroleum, China, E-mail: wwsheng@cup.edu.cn

Yuting **Wu**, MRRC, University of Cambridge, UK, E-mail: yw316@cam.ac.uk

Yang **Xia**, Oakland University, USA, E-mail: xia@oakland.edu

Lizhi **Xiao**, China University of Petroleum, China, E-mail: xiaolizhi@cup.edu.cn

Dan **Xiao**, University of New Brunswick, Canada, E-mail: d.x@unb.ca

Ranhong **Xie**, China University of Petroleum, China, E-mail: xieranhong@cup.edu.cn

Qingming **Xie**, Chongqing Institute of Geology & Mineral Resources, China, E-mail: mingming8842@126.com

Ruina **Xu**, Tsinghua University, China, E-mail: manyaxu@gmail.com

Zheng **Xu**, Nottingham Trent University, UK, E-mail: zheng.xu@ntu.ac.uk

Andrew **York**, Johnson Matthey Technology Centre, UK, E-mail: ayork@matthey.com

Gary **Zhang**, University College London, UK, E-mail: gary.zhang@ucl.ac.uk

Yan **Zhang**, RWTH Aachen, ITMC, Germany, E-mail: yzhang@itmc.rwth-aachen.de

John **Zhen**, Victoria University of Wellington, New Zealand, E-mail: john.zhen@ecs.vuw.ac.nz

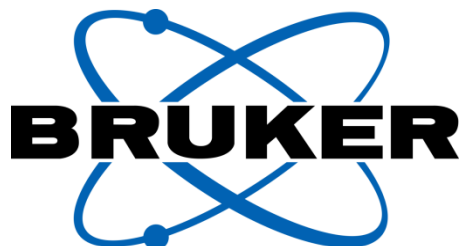
Qingyuan **Zheng**, MRRC, University of Cambridge, UK, E-mail: qz240@cam.ac.uk

Kostas **Ziovas**, MRRC, University of Cambridge, UK, E-mail: kr236@cam.ac.uk

Corporate Sponsorship of the 12th ICMRM

We gratefully acknowledge financial support from:

Gold level



EPSRC

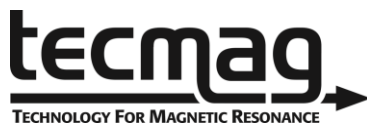
Engineering and Physical Sciences
Research Council

Silver level



Schlumberger

Other sponsors and exhibitors



OXFORD
UNIVERSITY PRESS